A Systematic, Large Phase Space Study of Pion ($\pi^{\pm}$), Kaon ($K^{\pm}$), and Proton (p,$\bar{p}$) Production in Au+Au Heavy-Ion Collisions from the RHIC Beam Energy Scan Program at STAR

By

Christopher Edward Flores
B.S. Physics (St. Mary's University) 2010
B.A. Mathematics (St. Mary's University) 2010
M.S. Physics (University of California, Davis) 2012

Dissertation

Submitted in partial satisfaction of the requirements for the degree of

Doctor of Philosophy

in

Physics

in the

Office of Graduate Studies

of the

University of California

Davis

Approved:

Daniel A. Cebra, Chair

Manuel Calderón de la Barca Sánchez

Ramona Vogt

Committee in Charge

2017

To Gina,

May the completion of this chapter

be the beginning of many new ones.

Contents

List of Figures

List of Tables

Abstract

A Systematic, Large Phase Space Study of Pion ($\pi^{\pm}$), Kaon ($K^{\pm}$), and Proton (p,$\bar{p}$) Production in Au+Au Heavy-Ion Collisions from the RHIC Beam Energy Scan Program at STAR

The Beam Energy Scan (BES) program at the Relativistic Heavy-Ion Collider (RHIC) was designed to explore the phase diagram of nuclear matter. In this document data collected using the Solenoidal Tracker at RHIC (STAR) during the BES program are used to study the production of pions ($\pi^{\pm}$), kaons ($K^{\pm}$), and protons ($p, \bar{p}$) across seven collision energies, $\sqrt{s_{NN}}$ = 7.7, 11.5, 14.5, 19.6, 27.0, 39.0, and 62.4 GeV. The results are presented differentially in nine centrality bins and over as broad a transverse mass and rapidity range as the detector capabilities allow. The yields of each particle species are first presented as transverse mass spectra. The spectra are then fit with spectral shapes to extract rapidity density distributions. Full phase space yields are also obtained for the case of the pion. These results help characterize the nature of the medium produced in heavy-ion collisions. In particular, the dependence of the medium's chemistry, expansion properties, and thermal condition on collision energy, event centrality, and kinematic phase space are now accessible using the results of this study.

Acknowledgments

The completion of this thesis represents the end point in a trajectory of education that has been unbroken for over a quarter century. At each step along the way I have had the good fortune of being surrounded by encouraging people. There are too many to mention by name, but I would like to express my gratitude to each and in particular to those below.

To my advisor, Daniel Cebra: thank you for the many long hours of discussion and instruction, especially early in my graduate career, which set me on this successful course. I credit you for my development into an independent scientist. I will miss the group barbecues and our planning of them.

To my advisor, Manuel Calderón de la Barca Sánchez: thank you for your endless and infectious enthusiasm for this subject. Thank you, as well, for your constant willingness to engage in deep conversations about technical topics.

To the graduate students who were my senior contemporaries: Anthony Kesich, Michael Gardner, Samantha Brovko, and Evan Sangaline, thank you all for the help and encouragement in my initial years of being a graduate student and for making the UC Davis Nuclear Group such an enjoyable environment to be a part of.

To the graduate students who are my junior contemporaries: I have come to know the field of heavy-ion physics much better for having helped you. Thank you for the opportunity to do so. Thank you in particular to Kathryn Meehan for never letting me get away with anything. May each of you be successful in your own career.

To Roppon Picha and Jennifer Klay: thank you for the time and effort you invested in your theses. I have found them to be invaluable and have referred to them constantly. I have done my best to model my thesis after your superb examples in hopes it will be as valuable to others as yours have been to me.

To Juan Romero: thank you for your careful first readings of this document and for the many comments and suggestions. This thesis is far better because of your efforts.

To my thesis committee: Daniel Cebra, Manuel Calderón de la Barca Sánchez, and Ramona Vogt, thank you for all your comments, suggestions, and corrections.

To my parents, Edward and Connie Flores, and my siblings, Matthew and Nicole Flores: thank you all for your love and support. Surely it was your influence which ultimately set the track for the successful completion of this degree.

To my wonderful future wife, Gina: thank you for your endless love, support, encouragement, and patience. When I needed inspiration, the thought of you always provided it. May we always look back at our time and Davis fondly and may our future hold more wonders than we can imagine.

Chapter 1

Introduction

At its core the study of physics is the study of the transformation of energy from one form or state to another. In performing these studies we observe changes in structures which result from energy transformations and characterize the processes in which the transformations occur. This thesis concerns itself with the study of the energy transformations and structures relevant to the processes in the field of heavy-ion physics. In this sense we observe the particles (structures) that result from collisions (energy transformations) between heavy-ions traveling near the speed of light. The resulting particles and their energy distributions allow the properties of the infinitesimally existent medium produced during the collision to be inferred. It is the properties of the medium that are the sought-after results which give the field its purpose.

The medium of interest is a hot, dense form of nuclear matter in which the protons and neutrons lose their distinctness and their constituents form a continuous phase of matter known as the Quark-Gluon Plasma (QGP). The properties of this plasma are desired because they permit the study of the Strong Force and hence Quantum-Chromodynamics (QCD). No other mechanism, save exotic astrophysical phenomena, permits such a direct study of this type of matter.

The goal of the enclosed work is an ambitious one, easily many times larger than any single similar analysis attempted previously. It aims to measure the yield of pions ($\pi^{\pm}$), kaons ($K^{\pm}$), and protons ($p, \bar{p}$) in heavy-ion events ranging across seven collision energies, up to three event configurations, nine centrality bins, and across as broad a

two-dimensional kinematic phase space as possible. In doing so it desires to shed light on how the medium produced in the heavy-ion collisions evolves to its final state.

In this first chapter, a brief overview of the relevant aspects of the field are presented to give context to the work presented in this thesis. We begin by discussing the field generally and then proceed to build a case for the importance of the present analysis.

1.1 Ultra-Relativistic Heavy-Ion Physics

The field of heavy-ion physics has been evolving from its origins in the middle of the twentieth century when Enrico Fermi and Lev Davidovich Landau each published theories which became the foundational principles of the field. In this section we briefly investigate the history and development of the field by discussing its essential highlights. Where relevant we provide primary sources for the interested reader. We begin with the theoretical foundations of the field and then proceed to the experimental results.

1.1.1 Theoretical Foundations (1950-1990)

In his 1951 paper simply titled *High Energy Nuclear Events* [1], Fermi first develops a statistical model for explaining the number of π mesons produced in low energy nucleon collisions. He then extends his thoughts to consider high energy nucleon collisions:

> "In discussing the collision of two nucleons with extremely high energy one can simplify the calculations by assuming that all the various particles produced are extreme relativistic and that thermo-dynamics may be applied instead of a detailed statistical computation of the probabilities of the various events. [...]
>
> The extremely high energy density that is suddenly formed in the volume Ω will give rise to multiple production of pions and of pairs of nucleons and anti-nucleons. Since both kinds of particles are extreme relativistic, the energy density will be proportional to the fourth power of the temperature, T, as in Stefan's law.
>
> The pions, like the photons, obey the Bose-Einstein statistics. Since we fur-

ther assume that the temperature is so high that the rest mass is negligible, their energy momentum relationship will be the same as for the photons. Consequently the Stefan's law for the pions will be quite similar to the ordinary Stefan's law of the black body radiation."

Fermi's insight is that the emission of mesons from a high energy nuclear collision can be modeled similarly to the emission of photons from an object radiating as a black body. This has the important implication that the medium resulting from the nuclear collision must have thermally equilibrated. Both Fermi's thermodynamic treatment of the particle production and its implication of an intermediate state of thermal equilibrium are ideas which are central to the field of heavy-ion physics in the present some seven decades later.

Essential as they are to the field of heavy-ion physics, Fermi's idea of particle production was developed by considering single nucleon-nucleon interactions and largely forewent understanding of the intermediate stages between the initial collision and particle emission. In 1953 Landau considered what the initial conditions of a nucleus-nucleus condition may be [2]. As described in [3] he posited the system resulting from a nucleus-nucleus collision begins at rest in the center of mass frame and then expands according to relativistic hydrodynamics. This implies that there is some transient medium whose constituents interact. The expansion continues until the interaction cross-section of the produced particles is negligible at which point the system is said to "freeze-out." Interestingly Landau expected the temperature at freeze-out to be comparable to the pion mass.

The combined ideas of Fermi and Landau lead to a notion of a thermally equilibrated, transient state of matter. Could this be a new type of matter? A new phase of nuclear matter? Arguably the next foundational step in the field was taken by Rolf Hagedorn and Johann Rafelski in their 1980 paper entitled *Hot Hadronic Matter and Nuclear Collisions* [4]. In it, the pair use a Statistical Bootstrap Model previously developed by Hagedorn to conclude:

"[. . .] we have shown how a theory of hadronic matter that includes important features of hadronic interactions and limiting hadronic temperatures may be formulated and applied to the description of relativistic heavy ion collisions."

In particular, the paper argues that for very large collision energies the limiting hadronic temperature is of order 160 MeV; a quantity remarkably consistent with the pion mass predicted to be the freeze-out temperature by Landau. The term "limiting temperature" is used by the authors to describe a boundary beyond which "the usual hadronic world ceases to exist." This implies that either new physics must be found or else a new phase of matter must exist - a phase of deconfined hadronic matter - the Quark Gluon Plasma (QGP).

Theoretical evidence for the existence of QGP continued to mount with the advent of lattice QCD. Analytic QCD calculations often diverge at finite energy scales due to the large coupling constant, α_s. To get around this problem theorists discretize the space-time continuum onto a lattice of points and simulate QCD matter using computers. Despite the (retrospectively) minimal computational resources available in the late 1980's, simplifying assumptions permitted simulations which predicted a phase transition in QCD matter. In his 1988 paper *Lattice QCD at Finite Temperature: A Status Report*, Karsch offers one of the first quantitative predictions for the QCD critical temperature: $T_c = 197 - 254$ MeV. [5] He concludes in part:

> "Algorithms have been developed which have small enough systematic errors so that they can be used for simulations with small quark mass on large lattices. First results are encouraging. They have established the existence of a first order chiral phase transition [...] the results found in the pure gauge sector seem to be a good guide for continuum physics."

Karsch's value for the critical temperature is larger than the pion mass predicted by Landau and the limiting temperature of Hagedorn, but given the many assumptions required to make the model computable it is remarkably close. The substantial improvement of computational resources in the intervening decades has allowed for increasingly precise investigations of QCD matter using lattice algorithms. Today, models are able to simulate QCD matter past several leading orders in baryon, strangeness, and electric charge potentials. These models predict phase transition temperatures of around 154 MeV [6].

Discussion quickly turned from the hypothetical existence of QGP to its possible properties. Numerous signatures of QGP were proposed, far too many to consider here, but we make one exception for the theory of quarkonia suppression proposed by Matsui and Satz due to its unambiguity. In their 1986 paper *J/ψ Suppression by Quark-Gluon Plasma Formation* ([7]) the pair argue that a mechanism such as Debye Screening, which was previously observed and studied in electro-magnetic plasma, should also exist in the QGP. They suggest that just as Debye Screening impedes the interaction between two free electromagnetic charges in an electromagnetic plasma so too will the interactions between two color charges be impeded in a colored plasma. In particular they predict the production of the bound state of charm and anti-charm quark ($c\bar{c}$) known as the J/ψ meson should be reduced. They say in part :

> "If [...] the c$\bar{\text{c}}$ production occurs in a nuclear collision, and if such collisions result in a quark-gluon plasma, then the produced c$\bar{\text{c}}$ finds itself in a deconfining environment. Provided the temperature of this environment is sufficiently high [...] then the resonance interaction cannot become operative and J/Ψ production will be prohibited."

Their discussion includes two important conditionals which are now used as essential tools in the study of QGP. First, they propose that the suppression of the J/Ψ meson will be an indicating signature of the QGP. This idea has now been extended to other forms of quarkonia such as the Υ meson. Second, they condition the suppression of the state by noting that the temperature of the medium must be sufficiently high. In terms of Debye screening this means that the screening radius must be smaller than the binding radius. This temperature dependence has been exploited to measure the initial temperature of the QGP and has given rise to the "Sequential Melting" model [8] which predicts that the more tightly bound a state of quarkonia is the less it will be suppressed.

1.1.2 Experimental Progress and the Onset of Deconfinement (1990-2008)

With an exciting new phase of matter to find, the stage was set for the experimental side of heavy-ion physics to gain traction and make headway. The first heavy-ion accelerators were brought online by modifying existing proton accelerators. A booster was added to the Alternating Gradient Synchrotron (AGS) at Brookhaven National Lab in 1991 which allowed it to accelerate a variety of ions. In particular, the heaviest ion it was able to accelerate was gold (Au^{79+}) resulting in collisions with fixed targets at energies in the range $\sqrt{s_{NN}} = 2.6 - 4.85$ GeV. Soon after the Super Proton Synchrotron (SPS) at CERN began colliding ions as well. The heaviest ion it was able to accelerate was lead (Pb^{82+}) which resulted in fixed target collisions at energies between $\sqrt{s_{NN}} = 6.4 - 17.3$ GeV.

In this section we focus on the cumulative efforts of the experiments at the AGS and SPS in the area of light hadron production and their interpretation within a statistical model of particle production. In particular we focus on understanding the four signatures colloquially referred to as the *kink, horn, step,* (sometimes collectively referred to as the Signs of Marek [9, 10]) and *dale* as they have been used by the NA49 collaboration to claim observation of the onset of deconfinement ([11]) and are of central importance to the physics goals of this thesis.

1.1.2.1 The Kink, Horn, and Step - The Signs of Marek

The Signs of Marek - so called because they were made explicit by Marek Gazdzicki in a series of papers [9, 10] - interpret the pion and kaon particle production collected at the AGS and SPS in the framework of a statistical model that can trace its origins back to the model develop by Fermi. The central idea is that a phase change in nuclear matter should result in an increase in the number of degrees of freedom available to the system. This is identical to phase change properties of normal matter; the melting of ice into water, for example, results in new rotational degrees of freedom available to water molecules. This increase in degrees of freedom is equally described as an increase in entropy.

What would be the signs of such a change in the degrees of freedom available to nuclear matter? Consider the initial constituents of a heavy-ion collision. The incoming nuclei

are composed of protons and neutrons which are themselves composed of up and down quarks. Naively, then, the particles resulting from the collision of two ions should be composed exclusively of up and down quarks. Since the pions are the lightest meson and made of such quarks it seems natural that as the collision energy increases it simply gets converted into proportionally more pions.

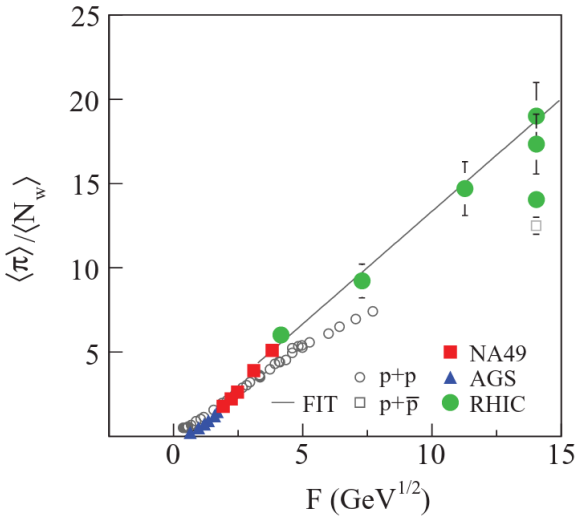

Figure 1.1: The mean pion multiplicity scaled by the number of wounded nucleons (participating nucleons) as a function of the Fermi quantity. The change in slope is referred to as the "kink". The figure was obtained from [11].

A test of this expectation is demonstrated in figure 1.1. It shows the ratio of the mean number of pions, $\langle\pi\rangle = 1.5(\langle\pi^+\rangle + \langle\pi^-\rangle)$, to the mean number of wounded/participant nucleons, $\langle N_w\rangle$, as a function of the Fermi measure. The quantity N_w represents the number of nucleons in the overlaping region of the two colliding nuclei and the Fermi measure is defined as $F = \left[(\sqrt{s_{NN}} - 2m_N)^3/\sqrt{s_{NN}}\right]^{1/4}$ and used because pion production is expected to have a more linear relationship with it than with $\sqrt{s_{NN}}$. In contrast to our naive expectation the rate of pion production changes near the low energy region of the NA49 measurements. This difference in slope is known as the "kink." This indicates, Marek would argue, that the energy deposited into the resulting medium from the heavy-ion collision is not simply used for an increase of pion production, but instead is used to create other particles such as kaons, which have strange quarks. The expectation that the system will produce strange quarks is natural since the strange quark is the next quark

in the mass hierarchy. It is the ability of the system to produce strange quarks, which indicates that new degrees of freedom are available to it.

Building on the observation of the kink, and expecting kaon production may be interesting to observe, the properties of the kaon are examined next. The left pane of figure 1.2 represents the ratio of the full phase space yields of positive kaons and pions. A curious maximum is observed around the low energy NA49 results - the same region as the kink. To understand the nature of this maximum we must defer to models. However, to do so we must have a quantity that we can directly compare to a model prediction. Such a quantity is the strangeness to entropy ratio, E_s. Experimentally this quantity is defined using the yields of the most numerous strangeness-carrying particles and the pion yield as a proxy for entropy as argued in the interpretation of the kink. Namely, the quantity is defined as: $E_s = (\langle\Lambda\rangle + \langle K^+ + K^-\rangle)/\langle\pi\rangle$.

The strangeness to entropy ratio is computed using the AGS and SPS results and shown in the right pane of figure 1.2 along with several model predictions. As expected the previously observed maximum in the data is present and referred to as the "horn." The only model which reproduces the structure of the horn is the Statistical Model of the Early Stage (SMES) [12] and it is also the only model which contains a phase change.

The final sign of Marek is called the "step" and refers to the energy independence observed in the inverse slope parameter, or temperature, of the kaon spectra in the region of the NA49 measurements. The feature can be observed clearly in figure 1.3. There are two important things to note about the contents of the figure. First, the temperature of the kaon spectra obtained from $p + p$ collisions is also included on the left pane of the figure. Although the $p + p$ values are widespread they do not seem to show any sign of a similar step feature, indicating that it is a property exclusive to heavy-ion collisions. Second, the figures include several model predictions. As before the only model which is able to reproduce the step feature is also the only model which includes a phase transition, Hydro+PT.

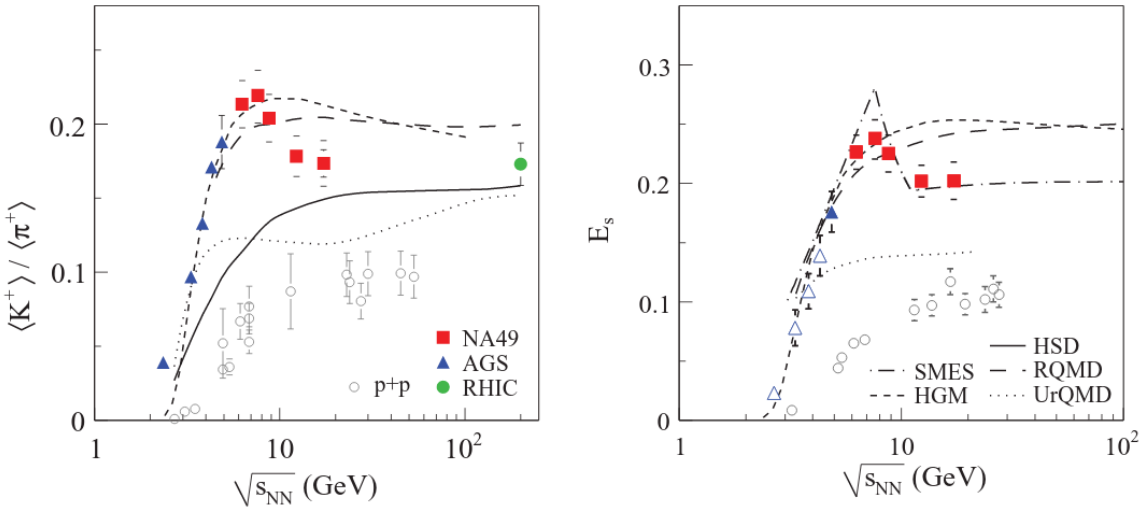

Figure 1.2: Left: The ratio of the full phase space yields of positive kaons and pions as a function of collision energy. Right: The strangeness to entropy ratio as defined in the text as a function of collision energy. The maximum in the low NA49 energy range is referred to as the "horn." The figure was obtained from [11].

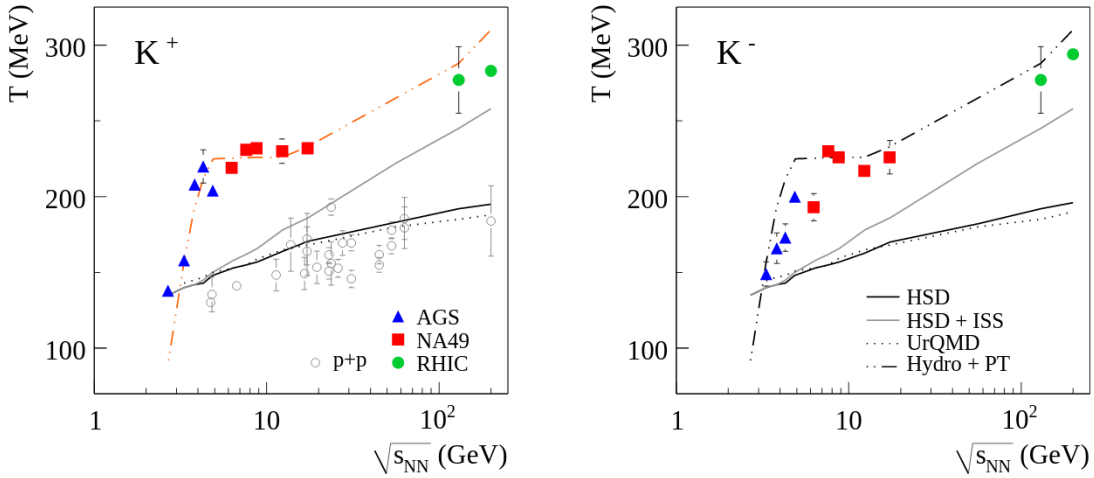

Figure 1.3: The inverse slope parameter, T, of kaons as a function of collision energy. The flat region in the energy range of the NA49 results is referred to as the "step." The figure was obtained from [13].

1.1.2.2 The Dale

We now return to a discussion of Landau Hydrodynamics. Recall that the central assumptions of the Landau model are that the medium produced by the collision of heavy-ions comes to thermal equilibrium and begins its expansion from a state of rest. As noted in

[14] several more simplifying assumptions can be made. First, that all chemical potentials vanish. Second, that the speed of sound in the medium is independent of its temperature. And third, that the system is composed of massless quarks and gluons so that its equation of state (EoS) can be described by a simple relationship between its pressure and energy density: $p = c_s^2\epsilon$, where p is the pressure, c_s is the speed of sound, and ϵ is the energy density. Under all of these conditions the shape of the rapidity distribution is predicted to be Gaussian as in equation 1.1 with width given by equation 1.2. Note that the quantity K is an overall normalization constant.

$$\frac{dN}{dy} = \frac{K^{1/4}}{\sqrt{2\pi\sigma_y^2}} \exp\left(-\frac{y^2}{2\sigma_y^2}\right) \tag{1.1}$$

$$\sigma_y^2 = \frac{8}{3}\frac{c_s^2}{1-c_s^4} \ln\left(\frac{\sqrt{s_{NN}}}{2m_p}\right) \tag{1.2}$$

The above assumptions may seem to be exceptionally naive, but in fact the rapidity density distributions of pions are very well described by single Gaussian functions over a wide range of energies. These include energies as low as those run at the AGS ([15]) and SPS ([16, 17]), at top RHIC energies ([18]), and, as will be shown in this thesis, at energies in between. The success of the simple Gaussian model lends credence to the underlying assumptions and encourages the use of the model for physics interpretations.

Using the measured widths of the rapidity density distributions of pions the speed of sound can be obtained from equation 1.2. The results of this process are shown in the right pane of figure 1.4. Alternatively, a default value for the speed of sound, $c_s^2 = 1/3$ (the speed of sound of a system of massless quarks and gluons), can be chosen and the ratio of the measured pion rapidity width to that expected by Landau hydrodynamics can be computed as shown in the left pane of figure 1.4. In both cases a clear minimum, referred to as the "dale," is observed at the low SPS energies. This minimum in the speed of sound is consistent with a system existing in a state of maximum compressibility or at its "softest" EoS. This maximum state of compressibility is a signature of a system in a mixed phase; in this case a mixed phase of hadronic and partonic matter.

As an aside, the author finds it humorous that the same physics can be observed as

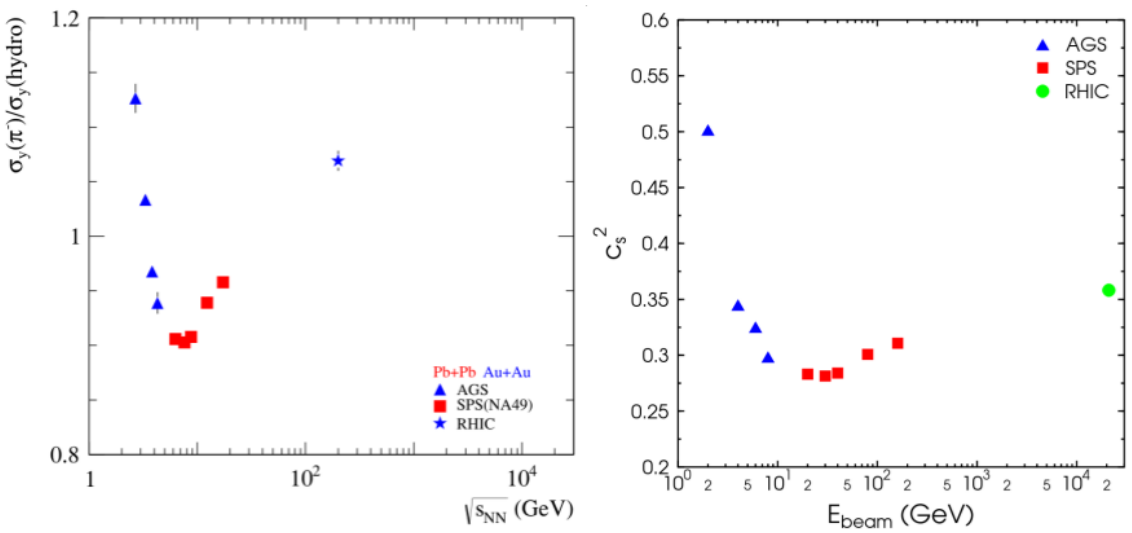

Figure 1.4: Left: The measured width of the pion rapidity density distribution scaled by the expected width using Landau hydrodynamics as a function of collision energy.[19] Right: The speed of sound, c_s, extracted from the numerators of the values on the left. [14] The term "dale" is used to describe the minimum seen in both.

the "Hot Chocolate Effect" [20]. In the demonstration found in reference [21] the instant coffee grounds contain trapped gasses. When the grounds are added to a hot liquid and stirred the gasses escape creating a mixed phase of air and liquid. In this case the speed of sound affects the resonant frequency of the glass+medium system and tapping on the glass repeatedly as the air rises to the top and out of solution results in a sound which rises in pitch. The system's speed of sound is at a minimum, and thus the system is most compressible, when the pitch is the lowest.

1.1.3 The Modern Era and QGP Signatures (2000-Present)

The heavy-ion reactions provided by the AGS and SPS lay important experimental, technical, and scientific foundations for the field, but the collision energies were too low to access many of the proposed signatures of the QGP. To find the QGP new accelerators were needed that would be able to provide heavy-ion interactions at much higher energies. Finally, the modern era of heavy-ion physics was ushered in by the Relativistic Heavy-Ion Collider (RHIC) at Brookhaven National Lab in the year 2000. It began providing Au+Au interactions at $\sqrt{s_{NN}} = 200$ GeV. Most recently the Large Hadron Collider

(LHC) at CERN began providing Pb+Pb collisions in 2010 at TeV scale energies.

Since RHIC began colliding beams of gold nuclei, many experimental measurements have been made that together provide strong evidence for the existence of the QGP. The general consensus of the field is that the QGP has indeed been found, but curiously none of the experimental collaborations have definitively claimed discovery. Most of the individual experimental results that have been reported are inconsistent with a purely hadronic medium, many are consistent with what would be expected if a QGP did exist, and yet several were inconsistent with theory at the time of their publication. In particular, no observable at the time showed dramatic fluctuations as a function of collision centrality as might be expected if QGP was formed only above some centrality. In this section we discuss a few of the many essential results that have been used to argue the case for the existence of QGP.

1.1.3.1 Collective Behavior: Elliptic Flow, Perfect Fluidity, and n_q Scaling

One of the many ways a medium can be characterized is via its collective behavior. That is, understanding how the medium as a whole moves can give insight into how its constituents interact within it. For example the large differences in the inter-molecular forces in water and molasses result in their very different flow properties. Similar ideas can be applied to the medium produced in heavy-ion reactions. In fact, many of the hydrodynamic properties used to model ordinary matter have been successfully modified and repurposed to describe the medium produced in heavy-ion collisions. As a result much of the vocabulary developed for use in describing the hydrodynamics of ordinary matter has been adopted for use in heavy-ion physics. In this subsection we consider one type of flow known as elliptic flow and discuss its interpretations.

As shown in figures 1.5 and 1.6, non-central collisions of heavy-ions result in almond-shaped overlap regions. As figure 1.6 also shows, the anisotropic geometry of the overlap region results in azimuthally-varying pressure gradients. The azimuthal angle is defined in the transverse plane which is the plane containing the impact parameter and a second vector perpendicular to the beam axis. Note that this is different from the reaction plane of figure 1.5 which is defined as containing the impact parameter vector and the beam

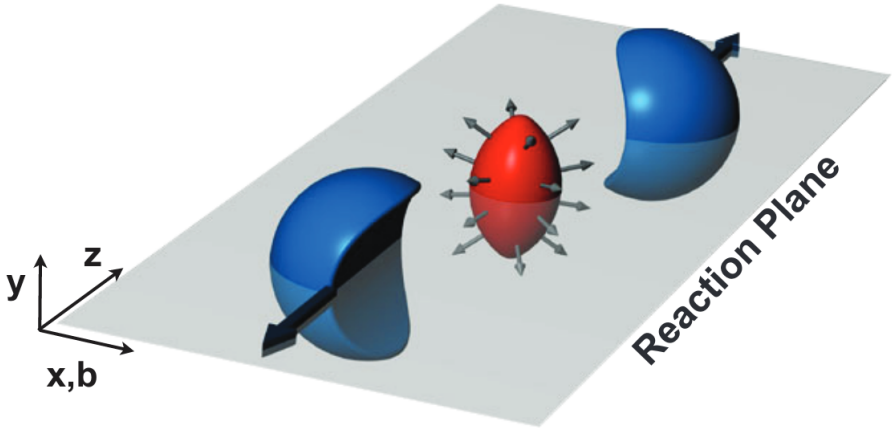

Figure 1.5: Schematic of the almond-shaped overlap region (red) resulting from a mid-central heavy-ion collision and the spectator nucleon volumes (blue). The plane (gray) defined as containing the beam axis and the impact parameter vector is known as the reaction plane. The figure was obtained from [22].

axis. The direction of the impact parameter vector, which is common to both the reaction plane and the transverse plane, is called simply *in-plane* and the direction in the transverse plane which is perpendicular to the impact parameter is called *out-of-plane*.

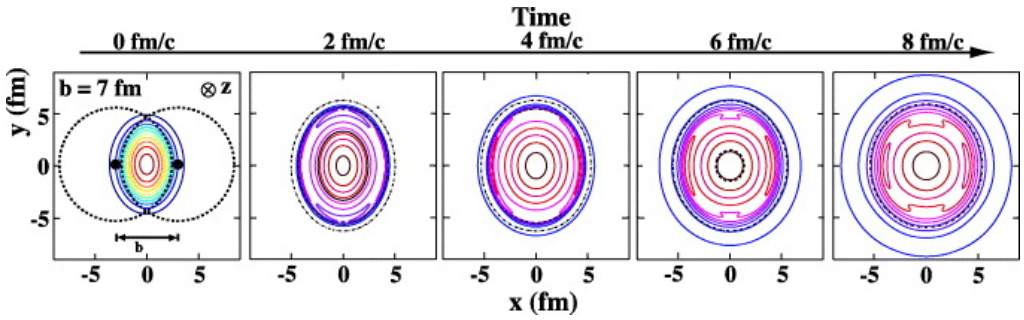

Figure 1.6: The evolution in time of the initial overlap region as it expands due to differing pressure gradients along its x and y coordinates. The figure was obtained from [22].

The azimuthally-varying pressure gradients impart correspondingly varying impulses to constituents of the medium. Thus, the geometric anisotropy of the initial overlap region manifests itself as a momentum anisotropy in the measured momenta of the resulting particles. This momentum anisotropy can be decomposed as a function of the azimuthal angle using a Fourier expansion, and the coefficients of the expansion (v_n) can be used

to understand how the medium flows. Of particular interest presently is the $n = 2$ coefficient because it describes the elliptic flow. Positive values of v_2 indicate that the in-plane pressure gradient is larger than the out-of-plane pressure gradient giving rise to in-plane elliptic flow. On the other hand, negative values of v_n indicate the opposite relationship between the pressure gradients and result in out-of-plane elliptic flow known as "squeeze-out."

As shown in figure 1.7 the sign of v_2 changes from positive to negative and back to positive again as a function of collision energy. Although interesting, this sign change is uncompelling, since this behavior is expected. For the lowest energy events, the heavy-ion reaction results in excited nuclei which de-excite by emitting particles in-plane due to conservation of angular momentum. For slightly higher energy events the spectator nucleons are still present around the overlap region during the time of initial expansion. This constrains the expansion in the in-plane direction forcing the expansion to be out-of-plane. As the collision energy increases, the spectator nucleons move away from the overlap region with sufficient speed so as not to impede the in-plane expansion and hence a positive v_2 results.

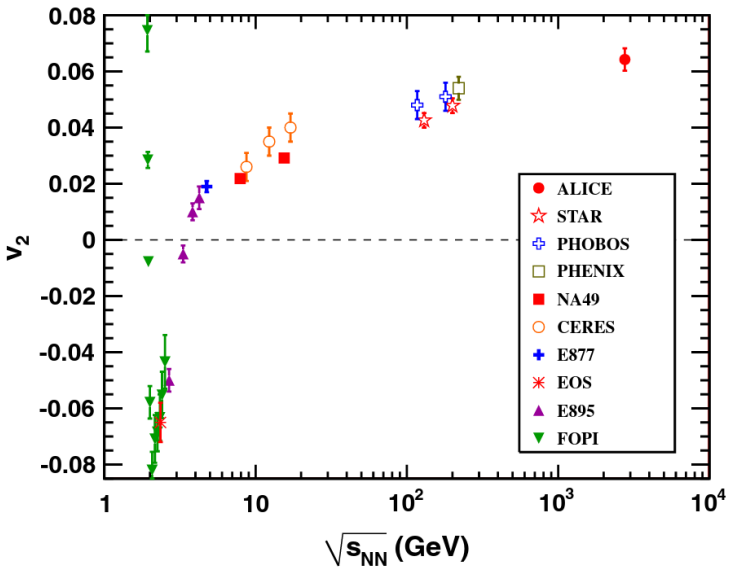

Figure 1.7: The collision energy dependence of elliptic flow. The figure was obtained from [23].

Another interesting but expected property of elliptic flow is its vanishing trend as a

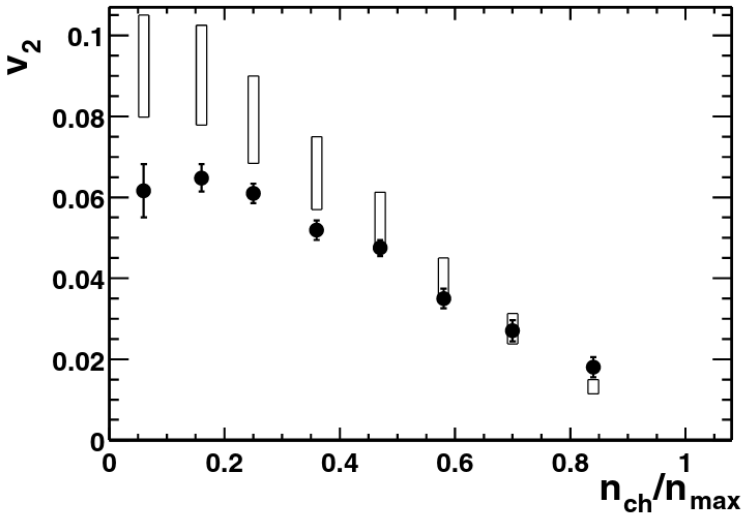

Figure 1.8: The centrality dependence of elliptic flow of all charged particles as measured in Au+Au collisions at $\sqrt{s_{NN}} = 130$ GeV at STAR (closed symbols) and a range of values expected in the hydrodynamic limit scaled by the eccentricity of the overlap region (open rectangles). The figure was obtained from [24].

function of centrality. As shown in figure 1.8, which reports the elliptic flow for charged particles as a function of centrality, the magnitude of v_2 decreases with increased centrality. This is expected since the almond-shapedness of the overlap region vanishes with increasing centrality.

What then is so compelling about elliptic flow? The answer comes in two forms, both of which illuminate properties of the medium: *constituent quark scaling* and *perfect fluidity*. First, consider the meaning of figure 1.9. It shows the elliptic flow results of identified particles as a function of transverse momentum. However both the v_2 and transverse momentum of each particle species have been scaled by the number of constituent quarks of the respective particle species. When scaled in this way the flow characteristics of all of the particles agree. This implies that when the pressure gradients are imparting flow dynamics to the medium the constituents of relevance are the individual quarks. This is argued to demonstrate that the medium has partonic degrees of freedom [25] - a necessary signature of a deconfined phase of QGP.

We began this subsection by describing how the equations of hydrodynamics have been modified and adapted for use in describing the expansion dynamics of the medium

resulting from heavy-ion collisions. We conclude it now by returning to hydrodynamics to infer an important property of the produced medium. In hydrodynamics a fluid is considered good if it converts very little of its kinetic energy into heat and hence has a low viscosity. A physical lower bound on the shear viscosity, computed using Anti-de Sitter/Conformal Field Theory (AdS/CFT) and known as the KSS Bound [26], imposes itself on a strongly-coupled medium with a large number of charges. In natural units and computed as the shear viscosity to entropy ratio the bound is given by $\eta/s = 1/4\pi \approx 0.08$. As observed in figure 1.10 the η/s ratio which most closely matches the data reported by STAR at $\sqrt{s_{NN}} = 200$ GeV is just twice that of the KSS bound. This indicates the medium produced in heavy-ion collisions a nearly perfect fluid and provides evidence that it is a strongly-coupled medium.

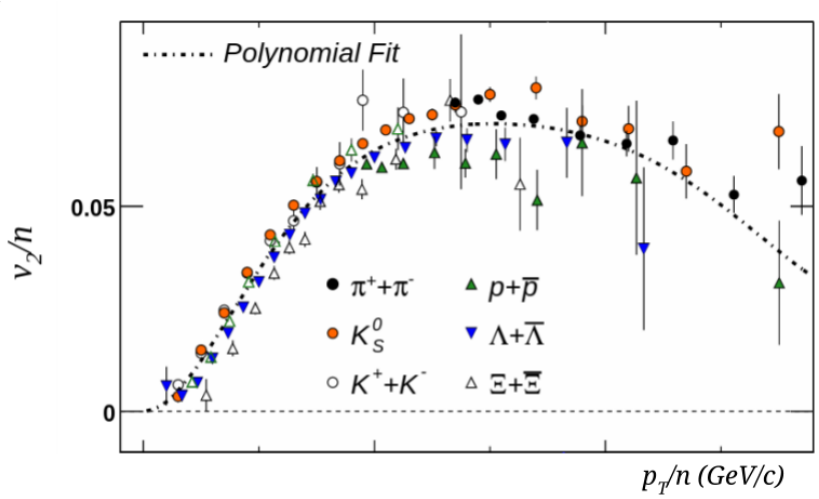

Figure 1.9: The elliptic flow of identified particles from Au+Au events at $\sqrt{s_{NN}} = 200$ GeV scaled by the number of their constituent quarks as a function of transverse momentum scaled identically. The figure was obtained from [25].

1.1.3.2 Hadron and Jet Suppression

If the matter created in heavy-ion collisions is a deconfined phase of partons, then colored probes should be sensitive to its effects. Unfortunately the short lifetime of the medium prevents the use of external probes, but particles produced by the collision itself can be used instead. In particular high-momentum partons which are the products of hard scatters in the initial phase of the collision are expected to lose energy via gluon radiation as

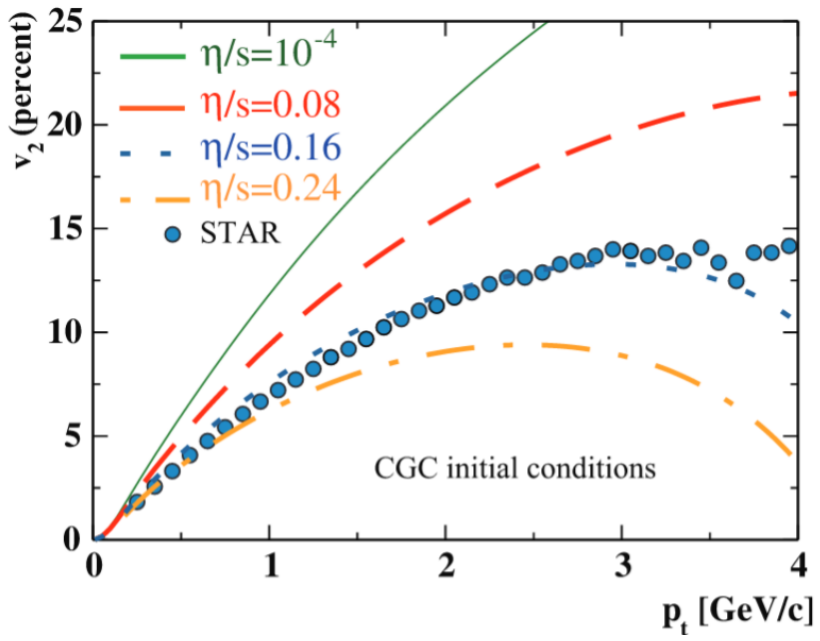

Figure 1.10: The elliptic flow of identified particles scaled by the number of their constituent quarks as a function of transverse momentum scaled identically. The figure was obtained from [22].

they transit the medium. As a result one should expect a suppression of high momentum hadrons. Two methods can be used to assess the level of suppression.

Jets are collections of highly collimated particles which originate from two or more high momentum partons which themselves resulted from hard scatters. These initial partons pull new quark-antiquark pairs out of the vacuum to produce colorless hadrons. In doing so they must conserve momenta and thus the resulting hadrons are highly aligned with the original partons. The original partons must also have conserved momenta from the hard scatter that produced them, so in the case of a scatter which produces two partons they must be back-to-back in the transverse plane and so too must be their resulting jets.

The original high-momentum hadrons are only in vacuum when they are outside of the medium produced by the bulk of the heavy-ion collision. If the initial hard scatter was near the edge of the overlap region as shown in figure 1.11 then one parton will traverse very little of the medium while the other must travel through its bulk. The parton which traverses the least amount of medium will lose the least energy and will be observed as a high-energy jet. This is known as the *leading jet*. The other parton will lose some or all

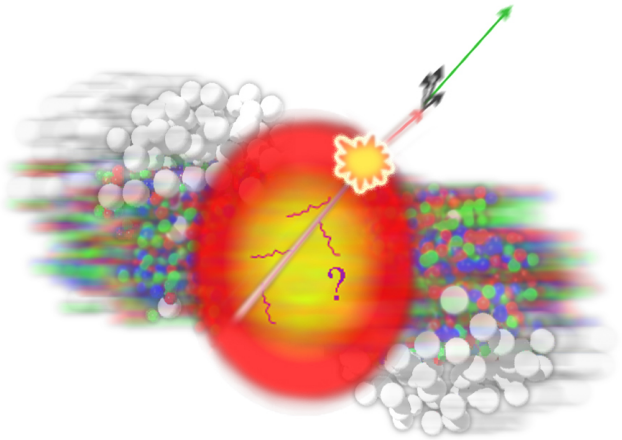

Figure 1.11: A cartoon schematic illustrating a hard scatter at the edge of the overlap region of a heavy-ion collision.

of its energy as it traverses the medium by means of radiative losses and be observed as a lower energy jet if at all. This is known as the *away-side jet*.

Figure 1.12 shows the results of a similar analysis [27]. Jet reconstruction is difficult and so the highest momentum hadron was used as a proxy for the leading jet. The distributions then consist of all other charged hadrons with $p_T > 2$ GeV/c and whose azimuthal angle is measured with respect to the leading hadron, $\Delta\phi$. In both the top and bottom panes the black histogram represents the results obtained from $p + p$ collisions. The two distinct peaks π radians apart are interpreted as the leading and away-side jets. The top pane also shows the distributions resulting from the collision of d+Au, which will produce a larger overlap volume than a $p + p$ collision, but smaller than a heavy-ion collision. The dual peaks remain. Finally, in the bottom plot the results from central Au+Au collisions are shown in blue stars. The away-side jet is clearly suppressed providing evidence that the produced medium affects colored objects.

In the same paper ([27]) the analyzers offer a second means of obtaining a similar understanding of the produced medium but as a function of its volume. As will be discussed in chapter 3, a naive conception of a heavy-ion collision could be that it is simply a superposition of many individual nucleon-nucleon collisions. As already noted, most high p_T (> 2 GeV/c) hadrons are the result of hard scatters. Such processes scale

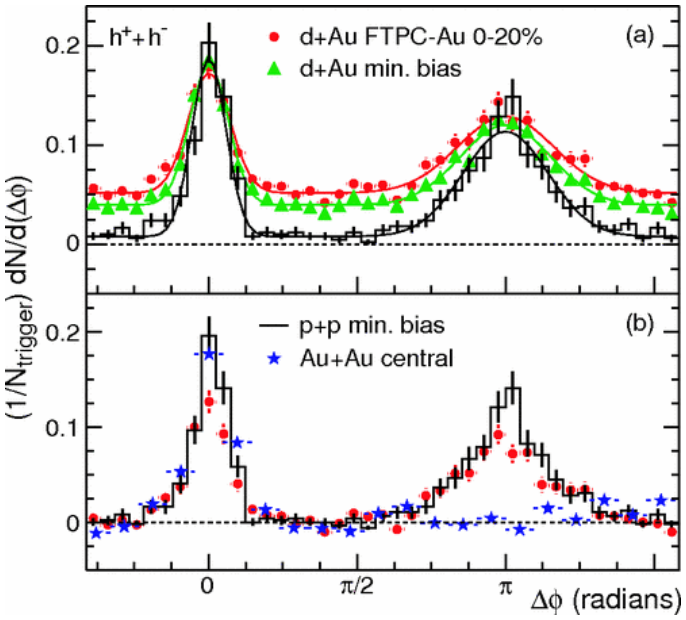

Figure 1.12: Two-particle azimuthal distributions. See text for details. The figure was obtained from [27].

as the number of binary collisions (nucleon-nucleon) collisions. If high p_T hadrons were produced equally in heavy-ion and p+p collisions, to within a scaling factor of the number of binary collisions, then arguably no interesting processes exist in the heavy-ion system.

Analyses such as these, which investigate the difference between a heavy-ion collision and a superposition of an equal number of nucleon-nucleon collisions, generally aim to compute a *nuclear modification factor*, denoted as R_{XX}. The subscripts represent the systems being compared. Figure 1.13 shows the ratio of the charged hadron spectra obtained from the d+Au and central Au+Au collision systems to the charged hadron spectrum obtained from $p + p$ events, R_{AA} (or in this case generalized to R_{AB} for comparison to the d+Au system). The ratio of the central Au+Au system shows suppression throughout the p_T range, but the trend is particularly striking for hadrons with high p_T. This again provides evidence that the medium produced in heavy-ion collisions is opaque to colored objects moving though it.

1.1.3.3 Quarkonia Suppression

We conclude our brief discussion of QGP signatures by returning to the signature initially proposed by Matsui and Satz - that of quarkonia suppression. Recall that their initial

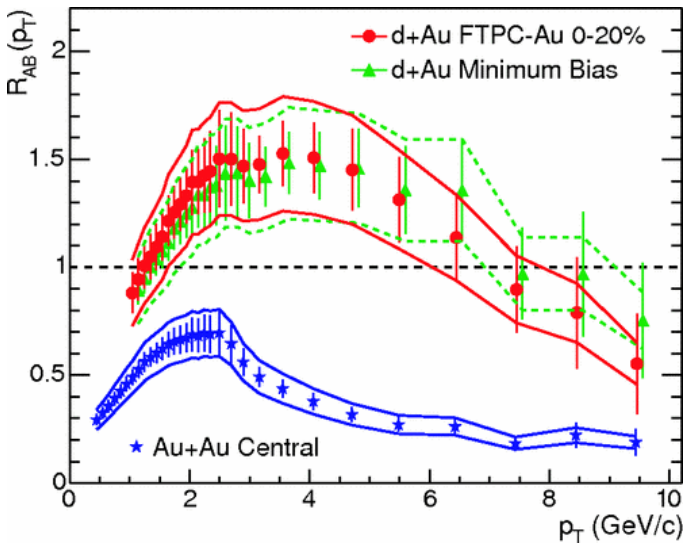

Figure 1.13: The nuclear modification factors of central Au+Au events (blue) and for d+Au (red,green) as a function of p_T. The Au+Au events show clear signs of suppression for high p_T hadrons. The figure was obtained from [27].

prediction was for the suppression of the J/Ψ meson, but that the prediction had been extended to the Υ meson and used to predict the sequential melting of quarkonia as well. Quarkonia suppression analyses are another nuclear-modification-type analysis in that they aim to measure the difference between the yield of quarkonia states in heavy-ion collisions compared to an equal number of nucleon-nucleon collisions. In doing so they compute the quantity R_{AA}. If the R_{AA} is equal to unity then the number of quarkonia mesons measured in the heavy-ion reaction is the same as would be expected for a superposition of N_{Bin} nucleon-nucleon interactions. Here N_{Bin} is the number of binary nucleon-nucleon interactions for the centrality class of heavy-ion collision of interest.

Measurements of Υ suppression have been made by both STAR ([28]) and CMS ([29]) as shown in figures 1.14 and 1.15 respectively. The STAR result shows Υ suppression is observed in the most central collisions. Confoundingly, the STAR results also show that Υ production is equally suppressed in the much smaller d+Au system, which was unexpected. The CMS results show clear suppression for both the Υ(1S) and Υ(2S) states for all but the most peripheral collisions where suppression is not observed for the ground state. The CMS results also demonstrate sequential melting as the more tightly bound ground state is less suppressed across all centralities compared to the excited 2S state.

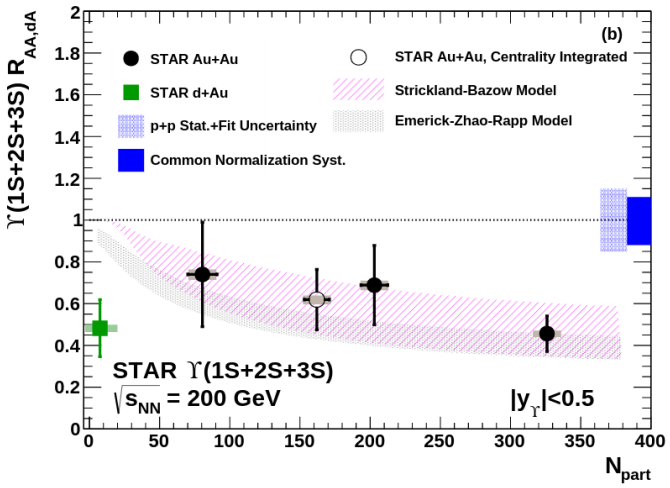

Figure 1.14: The nuclear modification factors, R_{AA} and R_{dA}, of inclusive Υ production as a function of event centrality as measured by STAR in Au+Au and d+Au events. The figure was obtained from [28].

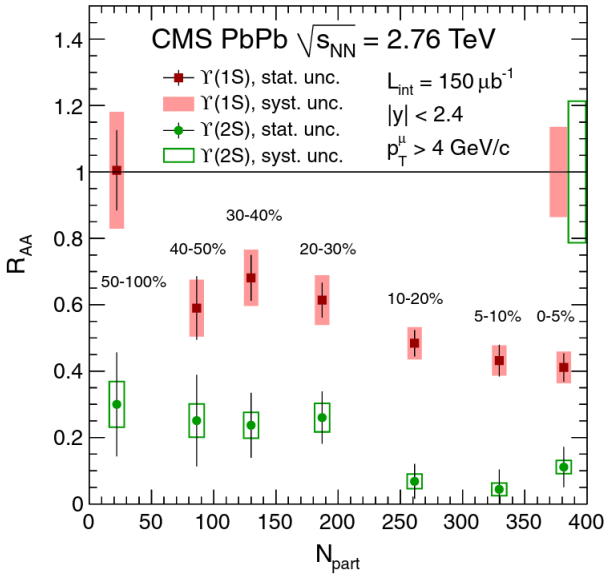

Figure 1.15: The nuclear modification factor R_{AA} of the individual Υ(1S) and Υ(2S) state production as a function of event centrality as measured by CMS in Pb+Pb events. The figure was obtained from [29].

In both cases the measured suppression is consistent with what would be expected if the medium produced in heavy-ion collisions provides the color screening mechanism of the QGP as proposed by Matsui and Satz. Presently more detailed analyses are making measurements of Υ suppression for the 3S state and exploring suppression differentially in rapidity and p_T for all states.

1.2 The Beam Energy Scan (2010-Present)

The existence of a strongly interacting QGP has generally been accepted by the field and the purpose of the community has since evolved from trying to discover QGP to characterizing its properties. The Beam Energy Scan (BES) program which began at RHIC in 2010, in particular, was developed with the intent of discovering the phase properties of the medium produced in heavy-ion collisions. As shown in figure 1.16 various regions of the nuclear-matter phase space can be investigated by varying the collision energies of the heavy ions. In this section, we begin by describing the phase diagram of QCD Matter and then proceed to cover a few of the many essential results from the BES program that contribute to our current understanding of the medium. For a more detailed description of each and their analysis methodologies we point the curious reader to the sources provided.

1.2.1 The Phase Diagram of Nuclear Matter

The phase diagram of nuclear matter in temperature, T, and baryon chemical potential, μ_B, space can be seen in figure 1.16. For orientation, normal nuclear matter at room temperature exists at the black point located at ($T \approx 0, \mu_B = m_N \approx 1000$ MeV). Further, the temperature of the core of the sun is around 15 million Kelvin or about 1200 eV = .0012 MeV. The black stars with energy labels represent the approximate (T, μ_B) coordinates of the initial medium formed in Au+Au collisions at those energies. Clearly the medium produced in such collisions is exceptionally hot.

The areas of interest are the Hadronic Gas and the QGP phases. The boundary which defines their separation is the primary subject of study of the BES program. Lattice QCD studies ([30]) have been used to predict the nature of the transition. At low μ_B the transition from hadronic gas to QGP is predicted to be a continuous crossover. In this case no experimental signatures of the phase change are expected. At high μ_B the transition is expected to be a first order transition. In this case discontinuities in measurable quantities are expected. A critical point is expected to exist at the point where the crossover transition turns into a first order transition.

With these predictions the goals of the BES program are clear: first, observe the turn

off of the QGP signatures previously used to argue for its existence; second, find evidence of the first order phase transition; and third search for the critical point. We will discuss some of the results of the BES program in the following sections but first we return our attention to the features of the phase diagram.

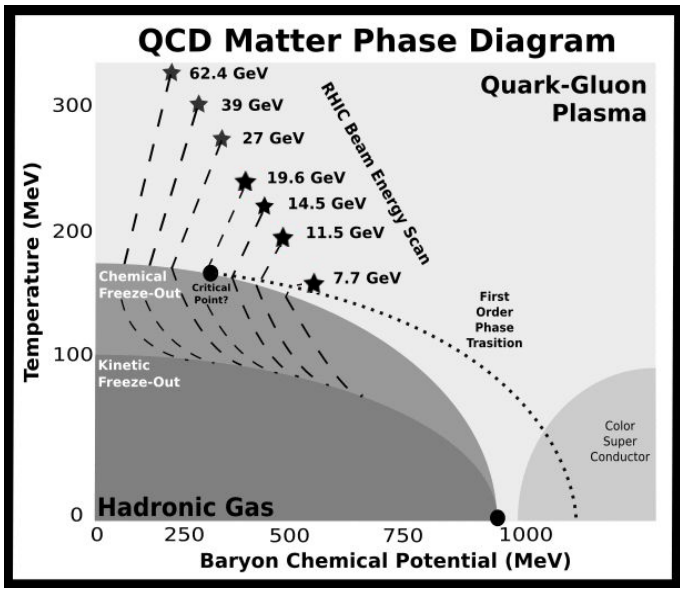

Figure 1.16: The phase diagram of QCD matter.

1.2.1.1 Baryon Stopping

The temperature axis is at least intuitive, but most phase diagrams do not include a chemical potential axis and definitely not a μ_B axis. Recall that in general a chemical potential is defined as the partial derivative of internal energy with respect to a number of constituents of the system while holding the entropy and volume of the system constant: $\mu = (\partial U/\partial N)_{S,V}$. Thus, it measures the change in internal energy of the system resulting from a change in the number of constituents of interest. An intuitive way of thinking about μ is in the framework of diffusion. If a particle of type A is surrounded by many other particles of type A then it is said to be in a high concentration and thus at a high μ. Since systems always seek a state of lowest energy, the particles of type A will try to move (diffuse) to regions of lower concentration and lower μ. This interpretation allows us to conclude that the medium produced in lower energy heavy-ion collisions is more rich in baryons than the medium produced at higher energies. But why?

The answer involves the same principles used in microscopy. If you want to resolve small details like a cell in a plant you can use regular visible light because the size of the cell is larger than the wavelength of visible light. If you want to resolve details as small as the structure of molecules you need a much shorter wave length so you need to use x-ray crystallography, for example. If you want to resolve detail as small as individual atoms you need something with an even smaller wavelength and so you use electron microscopy. The point is that the feature desired to be "imaged" must be larger than the wavelength of the probe.

In the case of electron microscopy, the probe (the electron) has mass and so its wavelength is given by the de Broglie wavelength: $\lambda = 1/p$. Likewise, in the case of heavy-ion experiments both the probe and targets are the constituents of the incoming nuclei and their de Broglie wavelengths are determined by the momentum of the beam. Beams of low momentum result in low energy heavy-ion collisions whose constituents have relatively large de Broglie wavelengths. On the other hand, beams of high momentum result in high energy collisions and very small de Broglie wavelengths.

If the wavelengths are of the order of the size of the nucleon, as they are in lower energy collisions, then the collision occurs at the interaction scale of the nucleons. In this case the interacting baryons are said to encounter a *stopping* effect. Baryon stopping describes the process of changing the rapidity of an incoming baryon from beam rapidity toward mid-rapidity. If the momentum of the incoming baryon (which has only longitudinal momentum) is observed to have only transverse momentum in the final state it is said to have been *fully stopped*. More precisely, baryon stopping describes the process by which the baryon number carried by the incident nucleons is deposited into the medium resulting from the heavy-ion collision. When a large amount of the incident baryon number is deposited into the medium, the medium is said to be *baryon rich* and consequently has a high μ_B.

As the beam energy increases and the wavelengths decrease, the relevant length scales move from the size of the nucleons to the size of the partons. As a result the incoming baryons develop transparency to each other and the interactions that define the produced

medium occur increasingly on the partonic scale. As a consequence, less baryon stopping occurs, the produced medium becomes less baryon rich, and accordingly has a lower μ_B.

Since the total baryon number must be conserved, the only "excess" in baryon number (over anti-baryon number) is that which was deposited into the system initially by the stopping mechanism. Any new baryons created during the evolution of the medium must be balanced by the production of anti-baryons. For this reason μ_B is frequently referred to as expressing the baryon to anti-baryon asymmetry of the medium. The medium produced in very high energy collisions is nearly equal parts baryon and anti-baryon and so has a small μ_B. Conversely, the medium produced in lower energy collisions has the excess baryon number contributed from stopping and so has a larger μ_B.

1.2.1.2 System Evolution and Phase Trajectory

The dashed line originating at each star represents a possible phase trajectory taken by the medium produced in a heavy-ion collision as it expands and cools. Clearly the temperature must decrease for the cooling to occur. The decrease in μ_B is due to the system's expansion reducing the medium's baryon density. As the system continues to cool it transitions from the QGP phase to the hadronic gas phase either via a crossover transition for high collision energies or via a first-order-transition for low collision energies.

The hadrons can continue to interact inelastically until they reach the stage of *chemical freeze-out*. This is not a phase transition boundary as the system already exists as a hadronic gas. Instead it defines the boundary after which no new particles can be created. As such, when the system's phase trajectory passes through this boundary its chemistry is set: the abundances of the various mesons and baryons are fixed. As the system continues to cool and expand, its phase trajectory must begin to point towards its ultimate destination, the point of normal nuclear matter.

The hadrons can continue to exchange momenta via elastic collisions until they reach the stage of *kinetic freeze-out*. At this stage the expanding system is so diffuse that no interactions between the hadrons take place. This means that there is no longer any exchange of momenta and the hadrons continue free streaming toward the detector where they are measured and analyzed.

Having followed the progression of the system from initial collision to free streaming particles we now consider some of the experimental measurements obtained by the BES program in regards to its three main objectives.

1.2.2 The Turn Off of QGP Signatures

An important goal for the BES program is to observe that results previously used to argue for the existence of QGP disappear at lower collision energies. Since the NA49 collaboration had previously argued that they observed the onset of deconfinement around $\sqrt{s_{NN}} = 7.7$ GeV the BES program desired to reach energies equally as low. Fortunately, the magnet lattice of RHIC, which had been designed to collide heavy-ions at $\sqrt{s_{NN}} = 200$ GeV, was sufficiently well known to allow for such low energy collisions. Over the course of three years seven collision energies were investigated: 7.7, 11.5, 39.0, and 62.4 GeV in the year 2010; 19.6 and 27.0 GeV in the year 2011; and finally 14.5 GeV in the year 2014. The multiple collision energies allowed for an investigation into how the signatures of QGP changed as a result.

Recall that one of the interesting features observed in $\sqrt{s_{NN}} = 200$ GeV collisions was that the QGP was a strongly interacting medium which suppressed the yield of high p_T (> 2 GeV/c) hadrons due to its color opacity. This effect was observed in the R_{AA} results previously discussed. Figure 1.17 shows a similar analysis done for each of the colliding energies of the BES program. In this case, rather than forming the nuclear modification factor by comparing heavy-ion systems to p+p collisions, the ratio is formed by comparing central and peripheral heavy-ion collisions, R_{CP}. Note that similar suppression ($R_{CP} < 1$) of high p_T hadrons is observed at 62.4 and 39.0 GeV. Unfortunately as the colliding energy decreases, overall particle production also decreases. When coupled with the exponential falloff of particle yield as a function of p_T, these two effects mean that it is very difficult to get statistically significant samples to equally high p_T at each energy. However, at 27.0 GeV no suppression is observed for high p_T hadrons in the measured range. Further, the trend of the curves observed in 19.6 GeV and lower energies make it very clear that suppression does not exist in the medium. The turn off of high p_T hadron suppression has been argued to be a "necessary, but not sufficient" observation that the QGP medium is

no longer created.

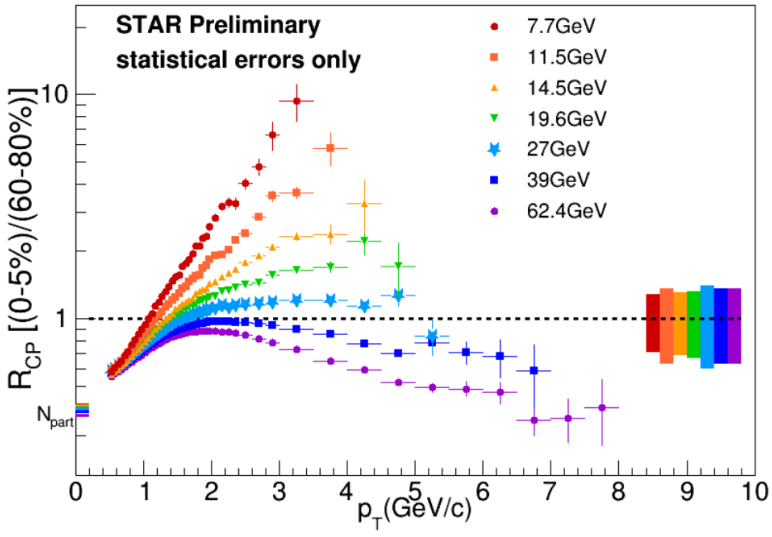

Figure 1.17: Hadron suppression results from the BES program shown in the form of R_{CP} as a function of p_T at each collision energy. The figure is obtained from [31].

Another compelling feature observed in heavy-ion collisions at $\sqrt{s_{NN}} = 200$ GeV was the observation that the flow dynamics resulting from the pressure gradients of the overlap region were imparted to the quarks, which implied partonic degrees of freedom. As previously discussed this observation came in the form of scaling the v_2 of identified particles by their constituent quarks and noticing that the resulting curves of all species agreed. Precisely the same analysis was performed using the data collected in the first two years of the BES program and the results are shown in figure 1.18. Notice that the curves of all particles match for collision energies of 19.6 GeV and higher. However, the flow of the ϕ meson deviates from the trend in the 7.7 and 11.5 GeV results. This breaking of constituent quark scaling has been used to argue that at these low energies the quark degrees of freedom are turning off.

1.2.3 Phase Change Phenomena

We have already discussed the interplay between a system's compressibility and its equation of state (EoS) during the investigation of the dale observable. We concluded that a system undergoing a first order phase transition would exist in a mixed-phase state

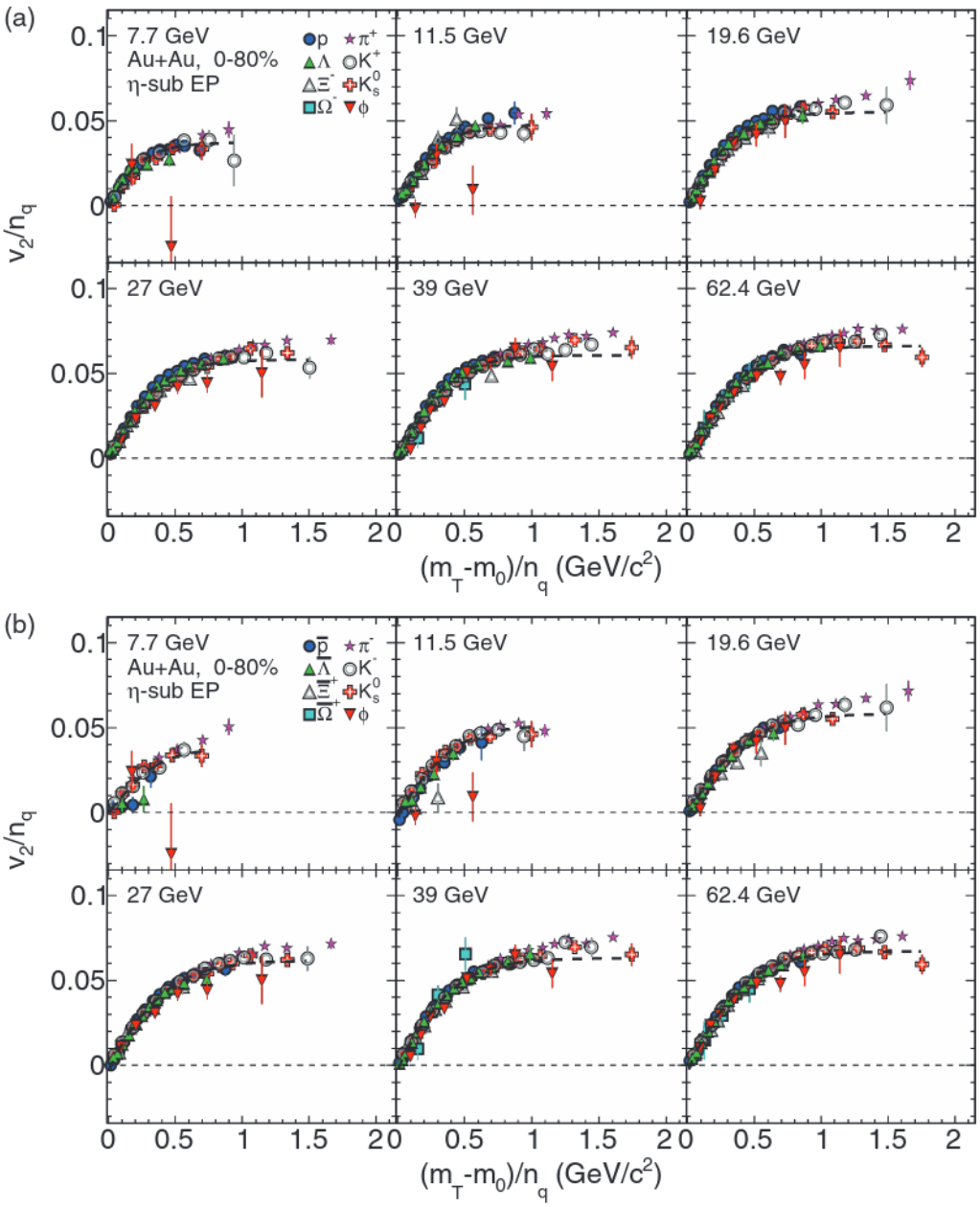

Figure 1.18: The elliptical flow of several identified particle species (a) and anti-particles (b) as a function of transverse mass. Both quantities have been scaled by the number of constituent quarks contained in each particle species. Each pane shows the results at different collision energies. The figure is obtained from [32].

consisting of both hadronic and partonic matter. Further, we concluded that such a mixed-phase state would have the signature of being at its softest EoS or equally at its most compressible state. A second observable is expected to be sensitive to the compressibility of the state and is related to the directed flow, v_1, of the system. The directed flow is obtained similarly to the elliptic flow and thus the quantity v_1 is the first coefficient of the Fourier expansion.

The slope of the directed flow, dv_1/dy, of *stopped* or *transported* baryons near mid-rapidity has been shown to exhibit non-monotonic behavior in hydrodynamic calculations which include a first-order phase transition. The qualification that the baryons of interest must be the stopped baryons is important, as only those baryons are sensitive to the compressibility of the system. In practice it is difficult to obtain the flow of all of these baryons because light nuclei and neutrons (which are not measured due to their lack of charge) are produced. Instead we use the protons as a proxy for all baryons and the anti-protons (which are scaled) as a proxy for produced baryons. To isolate the v_1 of stopped protons we simply remove the v_1 of the produced protons from the v_1 of all protons. The result is known as the v_1 of "net protons."

The above methodology can be repeated for each rapidity bin and the slope can then be obtained in the mid-rapidity region. The results of this procedure are shown in figure 1.19 as a function of the collision energy. The minimum between 11.5 and 19.6 GeV has been interpreted as possibly indicating the softest EoS of the medium and hence as an indicator of a phase change.

1.2.4 Critical-Point Fluctuations

The final goal of the BES program is to find the critical point which defines where the crossover transition at low baryon chemical potential changes to a first order phase transition. One of the most exciting results produced by the BES program thus far is the observation of fluctuations in the product of the kurtosis and variance, $\kappa\sigma^2$, of net protons. In this subsection we attempt to briefly motivate the importance of this signature. The reader is cautioned that the subject of bulk fluctuations is enormously nuanced both theoretically and experimentally, and is referred to an excellent introductory article on

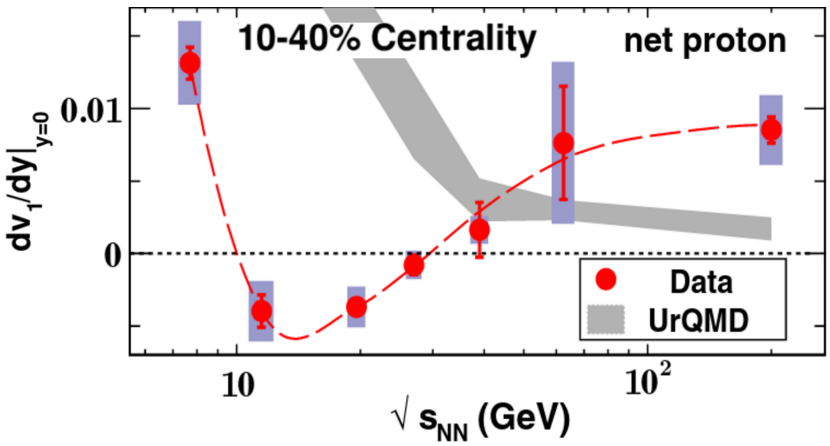

Figure 1.19: The slope of the directed flow of net protons as a function of collision energy from mid-central Au+Au collisions. The dashed red curve is present to make the trend clear. For more details see the main text. The figure is obtained from [33].

the topic [34].

Generally the existence of a critical point is identified by the divergence of a correlation length. By correlation length, which is typically assigned the Greek character ξ, we mean any measure which quantifies how variables co-vary across space-time. By divergence we mean that $\xi \to \infty$. It was shown in [35] that moments of event-by-event multiplicity distributions were sensitive to ξ. In particular the variance, skewness, and kurtosis (related to the second, third, and fourth moments respectively) of the event-by-event multiplicity distributions were shown to have the following relations: $\sigma^2 \sim \xi^2$, $S \sim \xi^{4.5}$, and $\kappa \sim \xi^7$.

Event-by-event multiplicity distributions are measured in heavy-ion collisions by counting the number of particles in each event. Further criteria can be applied such as binning the events by centrality to obtain the distribution by centrality class or by requiring particle identification cuts to construct the distribution for certain particle species. Of notable importance is the distribution of net-protons since it serves as a proxy for net-baryons, which is a conserved quantity, and thus prone to fluctuations at the critical point. Of further interest is the kurtosis of the net-proton multiplicity distribution since it was explained in [36] that the kurtosis is always negative when approaching the critical point from the side of the crossover transition. It was further clarified in [37] that as a phase trajectory nears the critical point the kurtosis of its net-baryon distribution becomes posi-

tive due to the development of "asymmetry around a peak" before returning to a baseline value.

As illustrated in figure 1.20 this means that in heavy-ion collisions the volume-corrected kurtosis of the event-by-event, net-proton multiplicity distribution should be less than some baseline value for high energy collisions whose phase trajectories pass the critical point on the low μ_B side; undergo a fluctuation from below the baseline to above at collision energies with phase trajectories which pass very near the critical point; and then return to the baseline at collision energies with phase trajectories that pass the critical point on the high μ_B side.

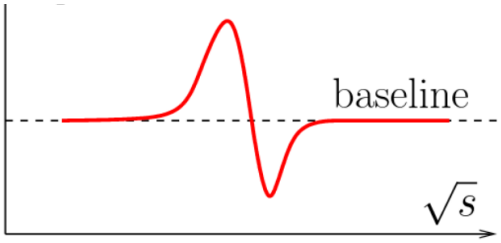

Figure 1.20: A sketch of the behavior of a volume-corrected, kurtosis-like value (vertical axis) as a function of collision energy. The figure is obtained from [37].

The volume dependence of the kurtosis can be canceled experimentally by multiplying the kurtosis by the distribution's variance. STAR has made such measurements and the results are shown in 1.21. In this case the baseline value is unity. The trend of the $\kappa\sigma^2$ measurements is remarkably similar to that predicted in figure 1.20. Beginning at high energies and proceeding toward lower energies the $\kappa\sigma^2$ signal becomes less that the baseline and then rises and becomes greater than the baseline just as expected. This has been used as suggestive evidence that collisions at $\sqrt{s_{NN}} = 19.6$ GeV may be passing very near the critical point.

Several issues relating to this measurement must be stated. First, the $\kappa\sigma^2$ signal must be confirmed to return to the baseline at lower energies in accordance with the prediction. Measuring this signal at lower collision energies is a driving factor of the fixed-target program currently in development at STAR, a program to which the author of this document has made substantive contributions. Second, the relatively large statistical errors of the low energy data points must be reduced to achieve statistical significance.

To accomplish this, and to achieve more precise measurements of other quantities, a second phase of the BES program, BES-II, has been planned. Finally, the $\kappa\sigma^2$ signal is remarkably sensitive to kinematic cuts and detector acceptances. These effects must be understood and controlled to limit the associated systematic errors.

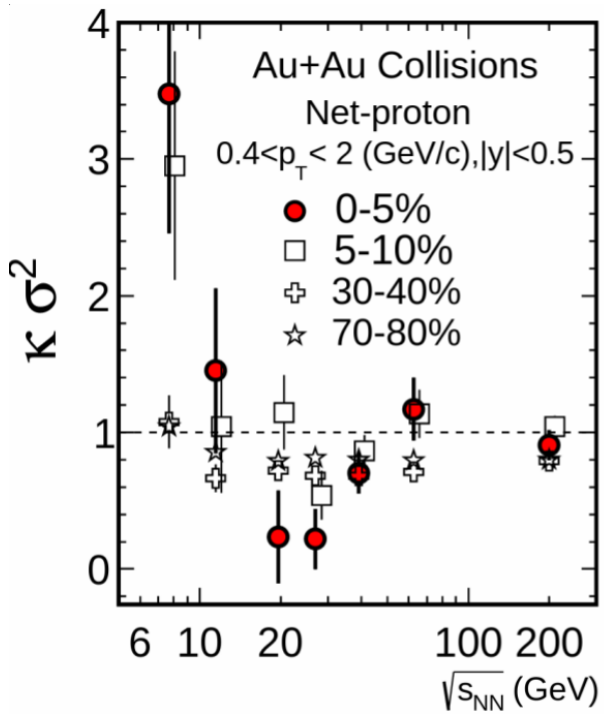

Figure 1.21: Net proton kurtosis times variance as a function of collision energy. The figure is obtained from [38].

1.3 Overview of Work in This Thesis

Having explored the history of the field and investigated many of the measurements that define its progress, we conclude this chapter by considering the work included in this thesis. The goal of the enclosed work is to provide a systematic accounting of the production of light hadrons ($\pi^+.\pi^-, K^+, K^-, p$, and $\bar{p}$) over as broad a range of kinematic space as possible and differentially in nine centrality bins. This task will be repeated for each of the seven energies of the BES program. The STAR collaboration has previously reported the yields of these particles at mid-rapidity [39]. However, as demonstrated by observables such as the kink, horn, and dale, having a full accounting of the production of these particles can yield essential insights into the properties of the medium produced in heavy-

ion collisions. For example, the results of this thesis can be used to extract the chemical and kinetic freeze-out coordinates differentially in rapidity so that an investigation of baryon stopping and its effects could be carried out.

To achieve this goal we must first consider the experimental apparatus and its particulars in chapter two. We then consider the process by which events are binned into centrality classes in chapter three. The process of data collection is reviewed in chapter four. Notes regarding the extensive effort invested by the author into developing data structures and techniques to permit efficient computation with the large data set of the analysis are included. Chapter five concerns the important task of understanding the deficiencies of the STAR detector and the corrections that must be applied to account for them. The contents of chapter six involve removing the effects of background associated with the measured quantities. Chapter seven turns its attention to the multi-step process of extracting the particle yields from the data. In chapter eight the corrected yields of the particles are presented: first as transverse mass spectra, then as rapidity density distributions, and finally as full phase space yields were applicable. The yields reported in chapter eight are further analyzed in chapter nine. Finally, a summary and conclusion are provided in chapter ten.

1.3.1 Paper Proposal Page

This document contains plots which are intended to illustrate the necessary steps of the analysis. The many other plots which make up many thousands of pages are included in external addenda and can be found in digital form at the paper proposal page, `http://www.star.bnl.gov/protected/lfspectra/cflores/IdentifiedRapidityDensity/` and `http://nuclear.ucdavis.edu/~cflores/protected/IdentifiedRapidityDensity/`, its mirror.

Chapter 2

Experimental Apparatus

The data used in this analysis were collected during the Beam Energy Scan Program in 2010, 2011, and 2014 using the Solenoidal Tracker at RHIC (STAR) which is an experiment on the ring of the Relativistic Heavy-Ion Collider (RHIC) located at Brookhaven National Laboratory (BNL). The laboratory itself is a multidisciplinary facility that supports several fundamental fields of science such as biology, chemistry, and physics, as well as several applied science and engineering programs including computer science, nanomaterials, and energy production. In this chapter the accelerator and detector used to collect data for this analysis are generally introduced. Details of subsystems are also discussed when they are pertinent to either the data collection or analysis.

2.1 The Relativistic Heavy-Ion Collider Facility

The RHIC facility is a multi-part accelerator complex that is capable of accelerating a range of nuclei to relativistic speeds. A schematic of the facility, drawn from a bird's eye view, can be seen in Figure 2.1. The facility was designed to provide $\sqrt{s_{NN}} = 200$ GeV Au+Au collisions and polarized $p + p$ collisions at $\sqrt{s} = 500$ GeV. Since this analysis focuses solely on Au+Au collisions the remainder of the discussion will pertain to RHIC as a heavy-ion facility.

2.1.1 Acceleration Procedure

To achieve the high energies required, the Au nuclei are accelerated in stages as described in [40] and summarized here. The process begins with the vaporization of solid gold using a sputter ion source. The ion source adds an electron, giving the gold atom an overall negative charge. This negative beam is extracted into a Tandem Van de Graaff accelerator which accelerates the ions to 1 MeV and strips off 33 electrons giving Au^{32+}. The ions then reach the booster synchrotron via the heavy-ion transfer line. The booster accelerates the ions to approximately 1 GeV and separates the ions into six bunches. When the ions exit the booster they are incident on a stripping foil, which removes all but two electrons, resulting in Au^{77+}. The booster cycle is repeated four times so that the Alternating Gradient Synchrotron (AGS) can be filled with 24 bunches. The AGS first debunches and rebunches the ions so that there are four final bunches and then accelerates the ions up to the RHIC injection energy. The final two electrons are stripped as the ions are transferred to RHIC. The entire process is repeated up to 14 times so that RHIC can be filled with 56 bunches each with 10^9 ions.

The injection energy of the ions from the AGS into RHIC depends on the required operating procedure. If RHIC is meant to provide Au+Au collisions at $\sqrt{s_{NN}} = 19.6$ GeV or below, then the injection energy is $\sqrt{s_{NN}}/2$ GeV. During these running configurations RHIC then serves as a storage ring for the duration of the data collection time. If collisions higher than $\sqrt{s_{NN}} = 19.6$ are required then the injection energy is 9.8 GeV and the ions are further accelerated by RHIC until the desired energy is reached.

2.1.2 The RHIC Design

RHIC itself is an intersecting synchrotron type accelerator that was designed with remarkable scientific flexibility in mind. A synchrotron, like a cyclotron, is a class of cyclic accelerator. Cyclic accelerators are typified by designs which recycle beams around a ring so that acceleration of the beam can take place over multiple revolutions. These accelerators require both bending magnets to steer the beam around the ring and an electric field to provide acceleration. The synchrotron and cyclotron designs differ in the particular implementation of bending magnets and electric fields.

Cyclotrons have a single, large, constant magnetic field oriented perpendicular to the plane of beam rotation that is provided by two large "D" (named for their shape) electromagnets. The small gap between the "D" magnets is filled with a radio frequency oscillated electric field so that the particle is accelerated twice during each revolution. A particle is injected into the cyclotron at its center and as the particle's velocity increases it spirals outward eventually being ejected tangentially. Although simple in design, the top energy in a cyclotron is inherently limited by the size and strength of the single, large magnetic field, since it must encompass the entire plane of beam rotation.

Synchrotrons, such as RHIC, bend the beams around a ring using several dipole magnets that are configured in a "racetrack" orientation. That is, the ring of a synchrotron is really an n-sided regular polygon, where the corner sections of the polygons contain the dipole magnets responsible for bending the beams, and the straight sections house the experimental detectors. Acceleration is provided by radio frequency (RF) cavities in one or more of the straight sections. Synchrotrons derive their name from the acceleration process which requires that the magnetic fields of the bending magnets be increased synchronously with the momentum of the beam.

RHIC is hexagonal in shape as can be seen in Figure 2.1, with a circumference of approximately 3.8 km. The six straight sides of the ring have been used for the RF cavities, a service building, and four experiments: STAR, PHENIX, PHOBOS, and BRAHMS which were located at the 6, 8, 10, and 2 o'clock positions respectively. At the time of this writing (June 2017) only STAR remains as an operational detector. However, plans to resume operations at the PHENIX interaction region using a new detector dubbed sPHENIX are well underway.

When RHIC began operations in 2000 it was the highest energy heavy-ion collider in the world and remains the most powerful source of polarized proton beams for spin studies. As previously noted it was designed with remarkable scientific flexibility in mind. From the heavy-ion perspective this flexibility is derived from two unique design characteristics. First, RHIC is a dual-ring intersecting synchrotron which means it is capable of simultaneously accelerating beams of different species in opposite directions and steering them

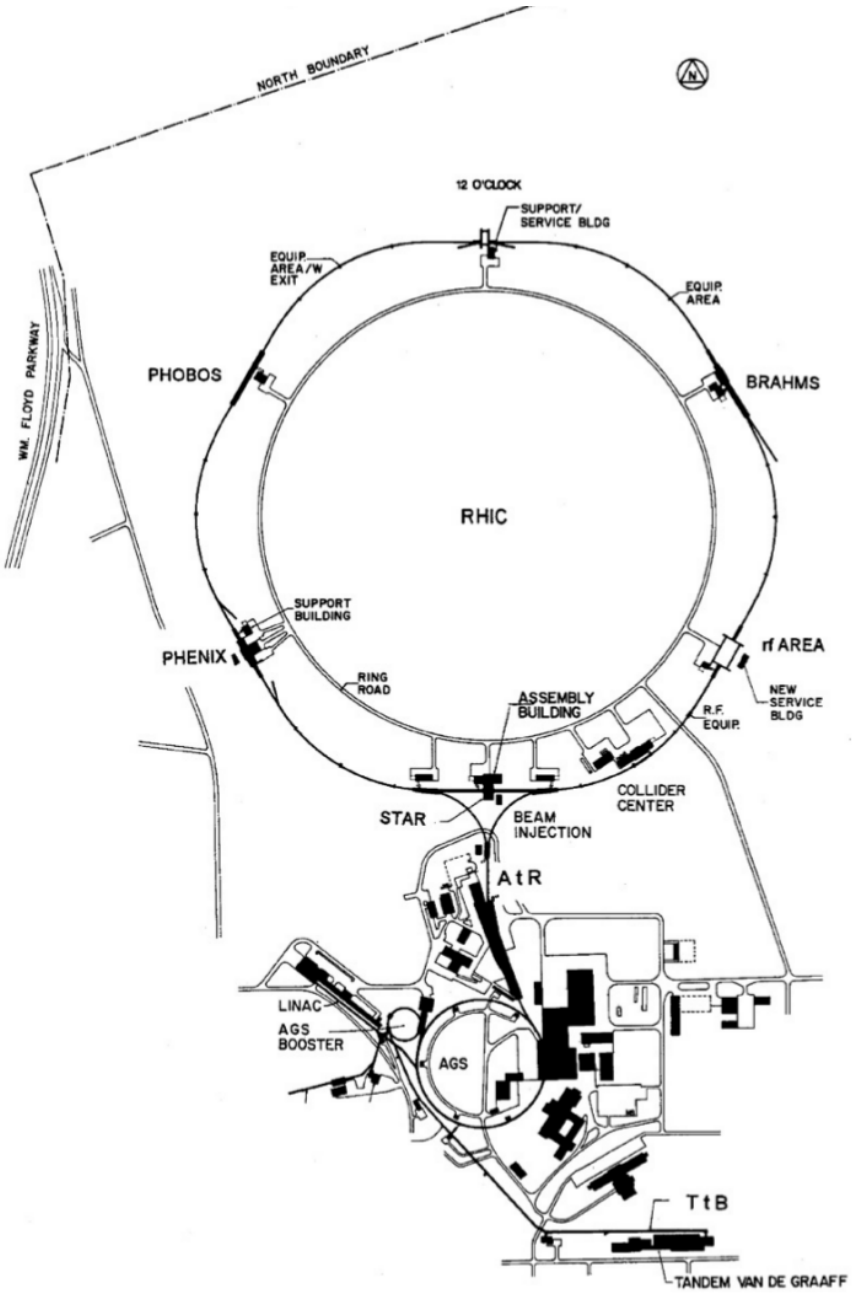

Figure 2.1: A schematic of the RHIC accelerator complex layout obtained from reference [40].

into collisions. Thus it can provide collisions between asymmetric systems such as p+A. This capability is important because understanding how results of heavy-ion experiments differ from those of a superposition of $p+p$ collisions can offer crucial insights about the produced medium. Second, it was designed to be capable of accelerating multiple nuclear species to various energies between injection energy and its top energy. The variety of energies permits results to be understood as a function of collision energy starting from the energies of its predecessors. This capability is also important because it allows us to probe various regions of the nuclear matter phase space as described in chapter one. It is the second capability that is essential for the Beam Energy Scan program and therefore in this analysis.

2.2 The STAR Detector

The Solenoidal Tracker at RHIC (STAR) detector, shown in Figure 2.2, was built purposefully to study heavy-ion collisions. This means that it must provide tracking and particle identification over a large solid angle and in high-multiplicity environments. The multiple subsystems and half-Tesla magnet of the detector are designed to satisfy these requirements over a geometric region covering the full 2π in azimuth and $|\eta| \leq 1.5$ in pseudorapidity. In addition, the subsystems are designed to exhibit (with few exceptions) both azimuthal and longitudinal symmetry.

The coordinate system of the detector is described in [41] and is defined as being right-handed with respect to the collider. Its origin is defined to be the center of the STAR solenoid. The positive x-axis points radially outward from the center of RHIC (approximately south). The positive y-axis points upward - away from the center of the earth. Finally, the positive z-axis points in the same direction as the clockwise circulating beam as it passes through the detector (approximately west). The azimuthal angle, $\phi = [-\pi, \pi]$, is measured in the x-y plane and symmetrically from the positive x-axis. The polar angle, $\theta = [0, \pi]$, is measured from the positive z-axis.

The present analysis requires the tracking and particle identification capabilities of the STAR detector. Tracking is provided by the Time Projection Chamber (TPC) and particle

identification is provided by both the TPC and the Time of Flight (TOF) detector. As a result the following discussion will focus on the details of these subsystems in particular. If the reader desires a more general introduction to the STAR detector as a whole we defer to [42].

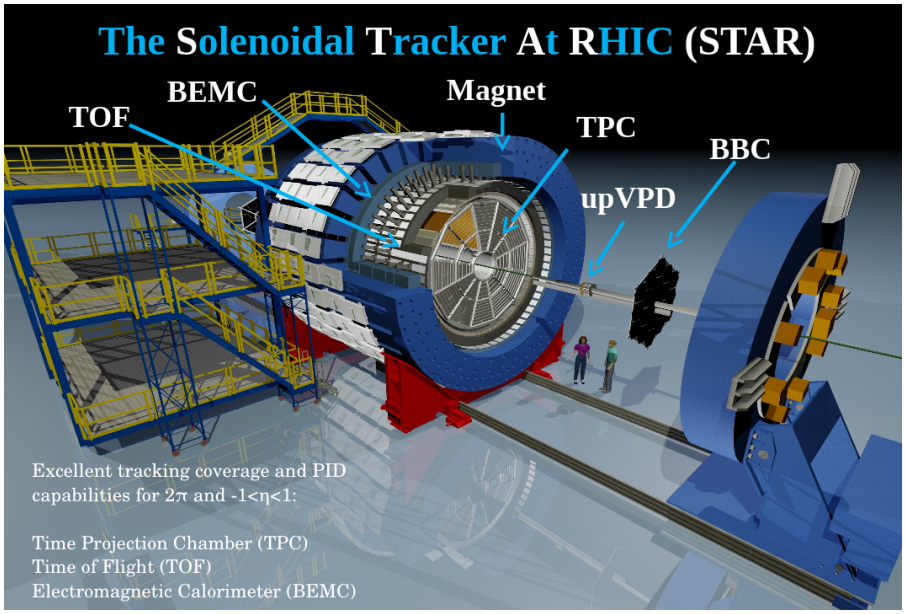

Figure 2.2: A 3D CAD rendering of the STAR detector courtesy of [43].

2.2.1 The Time Projection Chamber

The Time Projection Chamber (TPC) is the defining subsystem of the STAR detector. It is a cylindrical volume spanning 4.2 m in length and has an inner radius of 50 cm and outer radius of 200 cm. Its length is coaxial with and encloses the beam pipe. A schematic of the subdetector can be seen in Figure 2.3. A more detailed description of the TPC is available in [44]. A summary of the most important operational details is provided here for completeness.

The volume of the TPC is filled with P10 gas (90% Argon, 10% Methane). The gas in the TPC is kept slightly above atmospheric pressure so that oxygen and water vapor do not enter sensitive volume and oxidize the surfaces. The P10 gas was chosen because its main constituent, the argon, is extremely stable which limits spurious ionizations and is relatively inexpensive - a necessary consideration for such a large volume, and has a very low affinity for free electrons. The methane is present as an absorber of energy.

Its relatively large mass and multiple degrees of freedom (rotational, vibrational, etc.) allow it to absorb kinetic energy from: drifiting electrons - giving them a constant drift velocity, ionized argon atoms - resulting in their minimal drift distances, and UV photons - preventing confounding avalanches.

The large volume of gas is divided along the z-axis into two drift chambers by a central membrane which is kept at 28 kV relative to the endcaps, which are grounded. The resulting electric field of about 133 V/cm is kept uniform along the z-axis by inner and outer field cages which are composed of several conductive rings connected with high precision resistors. The electric field results in a constant electron drift velocity of 5.45 cm/μs.

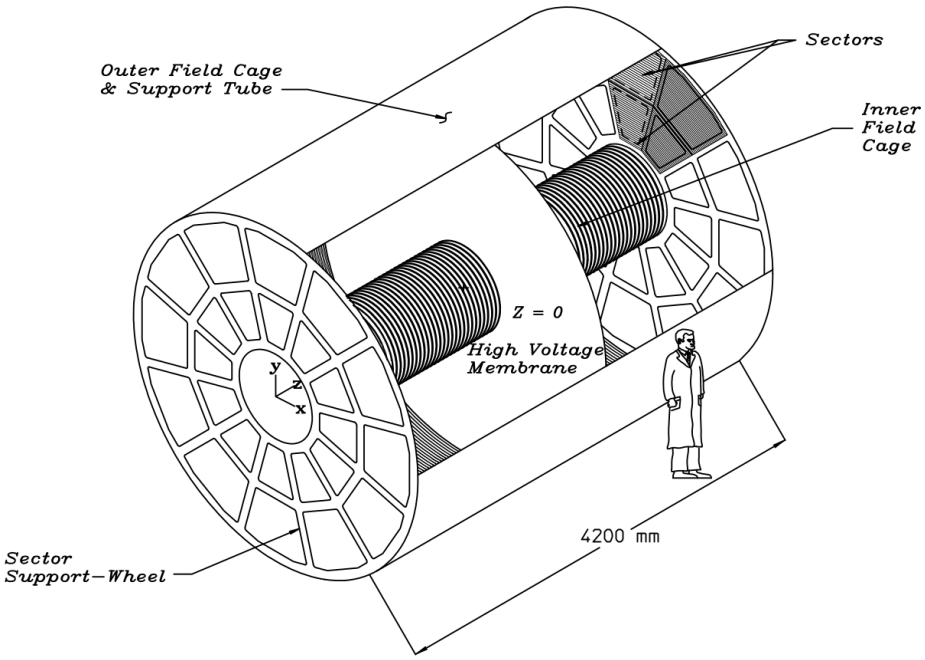

Figure 2.3: A schematic of the STAR TPC obtained from reference [44].

The readout electronics of the TPC are installed in a total of 24 pie-shaped Multi-Wire Proportional Chambers (MWPC) that divide each half of the TPC into 12 sectors in azimuth. A schematic of a single sector is shown in Figure 2.4. Each sector is divided radially into an inner sector and outer sector. The inner sector has 13 pad rows while the outer sector has 32. This means that each track can have its position and energy loss recorded up to 45 times. The direction of the wiring in the MWPCs was chosen to give

the best momentum measurements for high p_T tracks and so are oriented perpendicular to the direction such a track would travel.

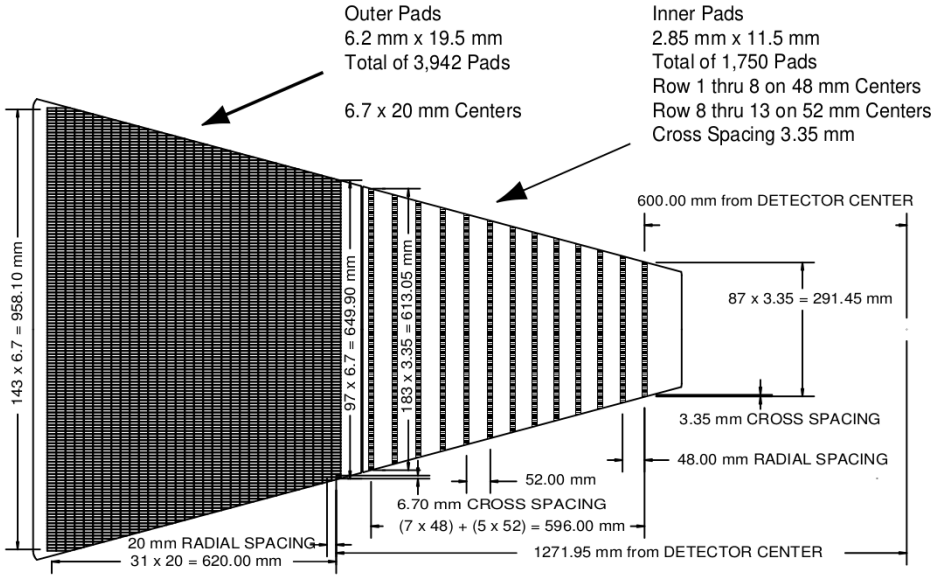

Figure 2.4: A schematic of a single anode sector of the TPC obtained from [44]. The inner portion of the sector is on the right and the outer is on the left.

2.2.1.1 Track Reconstruction

As the detector design suggests, the tracking function of the TPC is accomplished via gas ionization measurements. When a charged particle transits the gas it ionizes the Argon atoms. The resulting free electrons drift to the end caps of the TPC where they are collected into what is called a "hit." The x,y location of the readout pad is used to determine the hit's transverse location and the drift time is used to determine its z location. The determination of the z location by measuring the electron drift time gives the TPC its name. Figure 2.5 shows the status of free electrons at 15.2 μs after an event occurred. The free electrons have drifted from their ionization location toward their respective end caps.

The discrete hits observed in the TPC are interpreted into continuous tracks by a Kalman filtering process that involves iteratively fitting helices - the trajectory a charged particle in a uniform magnetic field is expected to have. The result of this reconstruction process is a set of global tracks. These tracks represent the trajectories of all the particles

traveling through the detector after the trigger was satisfied. The next step in the process is to associate the global tracks together into one or more vertices, known as primary vertices, that represent the location of an A+A collision. This is achieved by the vertexing algorithm and involves extrapolating the fit helices to the z-axis. By observing the density of tracks as a function of z, a set of candidate vertices are formed. The x and y locations of the helix extrapolations are then taken into consideration to exclude some candidate vertices and to provide a higher-precision vertex-position measurement.

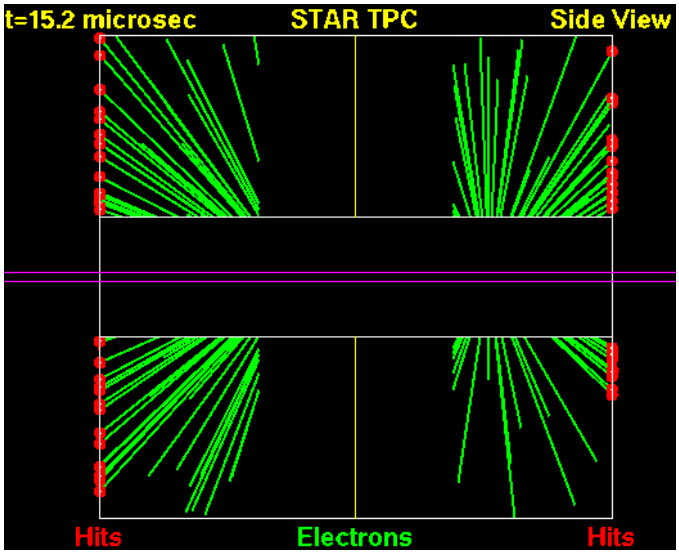

Figure 2.5: A simulation of free electrons drifting from their ionization location to the anode plane where they are read out. This snapshot was taking 15.2 μs after the event occured. Full animation is available here: `https://www.star.bnl.gov/public/tpc/hard/tpcrings/simTPC.html` courtesy of [45].

Now that the global tracks have been associated with a vertex, they are refit with helices using the vertex position as the first point in the helix. This provides a more precise measure of momentum thereby improving the momentum resolution of the tracks. When this refitting procedure is finished the tracks are known as primary tracks because their trajectories now originate from the primary vertex. It is important to note that there can be multiple primary vertices per trigger. However, the vertex finding algorithm is able to rank the vertices and only the most highly ranked vertex in each trigger is used in this analysis.

Kinematic measurements of the track are obtained from the helix fit. All tracks are

assumed to have unit charge. The sign of the charge is determined from the handedness of the helix. The track's transverse momentum is determined by the radius of curvature of the helix and the longitudinal momentum is determined by the helix pitch or turn density.

2.2.1.2 Particle Identification via Energy Loss

Particle identification in the TPC is accomplished by taking advantage of the way particles lose energy when they move through matter. The physics of this process is described by the Bethe-Bloch equation (equation 2.1,[46]) which predicts how much energy a particle will lose per unit of path length as a function of $\beta\gamma = p/m$. Particles of different masses, then, lose energy at different rates for a given value of $\beta\gamma$. Considerable effort was expended in [47] to understand the energy loss of particles in the P10 gas of the STAR TPC. This effort resulted in what are known as the Bichsel curves.

$$\frac{dE}{dx} = Kz^2\frac{Z}{A}\frac{1}{\beta^2}\left[\frac{1}{2}\log\left(\frac{2m_e c^2\beta^2\gamma^2 T_{max}}{I^2}\right) - \beta^2 - \frac{\delta(\beta\gamma)}{2}\right] \tag{2.1}$$

A = Atomic Mass of Absorber (g/mol)

$\frac{k}{A} = 4\pi N_A r_e^2 m_e c^2/A$ (cm^2/g)

N_A = Avogadro's Constant (1/mol)

r_e = Classical Electron Radius (fm)

m_e = Mass of Electron (MeV)

m_0 = Mass of Incident Particle (MeV)

z = Atomic Number of Incident Particle

Z = Atomic Number of Absorber

$$T_{\max} = \frac{2m_e c^2\beta^2\gamma^2}{1 + 2\gamma\,(m_e/m_0) + (m_e/m_0)^2}$$

= Max Energy Transfer (MeV)

I = Mean Excitation Energy (eV)

$\delta(\beta\gamma)$ = Density Effect Correction (Material Dependent)

The amount of energy a particle loses as it moves through and ionizes the gas of the TPC is proportional to the number of electrons measured for that track at each hit. Thus, by carefully calibrating the TPC a track's dE/dx can be measured. However, in practice some care must be taken when computing the dE/dx of a track. Recall that each track can have up to 45 hits associated with it and therefore up to 45 independent measurements of its dE/dx. The value of dE/dx at each hit is a Landau distributed random variable. Since the Landau distribution has a long, high-side tail a simple average of the 45 measurements would be skewed toward large values of dE/dx. To overcome this, the largest 30% of measurements are removed and the remaining are used to compute a 70% truncated mean. Figure 2.6 shows the measured dE/dx of tracks as a function of total momentum. The curves in the figures are the theoretically expected energy loss values predicted by the Bichsel curves. Clearly the Bichsel curves are an excellent descriptor of how tracks lose energy in the TPC. Clear separation can be seen between the tracks of different species at low momentum, however the merger of the energy loss bands at high momenta require an alternative method of particle identification.

2.2.2 The Time of Flight Detector System

Particle identification at higher momenta is provided by the Time Of Flight (TOF) and the Upgraded Pseudo Vertex Position (upVPD) detectors. Together these detectors are designed to act like a stopwatch that provides a measurement of the flight time of tracks. Both the upVPD and TOF systems are described in detail in [48], [49], and [50]. A summary of some of the important characteristics of the systems is included here.

2.2.2.1 The Upgraded Vertex Position Detector and Start Time

The upVPD system consists of two enclosures of extremely fast photomultipliers. As seen in Figure 2.2 there is an upVPD detector near the beam pipe positioned 5.7m from the center of the TPC on both sides of STAR. These cover $4.2 < \eta < 5.1$ and measure very forward photons from the collision and act as the start of the stopwatch. For energies less that $\sqrt{s_{NN}} = 39.0$ GeV it was found that the signals from the upVPDs were insufficient to determine the start time of the event. In these cases a "startless" method was used to determine the start time. This method assumes a pion mass for all tracks with $0.2 <$

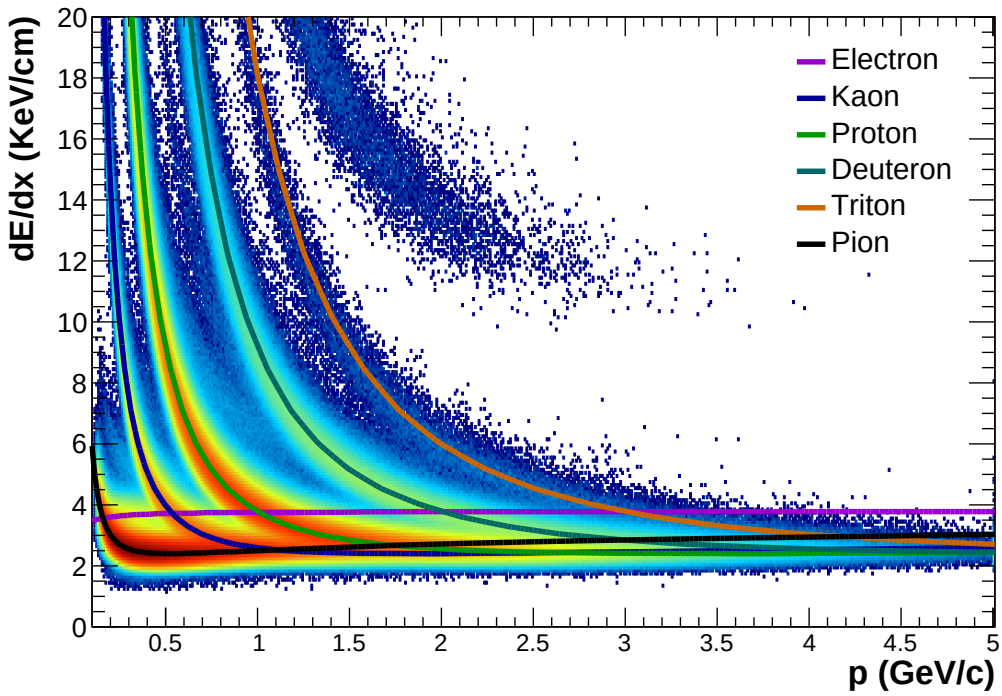

Figure 2.6: The energy loss (dE/dx) of tracks as measured in the TPC as a function of total momentum from the $\sqrt{s_{NN}} = 7.7$ GeV data set. The curves in the figure are the Bichsel curves described in the text.

.

$p_T < 0.6$ GeV and that are within two standard deviations from the expected dE/dx of a pion. This is an excellent assumption for this combination of p_T and dE/dx. The mass assumption is combined with the momentum and track length measured in the TPC to estimate the start time for each track. The estimates are then averaged to determine the start time of the event.

2.2.2.2 The Barrel Time of Flight Detector

The TOF system is a thin cylindrical shell that encloses the surface of the TPC. The detector system is composed of 120 trays, 60 for each the east and west half, of size 241.3 $\times$ 21.6 $\times$ 8.9 cm^3. Together the trays cover the full 2π in azimuth and $|\eta| \leq 0.9$. Each tray contains 32 Multi-Gap Resistive Plate Chambers (MRPC) set in a projective geometry so that tracks emanating from an average z-vertex location at the center of STAR will encounter them perpendicularly. A schematic of a single TOF tray with the projectively oriented MRPCs can be seen in Figure 2.7.

Figure 2.7: A schematic of a single TOF tray with the projectively oriented MRPCs. This figure is taken from [49] Note that this figure contains 33 rather than 32 MRPCs because it was a prototype design.

.

The internal structure of each of the MRPCs can be seen in Figure 2.8. It is composed of several resistive glass plates separated by gaps containing 95% R-134a and 5% isobutane gas. These plates are sandwiched between two graphite electrodes across which a high potential is applied. Finally, the electrodes are sandwiched between two layers of six copper readout pads. Hits are detected by gas ionizion measurements. As a track moves through the MRPC it ionizes the gas in the gaps between the plates creating electron avalanches. The resistive plates prevent the free electrons from streaming but are transparent to the electric fields created by the avalanches themselves. This transparancey allows the copper readout pads to measure the resulting image charge across the graphite electrode.

The readout pads are separated from each other by 0.3 cm and measure 3.15×6.1 cm^2. The isolation of the pads within each MRPC allow each pad to record a hit simultaneously. In addition, each pad is capable of providing the hit location with respect to its own coordinate system. This position discretion is taken advantage of in the track quality cuts discussed in Chapter 4. The pads and associated electronics are designed to provide a timing resolution for each hit of approximately 100 ps. However, in practice careful calibration and electronics correction often result in better timing resolution, down to 65 ps in the best cases.

2.2.2.3 TPC Track to TOF Hit Reconstruction

Tracks measured and reconstructed in the TPC can now be matched with hits observed in the TOF pads. This is performed by a matching algorithm that extrapolates the trajectory of a TPC track to the radius of the TOF. The extrapolated positions are then associated with the observed TOF hits. The efficiency of the matching procedure is discussed in

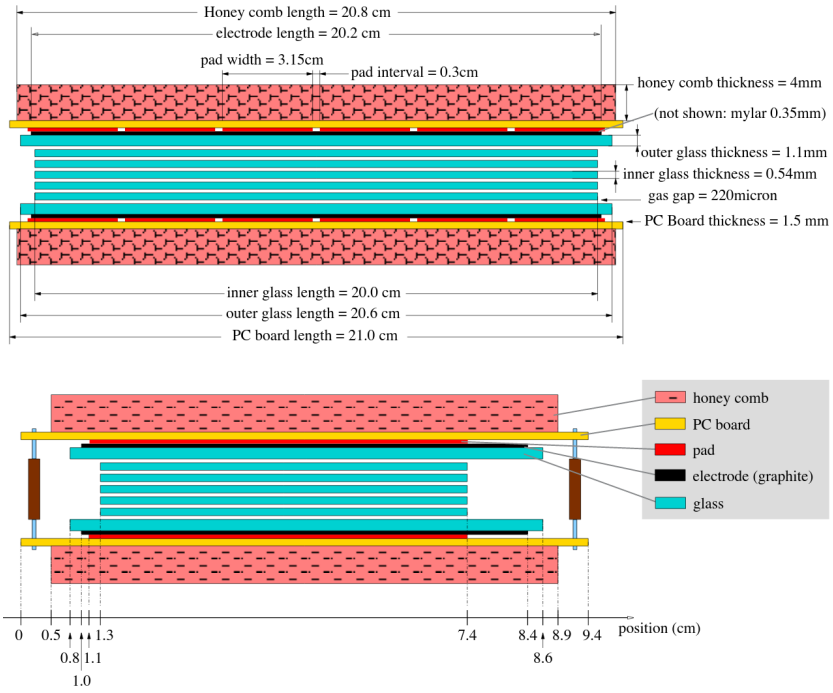

Figure 2.8: A schematic of the internal structure and pad layout within a single TOF MRPC. This figure is taken from [48]

more detail in Chapter 5, but is generally between 50-60% and is multiplicity dependent. Tracks in the TPC can be associated with multiple hits in the TOF and multiple tracks in the TPC can be associated with the same hit in the TOF. If a track is associated with one or more hits in the TOF detector it is said to have a "match" and the track is described as a "TOF Matched Track."

2.2.2.4 Particle Identification via Time Of Flight

Particle identification using the TOF detector is accomplished in one of two ways; by measurements of either velocity (equation 2.2) or mass squared (equation 2.3). Both methods require knowledge of the track's flight time and path length. The mass squared method also requires the track's momentum. As described, the TOF system gives the flight time and the TPC gives the momentum and path length.

In this analysis we utilize the velocity method because it does not introduce the uncertainties associated with the momentum determination into the particle identification methodology. This is especially useful since the errors on the momentum, path length, and flight time covary. Figure 2.9 shows the computed $1/\beta$ of tracks from measurements

of their flight time and path length as a function of total momentum. The curves in the figure are the expected $1/\beta$ as a function of momentum and have been computed assuming each species' mass. The various species are clearly discernible over a wide range of momenta and become indistinguishable as their momenta become much larger than their mass and their velocities approach the speed of light.

$$\frac{1}{\beta} = \frac{\Delta t}{L} = \sqrt{\frac{m^2 + p^2}{p^2}} \tag{2.2}$$

$$m^2 = \frac{p^2}{(\beta\gamma)^2} = p^2 \left(\frac{(c\Delta t)^2}{L^2} - 1 \right) \tag{2.3}$$

Δt = Time of Flight

L = Path Length

p = Momentum

$\gamma = \sqrt{1/(1-\beta^2)}$

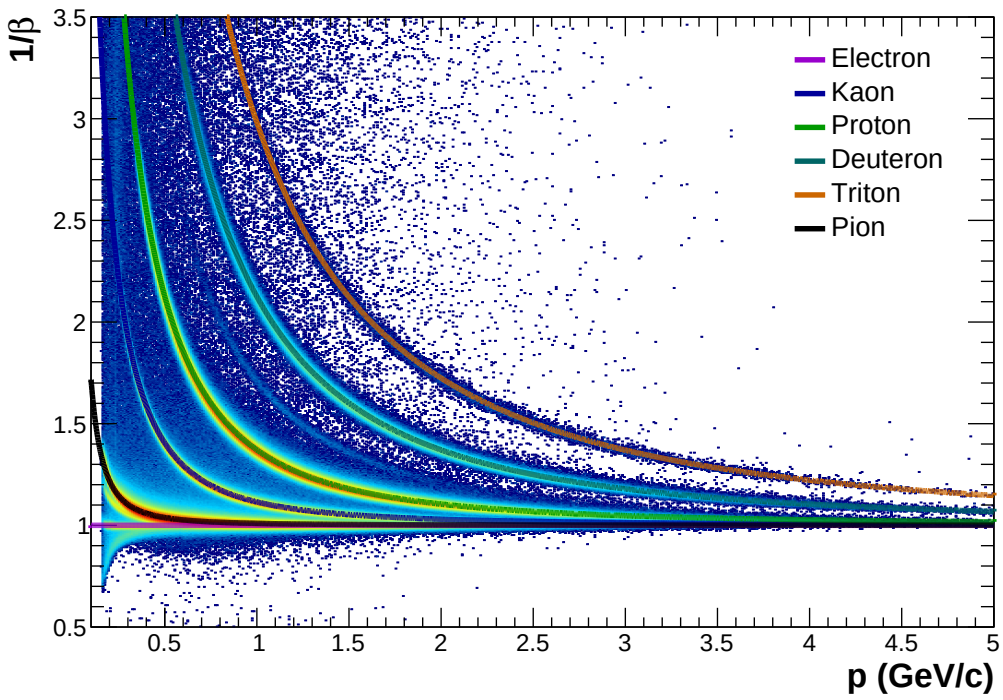

Figure 2.9: The $1/\beta$ computed using the time of flight measurements from the TOF detector as a function of total momentum from the $\sqrt{s_{NN}} = 7.7$ GeV data set. The curves in the figure represent the expected values given a particle's mass.

Chapter 3

Event Centrality Determination

An important feature of heavy-ion collisions is their expected dependence on system size. That is, the properties of the medium produced during the collision of two heavy-ions is expected to vary depending on the geometry of the overlap region between the colliding ions. Studies of how the medium's properties change as a function of system size can be accomplished by either altering the collision species or, in principle, by studying effects as a function of impact parameter. Events in which the impact parameter is small compared to the radius of the ions are said to be central while events with increasing impact parameters are said to be semi-central, semi-peripheral, and peripheral respectively.

Unfortunately, the impact parameter between two heavy-ions is not an accessible measurement. The centrality of an event must instead be inferred. In practice this inference is based on a presumption (because it has good observational support) that the observed particle multiplicity of an event increases monotonically with decreasing impact parameter. This permits a mapping from impact parameter to particle multiplicity and this, in turn, allows for event centrality to be binned in observed particle multiplicity as demonstrated in figure 3.1.

Despite the simple mapping, the centrality binning of an event by its multiplicity is complicated experimentally. Note that to determine a percentage of the multiplicity distribution of an ensemble of events it is first necessary to know the integral of the distribution. Given a perfect accelerator so that there are no background events, a perfect triggering system so that events of all centralities have equal probability of being mea-

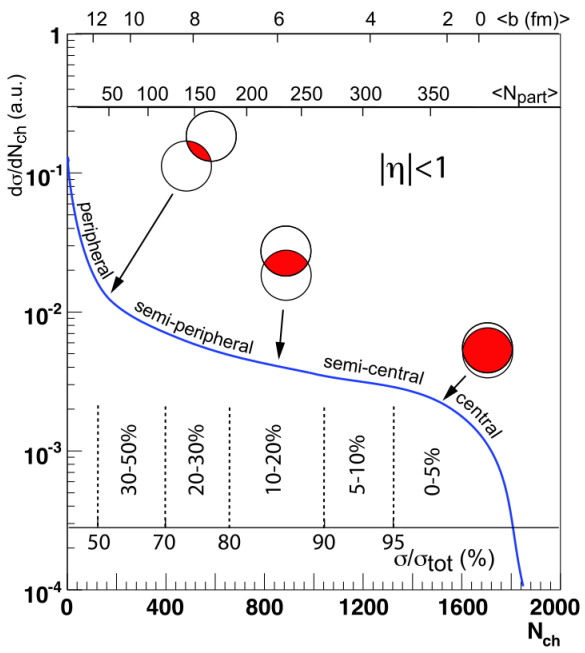

Figure 3.1: A schematic demonstrating the relationship between the observed number of charged particles N_{ch}, the impact parameter, number of participating nucleons, and the percent centrality. This figure was created by T. Ullrich and is taken from [51].

sured, and a perfect detector so that the measured multiplicity is independent of the event's location, the integral could be obtained directly from the data. Clearly this is optimistic. In practice significant effort is invested to correct for each of these effects.

The STAR collaboration has previously studied and corrected for all of these effects. The various corrections are implemented in the StRefMultCorr package. Hence, the standard method for obtaining the centrality classification of events in STAR is to simply query the StRefMultCorr class. However, this class only has centrality definitions implemented for events with $-70 \leq V_z \leq 70$ cm. Thus, the multiple event configurations of this analysis preclude its general use. Instead we implement a centrality classification scheme which is based on the same procedure as that used in StRefMultCorr, but which is implemented for events in the full range of $-200 \leq V_z \leq 200$ cm. We call this new class StRefMultExtendedCorr because of its implementation over an extended z-vertex range. A flow diagram summarizing the procedures implemented in this package

is shown in figure 3.2. In the following sections we describe the procedures in detail and demonstrate their effectiveness using examples from the $\sqrt{s_{NN}} = 14.5$ GeV dataset. Full documentation for all energies can be found at `http://www.star.bnl.gov/protected/lfspectra/cflores/StRefMultCorrExtended/` and the source code can be found at `https://bitbucket.org/chris_flores/strefmultextendedcorrcalibration`.

3.1 Data Collection and Event Selection for StRefMultExtendedCorr

The first step in the StRefMultExtendedCorr calibration procedure is the data collection phase. Information for each dataset used in the StRefMultExtendedCorr procedure is listed in table 3.1. The files for each run number are processed together to permit run averaged quantities to be computed. The files for each run number are obtained with the following query to the STAR file catalog:

```
<inputURL="catalog:star.bnl.gov?filetype=daq_reco_MuDst, tpx=1,
storage!=HPSS, filename st_physics, runnumber=&runNumber;
-distinct" singleCopy="true" nFiles="all" />
```

Event selection criteria was minimal so as not to produce a bias in the reweighting procedure below that would prevent the results from being generally useful. Only events with minimum bias triggers listed in table 3.1 were used in the procedure. Further cuts that events must satisfy include:

- Number of ToF Matched Primary Tracks 2 (Pile-Up Rejection)
- z-Vertex Location of $|V_z| \leq 205$ cm (Extended Vertex Range)
- r-Vertex Location of $|V_r| \leq 2.0$ cm (Beam-Spot Selection)
  - Except 14.5 GeV which requires $|V_r| \leq 0.5$ cm and where $|V_r| = 0$ is shifted to negative y-Vertex
- We also implement the following cuts to reduce computing time:
  - Random Gaussian pre-scale for events with $|V_z| \leq 95$ cm

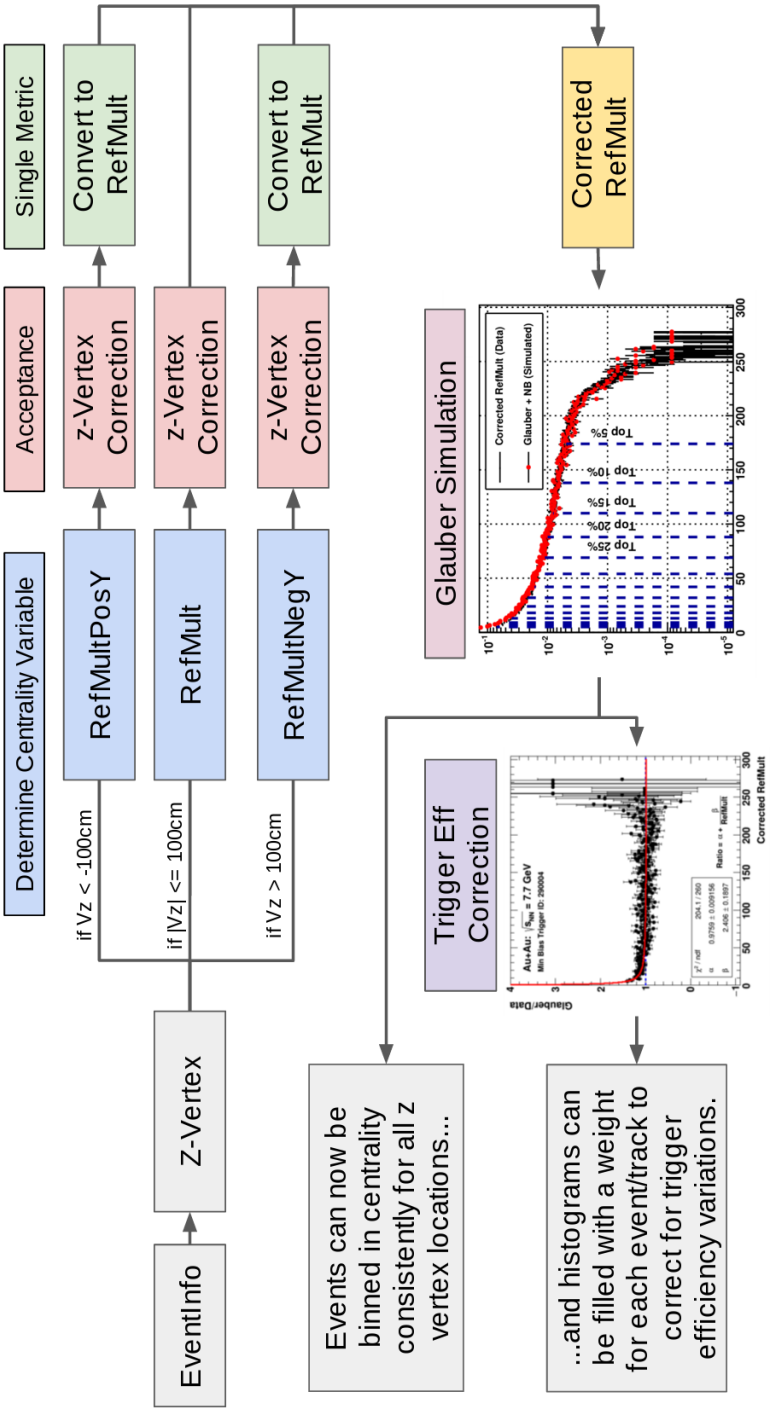

Figure 3.2: Summary of the features included in and processes involved with the implementation of the StRefMultExtendedCorr package.

$\sqrt{s_{NN}}$ GeV	STAR Library	Production	MB Trigger	Run Range
7.7	SL10h	P10ih	290001	11114074 - 11125099
			290004	11117093 - 11147027
11.5	SL10h	P10ih	310014	11148039 - 11158044
14.5	SL14i	P14ii	440015	15053000 - 15070021
19.6	SL11d	P11id	340001	12113079 - 12115069
			340011	12115070 - 12119029
			340021	12119030 - 12122019
27	SL11d	P11id	360001	12172043 - 12179097
39	SL10h	P10ik	280001	11099102 - 11112023
62.4	SL10k	P10ik	270001	11080054 - 11081037
			270011	11081052 - 11084037
			270021	11084038 - 11098056

Table 3.1: Datasets and minimum bias trigger IDs used in the StRefMultExtendedCorr calibration procedure.

The vertex distributions of events passing all of the above event selection criteria, including the pre-scale conditions, from the $\sqrt{s_{NN}} = 14.5$ GeV dataset are shown in figure 3.3. Note that the flatness of the V_z distribution near $V_z = 0$ and its sharp feature at $\pm$ 100 cm are due to the Gaussian prescale that ends at that z-vertex location.

3.2 Centrality Variables

The class StRefMultCorr is named for the centrality variable on which it is based, the reference multiplicity ($RefMult$ for short), which is defined as the number of charged particles ($dN_{\rm ch}/d\eta$) measured in the TPC for $|\eta| < 0.5$. For events with z-vertices near the center of the TPC this quantity is well suited for the task of being used as a centrality variable because the acceptance of the TPC does not change dramatically as a function of z-vertex. However, as can be inferred from figure 3.4a, the reference multiplicity of events with a z-vertex near the edge of the TPC will be affected by the rapidly falling η acceptance. To overcome this challenge we have found it necessary to introduce two addi-

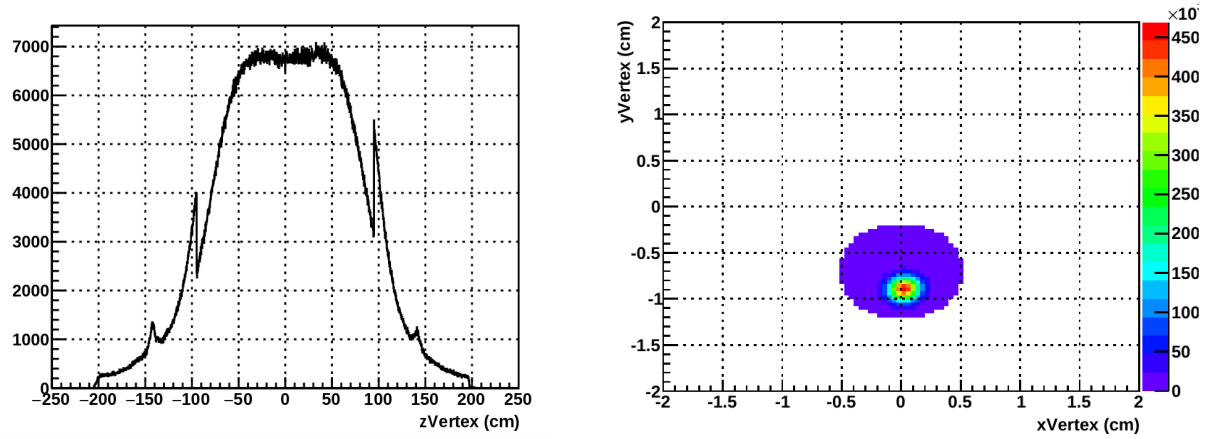

(a) V_z Distribution **(b)** V_{XY} Distribution

Figure 3.3: The V_z (a) and V_{XY} (b) distributions of events in the $\sqrt{s_{NN}} = 14.5$ GeV dataset that satisfy all of the event selection criteria listed in the main text.

tional centrality variables: $RefMultPosY$ and $RefMultNegY$. These variables measure the number of charged particles in one unit of positive ($0 < dN_{\rm ch}/d\eta < 1$) and negative ($-1 < dN_{\rm ch}/d\eta < 0$) rapidity respectively and can be seen in figures 3.4b and 3.4c.

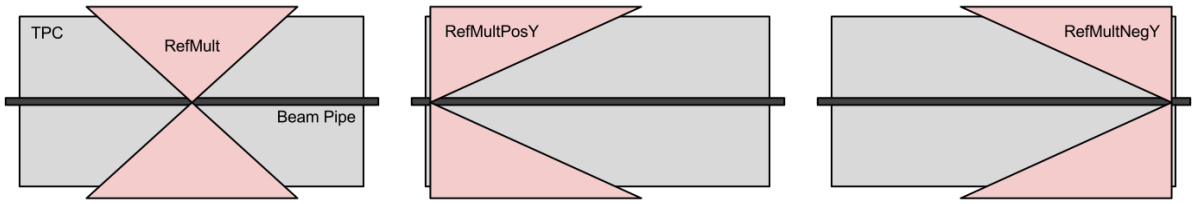

(a) $RefMult$ **(b)** $RefMultPosY$ **(c)** $RefMultNegY$

Figure 3.4: Schematic of the volume of the TPC (gray) and beam pipe (black) overlaid with the regions of acceptance (red) of the three centrality variables. The vertex of each acceptance cone is positioned to correspond to the z-vertex of an event from each of the three event configurations.

3.3 Acceptance Correction - Reweighting as a Function of z-Vertex Location

The first of the three corrections in this procedure is to correct the centrality variables for changes in acceptance as a function of an event's V_z location. The events are binned in 10 cm intervals over the full V_z range. The three centrality variables from each event

in the bin are placed in a histogram. The high multiplicity tail of each histogram is fit with an error function. The location of the half-maximum of the fit is found and referred to as $RefMultMax$, $RefMultPosYMax$, or $RefMultNegYMax$ depending on the centrality variable in question. Occasionally $RefMultMax$ will be used to refer to all three quantities generically. Figure 3.5 shows examples histograms of this procedure for each centrality variable.

The $RefMultMax$ value for each centrality variable is then plotted as a function of the center of its V_z bin as shown in the first column of figure 3.6. The maximum $RefMultMax$ is then found in the range $[-205, 205]$ cm and each point is scaled by this value to construct the correction factor as a function of the V_z location as shown in the second column of figure 3.6. Finally, to demonstrate the efficacy of this method, each centrality variable for each event is scaled by its respective correction factor and the binning/fitting procedure is repeated. The $RefMultMax$ values for each centrality variable after the correction is then demonstrated to be flat as a function of V_z location as shown in the third column of figure 3.6. This uniformity across the V_z range of interest for each centrality variable is the desired result.

3.4 Conversion of $RefMultPosY$ and $RefMultNegY$ to $RefMult$

The second of the three corrections of this procedure is to construct a conversion mechanism by which the two new centrality variables, $RefMultPosY$ and $RefMultNegY$, can be converted to $RefMult$. This is useful so that centrality bins can be defined and implemented in one variable. This, in turn, allows the centrality of events from all configurations to be evaluated on equal footing. After the V_z correction procedure above is performed $RefMultPosY$ and $RefMultNegY$ are plotted versus $RefMult$ as shown in figure 3.7. The scatter plot is fit with a first order polynomial. These fits then define the conversion from the two new centrality variables to $RefMult$.

With the conversion defined each event is then corrected for its V_z location and then has its centrality variable converted to $RefMult$. Events with $|V_z| \leq 100$ cm have their

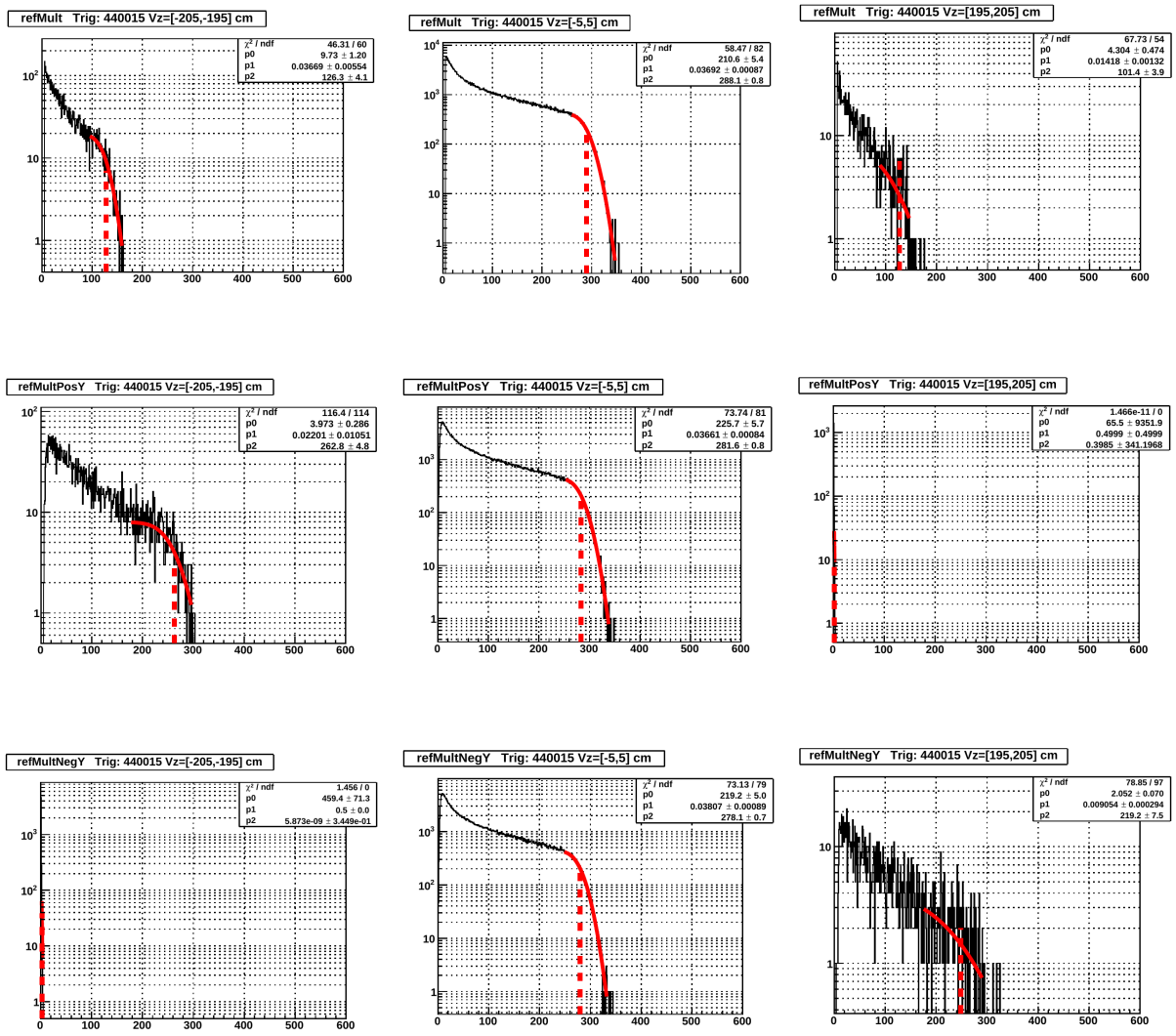

Figure 3.5: Example of the V_z binning and fitting of the centrality variable distributions as described in the main text. The three rows correspond to the three centrality variables while the columns are three V_z bins. Note that some histograms have no entries by construction - in those V_z regions the measured region lies outside the acceptance of STAR.

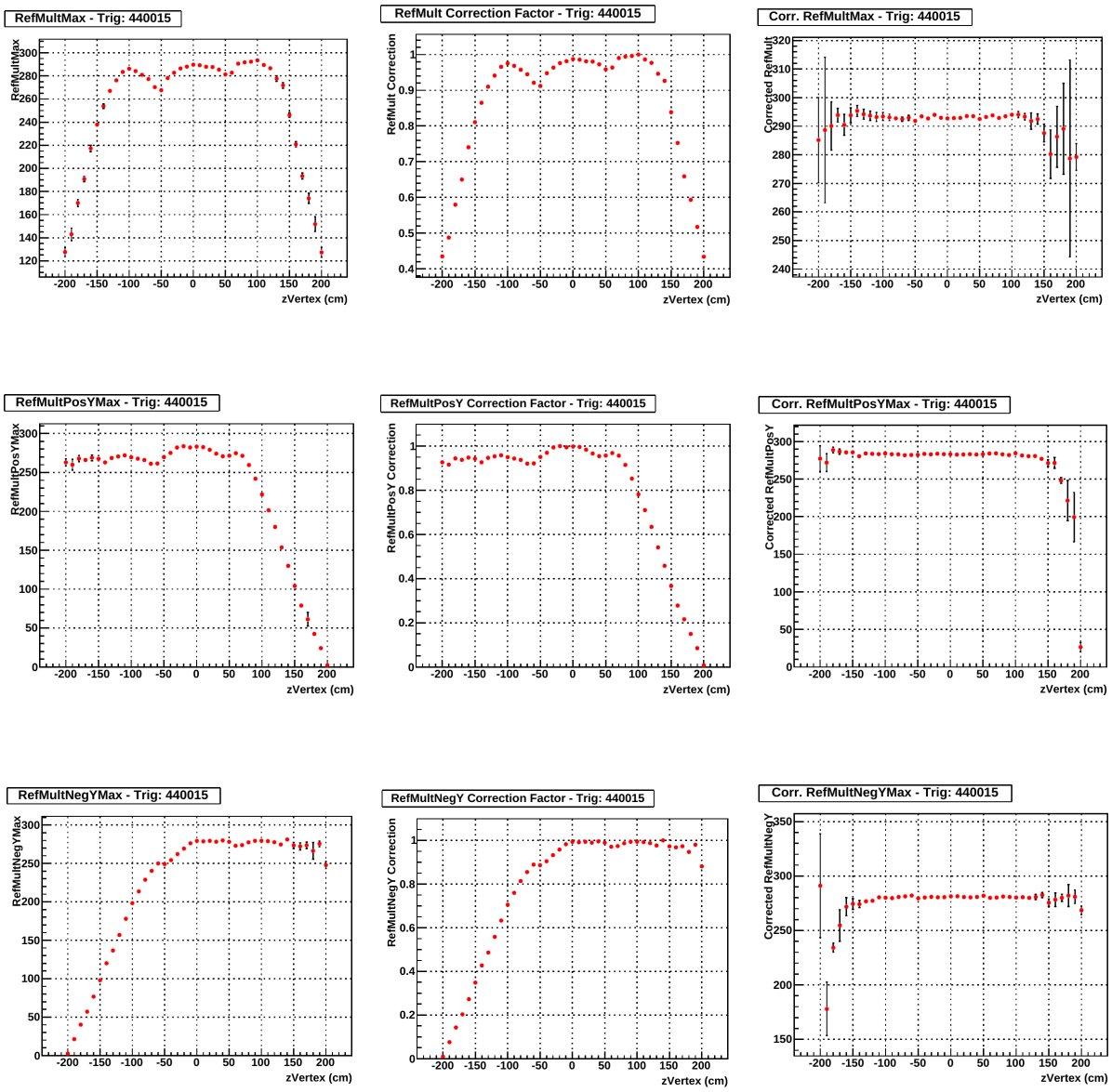

Figure 3.6: The reweighting procedure of the centrality variables as a function of z-vertex location for the $\sqrt{s_{NN}} = 14.5$ GeV dataset. The first column shows the uncorrected values of $RefMultMax$, the second column shows the correction factor, and the third column shows the values of $RefMultMax$ after the correction factor has been applied.

centrality defined by $RefMult$ and so do not need this last step. The binning/fitting procedure is repeated a final time and the result is shown in figure 3.8. As is clear from the figure the corrected values of $RefMultPosY$ and $RefMultNegY$ are now equivalent to $RefMult$.

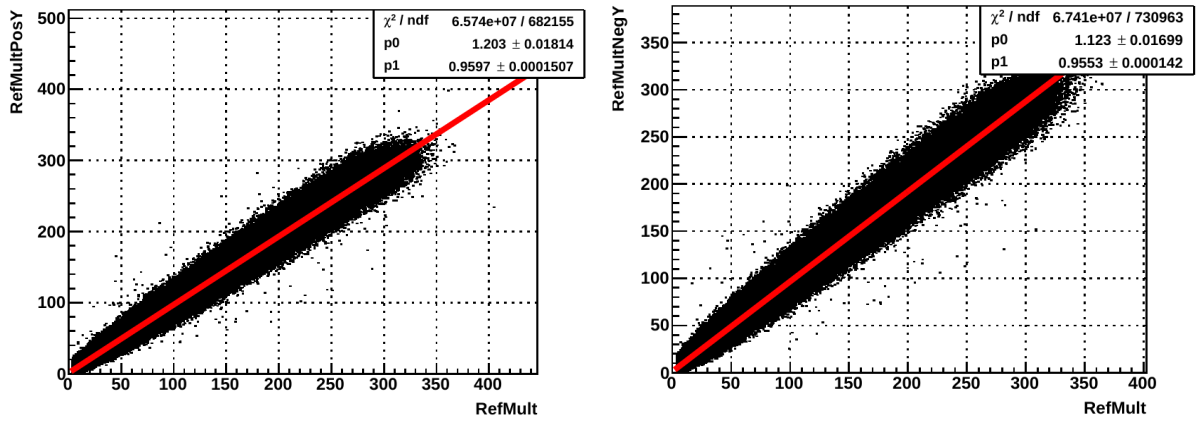

Figure 3.7: $RefMultPosY$ and $RefMultNegY$ plotted versus $RefMult$ from the $\sqrt{s_{NN}} = 14.5$ GeV dataset and fit with a line. This line defines the conversion from the two new centrality variables to $RefMult$.

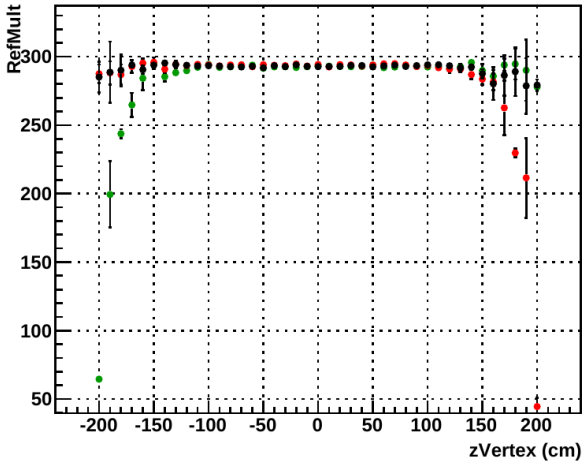

Figure 3.8: Fully corrected and converted centrality variables from the $\sqrt{s_{NN}} =$ 14.5 GeV dataset. The colors are as follows: $RefMult$ is shown in black, $RefMultPosY$ is shown in red, and $RefMultNegY$ is shown in green.

3.5 Centrality Bin Determination

Recall that we desire to classify events in bins of percent centrality. This implies that we need to know the *true* shape of the multiplicity distribution – the shape given by uniformly sampling the geometric cross section of the colliding nuclei – to take its integral. So far we have corrected the distribution to remove effects due to the change in the detector acceptance as a function of V_z. However, we have not yet considered the effects of how the trigger efficiency may change with multiplicity. For example, it is known that the min-bias trigger efficiency is smaller for peripheral events than for central events. Thus the present $RefMult$ distribution cannot be assumed to represent the full Au+Au cross section and hence cannot be used to compute the needed integral. Instead, it is necessary to simulate the observed multiplicity distribution by using a sequence of models: first, a Glauber Monte Carlo Model to simulate the colliding nuclei and second, a particle production model that can be tuned to match the data.

3.5.1 Glauber Monte Carlo Model

The Glauber Model, in its original, theoretical form [52], was developed to model the quantum scattering of composite systems. In the field of heavy-ion collisions this framework was simplified to its geometric basis to estimate the number of participating nucleons, N_{part}, the number of binary collisions, N_{coll}, and the impact parameter, b. For a more complete introduction to Glauber Modeling in heavy-ion collisions we defer to [51]. In this section we document the particulars of the Glauber Model used for the present analysis. An interested reader can find the source code for this model here: `https://bitbucket.org/chris_flores/glaubermcmodel`. This model is also included as a submodule in StRefMultExtendedCorr.

In almost all cases a reference to a *Glauber Model* is really a reference to a Glauber Monte Carlo Model. The "Monte Carlo" in the name refers to the method's repeated sampling of probability distributions as a means of assigning the initial conditions of each instance of the model. The model is remarkably straightforward at the highest level. It begins by randomly distributing the appropriate number of nucleons, A, for each of the given ion species within their respective three dimensional volumes. The nuclei are then

assigned a random impact parameter and one nucleus is translated appropriately. Finally, the values of N_{part} and N_{coll} can be computed by comparing the distances between the centers of the nucleons in each nucleus. If their separation distance is less than $\sqrt{\sigma_{\text{inel}}^{NN}/\pi}$, where $\sigma_{\text{inel}}^{NN}$ is the inelastic nucleon-nucleon cross section, the nucleons are said to have a binary collision. Nucleons which have had at least one binary collision are said to have participated in the reaction. The model as described is illustrated in figure 3.9 for $b = 6$ fm. Despite its high-level conceptual simplicity, the particulars of the model contain the majority of the complexity and are discussed below.

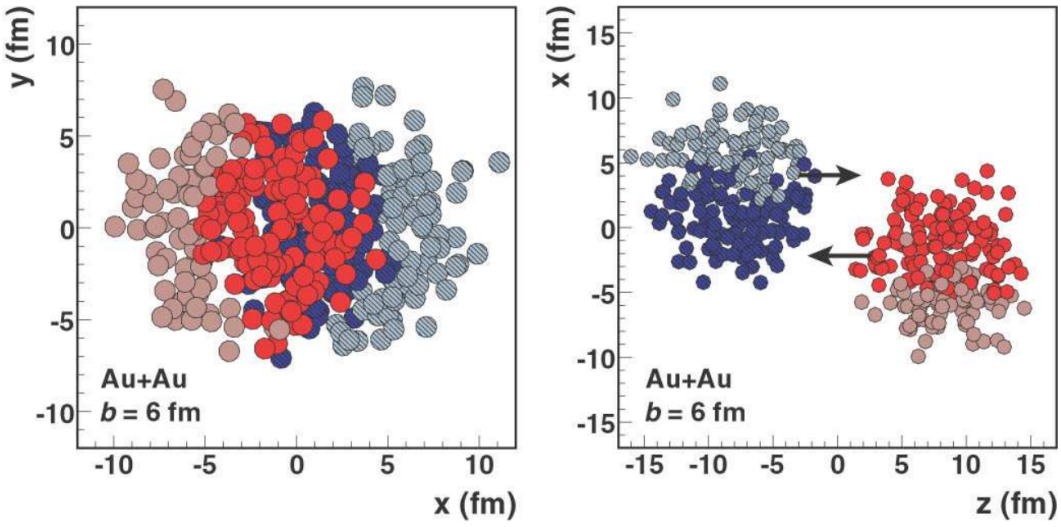

Figure 3.9: A Glauber Monte Carlo Au+Au event with impact parameter $b = 6$ fm shown in both the transverse plane (left) and along a plane containing the beam-axis (right). Nucleons are drawn to scale such that their radii are given by $R_N = \sqrt{\sigma_{\text{inel}}^{NN}/\pi}/2$. Nucleons with darker colors are those participating in the event and thus define the system size. Because the number of participating and colliding nucleons is dependent only on their transverse area, the effect of Lorentz contraction is not included in the right image. This figure is taken from [51].

3.5.1.1 Inelastic Nucleon-Nucleon Cross Section

The energy dependence of the Glauber Model, and therefore of N_{part} and N_{coll}, is entirely contained in the energy dependence of the inelastic nucleon-nucleon cross section, $\sigma_{\text{inel}}^{NN}$. Since the collision energy of a typical heavy-ion collision is much larger than the mass of the proton and neutron, $\sqrt{s_{NN}} \gg m_{p,n}$, the inelastic cross section is presumed to have

the property $\sigma_{\text{inel}}^{NN} = \sigma_{\text{inel}}^{pp} = \sigma_{\text{inel}}^{pn} = \sigma_{\text{inel}}^{nn}$ for any given energy. To obtain $\sigma_{\text{inel}}^{NN}$ for the energies of RHIC Beam Energy Scan (BES) program that were used in this analysis data tables for the $p+p$ total and elastic cross sections were obtained from [46]. The total cross section was fit with equation 3.1, the same as the function given in [46], except that the last term was removed to improve the stability of the fit and to give a positive definite result. The elastic cross section was fit with equation 3.2. Note that in both fits the independent variable, s, is in units of GeV^2 to cancel with the units of s_m. The fit parameters and reduced χ^2 values for both fits are given in table 3.2.

$$\begin{aligned} &\sigma_{total}^{pp}(s) = P + H\log_{10}^2(s/s_m) + R(s/s_m)^{-\eta} \\ &\text{where } H = \pi\frac{(\hbar c)^2}{M^2} \text{ and } s_m = (m_p + m_p + M)^2 \end{aligned} \tag{3.1}$$

$$\sigma_{elastic}^{pp}(s) = \alpha + \frac{\beta}{(s)^\gamma} + \delta\log_{10}(s) \tag{3.2}$$

	P, α	M, β	R, γ	η, δ	χ^2/ndf
σ_{total}^{NN}	30.31 ± 1.73	1.84 ± 0.05	12.25 ± 1.46	0.1305 ± 0.03	89.54/114
$\sigma_{elastic}^{NN}$	-2.01 ± 4.29	37.97 ± 3.67	0.09 ± 0.01	2.96 ± 0.3	144/78

Table 3.2: Resulting parameters and χ^2 values from fits to elastic and inelastic cross sections.

The data obtained from [46] and the results of the fits are shown in figure 3.10. The one σ error band on the fit of σ_{total}^{pp} is also included, but is too small to be seen. The set of coordinates representing the inelastic cross section are obtained by taking the difference between the value of the elastic cross section data points and the total cross section fit: $\sigma_{\text{inel},i}^{pp} = \left\{\left(s_i, \sigma_{total}^{pp}(s_i) - \sigma_{elastic,i}^{pp}\right)\right\}$. The errors on the points are the quadrature sum of the error associated with the elastic cross section point and the one σ fit error at that energy for the total cross section. The curve describing $\sigma_{\text{inel}}^{pp}$ is not a fit, but is the difference between the fits to the total and elastic cross sections: $\sigma_{\text{inel}}^{pp}(s) = \sigma_{total}^{pp}(s) - \sigma_{elastic}^{pp}(s)$. This curve shows excellent agreement with the inelastic points. Finally, the values of $\sigma_{\text{inel}}^{NN}$ needed for this analysis can be obtained by evaluating the curve $\sigma_{\text{inel}}^{pp}(s)$ at the necessary

energies and are shown inset in figure 3.10. Consistent with other analyses, a $\pm$ 5% error is assumed on all values of $\sigma_{\text{inel}}^{NN}$ and is used in the calculation of systematic errors.

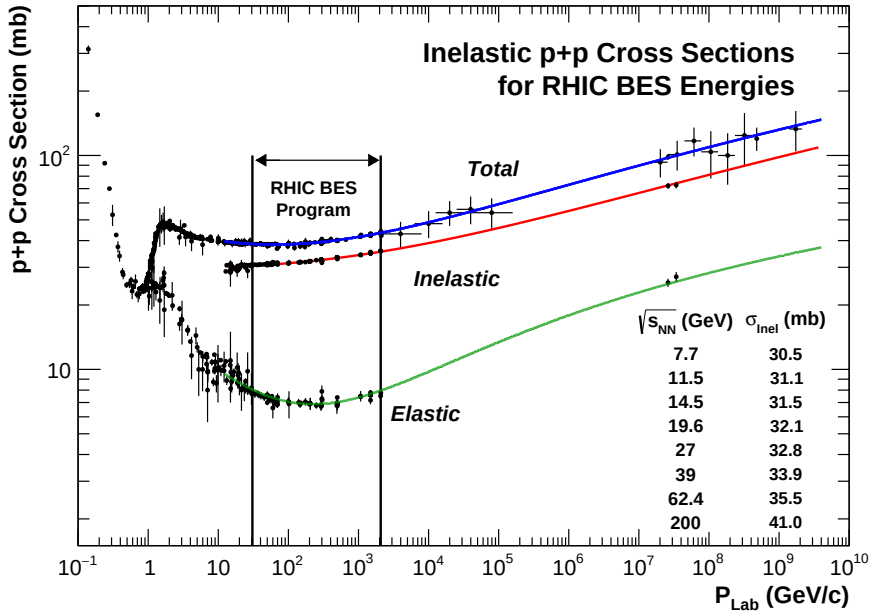

Figure 3.10: Data files from [46] were obtained for the total (blue fit) and elastic (green fit) cross sections and fit above $\sqrt{s_{NN}} = 5$ GeV. The points for the inelastic cross section were obtained by taking the difference between the blue curve and the elastic cross section data points. The red curve describing the inelastic cross section is not a fit, but the difference between the blue and green curves. The inelastic cross section curve is then evaluated at BES energies and tabulated in the inset.

3.5.1.2 Nucleon Distributions

Depending on the level of sophistication of a particular implementation of the Glauber Monte Carlo Model, the distribution of nucleons in the three-dimensional volume representing a nucleus can vary dramatically. In its simplest form one could estimate the radius of the nucleus with $R_A = 1.25A^{1/3}$ and uniformly distribute A nucleons within the spherical volume defined by radius R_A. This is a good zeroth-order approximation and an excellent starting point when developing one's own Glauber Monte Carlo implementation but it ignores the wealth of research done on nuclear structure.

A more sophisticated approach (and the one that is most common and therefore used here) is to rely on the results of electron scattering experiments. These experiments

measure the scattering patterns of beams of electrons that have been set incident on nuclei to construct charge density distributions. Historically, there have been many functional forms that have been used to describe the charge distributions of nuclei, but the Fermi Distribution and its variants have been most widely used. The most general form of the *Three Parameter Fermi Distribution* as found in [53] is given in equation 3.3. The three parameters alluded to in its name refer to the parameters $c, a,$ and ω which describe the half density radius, the skin-depth (sometimes referred to as diffuseness), and central charge suppression respectively. The last parameter is useful for modeling very heavy ions whose charge densities in their central regions suffer from non-negligible Coulomb repulsion.

$$\rho(r,\theta) = \begin{cases} \rho_0 \frac{1+\omega(r/c)^2}{1+e^x}, & r < c \\ \rho_0 \frac{1+\omega}{1+e^x}, & r \geq c \end{cases} \tag{3.3}$$

$$\text{where } x = \frac{r - c\left(1 + \beta_{20} Y_{20}(\theta) + \beta_{40} Y_{40}(\theta)\right)}{a\left(1 + \beta_{20}\gamma_2 Y_{20}(\theta) + \beta_{40}\gamma_4 Y_{40}(\theta)\right)}$$

The value of ρ_0 is chosen such that the volume integral of $\rho(r,\theta)$ over all spherical dimensions is equal to the mass number, A. The parameters β_{20} and β_{40} describe the quadrupole and hexadecapole ground-state deformations of a nucleus respectively and are useful when modeling nuclei like ^{238}U, which is prolate in shape. For spherical nuclei such as ^{208}Pb, $\beta_{20} = \beta_{40} = 0$. The parameters γ_2 and γ_4 are entirely model dependent per the discussion in [54]; formulations in which $\gamma_2 = \gamma_4 = 0$ are known as *Modified-c Fermi Distributions*, while $\gamma_2 = \gamma_4 = 1$ beget *Deformed Fermi Distributions*, and lastly $\gamma_2 = \gamma_4 = (c/2)\ln 3$ result in *Hard-Core Distributions*. Simplified forms of equation 3.3 in which $\omega = 0$ are called *Two Parameter Fermi Distributions*, or more commonly, *Woods-Saxon Distributions*.

The functions $Y_{20}(\theta)$ and $Y_{40}(\theta)$ are the spherical harmonics $Y_{lm}(\theta,\phi)$. Since $m = 0$ in both cases, the functions are independent of ϕ. The standard convention used in physics for the description of angles is retained: namely the polar angle $\theta \in [0,\pi)$ and the azimuthal angle $\phi \in [0, 2\pi)$.

Figure 3.11 shows equation 3.3 for several nuclei. For spherically-symmetric nuclei, a single value of the polar angle, θ is shown. For ^{238}U, which is a prolate spheroid, two values of θ are chosen to demonstrate the effect of the deformation parameters. The effect of a non-zero value for ω is also clear in the shape of ^{238}U at small values of r. With the exception of ^{238}U, whose parameters were obtained directly from [53], all of the Fermi Distribution parameters are obtained from [55].

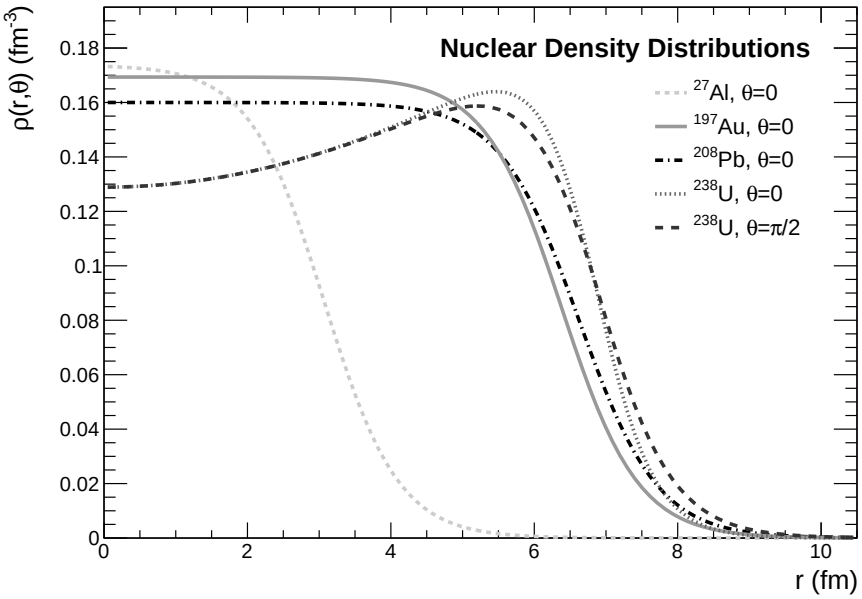

Figure 3.11: Nuclear charge densities as a function of radius for a variety of nuclei using equation 3.3. The effect of the central proton density parameter, ω, and the deformation parameters, β_{20} and β_{40}, can be seen in the distributions for Uranium.

For completeness, the following parameters for ^{197}Au are used in this study of Au+Au collisions: $\rho_0 = 0.169$ fm^{-3}, $c = 6.38 \pm 0.06$ fm, $a = 0.535 \pm 0.027$ fm, $w = 0$, and $\beta_{20} = \beta_{40} = \gamma_2 = \gamma_4 = 0$. The errors on the parameters are used during the estimation of systematic errors of $N_{\rm part}$ and $N_{\rm coll}$. Recall that the value of ρ_0 depends on the choice of values for the other parameters. Thus, it is recomputed when any parameter is changed. The choice of the deformations parameters suggest that the ^{197}Au nucleus is spherical. In reality it is an oblate spheroid, however its departure from perfect sphericity is so minor that it is frequently ignored. This choice is consistent with the standard STAR Glauber Monte Carlo Model.

The Fermi Distributions cannot be used to assign nucleon positions because they are density profiles. Instead, one must construct the two-dimensional probability density function (PDF) from the Fermi Distributions by multiplying by the differential volume elements $r^2 \sin\theta$. The two-dimensional PDF for ^{197}Au can be see in figure 3.12. Note that the PDF must ensure that each volume element of the nucleus is equally probable to be chosen as a position for the nucleon. The shape along θ prevents oversampling at the poles of the spheroid. The shape along r demonstrates that the accessible volume of the spheroid increases at a faster rate than r itself and then drops quickly at large r. The radial, r, and polar angle, θ, positions of nucleons within a nucleus can easily be obtained by repeatedly sampling this distribution. The final angle, ϕ, can be obtained by uniformly sampling in the range, $\phi \in [0, 2\pi)$.

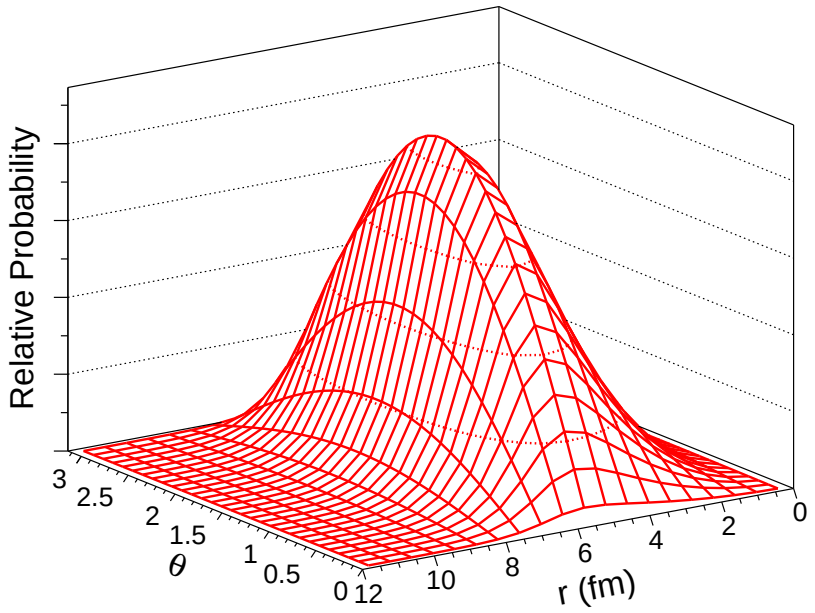

Figure 3.12: The two-dimensional probability density function of ^{197}Au. Nucleons are assigned their (r,θ) positions by repeatedly sampling a PDF such as this.

The subject of determining the charge density distributions of nuclei is extraordinarily rich in its history and methodology. As a result this author has spent more time than is advisable perusing articles on the subject and cannot resist the urge to make a few

recommendations of primary sources. For an insight into an electron scattering experiment that seems of uncommon importance please see [56]. For an excellent review of the subject as a whole consider [57]. For a tabulation of the charge density distribution parameters for a wide variety of nuclei see [55]. Finally, for a tabulation of ground state deformation parameters see [58].

Additional constraints can also be placed on the locations of the nucleons. A common constraint is to require some minimum distance between nucleons in the same nucleus. This requirement is often referred to as a *nucleon hard-core* model. The default in the Glauber Monte Carlo Model developed here is to permit the full overlap of nucleons within the same nucleus, but the effect of requiring a minimum distance is investigated during the calculation of systematic errors.

A final complication arises from the consideration of non-spherical nuclei - namely rotational degrees of freedom in the initial state configuration of the nucleon distributions. Currently there are no means of producing polarized heavy-ion beams in an accelerator. Thus any model meant to simulate the collisions of heavy-ions as they occur in the lab must allow for the initial nucleon distributions to be rotated. Although this physics study exclusively concerns ^{197}Au which was chosen to be modeled as spherical, this Glauber Monte Carlo Model was developed to be robust enough to model deformed nuclei. Rotations are implemented in this model via the *x-convention* of the Euler angles as described in [59]. The rotations are performed after nucleons have been distributed by randomly sampling their charge distributions but before the translation of the center of one nucleus due to the impact parameter.

3.5.1.3 Glauber Monte Carlo Model Results

We are now in a position to turn our attention to the results of the Glauber Monte Carlo Model. As previously noted the utility of the model is derived from its ability to compute the number of participating nucleons, N_{part}, and the total number of binary collisions, N_{coll}, for a collision with a given impact parameter, b. Figure 3.13 shows distributions for each of these values obtained from a Glauber Monte Carlo Model of 100k ^{197}Au + ^{197}Au collisions with $\sigma_{\text{inel}}^{NN} = 42$ mb (chosen to allow direct comparisons to [51]) and with

at least one binary collision. Each distribution is also shown for two classes of events: min-bias events and central events with $b \leq 2$ fm. The shapes of these distributions are typical for symmetric collisions of all but the smallest of nuclei.

Most of the features of the distributions can be intuited. The nominal nuclear radius of ^{197}Au is $R_{\mathrm{Au}} = 1.25(197)^{1/3} = 7.2$ fm. Simple geometry then dictates that there should be a sharp fall off in the impact parameter distribution for $b > 2R_{\mathrm{Au}} \approx 14$ fm; which is indeed observed. The increasing shape of the impact parameter distribution for $r < 2R_{\mathrm{Au}}$ is the result of the increasing probability of choosing larger values for b, which is the consequence of the uniform sampling (equal probability per unit area) of a circle. The long flat regions in the middle of the N_{part} and N_{coll} min-bias distributions are present because, for a sizable range of intermediate impact parameters, those values change slowly. The sharp rise at the low end of these distributions is due to the most probable value of b being about $2R_{\mathrm{Au}}$, but these configurations result in the smallest values of N_{part} and N_{coll}. The shape of the N_{part} and N_{coll} distributions for central collisions ($b \leq 2$ fm) demonstrate that even events within a narrow range of impact parameters can vary broadly - a feature which, as will be shown, must be taken into account when scaling physics measurements by an estimate of system size obtained from the average N_{part} of a centrality class.

The full scope of the Glauber Monte Carlo Model that was developed in support of this analysis can be observed in figure 3.14. In total, the Fermi Distribution parameters for forty-one nuclear species ranging from ^{14}N to ^{244}Pu were collected and are available for use in simulations. The figure shows the results of 100k symmetric collisions with $\sigma_{\mathrm{inel}}^{NN} = 42$ mb for a selection of the available nuclei. For each set of nuclei two models were run; one in which the nucleons were distributed according to the Fermi Parameters and the other in which the nucleons were distributed using the hard sphere model. For each case the values of $\langle N_{\mathrm{part}} \rangle$ and $\langle N_{\mathrm{coll}} \rangle$ are computed for both min-bias collisions and for collisions in which $b \leq 2$ fm and are shown as a function of the mass number, A.

To illustrate the effect of the method chosen for distributing the nucleons the ratio between each of the averages is shown in the bottom plot of the figure. In all cases the ratio shows a dependence on A, but the interpretation of this dependence is confounded by

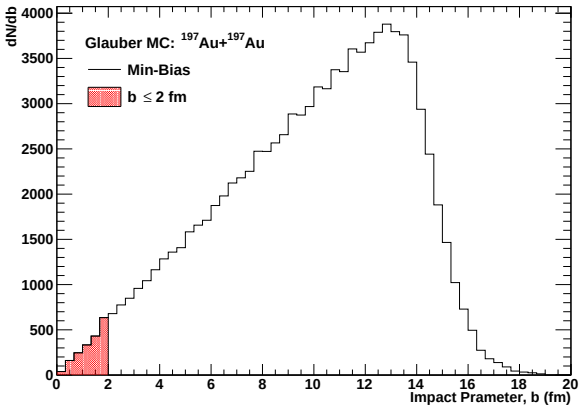

(a) Impact Parameter, b, Distribution

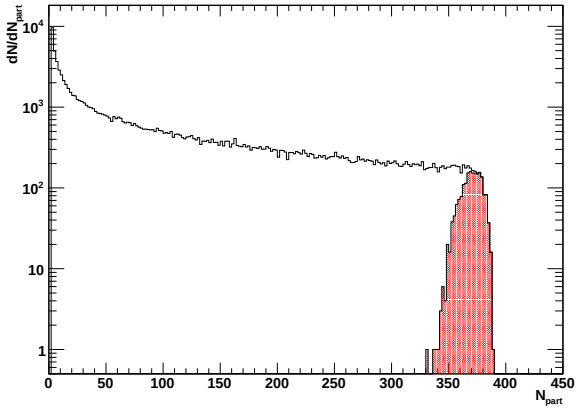

(b) Participant Nucleon, N_{part}, Distribution

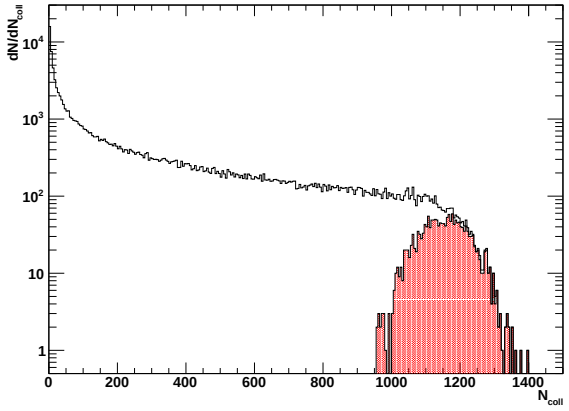

(c) Binary Collision, N_{coll}, Distribution

Figure 3.13: Results from a Glauber Monte Carlo Model consisting of a sample of 100,000 ^{197}Au+^{197}Au events with $\sigma_{\text{inel}}^{NN} = 42$ mb. Each figure shows the min-bias distributions and the distributions for central events satisfying $b \leq 2$ fm.

at least two effects: the fraction of the geometric cross section included in the calculation of $\langle N_{\rm part}\rangle$ and $\langle N_{\rm coll}\rangle$ changes dramatically with A for a fixed value of b; in addition, there is an effect caused by the inequality between the nominal nuclear radius used in the hard sphere model and the half density radius used in the Fermi Distribution, $R_A = 1.25A^{1/3} \neq c \approx 1.07A^{1/3}$. For nuclei with $\omega = 0$, this has the effect of concentrating nucleons closer to the center compared to the hard-sphere model.

3.5.2 Particle Production Model

Regardless of its level of sophistication the Glauber Monte Carlo Model results are not directly comparable to any measured quantity. Recall that the final goal of this procedure is to bin the events in centrality based on their observed particle multiplicity. Thus, to relate the Glauber Monte Carlo Model to data a particle production model must be layered on top of it. In this subsection we discuss the particle production model used in this analysis.

In the most naive conception of a reaction between two heavy-ions one is tempted to consider the system as a superposition of $A_1 + A_2$ protons undergoing $N_{\rm coll}$ scatters. Just such a model is used in heavy flavor analysis of R_{AA} measurements. This model works well for these types of analyses for two reasons. First, the principal purpose of these analyses is to elucidate the deviations of heavy-ion reactions from a collection of $p + p$ collisions. And second, the physics of interest - namely the production of quarkonia - scales as the number of hard scatters, which is most sensitive to $N_{\rm coll}$. However, the vast majority of the particles produced in heavy-ion reactions result from thermal (or soft) production as observed at the SPS [60]. This gave credence to the *Wounded Nucleon Model* of particle production [61]. This indicates that the model we use to simulate the total number of particles produced in a reaction of two nuclei must allow for the combination of these two effects, but be largely biased to $N_{\rm part}$. A commonly used model is based on the *Two Component Model* proposed by Kharzeev and Nardi [62] and is explained below.

Consider a heavy-ion collision at a nucleon-nucleon center-of-mass energy of $\sqrt{s_{NN}}$. Then each nucleon has energy $E_N = \sqrt{s_{NN}}/2$. Let the total energy available for particles production be $E_{\rm tot} \propto xE_{\rm hard} + (1-x)E_{\rm soft}$, where the value of x sets the scaling between

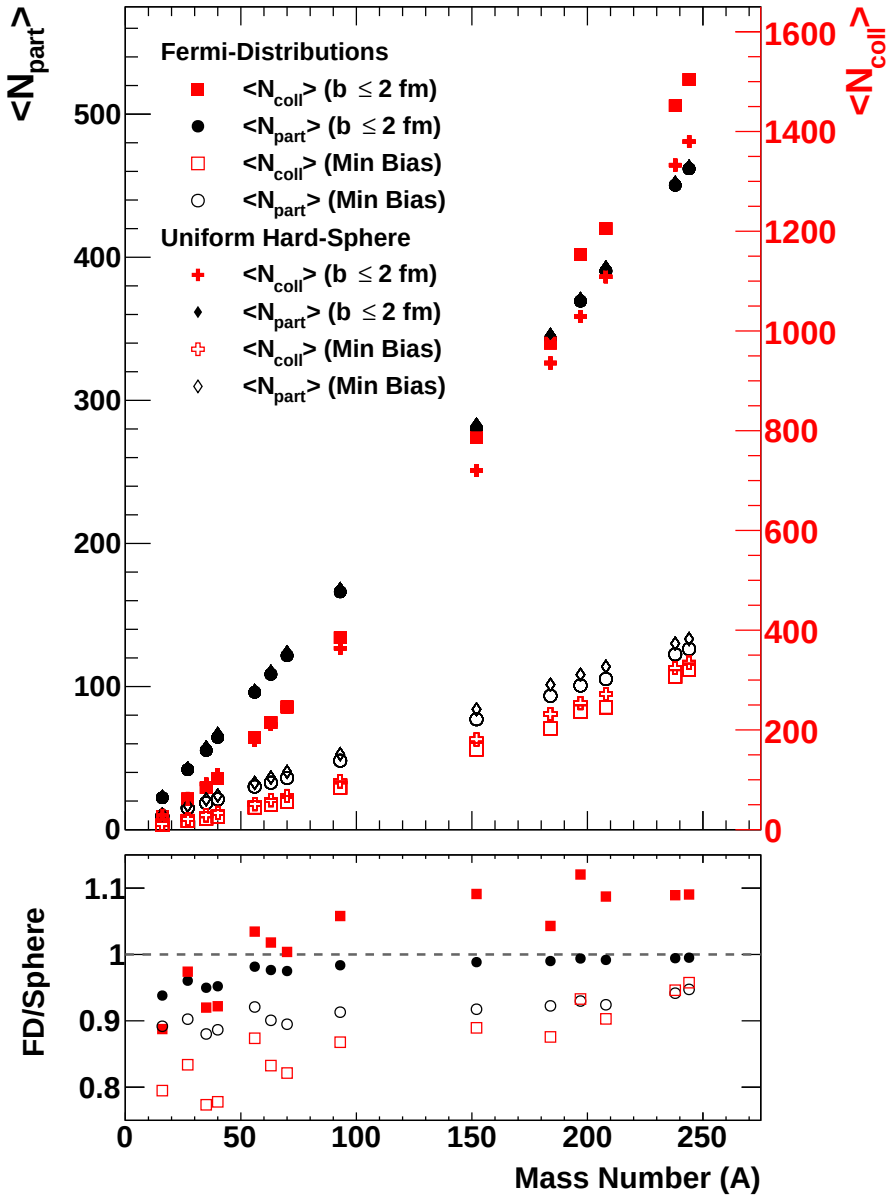

Figure 3.14: The results of the Glauber Monte Carlo Model for several different species of nuclei ranging from ^{16}O to ^{244}Pu. In all cases $\sigma_{\rm inel}^{NN} = 42$ mb. The *top* plot shows the dependence of the average values of $N_{\rm part}$ and $N_{\rm coll}$ on system size, A, for central events ($b \leq 2$ fm) and min-bias events using both the Fermi-Distribution and Uniform-Sphere methods of distributing the nuclei. The *bottom* plot shows the ratio of the nucleon distribution methods for each of the two classes of events.

the relative contribution to particle production from the hard and soft mechanisms. The energy available for the production of particles through hard process is given by the product of the number of possible hard collisions and the energy of each hard collision: $E_{\rm hard} = 2E_N N_{\rm coll} = N_{\rm coll}\sqrt{s_{NN}}$. The energy available for soft particle production is related to the energy density (ϵ) and volume (V) of the overlap region. The energy density can be measured in units of energy per nucleon volume, $\epsilon = 2E_N$, and the volume of the overlap region is given in units of nucleon volume by $V = N_{\rm part}/2$. Thus, $E_{\rm soft} = \epsilon V = 2E_N N_{\rm part}/2 = \sqrt{s_{NN}}N_{\rm part}/2$. This results in $E_{\rm tot} = \sqrt{s_{NN}}\,(xN_{\rm coll} + (1-x)N_{\rm part}/2)$. Dropping the factor of collision energy we define a new quantity $m = xN_{\rm coll}+(1-x)N_{\rm part}/2$ which allows us to express the number of produced particles as [62].

$$\frac{dN_{\rm ch}}{d\eta} = n_{pp}m = n_{pp}\left(xN_{\rm coll} + (1-x)\,\frac{N_{\rm part}}{2}\right). \tag{3.4}$$

The quantity n_{pp} is the multiplicity from a p+p collision of the same energy as the nucleon-nucleon center-of-mass in the heavy-ion collision of interest. Equation 3.4 has been shown by the PHOBOS collaboration [63] to have excellent agreement for the observed multiplicities from Au+Au collisions at $\sqrt{s_{NN}} = 19.6$ and 200 GeV for $x = 0.12 \pm 0.01 \pm 0.05$. The small value for the scaling parameter x is consistent with the expectation that the number of produced particles should scale most closely with the number of participant nucleon pairs rather than the number of binary collisions.

The last piece of the particle production puzzle is n_{pp}. Studies of the multiplicity distributions of $p+p$ collisions by UA5 in [64] demonstrate that they are best described by negative binomial distributions, NB($n_{pp}; \langle n_{pp}\rangle, k$). In this formulation the parameter $\langle n_{pp}\rangle$ is the average multiplicity of a $p+p$ collision at the energy of interest and the parameter k is related to the variance of the $p+p$ multiplicity distribution. Hence, the value of n_{pp} can be modeled by sampling from a NB distribution. In principle, the parameters for the NB distributions describing $p+p$ multiplicities can be collected and parameterized to find the set of parameters that should be used at any energy, but in

practice they are tuned to fit the heavy-ion multiplicity distributions.

$$\begin{aligned}
\frac{dN_{\mathrm{ch}}}{d\eta} &= \sum_{i=0}^{\lceil m \rceil} X_i \\
&\text{where } \; m = \left[x N_{\mathrm{coll}} + (1-x)\, N_{\mathrm{part}}/2 \right], \\
&X \sim \mathrm{NB}\left(n_{pp}; \langle n_{pp} \rangle, k \right), \text{and} \\
&\mathrm{NB}\left(n_{pp}; \langle n_{pp} \rangle, k \right) = \binom{n_{pp}+k-1}{k-1} \left[\frac{\langle n_{pp} \rangle / k}{1 + \langle n_{pp} \rangle / k} \right]^{n_{pp}} \frac{1}{\left[1 + \langle n_{pp} \rangle / k \right]^{k}}
\end{aligned} \tag{3.5}$$

The effect of the quantity m is to allow the particle production of a heavy-ion reaction to be modeled as a superposition of m p+p collisions rather than a superposition of A_1+A_2 $p+p$ collisions. The full method is concisely summarized in equation 3.5. The number of particles produced in a unit of pseudorapidity for a heavy-ion collision is modeled by summing over the results of sampling a NB distribution representing a $p+p$ collision at the same energy $\lceil m \rceil$ number of times. The value of m is determined by the Glauber Monte Carlo Model and the parameters for the NB distribution are permitted to vary until a good fit to the data is obtained. In this analysis the value of x is fixed at the value reported by PHOBOS for all energies, but is varied in the investigation of systematic errors.

Finally, the reconstruction efficiency of the STAR TPC is modeled by applying a multiplicity dependent efficiency of $\epsilon_{\mathrm{reco}} = 0.9\,(1 - N_{\mathrm{ch}}/2520)$, where the number 2520 was empirically determined in previous studies. For low multiplicity events the efficiency tends toward 90% which is approximately the efficiency observed in $p+p$ collisions. For high multiplicity events the efficiency tends toward 70% which is approximately the efficiency observed in central Au+Au collisions at full RHIC energies. Note that although this functionality is available, it is turned off by default and is not used to match the methodology in the standard STAR model.

3.5.3 Glauber Model + NB Fits to Multiplicity Distributions

We now have all of the components necessary to compare the model output to the observed charged particle multiplicity. However, as previously noted, the parameters of the negative

binomial distribution in the particle production model must be tuned to match the data. In this section the process of determining the values for $\langle n_{pp} \rangle$ and k are explained.

The process begins by performing a large sample of Glauber Monte Carlo simulations for the energy and species that we wish to match. Additionally, the observed multiplicity distribution of the collision species is required. To perform a direct comparison between the observed multiplicity distribution and the simulated one, the distributions must be normalized similarly. The normalization factor is obtained by first selecting a value of multiplicity, $(dN/d\eta)_{\rm norm}$, from the observed distribution in the region in which the number of events per bin varies slowly (e.g. "from the horse's back"). The integral of the observed distribution is computed in the range $[(dN/d\eta)_{\rm norm}, \infty)$ and the distribution is scaled by the integral.

The best choice of $\langle n_{pp} \rangle$ and k is found in the following manner: a value of $\langle n_{pp} \rangle$ and k are chosen from a two-dimensional parameter space; for each event in the simulation the particle multiplicity is computed as described above and used to construct the simulated particle multiplicity distribution; the simulated distribution is normalized using the same technique as above and using the same value of $(dN/d\eta)_{\rm norm}$; finally, to quantify how well the simulated distribution matches the observed distribution, their χ^2 is computed above the value of $(dN/d\eta)_{\rm norm}$. This process is repeated many times and the choice of $\langle n_{pp} \rangle$ and k that minimizes χ^2 is considered the most optimal.

Although simple, the above procedure is very computationally intensive because, for each new choice of $\langle n_{pp} \rangle$ and k, the simulated multiplicity distribution must be reconstructed using each event in the simulation. Further, the total number of events in the simulation must be large to achieve relatively small statistical errors in the high multiplicity bins required for good matching. Finally, this process must be performed for each energy and trigger combination investigated in this analysis. To reduce the compute time to a reasonable duration two techniques were utilized. First, the choice of $\langle n_{pp} \rangle$ and k were made using a hybrid Monte Carlo hill-climb method and a simulated-annealing algorithm. This method reduces the available parameter space from which to choose new values by removing areas which have shown poor matches in previous attempts. The result is that

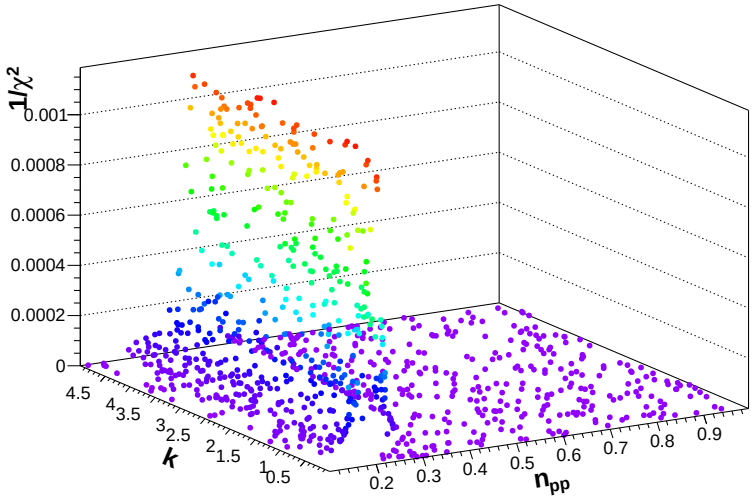

Figure 3.15: An example of the inverse χ^2 results for a large number of selections of $\langle n_{pp} \rangle$ and k from the $\sqrt{s_{NN}} = 14.5$ GeV dataset. Very little dependence on k is observed.

the search procedure is forced to converge to its optimal values more efficiently than using an exclusively hill-climb, grid search, or purely random search algorithm. Second, the entire method was implemented using a multi-threaded paradigm to take advantage of the many-core architecture of the STAR computing framework and modern desktop computers.

Figure 3.15 shows an example result of the inverse χ^2 values resulting from the procedure for the $\sqrt{s_{NN}} = 14.5$ GeV dataset. The figure illustrates that the optimum values for the negative binomial distribution are weakly dependent on k. This feature is observed in all energies and can be seen in table 3.3, which lists the optimum values for each collision energy and minimum bias trigger.

3.5.4 Centrality Binning

The simulated multiplicity distributions obtained from the optimal choice of $\langle n_{pp} \rangle$ and k can now be used to find the multiplicity cuts with which the centrality bins will be defined. The integral of the simulated distribution is computed and the multiplicities corresponding to 5% intervals of the total integral are tabulated to be used as the cut quantities. An example of the results from the $\sqrt{s_{NN}} = 14$ GeV data are shown in figure

3.16 and the results for all collision energies and triggers can be found in table 3.4.

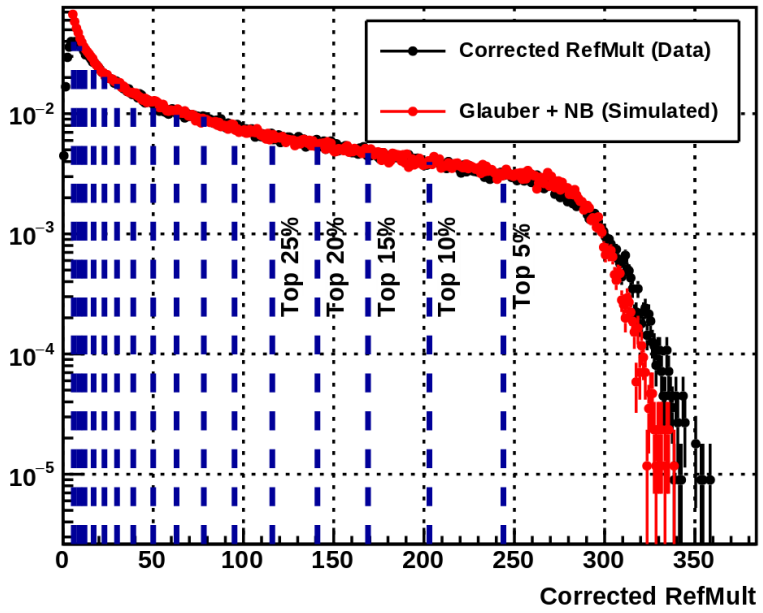

Figure 3.16: The observed (black) and simulated (red) multiplicity distributions for the Au+Au $\sqrt{s_{NN}} = 14$ GeV dataset. The vertical lines indicate the values of the multiplicity cuts.

3.6 Study of Systematic Errors

As alluded to in the previous sections, there are numerous effects that must be considered as contributors to the systematic errors during the centrality determination procedure. Each of the quantities discussed below were varied independently. The means of the distributions of N_{part}, N_{coll}, and impact parameter for each centrality bin, resulting from the variation of each quantity, were computed and used to measure the relative deviation from the default configuration. The total systematic error was obtained via the quadrature sum of the relative deviations within each centrality bin. In the remainder of this section we list the considered effects and describe why and to what extent they were varied.

We begin by considering the parameters of the Glauber Monte Carlo Model. Recall that the sensitivity of the model to collision energy is encapsulated in the quantity $\sigma_{\text{inel}}^{NN}$. Hence, we vary $\sigma_{\text{inel}}^{NN}$ by a generous $\pm$ 5% (consistent with StRefMultCorr) to evaluate any dependence and to observe that it is minimal. Dependence of the results on nuclear

densities and geometries are investigated by allowing the half density radius, c, and skin-depth, a, parameters of the Fermi Distribution to vary by $\pm 2\%$ and $\pm 10\%$ respectively. These percentages are approximately twice the relative error quoted in the data tables. Again, we observe minimal deviations from the default configuration when varying these quantities. We also investigate the possible effects of nucleon packing density by requiring a nucleon *hard-core* radius of 0.4 fm. This constraint prevents nucleons within the same nucleus from completely overlapping - e.g. the volume of one nucleon is not permitted within 0.4 fm of the center of another nucleon. This also results in minimal deviations from the default value.

Next we investigate the dependence of the results pertaining to the particle production model. The parameter responsible for controlling the hard-soft scaling in the *Two Component Model* is permitted to vary by $\pm 2.5\%$ and results in negligible deviations. The parameters, $\langle n_{pp} \rangle$ and k, of the negative binomial distribution are both permitted to vary by $\pm 5\%$. Consistent with the previous observation that the best negative binomial parameters are weakly dependent on k, we observe negligible devations as a result of varying it. However, variations of $\langle n_{pp} \rangle$ result in the second largest source of systematic uncertainty.

Finally, we vary the values of the multiplicity cuts themselves and observe that they are the largest source of systematic uncertainty. Their large influence requires careful consideration of how much they should vary to avoid under or over estimating their contribution. We suggest that the amount by which the cuts should be varied is related to how well the simulated and observed multiplicity distributions agree and that a good metric for evaluating their agreement is the ratio of their integrals above the default top 30% cut. This region is selected because it is far away from the low multiplicity region which is sensitive to trigger inefficiency effects and also the hardest region to match due to the decreasing bin statistics. As a result, the amount the cuts are varied is unique for each energy and trigger combination.

The results of the systematic error study for the example of the $\sqrt{s_{NN}} = 14.5$ GeV dataset for $N_{\rm part}$, $N_{\rm coll}$, and b are shown in figure 3.17 and are tabulated for all energies and

centrality bins in tables 3.5, 3.6, and 3.7. For energies in which more than one minimum bias trigger is available the average of the results and the largest error is used.

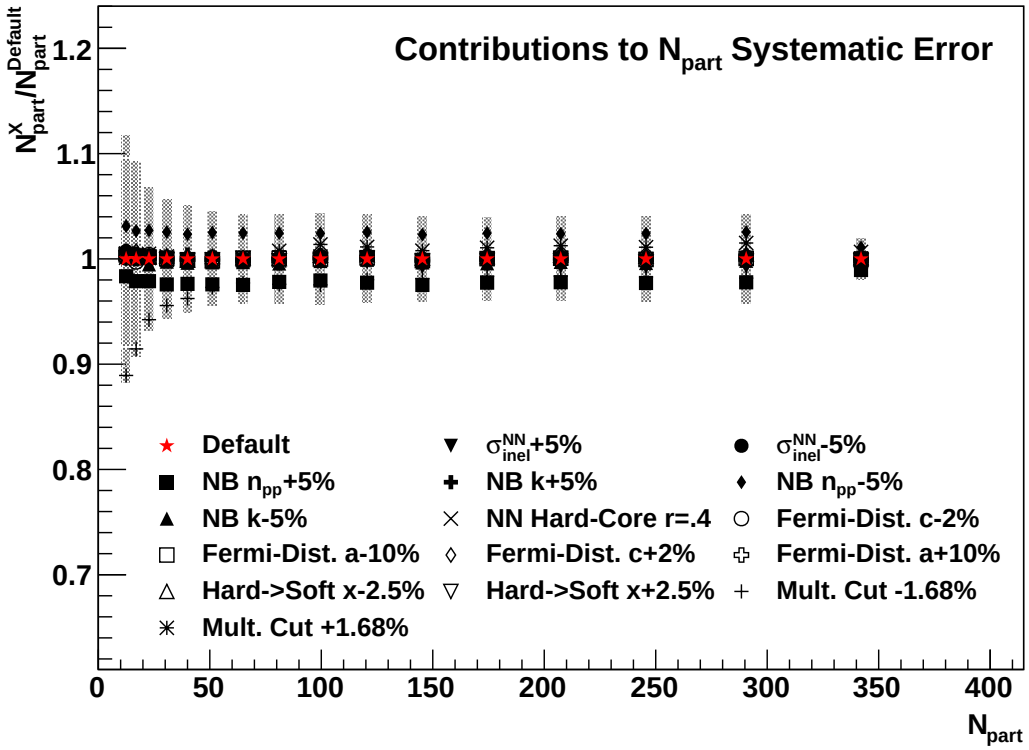

(a) Systematic Errors on N_{part}

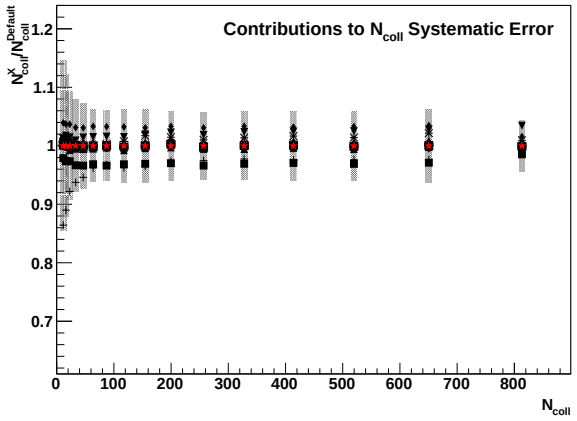

(b) Systematic Errors on N_{coll}

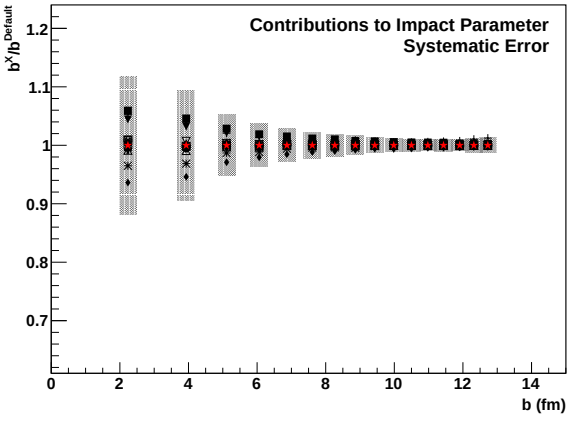

(c) Systematic Errors on b

Figure 3.17: The results of the systematic error study for the example of the $\sqrt{s_{NN}}$ = 14.5 GeV dataset. The effects considered as part of the study are presented in the legend in (a) and are applicable to figures (b) and (c).

3.7 Tabulated Centrality Bins

In this section we present the tabulated results of the centrality determination method developed in this chapter for all energies, triggers, and centralities. For completeness, we also present example distributions for N_{part}, N_{coll}, and b from select centrality bins from the $\sqrt{s_{NN}} = 14.5$ GeV dataset in figure 3.18.

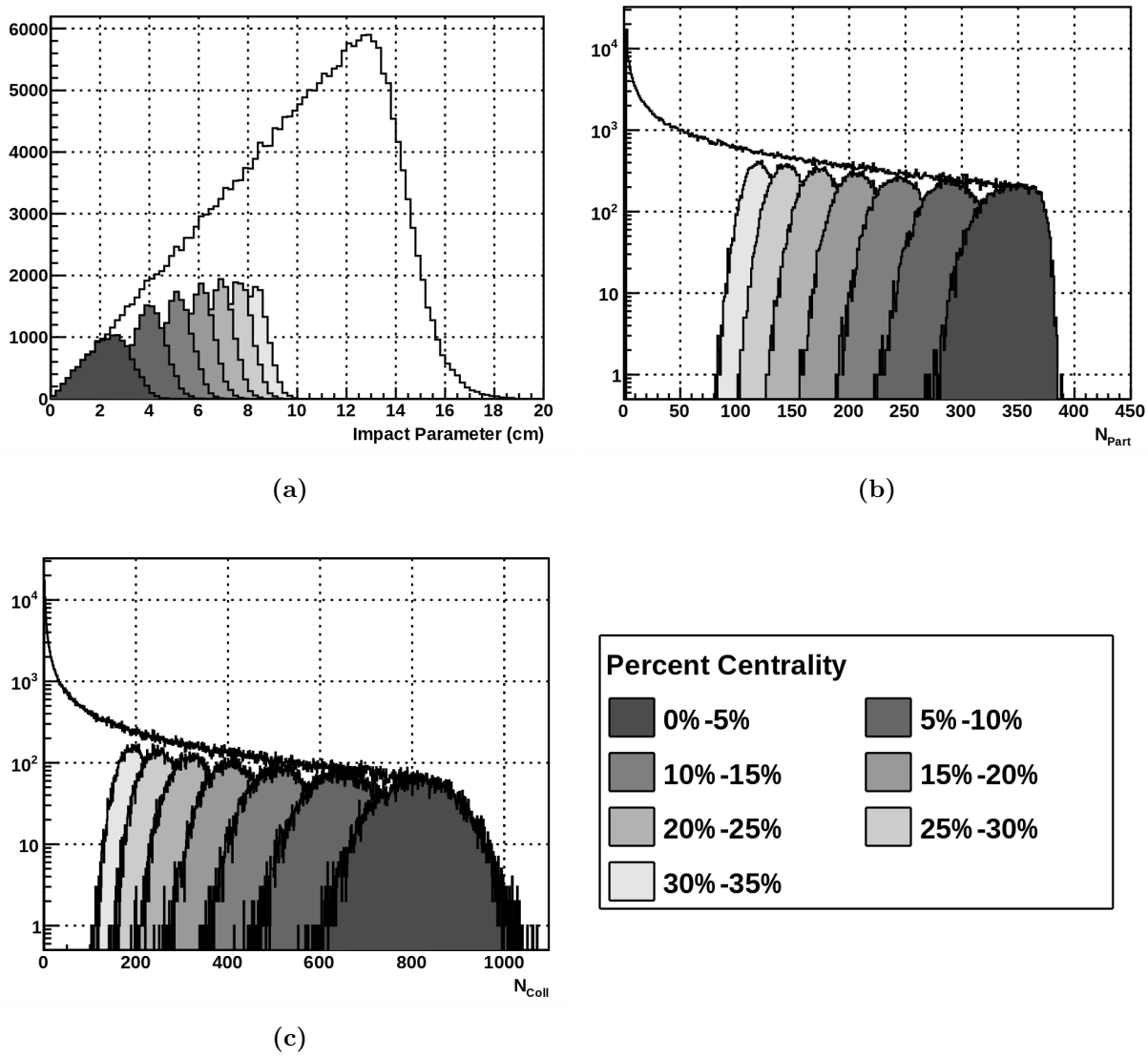

(a) (b) (c)

Figure 3.18: Centrality integrated and selected centrality bin distributions of the impact parameter, (a), number of participating nucleons, (b), and number of binary collisions, (c), from the $\sqrt{s_{NN}} = 14.5$ GeV dataset.

	Negative Binomial Parameters for Each Collision Energy (GeV) and Trigger ID											
$\sqrt{s_{NN}}$	**7.7**		**11.5**	**14.5**	**19.6**			**27**	**39**	**62.4**		
Trigger	290001	290004	310014	440015	340001	340011	340021	360001	280001	270001	270011	270021
n_{pp}	0.181	0.188	0.259	0.306	0.351	0.334	0.408	0.426	0.512	0.434	0.618	0.606
k	2.67	3.10	1.75	1.51	1.11	0.887	4.63	1.85	3.49	0.404	1.51	2.11

Table 3.3: The parameters for the negative binomial distribution for each collision energy and trigger that were obtained from the fitting procedure.

	Centrality Cuts for Each Collision Energy (GeV) and Trigger ID											
$\sqrt{s_{NN}}$	**7.7**		**11.5**	**14.5**	**19.6**			**27**	**39**	**62.4**		
% Central / Trigger	290001	290004	310014	440015	340001	340011	340021	360001	280001	270001	270011	270021
0-5	186	188	222	244	270	269	273	292	317	364	378	365
5-10	155	156	185	203	226	225	227	243	265	304	316	304
10-15	129	131	154	169	188	187	190	202	220	254	263	254
15-20	107	108	128	141	156	155	157	168	183	210	218	210
20-25	88	90	106	116	129	128	130	139	151	173	180	174
25-30	73	74	87	95	106	105	107	114	124	141	147	142
30-35	59	60	71	78	86	85	86	93	101	115	120	115
35-40	48	48	57	63	69	68	70	74	81	93	96	93
40-45	38	38	45	50	55	55	55	59	64	74	77	74
45-50	30	30	36	39	43	43	44	46	50	58	60	58
50-55	23	23	27	30	33	33	34	36	39	44	46	44
55-60	17	18	21	23	25	25	25	27	29	33	35	33
60-65	13	13	15	17	19	18	19	20	21	25	26	25
65-70	9	10	11	12	13	13	14	14	16	18	19	18
70-75	7	7	8	9	10	10	10	10	11	13	13	13
75-80	5	5	6	6	7	7	7	7	8	9	9	9

Table 3.4: Multiplicity cuts defining each centrality bin in 5% intervals for each collision energy and min-bias trigger.

	$\langle N_{\mathbf{part}} \rangle$ **for each collision energy**						
% Centrality / $\sqrt{s_{NN}}$	**7.7**	**11.5**	**14.5**	**19.6**	**27**	**39**	**62.4**
0-5	341±5	341±6	342±7	342±6	343±6	345±6	346±9
5-10	289±9	289±11	290±12	291±11	292±11	293±12	294±19
10-15	244±8	244±9	244±10	246±9	246±10	248±10	250±16
15-20	205±6	205±8	206±8	208±8	208±8	209±8	211±13
20-25	172±5	173±7	173±7	174±6	175±7	175±7	177±11
25-30	144±4	144±6	144±6	145±5	146±6	147±6	148±8
30-35	119±4	119±4	120±5	120±5	121±5	121±5	122±7
35-40	98±3	98±4	98±4	98±4	98±4	100±4	100±7
40-45	79±3	79±3	80±3	79±3	79±3	80±4	81±5
45-50	63±2	63±3	64±3	64±3	63±3	64±3	65±4
50-55	50±2	50±2	50±2	50±2	50±2	50±2	51±3
55-60	38±2	38±2	39±2	39±2	39±2	39±2	39±3
60-65	29±2	29±2	29±2	29±2	29±2	29±2	30±2
65-70	22±2	21±2	21±2	21±2	21±2	21±1	22±2
70-75	16±2	16±2	16±2	16±2	15±1	16±1	16±1
75-80	12±2	11±2	11±1	12±1	11±1	11±1	11±1

Table 3.5: The average number of participating nucleons and total error for each collision energy and centrality bin. For energies in which multiple triggers are available the average of the results is used along with the largest error.

	$\langle N_{\mathbf{coll}} \rangle$ **for each collision energy**						
% Centrality / $\sqrt{s_{NN}}$	**7.7**	**11.5**	**14.5**	**19.6**	**27**	**39**	**62.4**
0-5	788±33	802±34	812±36	828±31	846±32	873±27	912±33
5-10	628±31	638±35	646±41	663±39	675±39	696±42	727±64
10-15	503±25	509±29	515±31	528±28	536±19	554±32	579±53
15-20	399±20	404±23	410±24	418±23	425±25	439±25	458±39
20-25	315±15	320±18	324±19	330±18	336±19	346±20	360±32
25-30	248±12	251±15	252±15	259±15	263±16	270±16	280±23
30-35	192±9	195±11	196±12	199±12	203±12	210±12	215±18
35-40	147±7	149±8	151±10	151±9	154±9	159±9	165±16
40-45	110±6	111±6	114±7	114±7	115±7	119±9	124±12
45-50	82±5	83±5	84±5	85±6	85±5	87±6	92±8
50-55	60±4	60±4	60±4	62±4	63±4	63±4	66±6
55-60	43±3	43±3	43±3	44±3	44±3	45±3	46±4
60-65	30±3	30±3	30±3	30±3	31±2	30±2	32±3
65-70	21±3	20±2	20±2	20±2	20±2	21±2	22±2
70-75	14±2	14±9	14±2	14±2	13±2	14±2	15±2
75-80	10±2	9±2	10±2	10±2	9±2	9±1	10±1

Table 3.6: The average number of binary collisions and total error for each collision and centrality bin. For energies in which multiple triggers are available the average of the results is used along with the largest error.

	$\langle b \rangle$ (fm) for each collision energy						
% Centrality / $\sqrt{s_{NN}}$	**7.7**	**11.5**	**14.5**	**19.6**	**27**	**39**	**62.4**
0-5	2.2±.2	2.3±.2	2.3±.3	2.3±.3	2.3±.3	2.2±.3	2.3±.4
5-10	4.0±.3	4.0±.3	4.0±.4	3.9±.3	3.9±.3	4.0±.3	4.0±.5
10-15	5.1±.2	5.1±.2	5.1±.3	5.1±.3	5.1±.3	5.2±.2	5.2±.4
15-20	6.1±.2	6.1±.2	6.1±.2	6.1±.2	6.1±.2	6.1±.2	6.1±.3
20-25	6.9±.2	6.9±.2	6.9±.2	6.9±.2	6.9±.2	6.9±.2	6.9±.3
25-30	7.6±.1	7.6±.2	7.6±.2	7.6±.2	7.6±.2	7.7±.2	7.7±.2
30-35	8.3±.1	8.3±.1	8.3±.2	8.3±.1	8.3±.2	8.3±.2	8.4±.2
35-40	8.9±.1	8.9±.1	8.9±.1	8.9±.1	8.9±.2	8.9±.1	9.0±.2
40-45	9.5±.1	9.5±.1	9.5±.1	9.5±.1	9.5±.1	9.5±.1	9.5±.2
45-50	10.0±.1	10.0±.1	10.0±.1	10.0±.1	10.1±.1	10.1±.1	10.1±.2
50-55	10.5±.1	10.5±.1	10.6±.1	10.6±.1	10.6±.1	10.6±.1	10.6±.1
55-60	11.0±.1	11.0±.1	11.0±.1	11.1±.1	11.1±.1	11.1±.1	11.1±.1
60-65	11.5±.1	11.5±.1	11.5±.1	11.5±.1	11.5±.1	11.6±.1	11.6±.1
65-70	11.9±.1	12.0±.1	12.0±.1	12.0±.1	12.0±.1	12.1±.1	12.1±.1
70-75	12.3±.2	12.4±.1	12.4±.1	12.4±.1	12.5±.2	12.5±.1	12.5±.2
75-80	12.8±.2	12.8±.2	12.9±.2	12.8±.2	12.9±.2	12.9±.1	13.0±.1

Table 3.7: The average impact parameter (fm) and total error for each collision energy and centrality bin. For energies in which multiple triggers are available the average of the results is used along with the largest error.

Chapter 4

Data Collection, Storage, Selection and Binning

Several aspects of this analysis present logistical challenges that encumber accessing and analyzing the necessary data. Most of the challenges arise simply as a result of the scale of this analysis. To wit, we intend to measure the yield of soft particles for all BES energies binned by species and event centrality, over as much kinematic phase space as possible in two dimensions, and for three event configurations per energy. This means that the overwhelming majority of events and tracks that are collected during the physics running of the accelerator are included in this analysis. This has two effects. First, whenever the data needs to be reprocessed, a large amount of time and computational resources must be invested. And second, because the yield extraction process requires at least one histogram for each bin, trying to bin all of the data in one pass results in a minimum of approximately 250,000 histograms. This results is a memory footprint well over the permissible amount for a single instance of a user's job at the RHIC Computing Facility (RCF).

To overcome the challenge of working with such large data sets the author has developed a reduced data file format which is designed to be compact, in the sense that it only contains information which is needed for the spectra analysis, and topologically flat, in the sense that its internal data structure has as little depth as possible. The first feature ensures that the needed disk space for their storage is as minimal as possible. The second

feature greatly accelerates the read performance. We call these reduced data files DavisDsts. In addition, the author has developed a complementary data *API* (Application Programming Interface) which includes numerous routines designed to make interacting with the DavisDsts as easy and fast as possible. In this chapter we discuss the flow of data from the detector to the DavisDsts and the various cuts applied to the events and tracks used in this analysis.

4.1 Data Collection

The data used in this analysis were obtained by the STAR Collaboration as part of the Beam Energy Scan (BES) at the Relativistic Heavy Ion Collider (RHIC) located at Brookhaven National Laboratory in 2010, 2011, and 2014. During the physics running the data are streamed from the various detector subsystems to the data acquisition system where dedicated hardware known as "event builders" aggregate the raw signals obtained during each trigger into multiple binary files called "DAQ" files. These files are then transported to a High Performance Storage System (HPSS), a large magnetic-tape collection, for permanent storage. When the data-taking run is completed the performance of the detector during the run is studied and assembled into calibration libraries. When this is completed the data are "produced," meaning the raw signals stored in the DAQ files are interpreted into measurements that can be used in physics analyses. It is during the production of the data where the calibrations are applied.

The result of the data production is the standard STAR data format known as the MuDst. These files are designed to be the lowest common denominator for physics analyses in STAR. As a result the MuDst files contain an enormous amount of information - far more than is needed for any one physics analysis. As noted in Chapter 2, the subdetectors of interest for this analysis are the Time Projection Chamber (TPC) which is used for tracking and particle identification via ionization energy loss and the Time of Flight (TOF) detector which is used for particle identification via measurements of a particle's velocity. Hence, even though most of the events and tracks *cannot* be rejected for this analysis, most of the information associated with those events and tracks *can* be excluded. It is the

DavisDst data format that was designed for the purpose of containing the remaining, needed information.

The DavisDsts are produced from the MuDsts using the StDataCollector package also written by the author and available here: `https://bitbucket.org/chris_flores/stdatacollector/`. A user is able to specify several event and run level cuts in the StDataCollector package to perform an initial skimming. However, these are not analysis cuts and so will not be discussed here, with one exception. An important feature of the standard StRefMultCorr package is that it allows for bad run rejection. This feature was utilized during the production of the DavisDsts so that events from bad runs were rejected. The MuDst files used were obtained by querying the STAR file catalog. All queries have the following conditions in common: filetype=daq_reco_MuDst, tpx=1, filename~st_physics, storage!=HPSS, nFiles=all. In addition, table 4.1 contains the conditions that were applied for each energy and configuration.

Table 4.2 shows the required disk space to store the MuDst and DavisDst files. The large reduction in file size is accomplished by rejecting data from bad runs and keeping only the relevant event and track information for this spectra analysis.

$\sqrt{s_{NN}}$	STARVER	Prod. Tag	Target Setup	Run Range	
7.7	**SL10h**	P10ih	AuAu7_production	11114074	11147025
11.5	**SL10h**	P10ih	AuAu11_production	11148039	11158044
14.5	**SL14i**	P14ii	production_15GeV_2014	15053000	15070021
19.6	**SL11d**	P11id	AuAu19_production	12113079	12122019
27.0	**SL11d**	P11id	AuAu27_production_2011	12172043	12179097
39.0	**SL10h**	P10ik	AuAu39_production	11099102	11112023
62.4	**SL10k**	P10ik	AuAu62_production	11080054	11098056

Table 4.1: The STAR Library version number and parameters of the queries made to the STAR file catalog for each energy during the conversion of the MuDsts to DavisDsts.

Disk Space Requirements			
$\sqrt{s_{NN}}$	**MuDsts (GB)**	**DavisDsts (GB)**	**% Reduction**
7.7	4010	102	97.4
11.5	6386	452	92.9
14.5	39140	994	97.5
19.6	20798	1319	93.6
27.0	36335	2864	92.1
39.0	48634	4247	91.3
62.4	86264	4325	94.9
Total	241567	14303	94.1

Table 4.2: The cumulative disk space required for storage of the MuDst and DavisDsts files in GB. The large reduction in size is accomplished by rejecting bad runs and only keeping event and track information needed for this analysis.

4.2 Event Selection

Several event level cuts are applied to ensure the events observed in this analysis are of sufficient quality. The event cuts used in this analysis are summarized in table 4.4 and the reasoning behind each cut is explained in the following subsections. Table 4.3 shows the number of events that pass the event selection criteria for each energy and event configuration.

4.2.1 Event Configuration

Note that for the lowest four energies, three event configurations are measured: *Center*, *PosY*, and *NegY*. The *Center* event configuration describes events near the center of the TPC while the $PosY(NegY)$ configuration describe events located with very negative (positive) z-vertex locations with tracks measurable in the positive (negative) rapidity direction. The additional event configurations are chosen because their highly displaced vertex positions extend the rapidity acceptance of the detector and therefore the measurable range of the rapidity density distributions sought in this analysis.

The displaced vertex configurations are only applicable to the lowest four BES energies

because, for these energies, RHIC was used as a storage ring. That is, because the Radio-Frequency (RF) cavities in RHIC were not accelerating the ion bunches, the Coulombic repulsion along the z axis results in a more longitudinally diffuse bunch. This in turn increases the probability of having an Au+Au collision near the edges of the detector permitting a large enough sample of events to perform a spectra analysis.

4.2.2 Longitudinal Vertex Selection, V_z

In principle, the z-vertex range should be selected to optimize the competing effects of increasing the number of events and minimizing the change in the detector performance with respect to the z position. All event configurations measuring events at the center of the TPC have a symmetric z-vertex cut of ± 30 cm with the exception of the 7.7 GeV data, which is permitted to extend to ± 50 cm. The z-vertex ranges for all energies were chosen to be consistent with other BES spectra analyses. The larger range of the 7.7 GeV dataset is chosen to further increase the event statistics at that energy because: it has relatively few events compared to other energies; the number of tracks produced per collision at 7.7 GeV is fewer than any other energy; and the z-vertex distribution is widest of any energy. The last reason is again the result of the accelerator performance: namely, the lower beam energy has a smaller γ factor resulting in even more longitudinally diffuse bunches.

The z-vertex range of the $PosY$ and $NegY$ event configurations are chosen to maximize the rapidity acceptance of the detector while optimizing the number of events.

4.2.3 Radial Vertex Selection, V_r

A radial vertex selection is necessary to prevent including events that were the result of errant ions interacting with the beam pipe or detector material. The radial vertex cut is centered around the transverse location of the beam spot which varies slightly from energy to energy due to beam tuning. All event configurations for a given energy share the same radial vertex cut since the transverse location of the beam spot does not change significantly over the z-vertex range of STAR.

Note that the radial vertex locations for all energies and configurations are required to

satisfy $V_r \leq 2.0$ cm except for the 14.5 GeV dataset, which is required to satisfy $V_r \leq 0.5$ cm. The tighter cut at 14.5 GeV is required because of the installation of a narrower beam pipe during that year in support of the Heavy-Flavor Tracker (HFT) program.

4.2.4 ToF-Matched Tracks

The drift time of the TPC is approximately 40 μs which, because it is long compared to the bunch crossing rate, makes it susceptible to out-of-time pile-up events. These are events which occurred either immediately before or after the triggered event. To reduce the possible contamination of these events we require that the TOF detector - which is considerably faster than the TPC - have hits which match to some minimum number of tracks in the TPC. The minimum number of tracks must be small so as not to bias the most peripheral centrality bin, but large enough to be effective at rejecting the out-of-time events. It is found that requiring at least three ToF matched tracks is optimal.

4.2.5 Trigger ID Selection

All of the events used in this analysis are required to have satisfied the minimum-bias (MB) trigger conditions at each energy. For the BES energies the MB trigger conditions are defined as coincidences between the East and West Beam-Beam Counter (BBC) detectors. Note that not all available MB triggers are used in this analysis. This is because some trigger IDs have too few events to perform the centrality determination procedure in Chapter 3.

Number of Events			
$\sqrt{s_{NN}}$	**Center**	**PosY**	**NegY**
7.7	2,935,338	344,303	295,654
11.5	6,495,494	970,595	831,065
14.5	8,478,525	517,602	643,044
19.6	14,898,550	1,816,303	1,605,536
27.0	30,093,280	NA	NA
39.0	97,091,040	NA	NA
62.4	50,956,350	NA	NA

Table 4.3: The total number of events in each dataset satisfying all event selection criteria for each collision energy and event configuration.

Event Selection Criteria

$\sqrt{s_{NN}}$	Config.	V_z (cm)	$\lvert V_r \rvert$ (cm)	Beam Spot (x, y) (cm)	# ToF-Matched Tracks	Trigger IDs
7.7	Center	$[-50, 50]$	$[0, 2.0]$	(0.2,-0.25)	≥ 3	290001
	PosY	$[-200, -100]$				290004
	NegY	$[100, 200]$				
11.5	Center	$[-30, 30]$	$[0, 2.0]$	(0.1,-0.23)	≥ 3	310014
	PosY	$[-200, -100]$				
	NegY	$[100, 200]$				
14.5	Center	$[-30, 30]$	$[0, 0.5]$	(0.0,-0.90)	≥ 3	440015
	PosY	$[-200, -100]$				
	NegY	$[100, 200]$				
19.6	Center	$[-30, 30]$	$[0, 2.0]$	(0.37,-0.03)	≥ 3	340001
	PosY	$[-200, -100]$				340011
	NegY	$[100, 200]$				340021
27.0	Center	$[-30, 30]$	$[0, 2.0]$	(0.13,-0.07)	≥ 3	360001
39.0	Center	$[-30, 30]$	$[0, 2.0]$	(0.30,-0.07)	≥ 3	280001
62.4	Center	$[-30, 30]$	$[0, 2.0]$	(0.39,-0.06)	≥ 3	270001
						270011
						270021

Table 4.4: Event selection criteria for each energy and event configuration. Note that the radial vertex cut is centered with respect to the beam spot location and that all trigger IDs are permitted for any event configuration.

4.3 Track Selection

It is also necessary to apply track cuts to ensure that only high quality tracks are included in the analysis. Tables 4.5 and 4.6 summarize the track cuts used in this analysis. The cuts in the first table are required to be satisfied for all tracks. The cuts in the second table are required for a track's TOF hit information to be considered in the analysis. The cuts are explained in the following subsections.

Track Selection Criteria

Track Flag	Fit Points	dE/dx Points	Fit/Possible Points	glDCA (cm)
$[0, 1000)$	≥ 15	≥ 10	$\geq .52$	≤ 1.0

Table 4.5: Criteria tracks must satisfy to be considered for this analysis.

Additional Criteria for TOF Candidate

Match Flag	$1/\beta$	yLocal (cm)	zLocal (cm)
≥ 1	≥ 0	$[-1.6, 1.6]$	$[-2.8, 2.8]$

Table 4.6: Additional criteria applied to TOF matched candidate tracks to ensure a valid time-of-fight measurement.

4.3.1 Track Flag

The track reconstruction algorithm is able to assign descriptive flag values to the tracks during their reconstruction. A track's flag is a four digit number: $zxyy$. The first digit, z, gives pile up information and is either 1 for a pile up track or 0 otherwise. The second digit, x, indicates which detectors were used in the track refitting. The value can range from 1 (TPC only) to 9. Although this digit can be useful to gather information, it is not generally useful for quality cuts. The last pair of digits, yy, gives information about the status of the helix refit. There are several possible values for the pair, but they can be interpreted as either positive (good refit) or negative (bad refit). The sign of the last pair of digits is applied to the whole flag and thus only tracks that have positive flag values less than 1000 are permitted for this analysis. For a more detailed description of all the

possible values of the track flag see the comments at the top of the StTrack source code: `http://www.star.bnl.gov/webdata/dox/html/StTrack_8h_source.html`.

4.3.2 Fit Points

The number of fit points of a track describes the number of (x, y, z) coordinates that are used in the helix fit. It is important to consider that multiple detector subsystems can contribute hits that can be used in a track's reconstruction. For this analysis the term "Fit Point" will be used to mean fit point as measured *by the TPC*. As described in Chapter 2, there are a total of 45 readout pads in each sector of the TPC – 13 in the inner part of the sector and 32 in the outer. This means that a track can have a maximum of 45 hit points. By default a primary track must have at least 5 hit points which is the number of parameters in the helix fit. During track reconstruction the reconstruction algorithm can throw away some of the hit points if they are outliers. The remaining points are used in the helix fit and are therefore called fit points.

The minimum number of fit points required for a track to be considered must be chosen thoughtfully. The momentum resolution of the track improves with more fit points, but requiring too many fit points will limit the low p_T acceptance. A minimum of 15 fit points was determined to be a good value for this analysis. It is large enough to require hits from both the inner and outer sectors and small enough not to substantially limit the low p_T acceptance of the detector. The latter is an important consideration in this analysis since the majority of the particle yield is at low p_T and because the low p_T acceptance can change with rapidity.

4.3.3 dE/dx Points

Each hit point of a track in the TPC has an associated dE/dx measurement. Thus, a track may have up to 45 measurements of its ionization energy loss. As before, two competing factors must be taken into consideration to determine the minimum number of hit points used in the dE/dx calculation. First, the dE/dx resolution improves with a larger number of measurements. Second, as described in chapter 2, a 70% truncated mean method is used to find the average value of a track's dE/dx. This means that roughly one-third of

a track's dE/dx measurements are discarded. Hence, the minimum number of hit points used in the dE/dx determination should not approach the minimum number of fit points, but should be sufficiently many to provide good dE/dx resolution. It was found that a minimum of 10 dE/dx points was a good balance. The cut provides sufficient resolution and is two-thirds of the minimum number of fit points.

4.3.4 Ratio of Fit Points to Possible Points

A somewhat common problem that can occur during the track reconstruction process results from a single real track being reconstructed as two tracks. This can happen if the hits in one region of the detector are not associated with the hits in another region. These are known as split tracks. Tracks that pass through the central membrane are most prone to this issue, but the problem can also arise if hits in the outer sectors are not associated with hits in the inner sectors. To supress this problem it is common to require that the ratio of the number of hits used in the helix fit be greater than half, 52% to be precise, of the possible number of hits the track should have had based on its trajectory.

4.3.5 Global Distance of Closest Approach (DCA)

Spectral analyses of light particles, such as this, endeavor to report the spectra of particles directly produced by the medium resulting from the heavy-ion collision. As such it is necessary to try to ensure that the tracks included in the analysis come from a single heavy-ion collision and that they are not the result of long-lived particles which decay to light particles or particles that resulted from secondary collisions in the detector material. Corrections must be made to fully account for these effects, but requiring that a track's distance of closest approach to the primary vertex be small removes many of these confounding tracks, which may have been the result of pile up or decays. A common choice of cut to achieve these results is a maximum global DCA of 1 cm. The global DCA must be used since the primary DCA is defined to be 0 cm in the track refitting procedure. We use the 1 cm cut in this analysis.

4.3.6 ToF Match Flag

After tracks are reconstructed using the hit information from the TPC, a matching algorithm is used to pair hits observed in the Time-of-Flight (ToF) detector with the tracks observed in the TPC. The ToF match flag quantity ranges from zero, if the track has no matched ToF hit, to 3, if the track could have caused multiple hits observed in the ToF. For this analysis, as is done in other analyses, we require that the ToF match flag simply be nonzero to indicate that the track has a candidate hit in the ToF detector.

4.3.7 Inverse Beta

The inverse measure of a track's velocity provided by the ToF detector is required to be greater than zero for this analysis. The primary purpose of this cut is to remove the tracks that have an invalid velocity measurement (the value would be negative by default). One may be tempted to strictly require that the measurement be in the physical range bounded below by the speed of light at $1/\beta = 1$, but in practice we find that this is neither necessary nor advantageous. It is not necessary since very few tracks have super-luminal velocities that are valid. It is not advantageous because the tracks that do have such velocities are typically high momentum tracks, in which case the measurement resolution combined with the uncertainty in the start time calculation permits super-luminal velocities.

4.3.8 Local ToF Pad Coordinates

Each ToF pad has its own local coordinate system and can report the location of each hit relative to the pad origin. Cuts are made in the local coordinate space to ensure that the hit is near the center of the active volume of each pad. The purpose of this cut is to reduce the overall number of mismatches that cause background during the yield extraction process. ToF mismatches occur when the dE/dx of a track in the TPC suggests it is of a particular species while the $1/\beta$ measured in the ToF suggests it is another species. The mismatch rate increases the further the hit distance is from the center of the ToF pad so limits are placed on the hit location.

4.4 Data Binning

The data used in this analysis and that have passed the above quality cuts are binned in several dimensions. Events are first binned into event configurations using their z-vertex locations and then binned in centrality using the centrality bin determination procedure discussed in Chapter 3. It was decided that this analysis would utilize nine centrality bins divided into percentages of the total cross section: 0-5, 5-10, 10-20, 20-30, 30-40, 40-50, 50-60, 60-70, and 70-80%. The tracks belonging to events within each centrality bin are then binned by mass assumption (π,k,p), rapidity (bin width, $\Delta y = 0.1$), and in $m_T - m_0$ (bin width, $\Delta(m_T - m_0) = 0.025$ GeV).

Chapter 5

Detector Performance Corrections

Perhaps the most distinguishing philosophical difference between the disciplines of fundamental experimental science and those of applied science is that fundamental science aims to report measurements without qualification. That is, we desire to report our results as being what nature provided and not some convolution of what nature provided and how well we were able to measure it. This means we must correct our measured results given our knowledge of the deficiencies in our detectors and methods. Unsurprisingly, understanding the performance of our detector and how it changes over time, with centrality, and over the kinematic space of the measured quantities, is both remarkably nuanced and difficult.

In this chapter we discuss these detector deficiencies and the means we use to correct for them. These corrections are presented prior to the yield extraction procedure for two reasons: first, the TOF matching efficiency correction is determined via a data-driven method and the correction is applied prior to the yield extraction of the TOF portion of the spectra; and second, the energy-loss and tracking efficiency corrections are determined from a Monte Carlo simulation of tracks as they pass through a detector model. The model can be run and the correction factors can be determined either before or after the yield extraction process.

5.1 Errors of Efficiency Calculations

Before computing various efficiencies a brief discussion of how to compute the statistical errors on efficiency values is warranted. Frequently an efficiency is computed as the ratio of some quantity that passed certain conditions to the total number of that quantity. Thus the numerator of the ratio is a subset of the denominator. This has two important implications. First, both the ratio itself and its error are bound to the physically realizable range of [0,1]. This means that when the efficiency is near zero or unity the error on the efficiency cannot extend past either boundary. Second, the statistical error cannot be computed by assuming that numerator and denominator are uncorrelated. Both of these issues are resolved by using the Bayesian asymmetric error calculation method [65]. All errors on efficiencies in this analysis are computed with this method.

5.2 TOF Matching Efficiency

Recall from chapter two that tracks reconstructed in the TPC must be matched with hits in the TOF detector. The TOF matching efficiency quantifies the probability of this matching happening successfully. There are several reasons why a track in the TPC may not be matched with a hit in the TOF detector. The first is simply related to the geometric acceptance of the TOF detector itself. Although its description in chapter two suggests that it provides hermetic coverage, in reality its projective geometry in η and tray-wise instrumentation in ϕ leave gaps of non-sensitive regions where tracks cannot leave hits. Tracks may also not leave hits in the TOF detector due to the relatively high transverse momentum required to reach the radius of the TOF detector. Another possibility is that the algorithm responsible for matching a TPC track to a TOF hit may fail. The frequency of failure is dependent on the multiplicity of the event. That is, the more tracks present in the TPC the more difficult it is to accurately match any given track to any given hit in the TOF. Finally, the algorithm may match a TPC track to a TOF hit, but that TOF hit may not satisfy the TOF track requirements listed in chapter four.

The expected kinematic and multiplicity dependence of the TOF matching efficiency requires that the efficiency be studied for each particle species, centrality bin, rapidity

bin, and as a function $m_T - m_0$. The TOF matching efficiency is obtained for each of these bins using a data-driven method. For each bin the number of tracks with good TOF information (defined by the TOF cuts in chapter 4), $nTOF$, is divided by the number of tracks reconstructed in the TPC, $nTPC$. An example of this ratio as a function of $m_T - m_0$ for each particle species at mid-rapidity and from the top 5% most central events in the $\sqrt{s_{NN}} = 7.7$ GeV data set (*Center* Configuration) is shown in Figure 5.1. Note that, as expected, the efficiency graphs show a turn-on feature at low $m_T - m_0$ because it requires some minimum p_T to reach the TOF detector.

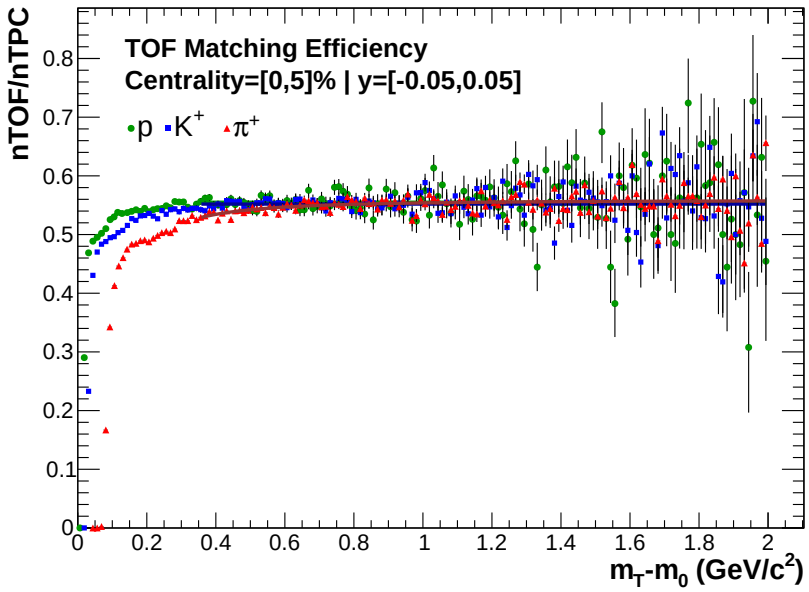

Figure 5.1: An example of the TOF matching efficiency parameterization for pions, kaons, and protons at mid-rapidity in the top 5% most central events in the $\sqrt{s_{NN}} = 7.7$ GeV dataset (*Center* Configuration). The parameterizations are either a constant or an error function depending on whether or not the ratio exhibits an $m_T - m_0$ dependence in the fitted range.

The curves in the figure are fits to the ratio above some minimum value of $m_T - m_0$, where the minimum is the greater of either 350 MeV/c^2 or the $m_T - m_0$ when the ratio first reaches 10%. The fit is performed above this minimum for two reasons. First, the shape of the turn-on region at very low $m_T - m_0$ is not well understood and second, the yield of identified particles from the TOF detector is only needed for the portion of the spectra for which $m_T - m_0 > 0.4$ GeV/c^2. The functional form used for the fit is either a constant or an error function, depending on whether or not the ratio exhibits an

$m_T - m_0$ dependence in the fitted range. The fits are used to reweight the tracks when they are being binned into Z_{TOF} histograms (see chapter 6) as part of the yield extraction procedure. Performing the correction at the track level is preferable because it will have the correct inter-bin dependence; that is, it is not necessary to assume that the value at the bin center is the correct one.

Despite applying the TOF matching efficiency as described above, the yield of particles extracted from the TOF is observed to be systematically lower than the yield extracted from the TPC. This is observed in this analysis and others ([66, 67]) as a small but sharp discontinuity between the TPC and TOF portions of the particle spectra. Since the TOF matching efficiency correctly accounts for any $m_T - m_0$ dependence of the TPC/TOF yield offset, the remaining offset is presumed to be an overall constant. This final correction constant is computed by taking the average of the ratio of the TOF yield to the TPC yield in $m_T - m_0$ bins where the spectra overlap. The average ratio is then used to correct the entire TOF portion of the spectra to match the TPC portion of the spectra.

5.3 Embedding

Some detector effects cannot be evaluated by clever data-driven methods. In those cases it is necessary to use a simulation of the detector to evaluate its response to tracks generated from a Monte Carlo model. GEANT [68] is a software framework designed to realistically simulate the passage of particles though matter. The various components (including structural) of the STAR detector and its subsystems are modeled in GEANT3. Monte Carlo tracks can then be sent through the model to evaluate how the detector responds to the tracks and how tracks respond as they transit the detector. In STAR this process is known as "embedding" because it involves embedding Monte Carlo generated tracks into real data. These data is then reconstructed using the GEANT detector model of STAR and the STAR reconstruction software.

We use the terms *embedded* track, *reconstructed* track, and *matched* track in the following way. An embedded track is a particle of a defined species whose kinematic properties were generated from a Monte Carlo model. Often the embedded tracks are given

a value of rapidity and $m_T - m_0$ or p_T by sampling a uniform distribution over some range of interest. A reconstructed track is a track that has been successfully reconstructed by the reconstruction software. A matched track is a reconstructed track that is also matched back to an originally embedded track. This last distinction is necessary since embedded tracks are embedded into events with real tracks. In the following discussions and plots we only utilize matched tracks which have *also* passed all of the track quality cuts defined in chapter four. Thus, mentions of track's reconstructed (embedded) momentum, for example, should be interpreted as the reconstructed (embedded) momentum of a "good" matched track.

5.3.1 Track Energy-Loss Correction

As particles pass through matter they lose energy either via ionization processes as described in chapter two or via other mechanisms. This energy-loss results in a continually changing momentum along the particles trajectory and, as a result, a continually changing radius of curvature. Without a correction to account for this effect, the momentum of a track as it is reconstructed would not be the momentum at which it was emitted from the medium resulting from the heavy-ion collision.

The track reconstruction software assumes that all tracks are pions and corrects their momentum given that assumption. However, other particle species lose energy differently in the detector material and additional corrections must be applied. The energy-loss corrections for kaons and protons can be obtained from the embedding procedure. Monte Carlo generated kaons and protons are embedded into events and are reconstructed by the STAR reconstruction software. We can then compare their embedded (Monte Carlo) momentum with their reconstructed momentum.

Figure 5.2 shows an example of this study for pions, kaons, and protons at mid-rapidity for events in the $\sqrt{s_{NN}} = 7.7$ GeV dataset (*Center* Configuration). The difference between the track's reconstructed and embedded momentum is shown on the vertical axis as a function of the track's reconstructed momentum. The curves in the figure are fits of the form $p_T^{\text{reco}} - p_T^{\text{emb}} = a + b(p_T^{\text{reco}})^{-c}$, where the values of a, b, and c are parameters of the fit. In the case of pions the parameter b is fixed to zero so that the fit becomes a constant. Note

that all centrality classes are combined to evaluate this correction because the energy-loss of a single track as it transits the detector material is independent of the number of tracks in the detector. In principle, these results are also independent of collision energy. However, in practice, changes in the detector (new subsystems, for instance) or subtle changes in the tracking software can occur run-to-run. Thus, this procedure is repeated for each energy as well.

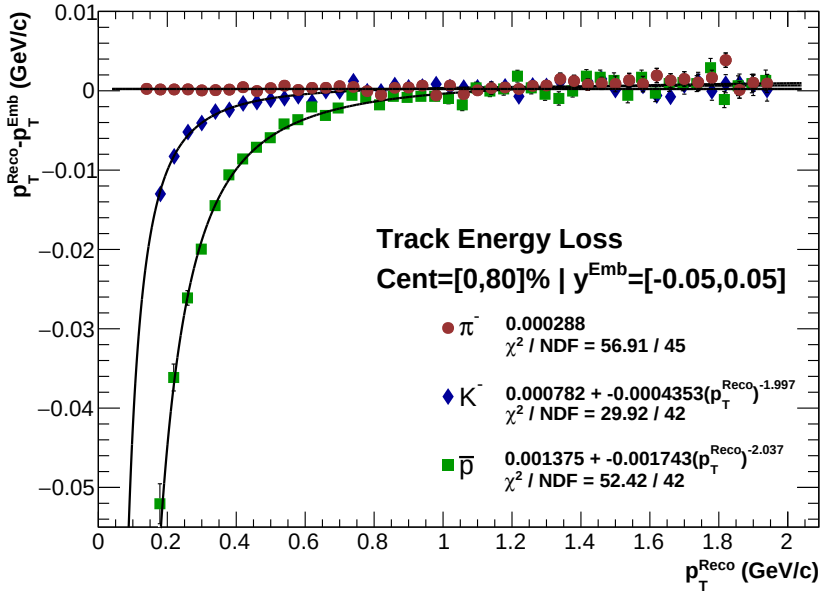

Figure 5.2: An example of the energy-loss parameterizations for pions, kaons, and protons at mid-rapidity in the $\sqrt{s_{NN}} = 7.7$ GeV dataset (*Center* Configuration). The energy-loss has no centrality dependence so events from all centrality classes are combined for this parameterization.

As expected, the pions require no additional correction because their energy-loss has already been accounted for in the track reconstruction software. The kaons and protons clearly require additional corrections. The corrections are applied after the uncorrected particle spectra have been obtained. Thus the bin centers of each point in the spectra are used to evaluate the parameterizations to determine the correction value.

5.3.2 Finite Bin Width

One of the normalization constants used in the determination of the invariant yield of the particles is the $m_T - m_0$ bin width. It was discussed in chapter four that this bin width is chosen to be 0.025 GeV/c^2. However, the tracks are binned according to their measured

momentum and not their true momentum. The two momenta differ as discussed in the previous section. Thus the bin width must also be corrected to account for the energy-loss correction. The energy-loss curves from above are evaluated at the low and high edges of each $m_T - m_0$ bin and used to determine the width of the true $m_T - m_0$ bin. The ratio of the defined width to the true width can then be used as a correction factor for the invariant yield.

5.3.3 TPC Tracking Efficiency

The most important correction that is applied to the extracted particle spectra is that of the detection probability. That is, it is necessary to know with what probability the STAR detector and reconstruction software will actually measure a track of a certain species given some number of other tracks occurring simultaneously in the detector and given its rapidity and $m_T - m_0$. There are two reasons that a track may not be measured. First, its trajectory may not impinge on an active volume of the TPC. It may travel between the TPC sector boundaries or may not have sufficient p_T to make it far enough into the TPC to be reconstructed. Tracks which are not reconstructed for such reasons contribute to the measure of the detector's acceptance. Second, tracks may not be reconstructed due to some failure in the detector or reconstruction software. These tracks contribute toward the measure of the detector's efficiency. The product of the efficiency and acceptance is the detection probability and is frequently simply called the tracking efficiency, since it answers the question: How likely is a particle to be reconstructed as a track regardless of the reason?

The tracking efficiency must be determined for each particle species, for each centrality class, and for each rapidity bin as a function of $m_T - m_0$. The embedding process is used to determine the tracking efficiency. The probability of a track being reconstructed can be determined by constructing the ratio of the number of matched tracks to the number of embedded tracks in each bin.

Figure 5.3 shows an example of the ratio of the number of reconstructed tracks to the number of embedded tracks for pions, kaons, and protons at mid-rapidity in the top 5% most central events in the $\sqrt{s_{NN}} = 7.7$ GeV dataset (*Center* Configuration). The curves

in the figure are fits in the full $m_T - m_0$ range of the form $\epsilon(x) = ae^{(-b/x^c)}$, where ϵ is the tracking efficiency, x is the embedded $m_T - m_0$, and a, b, and c are the fit parameters.

Note that the TPC tracking efficiency is presented as a function of the embedded $m_T - m_0$. This is because the tracking efficiency correction is applied to the spectra after the energy-loss correction has been applied. The order is important because the energy-loss correction converts the measured $m_T - m_0$ to the true (embedded) $m_T - m_0$, and then the center of the $m_T - m_0$ bin of the energy-loss-corrected spectrum is used to evaluate the tracking efficiency correction from the parameterizations.

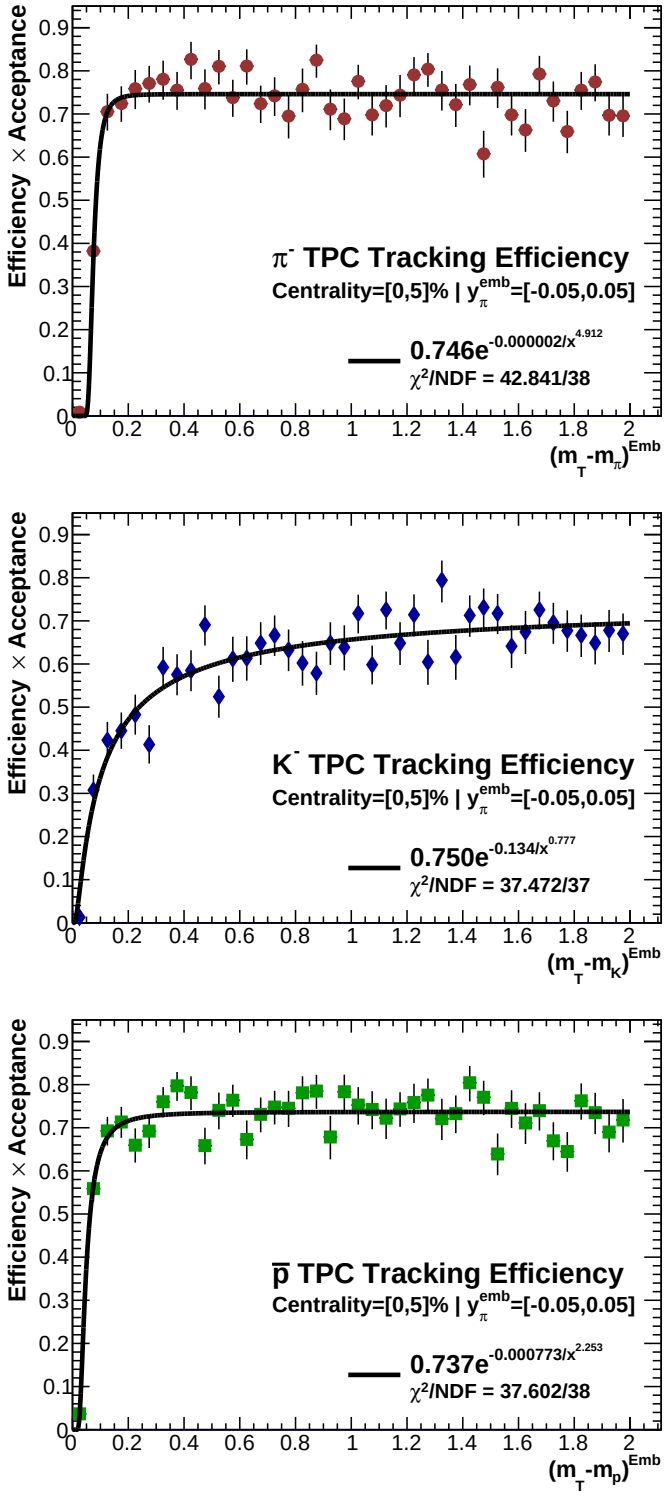

Figure 5.3: An example of the TPC acceptance and tracking efficiency parameterizations for pions, kaons, and protons at mid-rapidity in the top 5% most central events in the $\sqrt{s_{NN}} = 7.7$ GeV dataset (*Center* Configuration). The low transverse mass kaons have a reduced efficiency due to their tendency to decay in flight.

Chapter 6

Background Corrections

Having investigated the necessary corrections for the detector performance deficiencies that affect all of the particle species similarly in chapter 5, we now turn our attention to corrections that apply specifically to each particle species. Collectively the corrections addressed in this chapter are called background corrections because they aim to remove particles identical to or indistinguishable from the particle of interest but which were produced by mechanisms other than directly from the medium resulting from the heavy-ion collision. In the following sections we discuss the general methodology used to investigate the backgrounds relevant to each species and how the magnitude of the effects are quantified.

6.1 General Methodology: The Simulation Chain

Unless otherwise noted in the sections below, all of the background corrections were determined via the simulation chain shown in figure 6.1. First, Au+Au heavy-ion events are simulated for each collision energy using the Ultrarelativistic Quantum Molecular Dynamics, UrQMD [69, 70], model. The output of UrQMD is a formatted text file with a ".f" extension. This file is converted into ROOT trees for easier processing. As input, the detector simulator (GEANT3/STARSIM) requires the simulated event be formatted in the "STAR new text format", or .tx for short, and that they be assigned a vertex location within the geometry of the detector. Thus, the second step in the chain is to create these files from the ROOT trees. The vertex location of each event is chosen by sampling the

z- and xy-vertex distributions obtained from data. Third, the simulated events are then passed through STARSIM resulting in a "Zebra" (".fzd") file. This file contains all of the information about how the detector responded to the simulated event. Fourth, the Zebra files are processed by the reconstruction chain (BFC) to create ROOT trees in the "minimc" format. This is the same format which is used for the embedding analysis in the previous chapter. Fifth, the centrality of the events is determined using the same methodology outlined in chapter 3, that is: the events are characterized by either *RefMult*, *RefMultPosY*, or *RefMultNegY* depending on their z-vertex locations; the quantities are corrected for how the acceptance of the detector changes with the z-vertex position; *RefMultPosY* and *RefMultNegY* are converted to *RefMult*; and a Glauber Monte-Carlo and negative binomial particle production model are used to determine the centrality bin cuts. Finally, the simulated events in the minimc files are binned by centrality and analyzed using the methods discussed below to determine the background correction curves. The total number of reconstructed events for each combination of energy and event configuration are shown in table 6.1

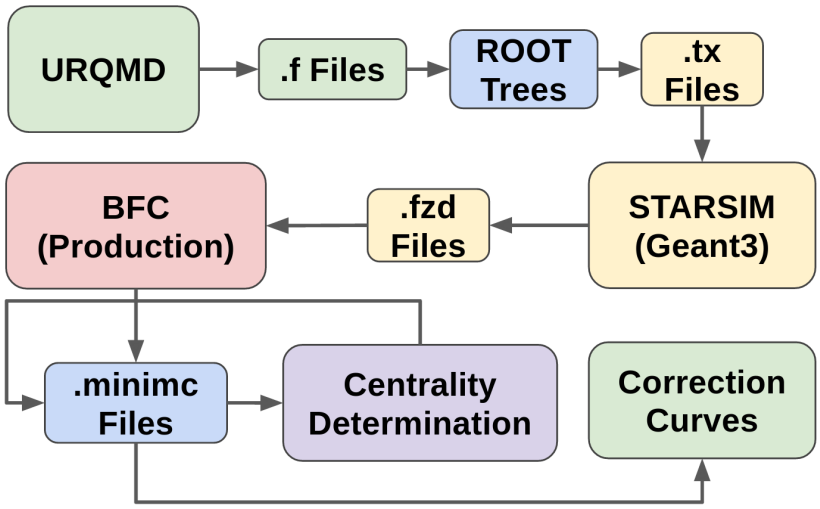

Figure 6.1: A schematic showing the steps in the simulation chain that result in background correction curves.

The tools necessary to perform the multiple steps of the simulation chain are provided by the author across four software repositories. The StUrQMD software repository, which is available here `https://bitbucket.org/chris_flores/sturqmd`, permits the

Number of Reconstructed Events			
$\sqrt{s_{NN}}$	**Center**	**PosY**	**NegY**
7.7	172,851	145,063	144,276
11.5	176,529	145,449	145,206
14.5	150,422	129,948	132,174
19.6	148,507	117,079	114,283
27.0	147,228	NA	NA
39.0	103,449	NA	NA
62.4	103,081	NA	NA

Table 6.1: The total number of reconstructed events in each simulated dataset. Note that a larger number of events is necessary at lower energy since there are fewer tracks per event.

user to perform all of the steps in the chain up to and including the creation of the minimc files. The centrality determination software is again provided by the GlauberMCModel repository available here: `https://bitbucket.org/chris_flores/glaubermcmodel`. The source code needed to process the minimc files is provided in the MiniMCReader repository here: `https://bitbucket.org/chris_flores/minimcreader`. Finally, the source code needed to determine the correction curves is provided as part of the DavisDSTAnalysis repository which is available here: `https://bitbucket.org/chris_flores/davisdstanalysis`.

6.2 Pion Corrections

The two primary sources of background for the pion spectra are muon contamination and decays of heavier particles into pions known as feed down. In the later case, decays can be divided into strong and weak categories. The strong decays occur on time scales short enough that the resulting pions would have come into existence prior to freeze-out. Hence, they carry useful information about the system and are not corrected for. The pions from weak decays, on the other hand, are created on longer time scales and do not carry information regarding the chemistry, thermal properties, or expansion of the

system. The pions from weak decays must therefore be corrected for. In this section we discuss these two background sources, muon contamination and weak decays, and detail how the magnitude of their contribution to the pion spectra was estimated.

6.2.1 Muon Contamination

The similarity between the pion and muon masses results in the two species being indistinguishable from each other given the methods of particle identification available in this analysis. Most of the muons produced in heavy-ion collisions are the daughters of charged pion decays ($\pi^+ \rightarrow \mu^+ + \nu_\mu$ or $\pi^- \rightarrow \mu^- + \overline{\nu_\mu}$). These are the very pions which we wish to measure. At first glance then, it might be seem desirous to *not* correct for the muon contamination since the number of measured pions plus the number of measured muons will be closer to the number of charged pions prior to any of their decays. However, the reconstruction efficiency for muons is not necessarily the same as for pions because the number of muons which make it into the final track sample is contingent on the global DCA cut and, most importantly, the charged pion decay is modeled by the detector simulator which means that the effect of the pion decay on their reconstruction efficiency is already accounted for. Consequently we must estimate the level of muon contamination in the pion spectra and adjust for its presence.

The muon contamination is estimated using the results of the simulation chain described above. Reconstructed muons which pass all of the track quality cuts in the analysis are binned by event centrality, charge, pion rapidity, and pion transverse mass as seen in figure 6.2a. Additionally, the sum of the reconstructed muons and pions, again all of which have passed the track quality cuts, are binned similarly and shown in figure 6.2b. The muon contamination fraction in each bin is then defined as $\mu_{\text{Bkgd}} = N_\mu / (N_\mu + N_\pi)$, which is computed as the ratio of the histograms. An example of the muon background fraction at midrapidity and as a function of transverse mass for the most central 5% of events in the Au+Au $\sqrt{s_{NN}} = 7.7$ GeV dataset is shown in figure 6.3 for both positive and negative pions. It is observed that muon contamination correction is quite small, reaching approximately 1% at its maximum. Despite the relatively large number of simulated events, after binning by centrality and rapidity, the results are unable to distinguish

between a simple exponential and power law parameterizations. Generally the power law fit is found to have the lower χ^2 of the two functions, thus it is used for the nominal correction of the spectra. The exponential fit and one sigma bands are used in the determination of the systematic errors associated with this correction as described below.

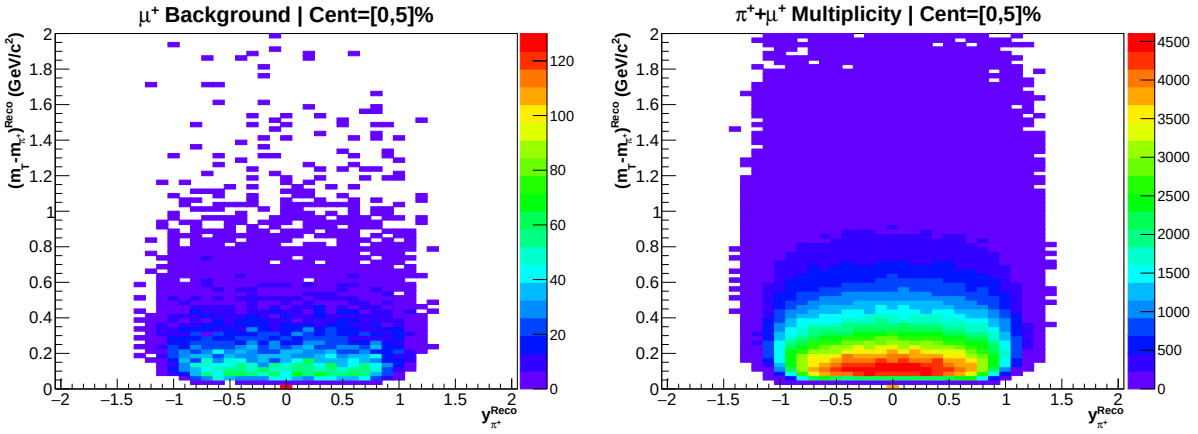

(a) Reconstructed muons. **(b)** Sum of reconstructed pions and muons.

Figure 6.2: The numerator (a) and denominator (b) of the muon contamination background fraction as described in the main text for the top 5% most central events (*Center* Configuration) in the Au+Au $\sqrt{s_{NN}} = 7.7$ GeV dataset.

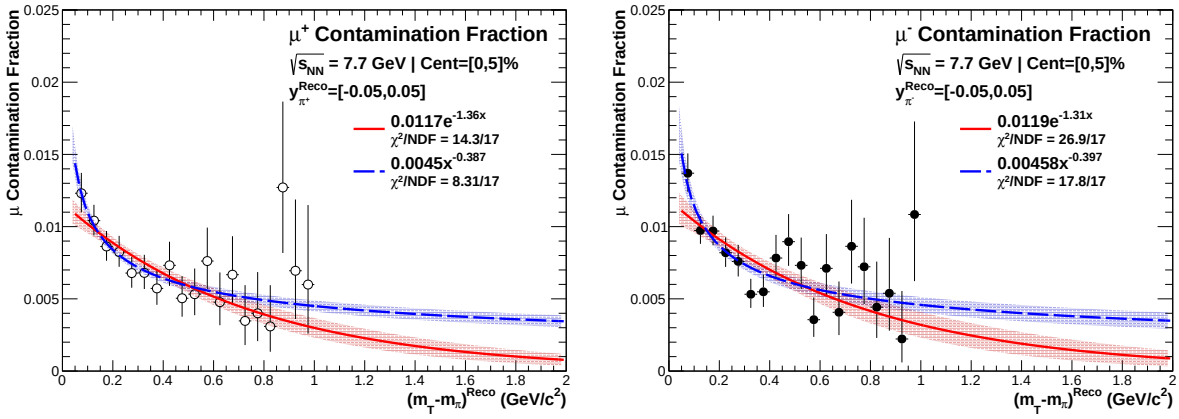

(a) π^+ **(b)** π^-

Figure 6.3: Examples of the muon contamination background fraction at midrapidity for π^+ (a) and π^- (b) as a function of transverse mass for the top 5% most central events (*Center* Configuration) in the Au+Au $\sqrt{s_{NN}} = 7.7$ GeV dataset. The red and blue curves are exponential and power law fits to the data respectively.

6.2.2 Feed Down

In addition to being thermally created by the medium resulting from the heavy-ion collisions, pions can also be the decay daughters of heavier particles. The majority of these pions are produced by weakly-decaying neutral mesons and various hyperons such as lambdas. Since the kinematics of these pions are defined by a secondary process they do not carry information about the dynamics of the medium and so their contribution to the pion spectra must be removed.

The results of the simulation chain are used to identify pions that come from weak decay processes. Events are binned by centrality and tracks identified as pions are binned by charge, rapidity, transverse mass, and parent ID. The parent ID signifies which particle species decayed to result in each pion. The results of this process are shown in figure 6.4 for a single transverse mass bin at midrapidity for the 5% most central events from the Au+Au $\sqrt{s_{NN}}$ = 7.7 GeV dataset. Pions with no parent ID (shown as NA) were created from the heavy-ion collision itself. All other pions are the decay products of their respective parents. The feed down background fraction is defined as $\pi_{\text{bkgd}} = N_{\text{decay}}/N_{\text{total}}$, where N_{Decay} is the number of pions coming from weak decays and N_{Total} is the total number of pions from all sources (histogram entries).

Figure 6.5 shows examples of the feed down background fractions as a function of transverse mass at midrapidity for positive and negative pions from the most central 5% of events in the Au+Au $\sqrt{s_{NN}}$ = 7.7 GeV dataset. The results are parameterized with exponential and power law fits. Although the χ^2 values of both functions generally indicate good agreement with the data, it is found that the exponential function consistently describes the shape of the low transverse mass region better. Hence, we use the exponential function as the default correction curve and use the power law and one sigma bands in the estimation of the systematic error associated with this correction, as described below.

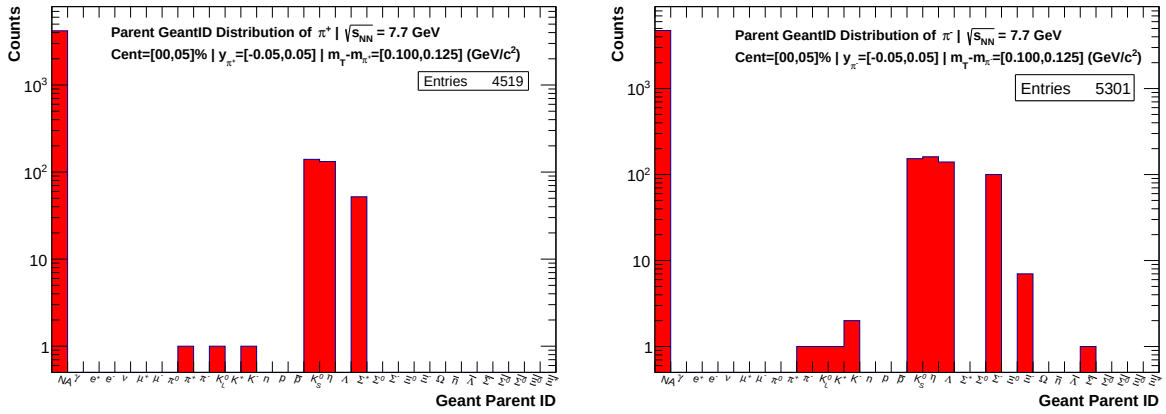

(a) π^+ **(b)** π^-

Figure 6.4: The distribution of parent particles that decay into π^+ (a) and π^- (b) for a single transverse mass bin at midrapidity for the top 5% most central events (*Center* Configuration) in the Au+Au $\sqrt{s_{NN}} = 7.7$ GeV dataset.

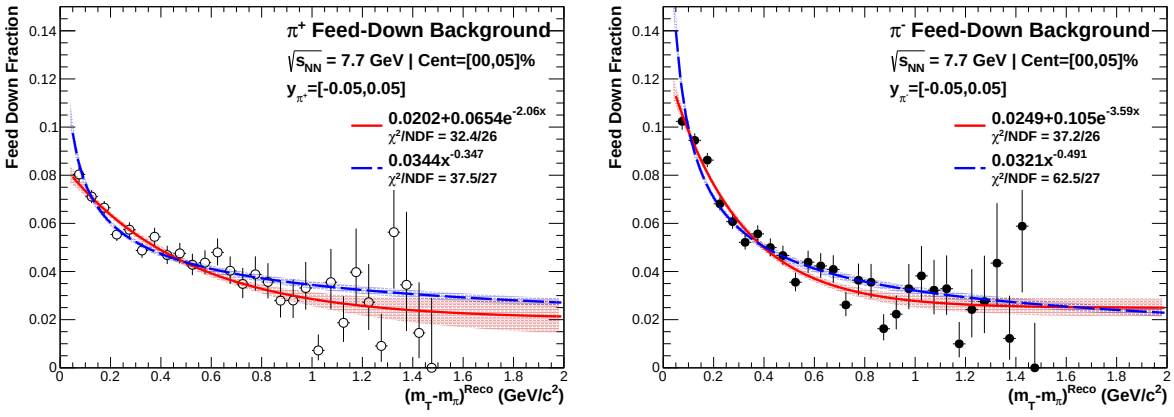

(a) π^+ **(b)** π^-

Figure 6.5: Examples of the pion feed down fraction as a function of transverse mass at midrapidity for π^+ (a) and π^- (b) for the top 5% most central events (*Center* Configuration) in the Au+Au $\sqrt{s_{NN}} = 7.7$ GeV dataset. The red and blue curves are exponential and power law fits respectively.

6.3 Proton Corrections

Protons also suffer from two main sources of background. The first source is the result of the protons present in the detector material itself and the second is the decay products of hyperons. In this section we discuss these two sources and the techniques used to estimate their contributions to the proton spectra.

6.3.1 Feed Down

Just as some of the measured pions are from decays of other particles, so too are some of the protons and anti-protons. In the case of the (anti)protons the decaying particles in question are primarily hyperons. For example, common decay modes of the Λ and Σ hyperons that result in the background of interest are $\Lambda^0 \rightarrow p + \pi^-$, $\Sigma^+ \rightarrow p + \pi^0$, $\overline{\Lambda^0} \rightarrow \bar{p} + \pi^+$, and $\overline{\Sigma^-} \rightarrow \bar{p} + \pi^0$. The background due to these decays is quantified using the same technique that was used for pions. The events and tracks resulting from the simulation chain must first pass the event and track cuts and are then binned by centrality, rapidity and transverse mass. Figure 6.6 shows the parent ID distribution of p and $\bar{\text{p}}$ for a particular transverse mass bin at midrapidity and for events in the top 5% of centrality from the $\sqrt{s_{NN}} = 62.4$ GeV dataset. Clearly a significant number of the measured protons and anti-protons come from the decays. Since the momenta of these tracks are defined by secondary processes their contribution to the spectra must be removed.

6.3.2 Knockout

As energetic particles travel through the detector they can collide with nuclei in the material. Such collisions can result in a proton being "knocked out" of the nucleus and be reconstructed as a track. Some of these tracks will satisfy all of the track quality cuts used in this analysis and will therefore be included in the proton spectra. Clearly, these protons carry no information about the medium produced in the heavy-ion collision and therefore their contribution to the spectra must be removed.

The magnitude of the background due to knockout proton contribution depends on two factors. Higher multiplicity events will result in larger knockout proton backgrounds because there are simply more tracks moving through the detector and changes in the

material budget of the detector can result in more or less knockout protons depending on the material density. Fortunately, the kinematics of the collisions that result in knockout protons are such that the protons typically have low momentum and therefore significant bending in the magnetic field. The result is that most knockout protons will be accurately tracked as having relatively large global DCA values. Thus the most effective cut for eliminating the knockout proton contribution is the global DCA cut.

Previous analyses ([71, 72, 73]) have used a global DCA cut of 3.0 cm and found that the knockout background can approach 40% in the low $m_T - m_0$ portion of the spectrum. To reduce this background this analysis used a global DCA cut of 1.0 cm. The remaining background in this analysis was evaluated using the results of the simulation chain. Figure 6.6 shows the parent ID distribution of p and $\bar{\text{p}}$ for a particular transverse mass bin at midrapidity and for events in the top 5% of centrality from the $\sqrt{s_{NN}} = 62.4$ GeV dataset. Note that in addition to the feed down protons originating from the Λ and Σ decays as discussed previously, there are also protons which have pions and kaons as parents. These protons are the result of the energetic pions and kaons undergoing knockout reactions with the detector material. Since there are no anti-protons in the detector material none can be knocked out and hence the parent GEANT ID distribution of the anti-protons is devoid of such entries.

6.3.3 Combined Feed Down and Knockout Background

Since both the feed down and knockout backgrounds of the protons can be evaluated using the same technique, we combine the two backgrounds to be the total background due to secondary processes. The background fraction is determined for each centrality, rapidity, and transverse mass bin from histograms such as those found in figure 6.6. The background fraction is computed as $p_{\text{bkgd}} = N_{\text{secondary}}/N_{\text{total}}$. The quantity p_{bkgd} is the background fraction of p or $\bar{p}$, the quantity $N_{\text{secondary}}$ represents the entries of the parent ID histogram that have a parent ID (i.e. not NA). The quantity N_{total} represents the total number of entries in the histogram. Figure 6.7 shows the background fraction for p and $\bar{p}$ at midrapidity as a function of transverse mass for events from the top 5% of centrality from the $\sqrt{s_{NN}} = 62.4$ GeV dataset. The background fraction is parameterized using

both power law and and exponential fits. The exponential fit is chosen as the default fit for correction and the power law fit and the confidence intervals are used in the processes of estimating the systematic error.

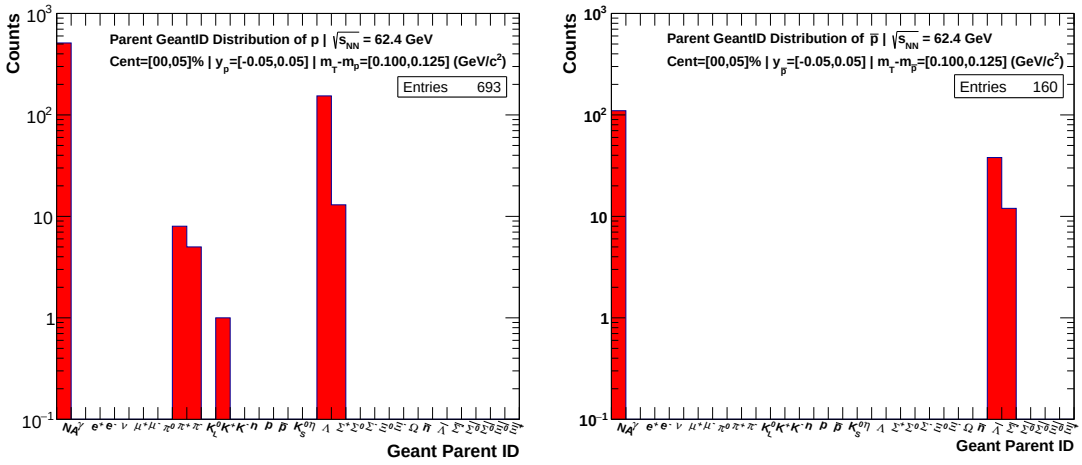

(a) p **(b)** $\bar{\text{p}}$

Figure 6.6: The distribution of parent particles that result in protons (a) and anti-protons (b) for a single transverse mass bin at midrapidity for the top 5% most central events (*Center* Configuration) in the Au+Au $\sqrt{s_{NN}}$ = 62.4 GeV dataset. Note that the protons with pions and kaons as parents are the result of knockout collisions.

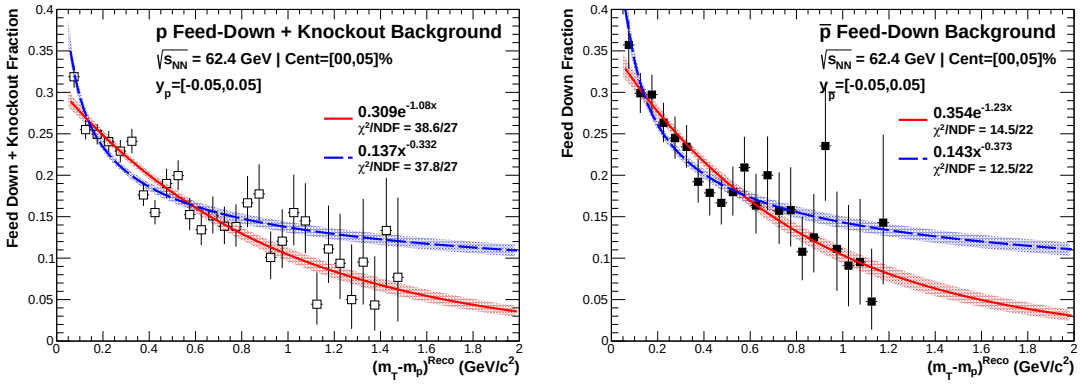

(a) p **(b)** $\bar{\text{p}}$

Figure 6.7: Examples of the proton (a) and anti-proton (b) feed down fraction - and knockout background in the case of protons - as a function of transverse mass at midrapidity for the top 5% most central events (*Center* Configuration) in the Au+Au $\sqrt{s_{NN}}$ = 62.4 GeV dataset.

6.4 Kaon Corrections

The feed down background contributions for kaons were investigated using the same techniques used for pions and protons. However, negligible background is observed as can be seen in figure 6.8. The figure shows the parent ID of kaons for a single transverse mass bin at midrapidity for central events in the $\sqrt{s_{NN}} = 62.4$ GeV dataset, where the background should be the largest. The negligible kaon background found in this analysis is consistent with the observations of previous spectra analyses at STAR. As a result no background corrections are needed for kaons.

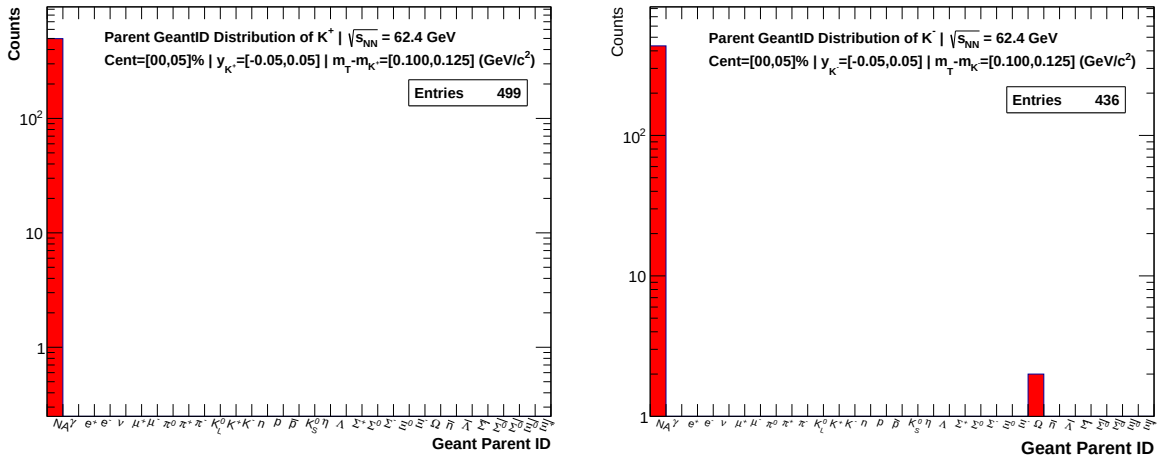

(a) K^+ **(b)** K^-

Figure 6.8: The distribution of parent particles that decay into K^+ (a) and K^- (b) for a single transverse mass bin at midrapidity for the top 5% most central events (*Center* Configuration) in the Au+Au $\sqrt{s_{NN}} = 62.4$ GeV dataset. The background is expected to be the largest at this collision energy.

Chapter 7

Particle Yield Extraction

The central problem that must be solved in this analysis pertains to the extraction of the identified particle yield from the dE/dx and $1/\beta$ measurements described in chapter 2. In general, the methodology that has been developed by STAR for extracting the yield of identified particles can be summarized in the following way. Tracks are binned according to a particle species mass assumption, the event centrality, charge, rapidity, and $m_T - m_0$. Note that a mass assumption must be made for each particle of interest as it is necessary for computing the rapidity and transverse mass of the track. For each of these bins the dE/dx and $1/\beta$ values (or some closely related value) of the constituent tracks are histogrammed. In effect, this methodology results in dE/dx and $1/\beta$ distributions of tracks within a very narrow slice of total momentum. As can be imagined from figures 2.6 and 2.9, the resulting distributions consist of peaks corresponding to each particle species. These distributions can be fit with a function consisting of a sum of several Gaussian functions. Typically, four Gaussians are used in the sum, one each for pions, kaons, protons, and electrons. The term corresponding to the particle species whose mass assumption was used for the binning process can be integrated to determine the yield of that particle species.

This methodology is well suited for the low momentum region at midrapidity because the peaks of the particle species are well separated and therefore easy to fit. However, as can also be inferred from figures 2.6 and 2.9, as one investigates the yield at increasingly high momenta (whether by increasing $m_T - m_0$ or by looking at forward rapidity bins), the

ability to clearly distinguish between the species is lost. This results in strong covariance between the parameters of the multi-Gaussian fit and either unnecessarily large systematic errors or erroneous results. The problem of extracting the identified particle yield is then reduced to constraining the mean and width parameters of the multi-Gaussian fit. Despite this clear objective, the variation of the means and widths as a function of rapidity and $m_T - m_0$ makes it exceedingly difficult to develop a simple and straightforward procedure.

In this chapter we discuss the iterative methods used in this analysis to extract the identified particle yield for pions, kaons, protons, and their antiparticles. The methods are generalizations and combinations of those that have been used in other identified particle spectra analyses. They have been generalized so that they are applicable to the wide range of rapidities for which yields are extracted in this analysis.

7.1 PID Calibration: Part 1

A common way to reduce the yield extraction error for the particle of interest is to recenter the dE/dx distribution around the expected mean of the particle of interest. This recentering process is done by transforming the dE/dx and $1/\beta$ values into $Z_{\mathrm{TPC}}(X) = \ln\left[(dE/dx)_{\mathrm{meas}}/(dE/dx)_{\mathrm{exp},X}\right]$ and $Z_{\mathrm{TOF}}(X) = (1/\beta)_{\mathrm{meas}} - (1/\beta)_{\mathrm{exp},X}$ respectively. Here, X represents the particle species of interest and the quantities subscripted with "meas" refer to the measured values. The quantities subscripted with "exp" refer to the expected values for a particle of species X. Note that in both cases it is necessary to know the expected value of the dE/dx and $1/\beta$. In principle both of these are known quantities. The expected dE/dx can be obtained from the Bichsel curves mentioned in Chapter 2 and the expected $1/\beta$ can be analytically computed as a function of momentum via $(1/\beta)(p) = \sqrt{1 + (m_x/p)^2}$, where m_x is the mass of the particle of interest. Analytically computing the value of $1/\beta$ gives an excellent approximation of the expected value for all combinations of rapidity and $m_T - m_0$, but the Bichsel curve breaks down away from midrapidity.

Hence, we begin by understanding how the mean of each species' dE/dx distribution will change as a function of rapidity and $m_T - m_0$. Tracks are binned by mass assumption

and rapidity and their measured dE/dx values are plotted as a function of $\beta\gamma = p/m$ using their measured total momenta. The track's mass is chosen using its measured dE/dx and $1/\beta$. If the track passes all of the requirements for a good track and good TOF track (see chapter 4) then it is presumed to have the mass of the species for which both its $1/\beta$ and dE/dx are within 20% of the expected values. The former is determined by the equation above and the second is determined from the Bichsel curve, which is sufficient for this purpose. If the track is not a good TOF track, but still passes the general track quality cuts and has an $m_T - m_0 < 0.4$ GeV/c^2, then it is presumed to have the mass of the species for which its measured dE/dx is within 20%. The electrons also have an exclusionary cut to remove most of the pions, kaons, and protons for which the expected electron mean overlaps. Note that the ionization energy loss of any given particle as it transits through the TPC is, to a very good approximation, independent of the total number of particles in the TPC. Thus, the parameterizations are done using centrality-integrated data.

Figure 7.1 shows an example of the outcome of this procedure for the pion mass assumption at midrapidity. As expected, the energy loss of the particle species, each represented by a different colored region, varies smoothly as a function of $\beta\gamma$. The curve in the figure is an unbinned fit of the form of equation 7.1 which was previously used in [73]. It is meant to reproduce the features of the Bethe-Bloch equation. Some of the parameters must be fixed to empirically determined values so that the fit converges. The parameters m_1, m_5, and m_6 are fixed to the following values: $m_1 = 1.2403$, $m_5 = 1.6385$, and $m_6 = 0.72059$.

$$\frac{dE}{dx}(\beta\gamma) = m_1 \left(1 + \frac{1}{(\beta\gamma)^2}\right)^{m_2} \times \left[\left|\ln\left(m_3(\beta\gamma)^2\right)\right|^{m_4} + m_5 \left(1 + \frac{1}{(\beta\gamma)^2}\right)^{m_6}\right] - m_7 \quad (7.1)$$

The above procedure is repeated for each combination of collision energy, event configuration, mass assumption and rapidity bin. The result of the entire process is a complete set of curves to describe the expected dE/dx of each particle species for each of the kinematic bins used in this analysis. These curves can then be used in the calculation of the Z_{TPC} and Z_{TOF} variables in the recentering process as described below.

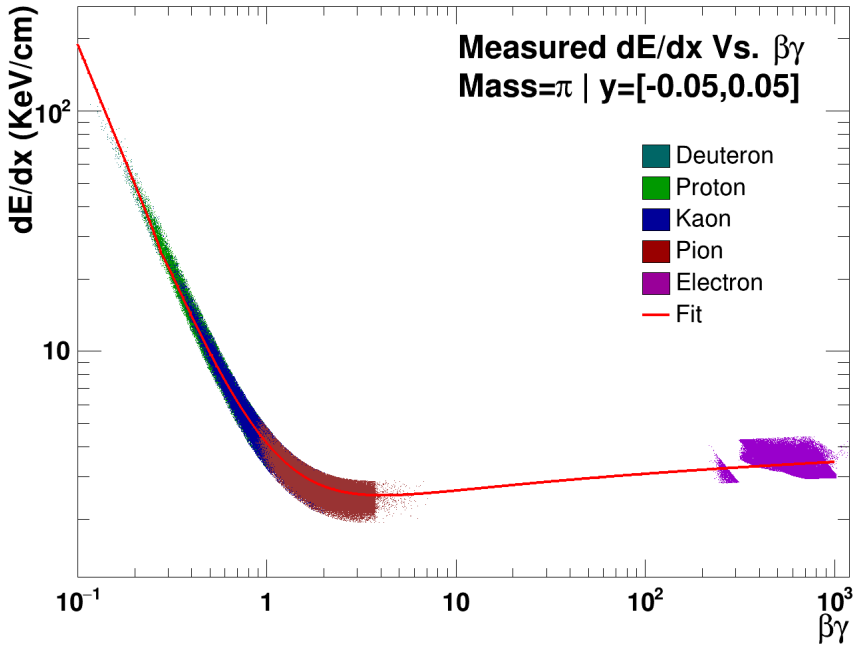

Figure 7.1: An example of the ionization energy loss parameterization as a function of $\beta\gamma$ for the pion mass assumption at midrapidity in the $\sqrt{s_{NN}} = 7.7$ GeV dataset (*Center* Configuration). The energy loss has no centrality dependence so events from all centrality classes are combined for this parameterization. The curve is an unbinned fit using equation 7.1.

7.2 Track Binning and Recentering

The one dimensional Z_{TPC} and Z_{TOF} distributions can be now constructed for each mass assumption, centrality, charge, rapidity, and $m_T - m_0$ bin. As noted previously, the reason for using these variables is that they recenter the dE/dx and $1/\beta$ distributions so that the peak of the particle of interest is centered at $Z = 0$. This has the important property of constraining one of the parameters of the multi-Gaussian fit. It also has the convenient property of making the measurement errors on dE/dx roughly constant for the particle of interest as a function of $m_T - m_0$. However, this is only true for the particle of interest and not for any of the other particle species. To solve this problem we use a nonlinear likelihood recentering procedure developed and used in [66] and [67].

Since the PID measurements dE/dx and $1/\beta$ are presumed to be normally distributed random variables, the likelihood function for a given species, X, and PID measurement, m, are given by the normalized Gaussian function of equation 7.2 as a function of mo-

mentum. The functions $\mu_X(p)$ and $\sigma_X(p)$ represent the mean and standard deviations of the quantities as a function of momentum. The mean is given by the curves acquired in the previous subsection and the standard deviations are fixed to be either 0.07 for dE/dx or 0.012 for $1/\beta$. These are the dE/dx and $1/\beta$ measurement resolutions respectively.

$$\mathcal{L}\left(X|p,m\right) = \frac{1}{\sigma_X(p)\sqrt{2\pi}} e^{\frac{(m-\mu_X(p))^2}{2(\sigma_X(p))^2}} \tag{7.2}$$

The nonlinear recentering for the particle species of interest, X', is then constructed according to equation 7.3. As described in [66], the first term is the likelihood-weighted average adjustment to the PID measurement for a particle of species, X, and average momentum, $\langle p \rangle$. The second term is responsible for subtracting the mean of the peak of the particle species of interest so that the distribution is recentered around $Z(X') = 0$.

$$\begin{aligned} Z(X') = & \frac{\sum_X \mathcal{L}(X|p,m)(m + \mu_X(\langle p \rangle) - \mu_X(p))}{\sum_X \mathcal{L}(X|p,m)} \\ & - \frac{\sum_X \mathcal{L}(X|p,\mu_{X'}(p))(m + \mu_X(\langle p \rangle) - \mu_X(p))}{\sum_X \mathcal{L}(X|p,\mu_{X'}(p))} \end{aligned} \tag{7.3}$$

Figure 7.2 shows examples of the resulting Z_{TPC} and Z_{TOF} distributions. The distributions in both figures show tracks from the top 5% most central events in the $\sqrt{s_{NN}} = 7.7$ GeV dataset (*Center* Configuration) at midrapidity with a pion mass assumption and positive charge. The two figures differ in their $m_T - m_0$ bin selections which were chosen so that the peaks of the various particle species are clearly distinguishable.

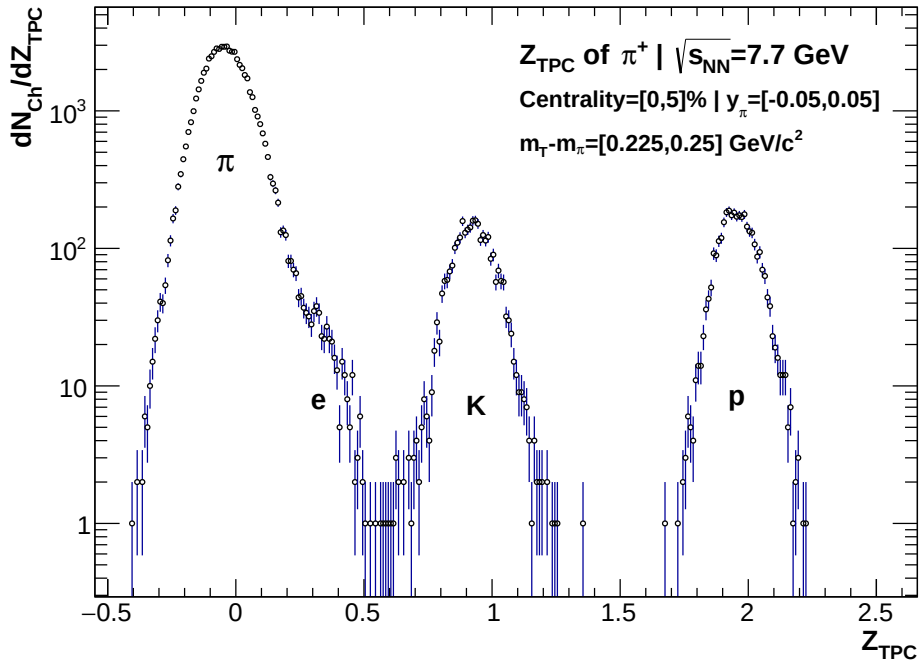

(a)

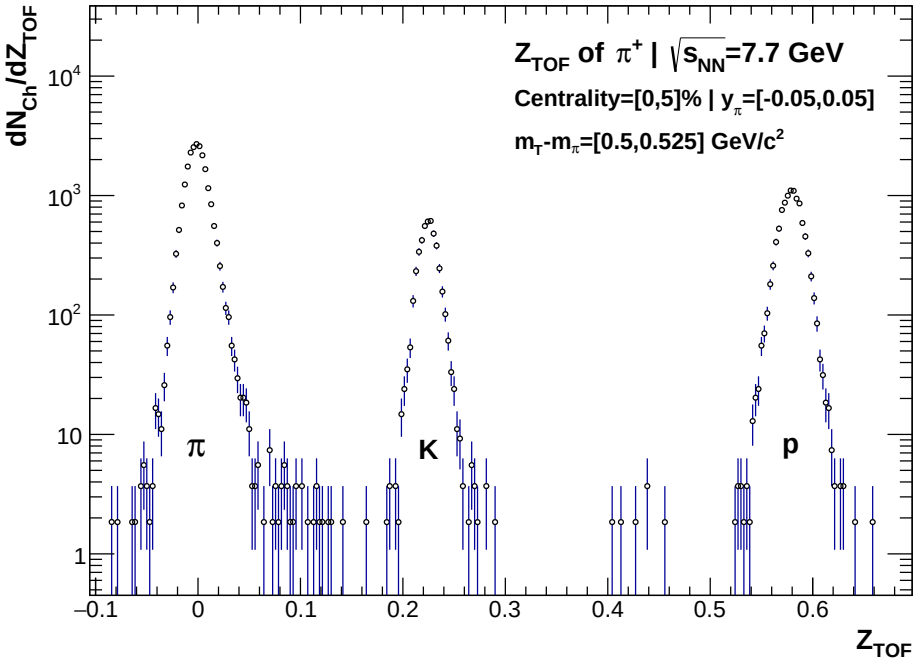

(b)

Figure 7.2: Examples of the (a)Z_{TPC} and (b)Z_{TOF} distributions for the pion mass assumption and positive charge at midrapidity in the $\sqrt{s_{NN}} = 7.7$ GeV dataset (*Center* Configuration). The two distributions are shown for two different $m_T - m_0$ bins.

7.3 PID Calibration: Part 2

The recentering procedure above removes much of the momentum dependence of the Z distribution within a given kinematic bin. However, the shape parameters can still vary as a function of $m_T - m_0$ within a rapidity bin and the description of the means using the parameterizations in section 6.1 can no longer be assumed valid after the Z transformation. The error on the extracted yield can be further reduced by studying the shape parameters of each particle's Z distribution in each transverse mass and rapidity bin. Since the shape parameters of Z distributions are not expected to vary with centrality or charge, the parameterizations need only to be done for each mass assumption, rapidity bin, and $m_T - m_0$ bin.

To aid in this procedure "TOF optimized" Z_{TPC} distributions are constructed for each species in each bin. This is done by plotting the Z_{TPC} value of tracks which are within 2% of the expected Z_{TOF} value for each species. The result is a decomposition of the Z_{TPC} distribution for each kinematic bin into constituent distributions belonging to each species as shown in the plots in figure 7.3. The plots illustrate an important attribute of the energy loss measurement - that although much effort was invested in making the resulting distributions normal, they are, in fact, skewed. This is an attribute which is a direct consequence of the Landau distributed nature of the individual dE/dx measurements for each track as discussed in chapter 2.

To account for the non-normality of the distributions we break from the typical multi-Gaussian fitting model used by other analyses and instead employ a skewed normal distribution of the form in equation 7.4 to fit each of the TOF optimized distributions. The parameter α is responsible for the skewness of the function and is a free parameter of the fit. The resulting fits can then be used directly in the yield extraction procedure described in a following section.

$$\begin{aligned} f(x) = \phi(x)\Phi(\alpha \times x) = \phi(x) \int_{-\infty}^{\alpha \times x} \phi(x)dx \\ \text{where } \phi(x) = Ae^{-\frac{(x-\mu)^2}{2\sigma^2}} \end{aligned} \tag{7.4}$$

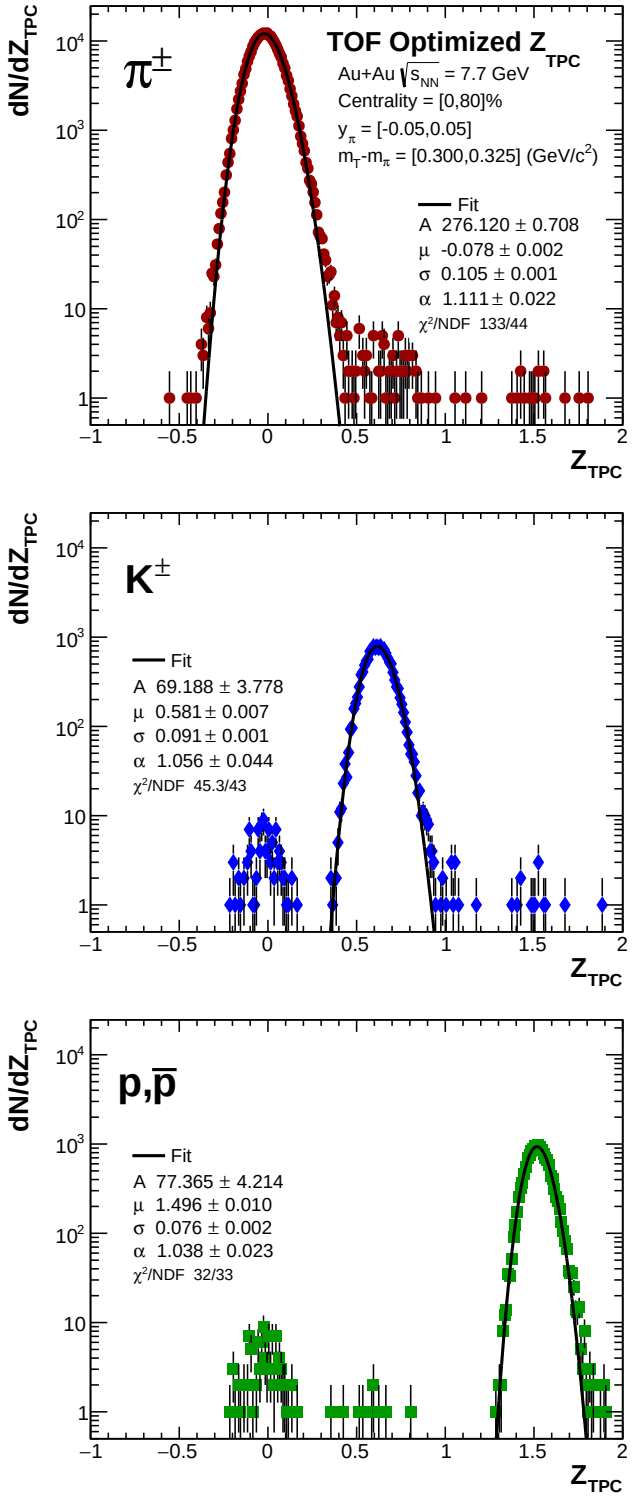

Figure 7.3: An example of the deconstructed Z_{TPC} distribution using "TOF Optimized" distributions for (top) pions, (middle) kaons, and (bottom) protons. The distributions are for the given $m_T - m_0$ bin and for a pion mass assumption at midrapidity in the $\sqrt{s_{NN}} = 7.7$ GeV dataset (*Center* Configuration).

Note that there is no parameterization for the electron distribution in this process. Due to its small mass the electron is relativistic in the entire momentum range studied. This means that its dE/dx changes very little as a function of total momentum, as can be seen in figure 2.6. As a result the Z_{TPC} distribution of the electron is found to minimally deviate from its expected mean and hence the mean predicted by the Z transformation of the Bichsel curve for the electron is used throughout the fitting procedure. Similarly, the width of the electron is found to change minimally as a function of total momentum. Consequently, the main contributor to the width of the electron distribution is then the measurement resolution itself. Since the dE/dx calibration is done with respect to pions, it is found that fixing the width of the electron distribution to the width of the pion distribution in each rapidity and $m_T - m_0$ bin is a very good estimate of its width. Finally, because the yield of electrons falls off rapidly as a function $m_T - m_0$, there is a negligible amount in the $m_T - m_0$ region in which the Z_{TOF} distribution is used to extract the yield. Hence, no Gaussian function for the electron is used in fits to the Z_{TOF} distributions.

7.4 Intra-Bin Transverse Mass Location

The last consideration that must be addressed prior to extracting the yield is to determine the specific $m_T - m_0$ value to which the yield in each bin should be assigned. It is common to simply choose the center of the transverse mass bin for convenience. This is acceptable so long as the transverse mass bin width is very small. However, it is also known that spectra for each particle species falls roughly exponentially as a function of transverse mass and that consequently the intra-bin transverse mass distribution should also be exponential. This implies that the average $m_T - m_0$ of the intra-bin track population is less than the bin center.

Although the difference between the bin center and the intra-bin population average is small for the narrow bins defined in this analysis, we invest the time to account for it for two reasons. First, knowing precisely where to evaluate the energy loss and tracking efficiency curves is essential to applying the spectra corrections accurately. And second,

engaging in such a study permits a sensible horizontal error to be attributed to each point in the spectra. This is important because too often the horizontal errors in spectra are assigned to describe the bin width or else are set to zero. Since neither case assigns a one-sigma value, the horizontal errors are incorrect for usage in quantitative assessments of the spectral shape such as fitting. The first case, while illustrative when plotting the spectra, dramatically overestimates the error and, if considered in a fit, will result in inappropriately small χ^2 values, excessively large statistical errors on the fit parameters, and/or unconverged fits. The second case underestimates the error and will result in the opposite effects when fitting.

The process of finding the intra-bin population transverse mass average begins by noting that we need the *true* distribution of *measured* transverse mass for tracks of a *specific* species of particle that is consistent with the mass assumption of the spectra. The three emphasized characteristics of the distribution are essential. Since the transverse mass spectra of identified particles will be constructed it is necessary to know the intra-bin average of the particle species of interest. Since the energy loss correction described previously will correct for the difference between the measured and true transverse mass, it is the mean of the measured transverse mass that must be computed. And finally, since the shape of the intra-bin transverse mass distribution will be affected by detector efficiency and acceptance, it is necessary to reweight the bin contents of the distribution by the requisite corrections.

Events are binned by centrality and tracks are binned in rapidity and $m_T - m_0$ after passing the standard event and track quality cuts respectively. Particle identification is accomplished in the following way. First, it is determined whether or not the track is a good TOF track. If the track's TOF measurements are valid then particle identification is jointly decided by both the TPC and TOF - the dE/dx and $1/\beta$ measurements must agree with their respectively expected values given the track's total momentum and particle species assumption. If the track is not a good TOF track then particle identification is accomplished solely by the TPC, but this method is used with the additional condition that the track's transverse mass must be below 0.400 GeV where the TPC has good PID

resolution for all particle species and for all rapidity bins.

After the track has been identified as a particular species, its transverse mass is corrected via the energy loss correction. If the track was identified with help from the TOF, it is reweighted with both the TOF matching efficiency and TPC tracking efficiency. If the track was identified only using the TPC, it is reweighted with only the TPC tracking efficiency. So that the intra-bin averages over the entire transverse mass range of the spectra can be compared directly, the difference between the measured transverse mass of the track and the low transverse mass bin edge is computed and histogramed. An example of such a histogram is shown in figure 7.4 for negative pions. For comparison, and to demonstrate the importance of the reweighting, both the weighted and measured (unweighted) distributions are shown. The intra-bin average is also computed and shown in the text of the plot for both distributions.

The intra-bin average for each transverse mass bin can then be studied as a function of transverse mass as shown in figure 7.5. Clearly, the difference between the intra-bin average and the bin center is small, but it is systematic as expected from the exponentially falling distribution. As demonstrated for the case of negative pions in the figure, the dependence of the intra-bin average on transverse mass is well described by a constant. This is observed to hold for all particles species and for all centrality and rapidity bins used in the analysis. The value of the yield in each transverse mass bin can then be assigned to the $m_T - m_0$ value that is obtained by adding the low edge of the bin to the constant obtained from the fit. Finally, the error on the fit constant is simply propagated through the sum to become the horizontal error on the yield.

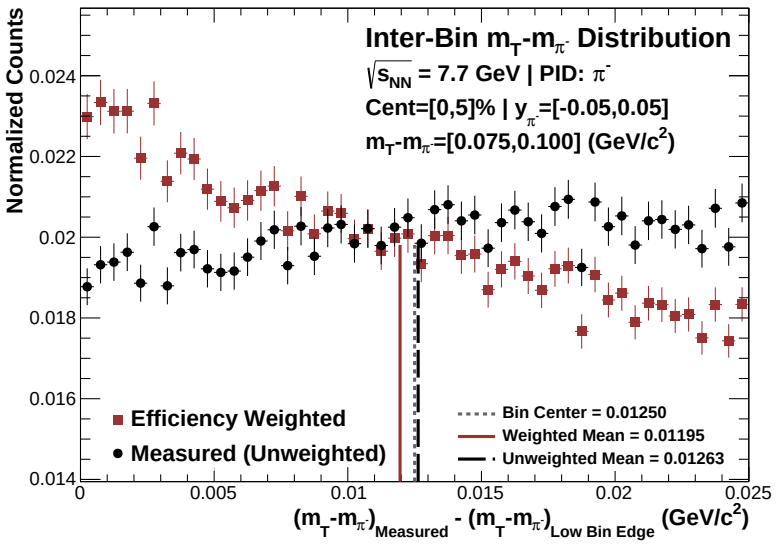

Figure 7.4: An example of the measured (unweighted) and efficiency weighted intra-bin transverse mass distributions of negative pions in a single transverse mass bin from the most central 5% of events at midrapidity from the $\sqrt{s_{NN}} = 7.7$ GeV dataset (*Center* Configuration). Note that the vertical axis is zero-supressed.

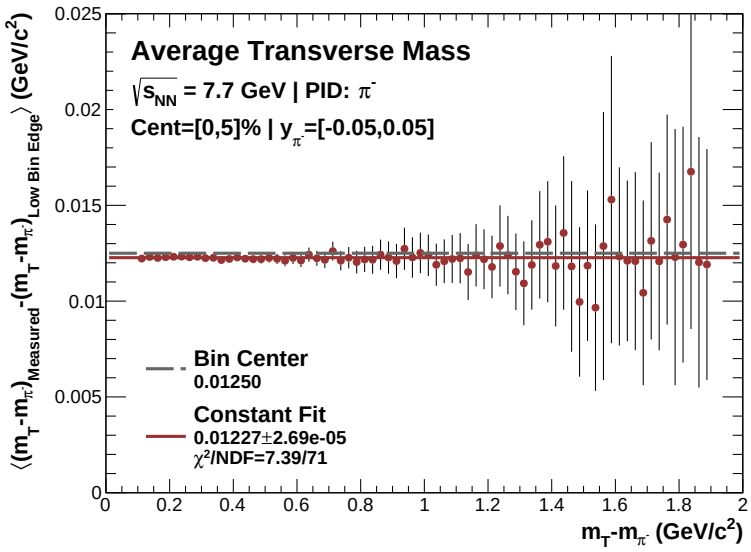

Figure 7.5: An example of the intra-bin average transverse mass as a function of transverse mass for negative pions at midrapidity in the most central 5% events of the $\sqrt{s_{NN}} = 7.7$ GeV dataset (*Center* Configuration).

7.5 Yield Extraction

Having carefully performed the PID calibration procedures above we are finally ready to extract the yields of the particles of interest and position their yields at the intra-bin transverse mass mean. In the following two sections we discuss how the yield extraction is performed for each of the two detectors.

7.5.1 Z_{TPC} Yields

The final yield extraction fit to the Z_{TPC} distribution of all simillary charged particles for a particular mass assumption and in a particular kinematic bin is a sum of the skewed normal functions for each of the primary particle species (π, K, p) and a Gaussian for the electron. The form of the fit can be seen in equation 7.5. Each of the skew normal functions has an associated multiplicative scaling factor, A, which are free parameters in the fit. The parameters of the electron Gaussian are treated as follows: the amplitude of the electron distribution is a free, but constrained, parameter of the fit; the mean of the electron distribution is fixed to the value predicted by the parameterized energy loss curves obtained as part of the PID calibration procedure above; and the width of the electron distribution is fixed to the width of the pion distribution. The functions within each term are defined as in equation 7.4. An example of the final fit can be seen in figure 7.6.

$$F(x) = A_\pi f_\pi(x) + A_K f_K(x) + A_p f_p(x) + \phi_e(x) \tag{7.5}$$

Despite the careful attempt in this analysis to accurately describe the shapes of the Z_{TPC} distributions, the final fits in highly populated kinematic bins often exhibit relatively large χ^2/NDF values. This ia a characteristic of many spectra analyses and is the result of two effects. First, in addition to the skewness of the Z_{TPC} distributions caused by the underlying Landau energy loss mechinism, there is also kurtosis caused by varying track length. An attempt was made to model the kurtosis, but it was ultimately decided that the effect on the results of the analysis was negligible. The second effect is simply related to the very large track population within each kinematic bin. The statistical errors of the individual histogram bins are so small that without exact knowledge of the shape of the

distributions any approximate fitting model with a small number of parameters is bound to have a poor χ^2/NDF. Consideration was given to the possibility of performing an even finer kinematic binning to reduce the statistics within each bin, but the dimensionality of the analysis was already so large that the track binning procedure impinged on the memory limits of the workstation used for the analysis.

7.5.2 Z_{TOF} Yields

The final yield extraction fit to the Z_{TOF} distribution of particles with the same charge sign for a particular mass assumption and in a particular kinematic bin is a sum of three Gaussian functions - one for each primary particle species (π, K, p). The electron is not modeled since they are few in number in the relatively high transverse mass region in which the Z_{TOF} distributions are used to extract the yield. First, the distribution of the positive particles is fit. The parameters of the Gaussians are seeded and bounded, but are otherwise free. This is unproblematic because the excellent timing resolution of the TOF detector means that the distributions of the individual particles are well separated. After fitting the distribution of positive particles, the means and widths of the Gaussians are extracted and used to fix the associated parameters in the fit to the distribution of negative particles. This is done because the means and widths of the Z_{TOF} distributions are entirely detector related and should not be sensitive to charge. Fixing the parameters in this way permits a more accurate yield extraction for very low multiplicity particles such as the anti-proton at low collision energies or far forward/backward rapidities. Further, this ensures that any difference in yield between the particle and antiparticle is exclusively the result of a physics mechanism and not due to variations in fit stability.

An example of such a fit can be seen in figure 7.6. The quality of the fit varies from energy to energy due to the increased particle yield at higher collision energies. In particular, the shoulders of the individual particle distributions are not well described by the simple multi-Gaussian model used to fit the distribution. This can cause the χ^2/NDF to be quite large for bins which have very large track populations. Fundamentally, the cause of the high χ^2/NDF value is that the multi-Gaussian fit model is incorrect. Like the Z_{TPC} distributions above, the true shapes of the Z_{TOF} distribution for each particle

species is unknown. However, unlike the Z_{TPC} distributions, a simple fit model can be used in the Z_{TOF} yield extraction because of the large separation between the individual particle species.

7.5.3 Probabilistic Yield Extraction

As mentioned, the fits to the Z_{TPC} and Z_{TOF} distributions can result in large χ^2/NDF values for bins in which the track population is large. This indicates that the fits should not be used directly to extract the yield and statistical error. The yield will be underestimated since the fit curve falls below the bin contents of the histogram in the tail regions. The errors on the free parameters will also be underestimated. Thus, the convariance matrix of the fit will not be valid and will therefore be unusable for computing the statistical error on the yield. Instead, the final fits and a probabilistic model are used to extract the yield and statistical error. The yield of the particle of interest, X', is computed at the center of each bin of the Z_{TPC} and Z_{TOF} histogram, c_i, as the product of the bin content, N_i, and the ratio of the value of the function of the particle of interest, $G_{X'}(c_i)$, and the total fit, $G_{\mathrm{total}}(c_i)$. The yield of the particle of interest, X', in a particular centrality, rapidity, and $m_T - m_0$ bin is then simply the sum of the per bin yields as shown in equation 7.6. The error on $N_{X'}$ is simply the associated counting error, $\sigma_{N_{X'}} = \sqrt{N_{X'}}$.

$$N_{x'}(\sigma_{\%}, y, m_T - m_0) = \sum_{i=0}^{i=nBins} N_i \times \frac{G_{X'}(c_i)}{G_{\mathrm{total}}(c_i)} \tag{7.6}$$

Finally, the *invariant* yield, $\mathcal{N}_{X'}$, of the particle of interest in each kinematic bin is then $N_{X'}$ scaled by the number of events in the relevant centrality class, the proper phase space factors, and a factor of $1/m_T$ as shown in equation 7.7. The last factor is the quantity needed to make the yield invariant. The error is also scaled by the collection of prefactors.

$$\mathcal{N}_{x'}(\sigma_{\%}, y, m_T - m_0) = \frac{1}{N_{\mathrm{event}}} \frac{1}{2\pi m_T} \frac{d^2N}{dm_T dy} \times N_{x'}(\sigma_{\%}, y, m_T - m_0) \tag{7.7}$$

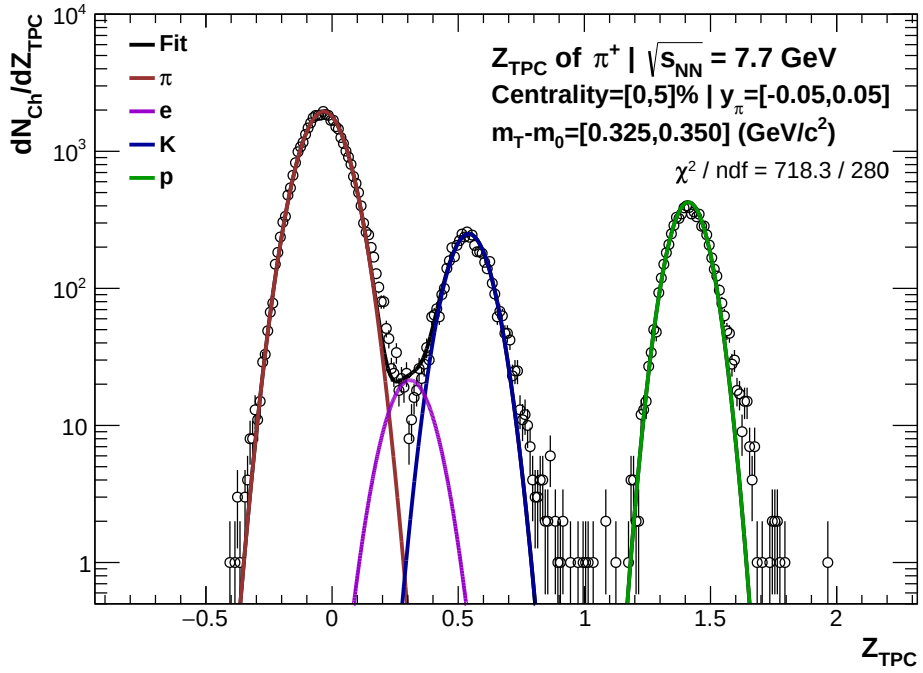

(a)

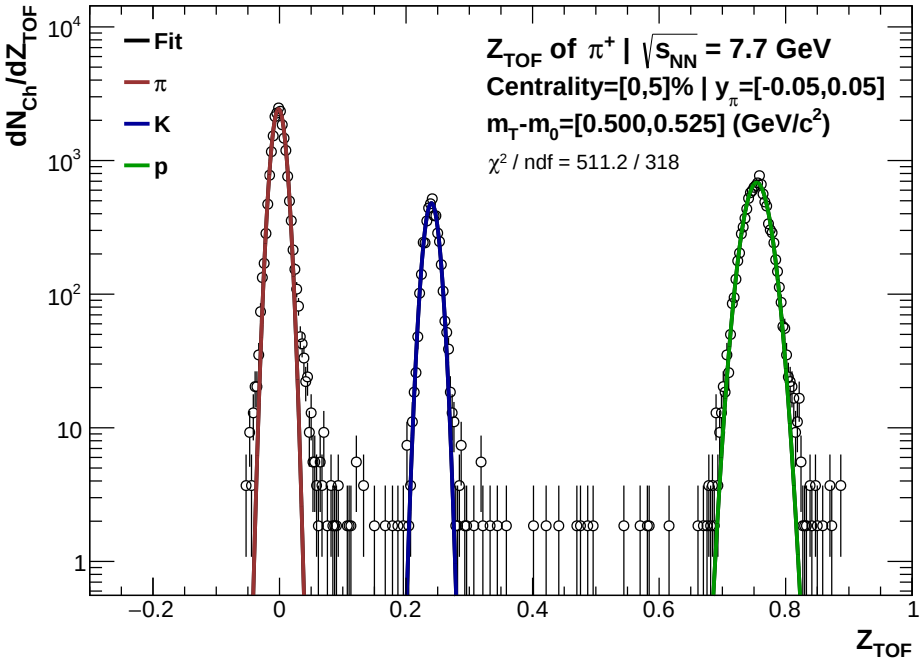

(b)

Figure 7.6: Examples of the final fits to the (a)Z_{TPC} and (b)Z_{TOF} distributions for the pion mass assumption and positive charge at midrapidity in the $\sqrt{s_{NN}} =$ 7.7 GeV dataset (*Center* Configuration). The two distributions are shown for two different $m_T - m_0$ bins.

Repeating the above procedure for each $m_T - m_0$ bin for a selected centrality and rapidity bin results in an uncorrected transverse mass spectrum of invariant yields of the particle of interest. An example of such a spectrum is shown in figure 7.7. The solid circles and squares are yields obtained from Z_{TPC} and Z_{TOF} distributions respectively. Both the vertical and horizontal error bars are present, but in both cases are smaller than the plotting symbol. Finally, by repeating the full procedure for all combinations of event configuration, energy, centrality, and rapidity, the full collection of the spectra is assembled, as will be shown in the following chapter.

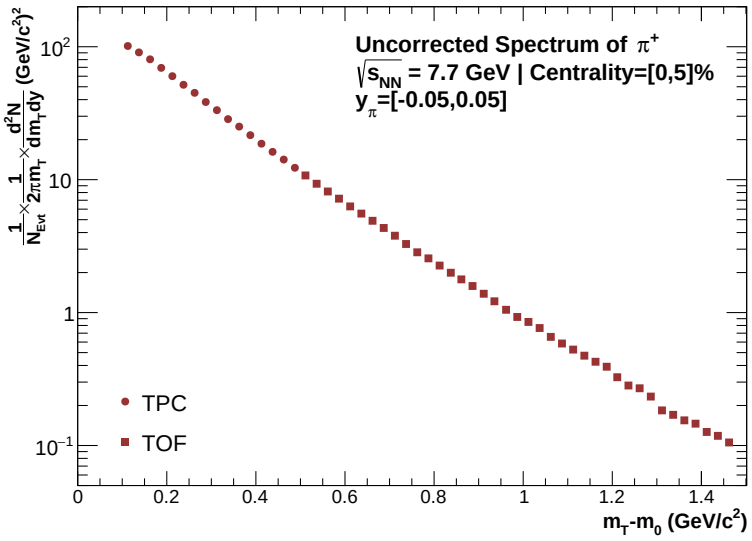

Figure 7.7: An example of the midrapidity, uncorrected spectrum of positive pions as a function of $m_T - m_0$ from top 5% most central events in the $\sqrt{s_{NN}} = 7.7$ GeV dataset (*Center* Configuration). The solid circles and squares are yields obtained from Z_{TPC} and Z_{TOF} distributions respectively. The error bars are smaller than the plotting symbols.

7.6 Application of Corrections

The various corrections to the spectra that were discussed in the previous two chapters are applied to the uncorrected spectra via the correction chain ordered as shown in figure 7.8. The uncorrected spectrum is first corrected for background contributions depending on particle species and then corrected for detector effects. In general, the order in which the corrections are applied is commutable, with the exception of the energy loss correction. Recall that the energy loss correction converts the measured transverse mass of tracks - or in this case bin averages - to the true transverse mass. Hence, any correction that is applied prior to the energy loss correction must be parameterized as a function of measured transverse mass while corrections applied afterwards must be parameterized as a function of the true transverse mass.

In this section we briefly discuss how the corrections are applied. The quantity $\mathcal{N}_{x'}$ is used as before to describe the invariant yield of particle species x' prior to the correction. The primed quantity $\mathcal{N}'_{x'}$ is used to describe the corrected yield. In all cases the multiplicative correction factor applied to the yield is also applied to the statistical error. Also note that the corrections accumulate so that the corrected yield after one correction is the uncorrected yield for the next correction.

7.6.1 Background Fraction Corrections

The background corrections for each particle were constructed as background fractions. Hence the multiplicative correction factor must be computed as the complement of the fraction. In the cases of the muon contamination, feed-down, and knockout backgrounds, the corrections are applied according to equation 7.8. The quantity $B_f(\sigma_{\%}, y)$ is the function describing the relevant background fraction for the particular centrality and rapidity bin of interest and is evaluated at the $m_T - m_0$ corresponding to the spectrum point - the intra-bin average transverse mass.

$$\mathcal{N}'_{x'}\left(\sigma_{\%}, y, m_T - m_0\right) = \mathcal{N}_{x'}\left(\sigma_{\%}, y, m_T - m_0\right) \times \left(1.0 - B_f(\sigma_{\%}, y)\mid_{m_T - m_0}\right) \tag{7.8}$$

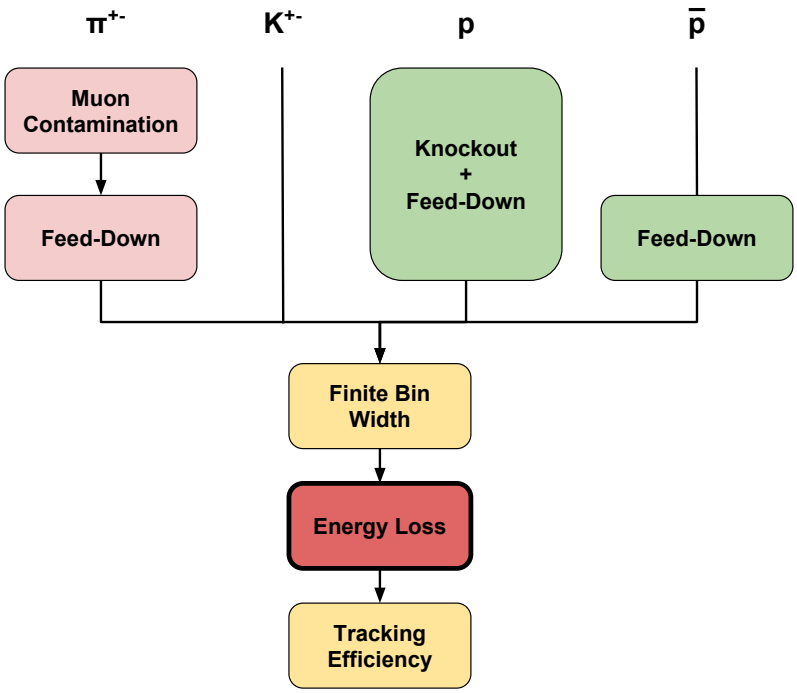

Figure 7.8: A cartoon showing the flow of the corrections applied to an uncorrected spectrum. The order of the corrections is unimportant with the exception of the energy loss correction. See the main text for details.

7.6.2 Finite Bin Width Correction

As previously noted, the finite bin width correction corrects for the difference in bin width between the measured and true transverse mass bins. Recall that the tracks were binned by their measured transverse mass in bins that were 0.025 GeV/c^2 wide. This bin width must now be converted to what the bin width would be in true transverse mass. This is accomplished by evaluating the energy loss curve at the high and low edges of each transverse mass bin. Recall that the energy loss curve is parameterized as a function of transverse momentum rather than transverse mass. Thus, the first step in the correction is to convert the low and high edges of each transverse mass bin to its corresponding values in p_T. The original width of the bin in units of p_T, $(\Delta p_T)_{\text{original}}$, is then computed. The low and high edges of the bin as measured in p_T are then converted to their true values via the energy loss curve via equation 7.10 for the energy loss correction. The two corrected bin edges can then be used to determine the width of the true p_T bin, $(\Delta p_T)_{\text{corrected}}$. The

multiplicative correction factor is then the ratio of the original bin width to the corrected bin width and is applied as in equation 7.9.

$$\mathcal{N}'_{x'}\left(\sigma_{\%}, y, m_T - m_0\right) = \mathcal{N}_{x'}\left(\sigma_{\%}, y, m_T - m_0\right) \times \frac{\left(\Delta p_T\right)_{\text{original}}}{\left(\Delta p_T\right)_{\text{corrected}}} \tag{7.9}$$

7.6.3 Energy Loss Correction

Unlike the other corrections which affect the spectrum along its vertical axis, the energy loss correction shifts the spectrum along the horizontal, transverse mass axis. Again, because the energy loss curve is parameterized as a function of measured p_T, the procedure begins by converting the $m_T - m_0$ of each point in the spectrum to p_T. The true p_T of the point is then obtained by subtracting the value of the energy loss function as in equation 7.10. Here the quantity $E_{\text{loss}}(y)\mid_{(p_T)_{\text{measured}}}$ is the function describing the energy loss for the relevant rapidity bin evaluated at the measured p_T of the spectrum point. Finally, the true p_T is then converted back to transverse mass and used as the horizontal coordinate for the point in the spectrum. In this case, no statistical error is assigned to the energy loss correction and hence the horizontal error on the spectrum is unchanged.

$$\left(p_T\right)_{\text{true}} = \left(p_T\right)_{\text{measured}} - E_{\text{loss}}(y)\mid_{(p_T)_{\text{measured}}} \tag{7.10}$$

7.6.4 Tracking Efficiency Correction

Finally, the tracking efficiency, which is parameterized as a function of the corrected transverse mass, can be applied with equation 7.11. Here the quantity $\epsilon\left(\sigma_{\%}, y\right)\mid_{(m_T - m_0)_{\text{corrected}}}$ represents the efficiency function for the relevant centrality and rapidity bin evaluated at the corrected transverse mass of the point in the spectrum.

$$\mathcal{N}'_{x'}\left(\sigma_{\%}, y, m_T - m_0\right) = \mathcal{N}_{x'}\left(\sigma_{\%}, y, m_T - m_0\right) \times 1/\epsilon\left(\sigma_{\%}, y\right)\mid_{(m_T - m_0)_{\text{corrected}}} \tag{7.11}$$

7.7 Treatment of Systematic Errors

In general, the results of analyses are desired to be both accurate and precise; accurate insofar as the measured quantities represent the *true* value of the quantity and precise insofar as repeated measurements using different methodologies will yield similar results. The large number of particles produced in heavy-ion collisions benefit the accuracy of

spectra analyses by ensuring very small statistical errors. However, the many steps of the analysis, the numerous corrections, and the various models associated with each correction do the precision of the analysis no favors.

In the case of the present analysis, the systematic errors are expected to be much larger than the statistical ones and thus are the dominant limitation of quantitative assessments of the results. In such a case, the burden of correctly accounting for the systematic errors of the analysis is a significant one. On one hand, if the systematic errors are overestimated, no conclusive results may be derived from the analysis. On the other hand, if the systematic errors are underestimated, the results may be erroneously interpreted as being stronger than the analysis methodology warrants. It is with these considerations in mind that we turn our attention to the estimation of the systematic errors associated with the yield extraction and correction procedure.

7.7.1 Systematic Error on the Uncorrected Yield

The systematic error associated with the extraction of the raw yield from the Z_{TPC} distributions is entirely due to the particle identification parameterizations. To estimate the error on the yield due to fixing the means and widths of the Gaussian functions used to fit each particle species, the uncorrected yield is extracted multiple times. Recall that only the amplitudes of the Gaussian functions were left as free parameters in the final fit to the Z_{TPC} distributions. They are allowed to remain free for each of the fits used in the estimate of the systematic error. Each time the yield is extracted the means and widths of the distributions are varied and fixed to a new value. The distribution is then re-fit and the yield is re-extracted. The means and widths are varied by a uniformly chosen percentage of up to $\pm 10\%$. The standard deviation of the resulting distribution of uncorrected yields is then considered the systematic error.

The systematic error due to the particle identification parameterizations is seen to be quite small for all bins used in this analysis. This is unsurprising since, by construction, bins in which the distributions of confounding species overlap with the species of interest are avoided. For example, when the particle of interest is a pion and the kaon Z_{TPC} distribution approaches the pion Z_{TPC} distribution, the yield extraction is performed via

the Z_{TOF} distribution instead.

Any systematic error associated with the TOF matching efficiency correction or yield extraction via the Z_{TOF} distributions is safely ignored. This is for two reasons. First, the observation that the systematic errors from the Z_{TPC} extraction were small suggests that the systematic errors on the yield extracted using a detector with a much better resolution will be even smaller. (This would be untrue if the spectra were extended to a transverse mass sufficiently high to observe the Z_{TOF} distributions merge. However, this analysis focuses on thermal production and hence the spectra are stopped prior to the merger of confounding particles with the particle of interest.) Second, and more generally, the importance of precisely estimating the systematic errors on the yield diminishes with higher $m_T - m_0$. This is the case because the majority of the yield occurs at low transverse mass and any interesting dynamics imparted to the particles by the expanding overlap region will affect low momentum particles much more than high momentum particles. Hence, understanding the systematics of the low transverse mass region is of greater importance for understanding the spectral shape.

7.7.2 Systematic Error on the Corrected Yield

Since we now know the systematic errors associated with the extraction of the uncorrected yield are small, it must be that the systematic errors associated with the correction procedure are the larger of the two. This too is unsurprising since each correction is model dependent, relying either on the detector and track reconstruction model or a particle production model or both. It is also worth noting that the corrections are not independent of each other. The location of the transverse mass in a particular bin (which has some uncertainty itself) determines where the correction curves are evaluated and hence how much of a correction is applied. The covariance between the energy loss and efficiency corrections is particularly important to model correctly in the low transverse mass range. At low transverse mass the energy loss correction can be large for kaons and protons and directly affect the magnitude of the efficiency correction, which is ultimately the largest correction to the extracted yield. The essential challenge of this process is ensuring the errors associated with each step in the correction chain are correctly propagated and that

their covariance is accounted for when applying the efficiency correction.

Simply varying each correction to its one-sigma value independently of the other corrections and repeating the process for each step in the correction chain ignores the important covariances between the corrections and will result in an error much larger than it should be. However, analytically propagating the errors through the correction chain with all of their covariances is simply not an option for an analysis in which the corrections have been parameterized for each collision energy, event configuration, particle species, centrality, and rapidity bin. Instead we employ a Monte Carlo approach to propagate the uncertainties and their covariances through the correction chain. Below we outline the methodology and describe how the correction was varied in each step.

7.7.2.1 General Methodology

We begin by developing the notation used in the methodology. The individual correction functions defined in the previous section for an individual point in a particular spectrum are abstracted into correction operators, $\mathbf{c_i}\left(\sigma_{\%}, y, m_T - m_0\right)$, where the i refers to the step index of the correction chain and the arguments refer the the centrality and kinematic bin of interest. The arguments of the operator will be dropped in future equations for brevity. The full correction chain for a single point in a particular spectrum can be written as: $\mathbf{C} \equiv \prod_i \mathbf{c_i}$. Functionally the operator is constructed so that when it is applied to the uncorrected yield of a particular bin the result is simply the corrected yield for that bin, $\mathcal{N}'_{x'}\left(\sigma_{\%}, y, m_T - m_0\right) = \mathbf{C}\mathcal{N}_{x'}\left(\sigma_{\%}, y, m_T - m_0\right)$.

Next, we define an uncorrected spectrum to be a set of k uncorrected yields, $\mathcal{S} \equiv \{\mathcal{N}_0, \ldots, \mathcal{N}_{k-1}\}$ and a corrected spectrum as a set of corrected yields, $\mathcal{S}' \equiv \{\mathcal{N}'_0, \ldots, \mathcal{N}'_{k-1}\}$. Further we define a set of correction operators as $\hat{\mathbf{C}} \equiv \{\mathbf{C_0}, \ldots, \mathbf{C_{k-1}}\}$. Then the relationship between an uncorrected spectrum and a corrected spectrum can be written as the element-wise operation: $\mathcal{S}' = \hat{\mathbf{C}} \circ \mathcal{S} = \{\mathbf{C_0}\mathcal{N}_0, \ldots, \mathbf{C_{k-1}}\mathcal{N}_{k-1}\} = \{\mathcal{N}'_0, \ldots, \mathcal{N}'_{k-1}\}$.

To find the systematic error associated with the correction procedure we perform the procedure for each spectrum n times. To accomplish this a set of n copies of the uncorrected spectrum, $\{\mathcal{S}_0 \ldots \mathcal{S}_{n-1}\}$, is constructed. The elements of the set are identical except that the transverse mass of the points in each spectrum are varied by choosing a deviate

from a Gaussian distribution that is defined to have a mean equal to the mean intra-bin transverse mass and with width equal to the statistical error on the mean. This implies that this methodology presumes that the systematic error associated with determining the intra-bin transverse mass mean is negligible. However, this is a valid presumption since the intra-bin distribution is known to be well described by an exponential and very little variation of the intra-bin mean was observed as a function of transverse mass.

Each spectrum of the set is then corrected using the correction operator as defined above which results in a set of n corrected spectra: $\{\mathcal{S}'_0, \ldots, \mathcal{S}'_{n-1}\} = \left\{\hat{\mathbf{C}}_\mathbf{0}, \ldots, \hat{\mathbf{C}}_\mathbf{n-1}\right\} \circ \{\mathcal{S}_0, \ldots, \mathcal{S}_{n-1}\}$. The correction factors within each $\hat{\mathbf{C}}_\mathbf{n}$ are varied as described below. By performing the systematic error study in this way the effect of the covariance between the steps in the correction chain are allowed to accumulate within each spectrum. Then by studying the distribution of the k corrected yields about the default value a systematic error can be ascribed.

Finally, because this method requires the repeated generation of random deviates, it is computationally intensive. To manage the computation time associated with the methodology for a large enough sample to be obtained for a precise assessment the systematic error, a multi-threaded software approach was utilized. Each spectrum in the set of uncorrected spectra was corrected in a simultaneously running thread to take advantage of the multi-core/multi-thread architecture of the workstation that was used.

An example of the results of this procedure using $n = 1000$ for the spectrum of negative pions at midrapidity from the top 5% most central events in the $\sqrt{s_{NN}} = 7.7$ GeV dataset can be seen in figure 7.9. The red points represent the spectrum as corrected with the default correction factors. What look like black bars in the main plot are in fact points of the spectra that have been corrected by varying the correction factors as described above. The spread of the points around the default value can be seen more clearly in the highlighted inset included in the plot.

The systematic error on each points in the corrected spectrum is computed as shown in figure 7.10. The difference along each axis between the default value and the values obtained from the method above for each point in the spectrum is computed and projected

along its respective axis. The mean of the absolute difference distribution is reported as the systematic error. The systematic error on the yield obtained from the study of the yield extraction, the systematic error obtained from the study of the correction method, and the statistical error on the yield are all summed in quadrature to compute the total error on the points of the spectra. Likewise, the systematic error associated with the transverse mass location of the point obtained from the correction procedure is summed in quadrature with the statistical error to compute the total error on the transverse mass location.

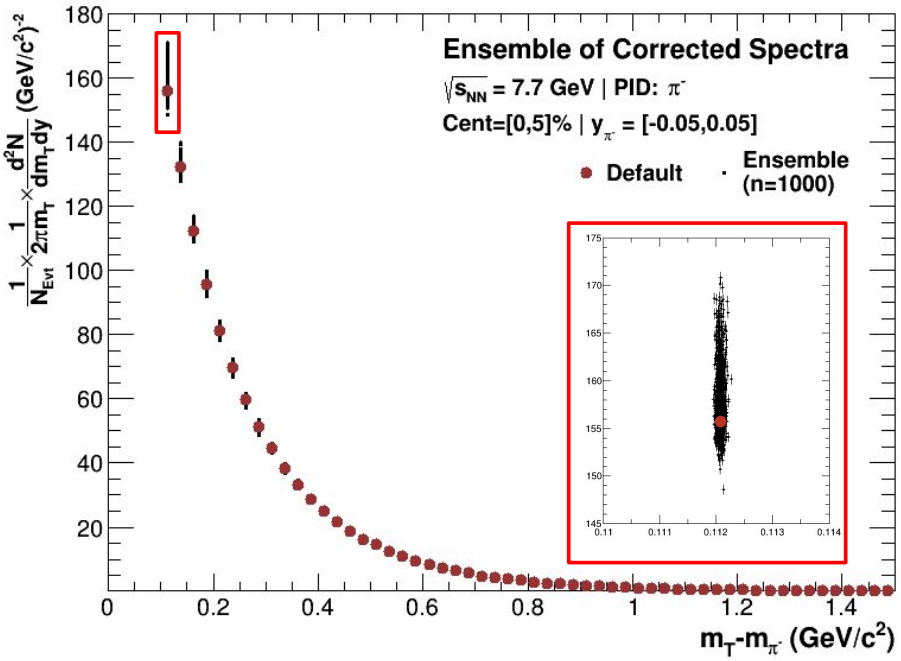

Figure 7.9: An example of a spectrum that has been corrected with the default correction values (red circles) and an ensemble of 1000 spectra that have been corrected by varying the correction values (small black points). What appears as vertical black lines in the main plot are, in fact, a cluster of points around the default value as shown in the highlighted inset. This particular example is for the spectrum of negative pions at midrapidity from the top 5% most central events in the $\sqrt{s_{NN}} = 7.7$ GeV dataset (*Center* Configuration).

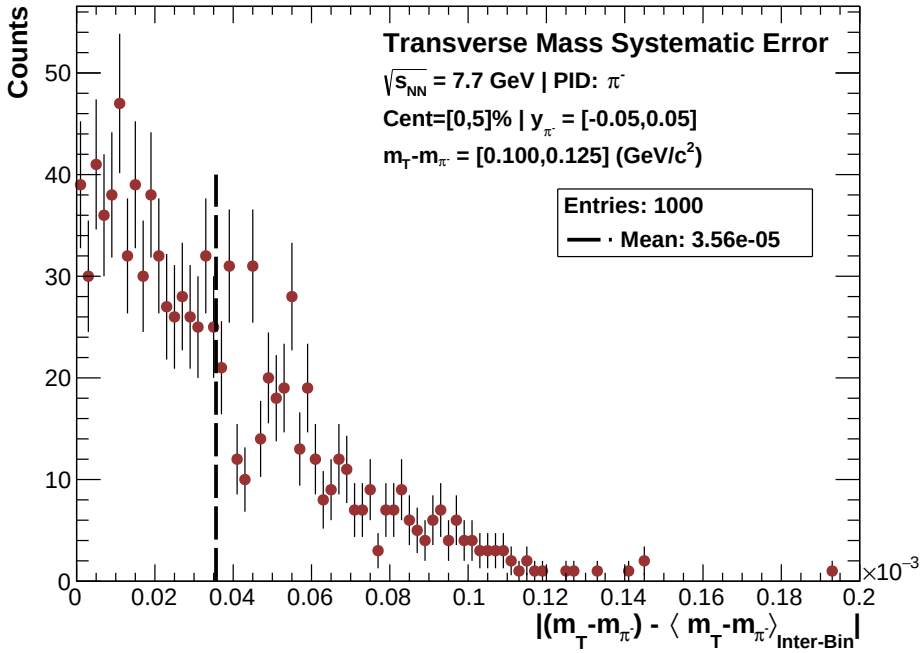

(a)

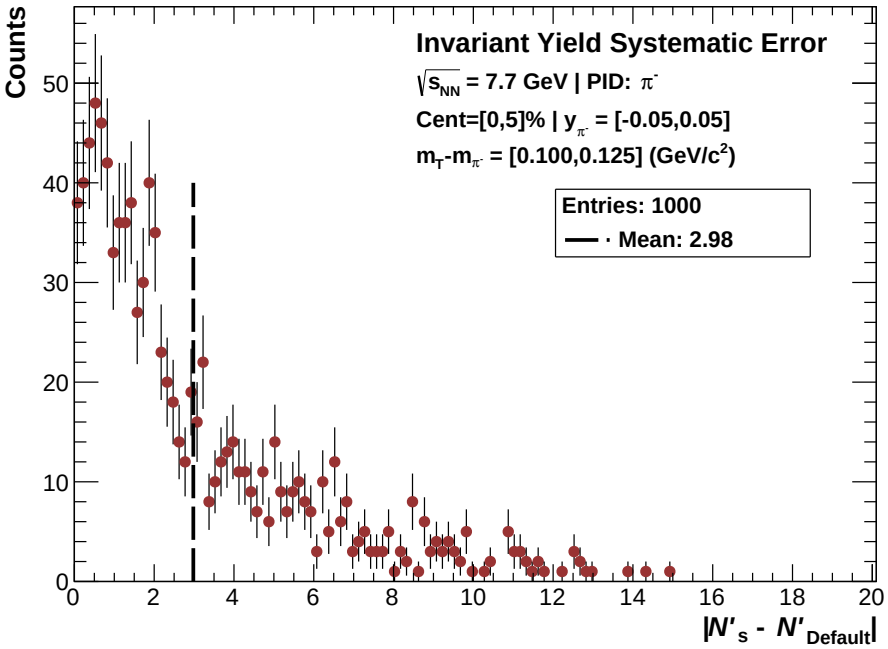

(b)

Figure 7.10: Example distributions of the absolute difference between (a) the varied $m_T - m_0$ value and the intra-bin transverse mass mean and (b) the varied yield and the default yield. The distributions show the result for a single transverse mass bin at midrapidity for negative pions from the top 5% most central events in the $\sqrt{s_{NN}} = 7.7$ GeV dataset. These particular distributions are obtained from the cluster of points in the inset of figure 7.9.

7.7.2.2 Variation of Individual Corrections

As seen in chapters 5 and 6, each correction is parameterized as a function of transverse mass for each combination of energy, event configuration, centrality, particle species, and rapidity bin. In addition to the default parameterization a second parameterization may exist when the errors permitted two models to describe the data equally well. Further, each parameterization has an associated one-sigma confidence interval. Below, when we say statements of the form "a value was chosen from the confidence interval" we mean the following. The fit curve associated with the confidence interval was evaluated at the transverse mass of the spectrum point. Then a Gaussian PDF was constructed with mean equal to the value of the function and with width equal to the width of the confidence interval evaluated at the same transverse mass location. The PDF is then sampled to obtain a deviate which will be the value of the "varied" correction factor. By sampling from a PDF defined by the width of the confidence interval we propagate the statistical uncertainty on the correction parameterization through to the systematic uncertainties on the spectral points. The following is a brief discussion of the particulars associated with varying each correction factor.

The muon contamination and feed down corrections are parameterized in each bin using two different functions. The correction factor for each is varied by first choosing with equal probability one of the functions and then choosing a value from the functions confidence interval to be the correction factor. In the case of the protons, the knockout proton background was included in the feed down correction curve and thus no additional variation is needed.

No other functional form was found that was able to describe the energy loss correction as well as the one shown. Thus the correction factor is varied for the finite bin width correction by selecting a value from the confidence interval independently at the transverse mass value associated with the lower and upper bin edges. Likewise the energy loss correction factor is varied by choosing a value from the confidence interval at the transverse mass of the spectrum point.

Rather than use a different functional form to parameterize the efficiency correction,

two sets of parameters were used. The first set of parameters contained fixed values which were obtained from the iterative procedure explained in the text. The second set of parameters was obtained without fixing the fit parameters to assess the systematic error associated with the iterative procedure. The efficiency correction factor is varied by selecting one of the two sets of parameters with equal probability and choosing a value from the confidence interval associated with that fit result. Note that in either case the value of the transverse mass that is used to select the new correction factor is the transverse mass value resulting from the energy loss correction in the previous step. This allows the correction procedure to assess the covariance between the corrections.

Chapter 8

Results and Analysis

In this chapter the main results of the analysis, namely the yields of pions, kaons, and protons, are presented. The particle yields for each combination of energy, event configuration, centrality, particle species, rapidity, and transverse mass bin are shown in the form of transverse mass spectra in section 8.2. The spectra are then fit with a thermal production model which is integrated to obtain the dN/dy - the yield of particles in each rapidity bin - and are presented as rapidity density distributions in section 8.3. Finally, for the case of the pions and kaons the full phase space yields (4π yields) are shown in section 8.4. We begin by discussing the particulars of the treatment of each particle species in the first sections. Then, in the last sections of the chapter, we interpret the results by analyzing the spectra and their fits in the context of results reported by previous experiments.

Note, as well, that at this point the displaced event configurations, $PosY$ and $NegY$, were deemed to not add sufficient value to the analysis to warrant their continued inclusion. Thus, they were dropped from the analysis and the results presented here pertain only to the *Center* configuration.

8.1 Spectral Model Fits

To extract the yield of each particle species in each rapidity bin we require a method to account for the particles that were produced in the regions of kinematic phase space that are not represented in the measured transverse mass spectra. In particular, it is necessary to account for the particles that are produced with such low transverse mass

that their curvature in the magnetic field disallows them to penetrate deep enough into the fiducial volume of the detector to be measured. Further, it is also necessary to account for the tracks which have high transverse mass and whose rarity prevents a statistically significant sample and thus a direct measurement. In other words a spectral fit function is required for each particle species which will allow for extrapolation to low and high transverse mass. This function can then be integrated to obtain the full yield for each particle species in each rapidity bin.

To zeroth order particle production in heavy-ion reactions can be modeled as thermal emission. This simple model is justified by observing that the transverse mass spectra of all the particles of interest fall roughly exponentially over several orders of magnitude. However, the properties of each particle species and how they are affected by the expanding nature of the medium produced in the heavy-ion reaction result in important modifications to their spectral shape and hence are an important contributor to the accounting of their total yield. In the following subsections we discuss these properties and our choice of spectral shape for each species.

8.1.1 General Fit Methodology

To impose some control over the shape parameters of the spectral functions, we take advantage of the symmetry of the colliding system of nuclei and their beam energies. These two symmetries and conservation of energy and momenta require that the resulting transverse mass spectra be equivalent in equal forward/backward rapidity ranges. To impose this requirement we perform a simultaneous fit of the spectra in each forward/backward rapidity bin where the parameters controlling the shape of the spectra are shared. This ensures that the spectra fits are equivalent up to a total normalization factor. The forward/backward asymmetry of the normalization factor is expressed as a forward/backward asymmetry in the dN/dy (integral) and can be used to asses the overall systematic error associated with the measurement as will be discussed below.

It should be noted that this methodology presumes that the shapes of the corrected spectra are themselves equivalent in equal forward/backward rapidity ranges. However, we observe that the resulting χ^2/NDF of the fits are generally quite good (see addenda)

indicating that this presumption is valid within the total error associated with the spectral points.

8.1.2 Pions

The transverse mass spectra of the pions exhibit a concave structure in all energy, centrality and rapidity bins. The excess at low transverse mass has previously been explained as contributions from strongly decaying resonances such as Δ baryons and ρ mesons. [74, 75] (Recall that only pions from weak decays have been removed from the spectra as part of the feed down correction in this analysis.) In such explanations the daughter pions are argued to contribute to the spectra as though they originated from an additional thermal source. Thus some authors [76] have chosen to fit pion spectra using a "double thermal" model consisting of the sum of two Boltzmann distributions; one distribution which has an effective temperature to describe the low transverse mass region and another which describes the high transverse mass region.

The contribution of the pions from strong resonances as a fraction of the total number of pions is expected to decrease with increasing collision energy. However, we observe the concavity of the spectra across all collision energies. Thus at least one additional effect must be present to explain the low transverse mass excess. The integer spin characteristic of the π^+ and π^- mesons suggests that Bose-Einstein statistics should underpin the model used to fit their spectra and the low transverse mass shape of the Bose-Einstein function (equation 8.1) lends itself as a natural description of the shape of the spectrum. Indeed, previous analyses ([73, 39]) in this collision energy range have used a Bose-Einstein function to successfully fit pion spectra. We too find that a Bose-Einstein function is a good description of the pion spectra and so employ it as the nominal method of fitting the pion spectra and obtaining the pion yield in each rapidity bin. As was done in [39], we use a pT-exponential function (equation 8.2) as an alternative means of obtaining the pion dN/dy so that the systematic error due to the extrapolation can be investigated.

$$f_{\mathrm{BE}}(m_T - m_0) = A\frac{1}{\exp(m_T/T) - 1} \tag{8.1}$$

$$f_{p_T}(m_T - m_0) = A\frac{1}{\exp(p_T/T)} \tag{8.2}$$

Previous analyses have found that the rapidity dependence of the slope parameter, T, of the $\pi^{\pm}$ spectra is well described by a Gaussian. As shown in figures 8.1 and 8.2, we also find this to be the case. Thus to limit the bin-to-bin fluctuations of the extracted dN/dy in rapidity we parameterize the slope parameter with a Gaussian after a first round of fitting and then fix the parameter in the second round. The dN/dy value is obtained from the spectra after the second round of fitting. The systematic error associated with this choice is considered to be negligible because it is within the range of covariance with the normalization parameter.

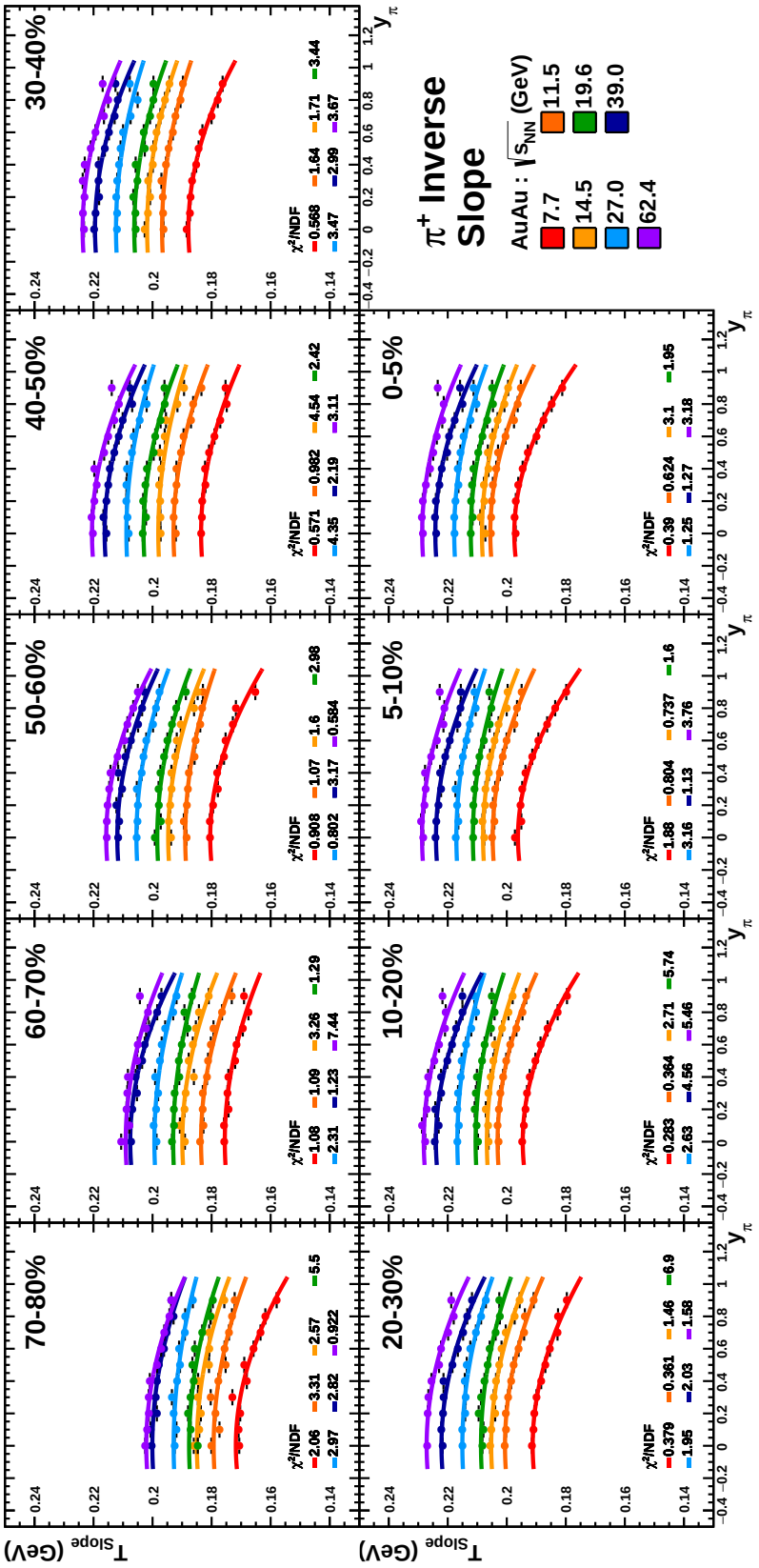

Figure 8.1: Temperature Parameter: π^+ ColliderCenter All Energies

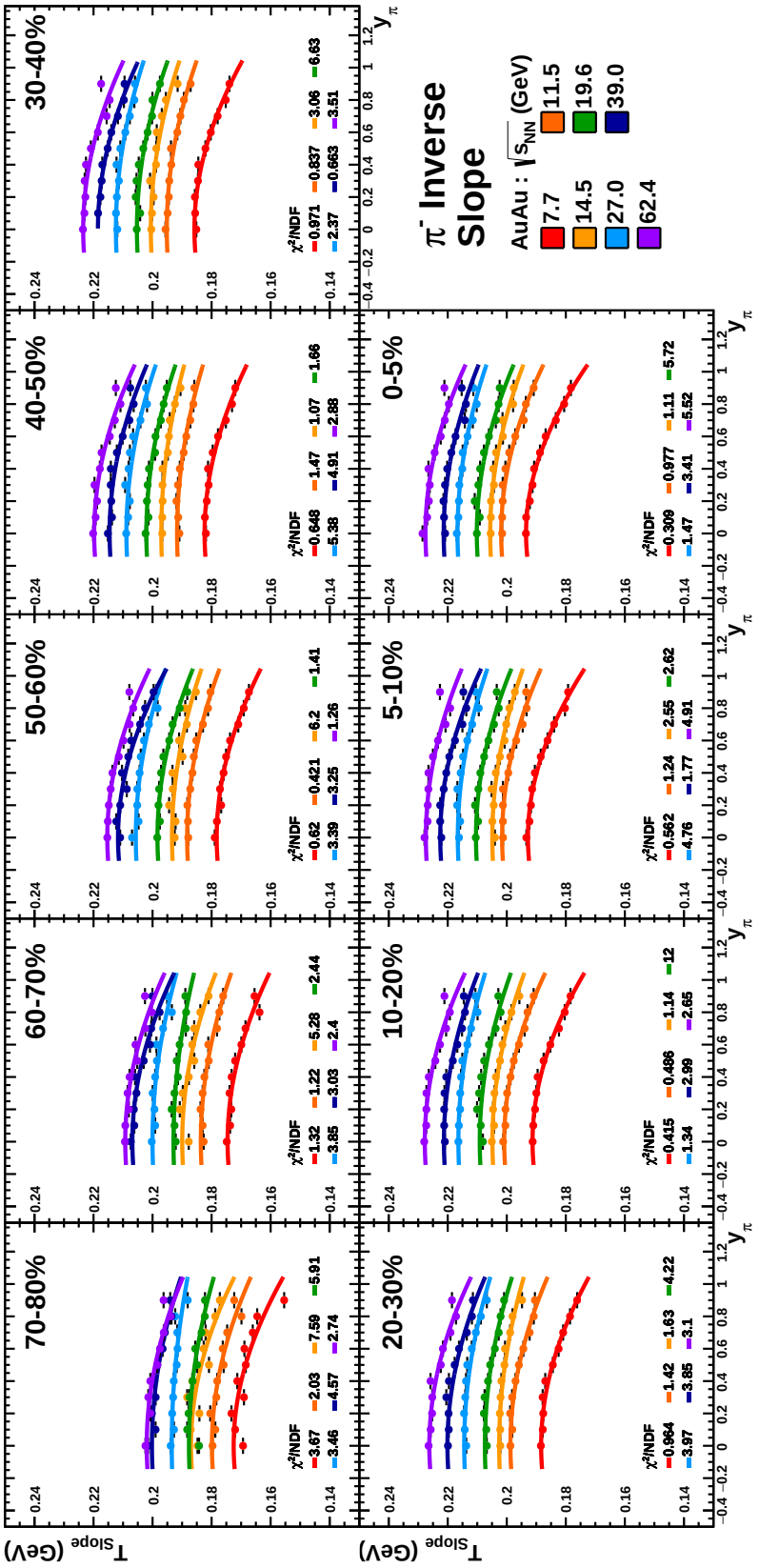

Figure 8.2: Temperature Parameter: π^- ColliderCenter All Energies

8.1.3 Kaons

Like the pion, the kaon meson has integer spin and is therefore a boson. Unlike the pion, however, the kaon spectra does not have a significant contribution from resonances and thus it is found to be well described by m_T-exponential (equation 8.3) and Boltzmann (equation 8.4) functions. The first is used to extract the nominal yield and the second is used to assess the systematics associated with the extrapolation to the unmeasured regions.

$$f_{m_T}(m_T - m_0) = A\frac{1}{\exp((m_T - m_0)/T)} \tag{8.3}$$

$$f_{\text{Boltz}}(m_T - m_0) = A\frac{m_T}{\exp(m_T/T)} \tag{8.4}$$

Also, like the pion, the rapidity dependence of the kaon temperature is parameterized as a function of rapidity. However, unlike the pion, the rapidity dependence of the temperature is found to be sufficiently well described by a constant. As before, two rounds of fitting are used. In the first round the temperature parameter is extracted and then parameterized. Then, in the second round, the temperature parameter is fixed and the dN/dy is extracted.

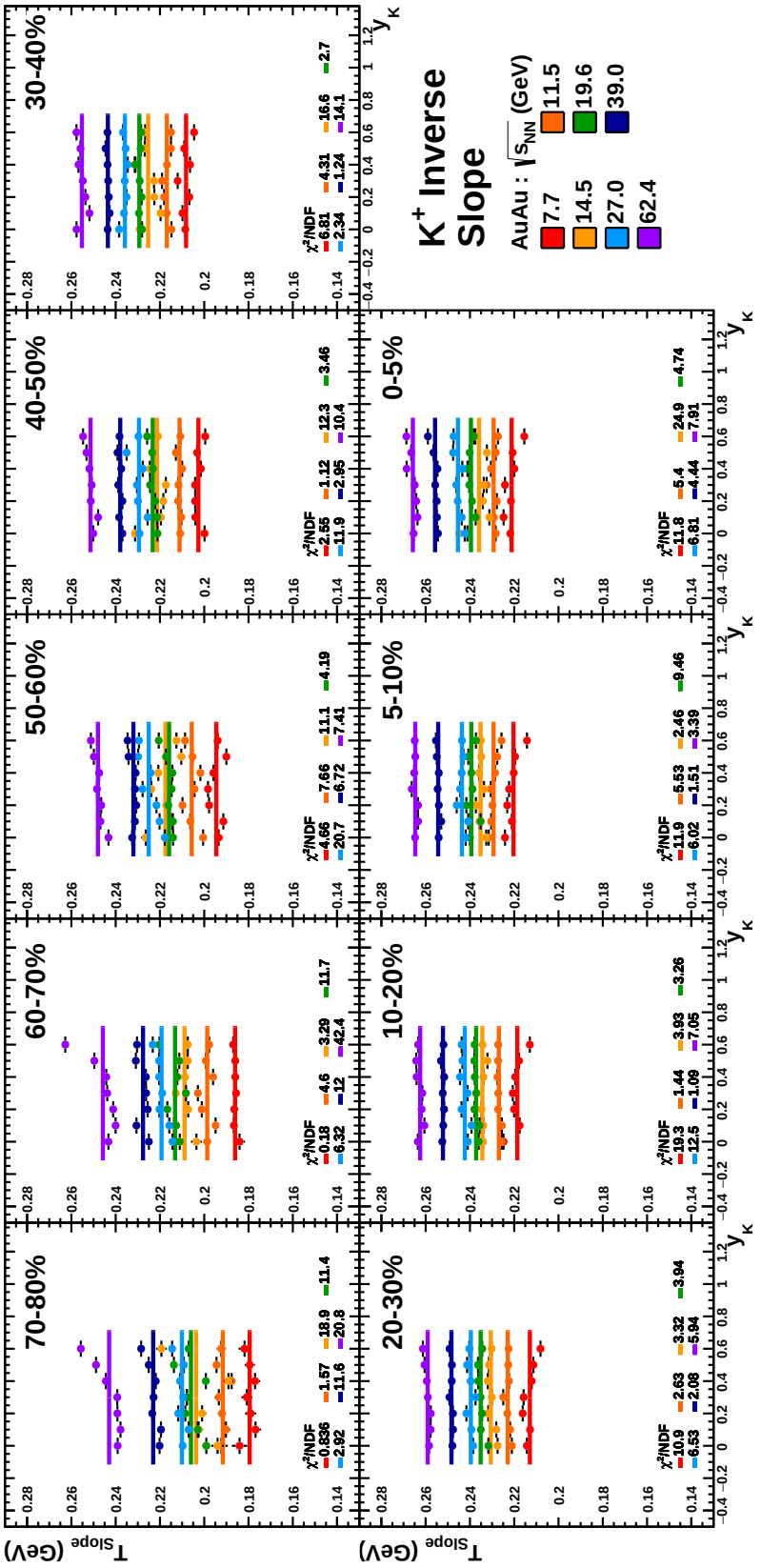

Figure 8.3: Temperature Parameter: K^+ ColliderCenter All Energies

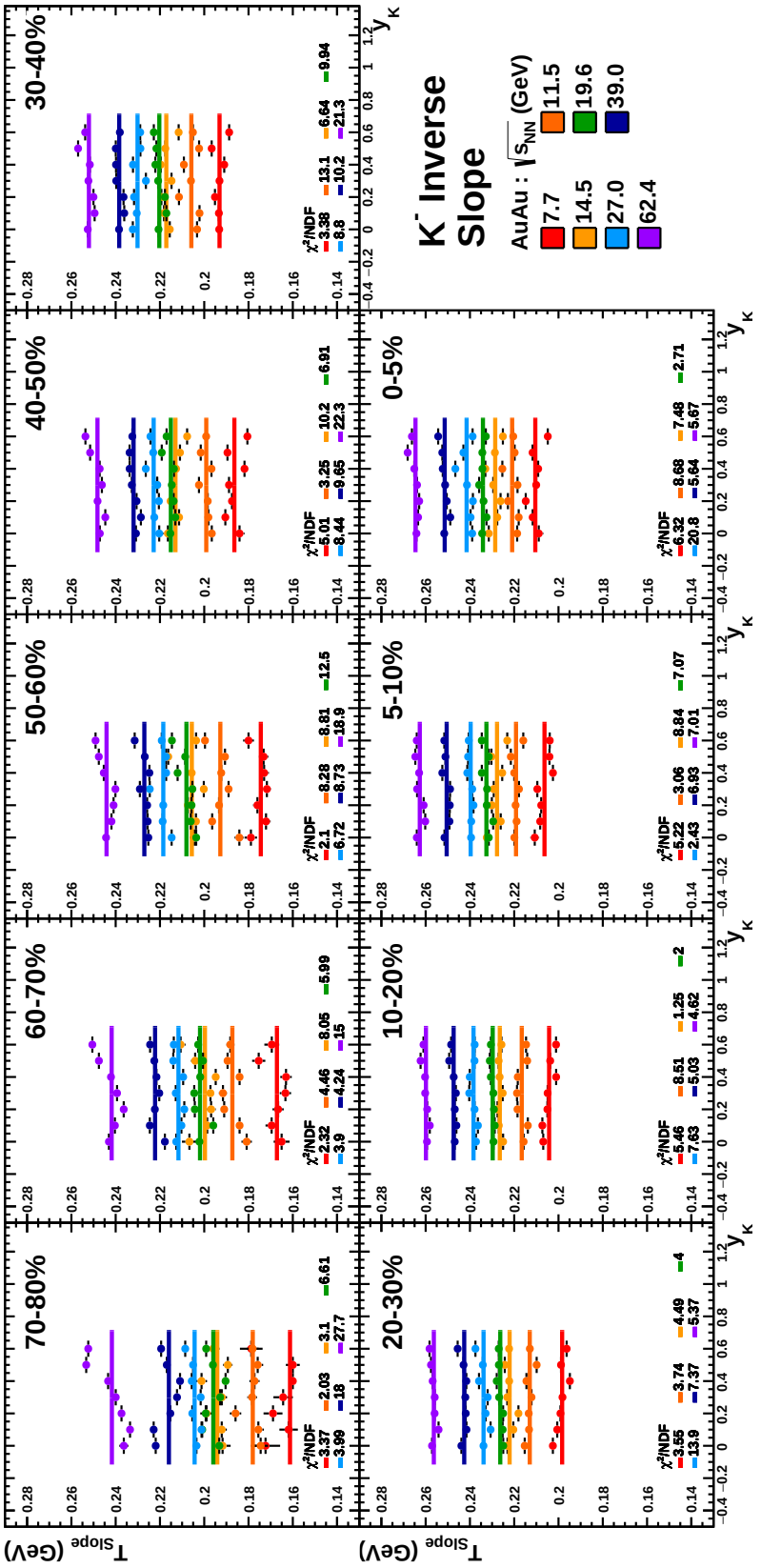

Figure 8.4: Temperature Parameter: K^- ColliderCenter All Energies

8.1.4 Protons

The proton spectra exhibit convex curvature (downward curve) in the low transverse mass region. This is due to the affects of radial flow. Radial flow is the zeroth component of the Fourier expansion that was discussed in the introductory chapter in the context of elliptical and directed flow. It describes the azimuthally symmetric outward change in momentum resulting from the pressure gradients formed in the initial overlap region of the heavy-ion collision. Radial flow affects particles of all species, but it is most consequential to the shape of protons because of their relatively large mass. Further, the effect is centrality dependent as it is strongest in the most central collisions and diminishes in peripheral collisions.

The effect of radial flow makes a purely statistical description of proton production incomplete. Previous authors have used double exponential functions [39] to capture the curved structure, but the meaning of the parameters in the first exponential are not physically motivated. This makes them difficult to constrain and interpret as they vary with rapidity and centrality. Fortunately, various *blast wave models* have been successfully used to describe the shape of the proton spectra and so we use them here. The two models used to fit the proton spectra are the Heinz, Schnedermann, Sollfrank model [77], sometimes simply referred to as the "Blast Wave Model," and the Siemens and Rasmussen model [78]. To avoid confusion, we will refer to them respectively as the HSS model and SR model in this text. In general, blast wave models aim to capture the effect of radial flow on the spectra by incorporating a radial velocity. The two models used here differ in their treatment of the radial velocity and in the assumptions about the symmetries of the expanding source.

The SR model (equation 8.5) assumes that the expansion of the system can be treated as being spherically symmetric and with single radial velocity β. The quantity T is the effective temperature of the expanding source, the quantity γ is the Lorentz factor, $\gamma = 1/\sqrt{1-\beta^2}$, and the quantity α is defined as $\alpha = \gamma\beta p/T$, where p is the momentum. Note that this has the convenient property that in the limit of $\beta \to 0$, the functional form becomes a Maxwell-Boltzmann distribution. The behavior in the limit of no radial flow is

important to capture the thermal shape of the spectra in the most peripheral collisions.

$$\frac{d^2N}{m_T dm_T dy} = A\exp(-\gamma E/T)\left(\frac{\sinh(\alpha)}{\alpha}(\gamma E + T) - T\cosh(\alpha)\right) \tag{8.5}$$

The HSS model (equation 8.6), on the other hand, assumes cylindrical expansion motivated by a boost-invariant midrapidity region. It is constructed, conceptually, by envisioning many thermal sources boosted in the region near midrapidity. In this case the radial velocity becomes a transverse velocity in the cylindrical coordinate system and is described by a radially dependent velocity profile, $\beta_T(r) = \beta_s\left(\frac{r}{R}\right)^n$. The quantity R represents the radial distance to the surface of the expanding fireball. The exact quantity chosen for R is irrelevant and so it is set to unity. The quantity r represents the distance from the center of the fireball and must satisfy the condition $0 \leq r \leq R$. It is not a fit parameter, but is used only to compute the integral. When $r = R$ then $\beta_T = \beta_s$ and so β_s is the surface velocity.

$$\frac{d^2N}{m_T dm_T dy} = A\int_0^R r dr m_T \times I_0\left(\frac{p_T \sinh\rho(r)}{T_{Kin}}\right) K_1\left(\frac{m_T \cosh\rho(r)}{T_{kin}}\right) \tag{8.6}$$

The quantity n controls the shape of the transverse velocity profile. Previous analyses, which have focused at midrapidity [39], have allowed n to be a free parameter in the fit. However, the quantity exhibits large errors and unexpected trends as a function of energy and centrality. Rather than allow it to be free we fix the parameter to $n = 0.5$ which permits an excellent description of the data across all centralities, rapidities, and energies. The function $\rho(r)$ is defined as the boost angle and is given by $\rho(r) = \tanh^1\beta_T(r)$. Finally, the functions I_0 and K_1 are modified Bessel functions of the first and second kind respectively.

The quantity T_{kin} is interpreted as the temperature of the system at kinetic freeze out. In keeping with the model's assumption that the source is a cylindrically expanding fireball, T_{kin} is fixed at all rapidities to be the value obtained from fitting the midrapidity spectrum. The surface velocity is left as a free parameter of the fit and only constrained to be in the physical range $0 \leq \beta_s \leq 1$. This is because it affects the boost angle which could

vary as a function of centrality or energy. Further, to reduce the error associated with extracting the anti-proton yield, the proton and anti-proton spectra are fit simultaneously such that they share all of the same parameters with the exception of β_s and the overall normalization constant,A.

Because the HSS model contains a more physically-realizable velocity profile (as opposed to single velocity as in the SR model) it is used as the nominal model to extract the yields of protons and anti-protons in this analysis. The SR model is used to assess the systematics associated with the extrapolation to the unmeasured regions. Note that in the case of the SR model no parameterization as a function of rapidity for any of the fit parameters is used.

8.2 Transverse Mass Spectra

In this section the complete library of transverse mass spectra obtained in this analysis is presented. Each third of the section contain the spectra for the $\pi^{\pm}$, $K^{\pm}$, p, and $\bar{p}$ respectively. Within each third the collision energies increase from least to greatest. Each page of the section contains a plot with nine panels - one for each of the nine centrality bins. The percent centrality is denoted in the top right of each panel. Within each panel are the transverse mass spectra obtained at each rapidity bin. In all cases the midrapidity spectrum is shown in red and is unscaled. All other rapidity bins are scaled either up or down by a successive factor (see legend) depending on their distance away from midrapidity. Each spectrum is divided into two parts as denoted by the different symbol shapes. Circular symbols represent yields obtained from the TPC while square yields represent yields obtained from the TOF. As discussed in the previous sections, the curves plotted on the spectra represent the nominal functional forms that were fit to the spectra to obtain the dN/dy values.

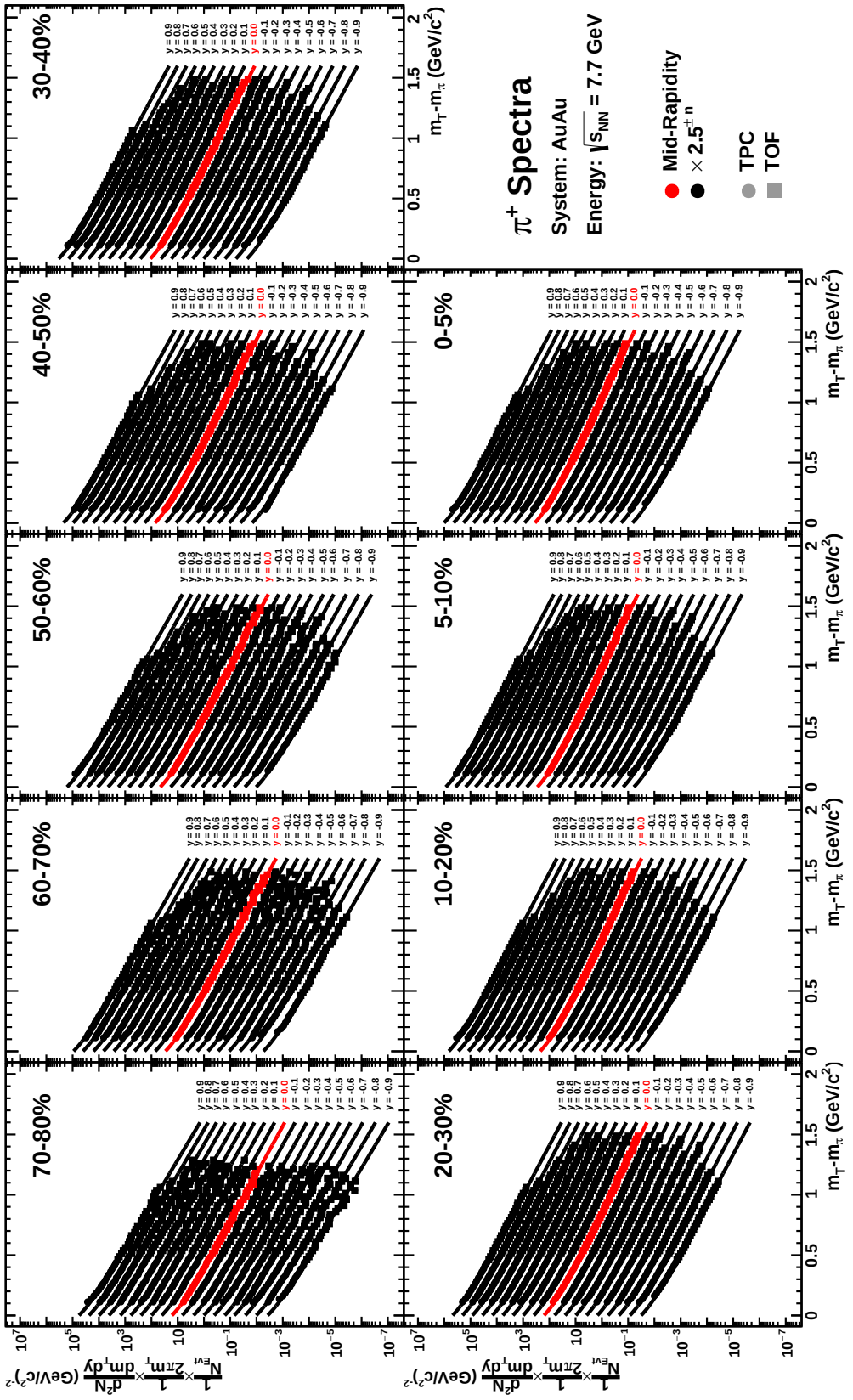

Figure 8.5: Transverse Mass Spectra: π^+ ColliderCenter $\sqrt{s_{NN}} = 7.7$ GeV

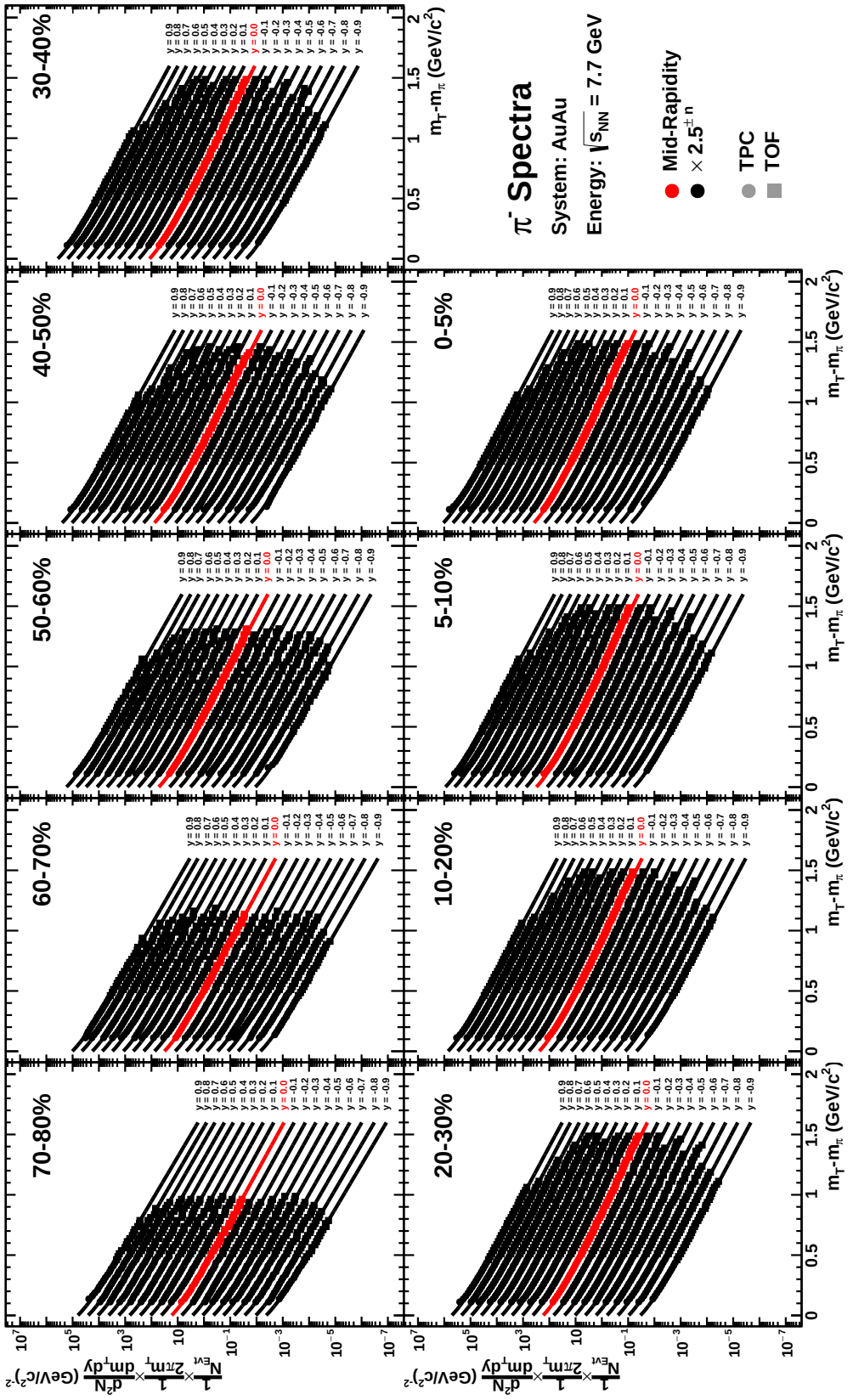

Figure 8.6: Transverse Mass Spectra: π^- ColliderCenter $\sqrt{s_{NN}} = 7.7$ GeV

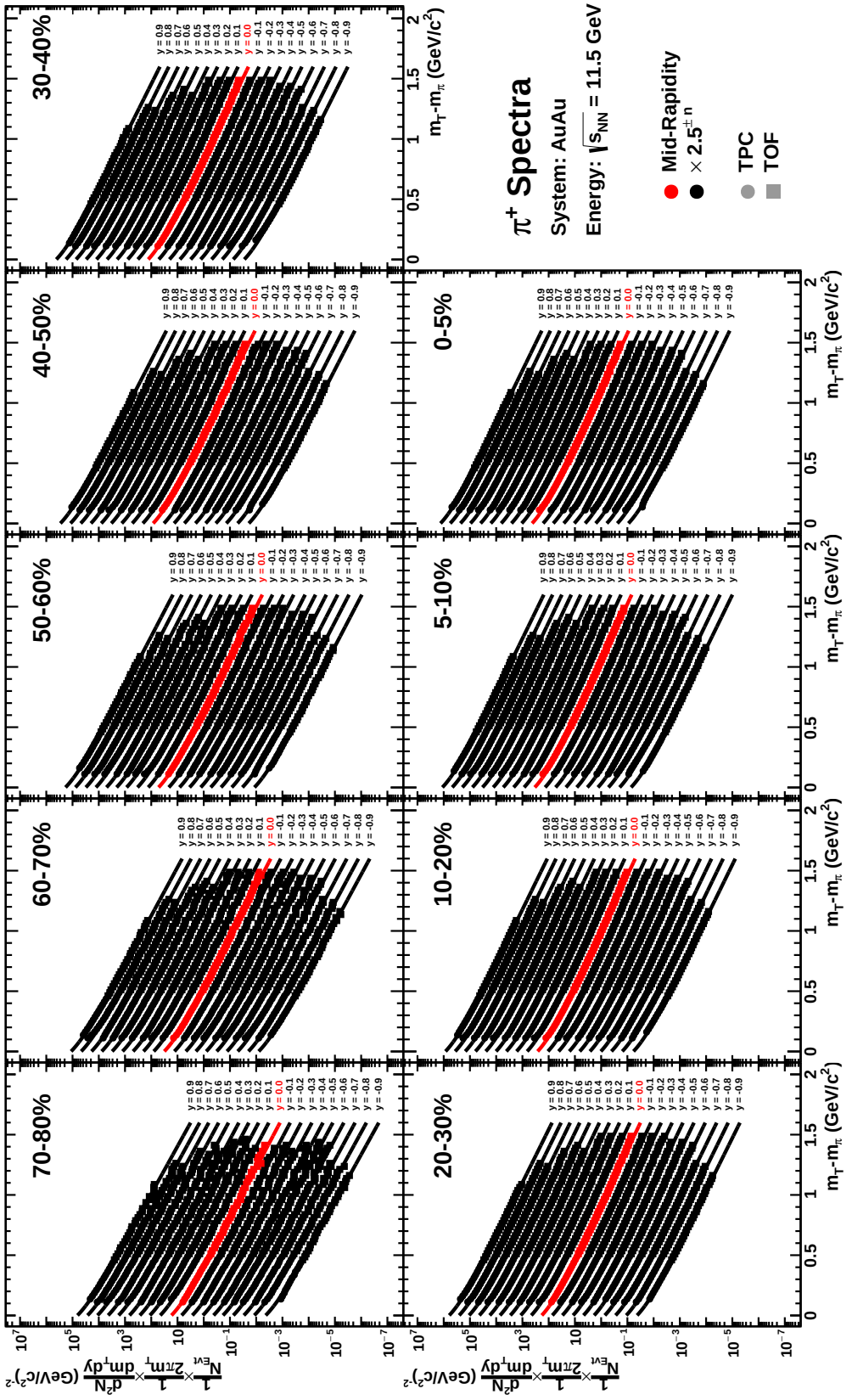

Figure 8.7: Transverse Mass Spectra: π^+ ColliderCenter $\sqrt{s_{NN}} = 11.5$ GeV

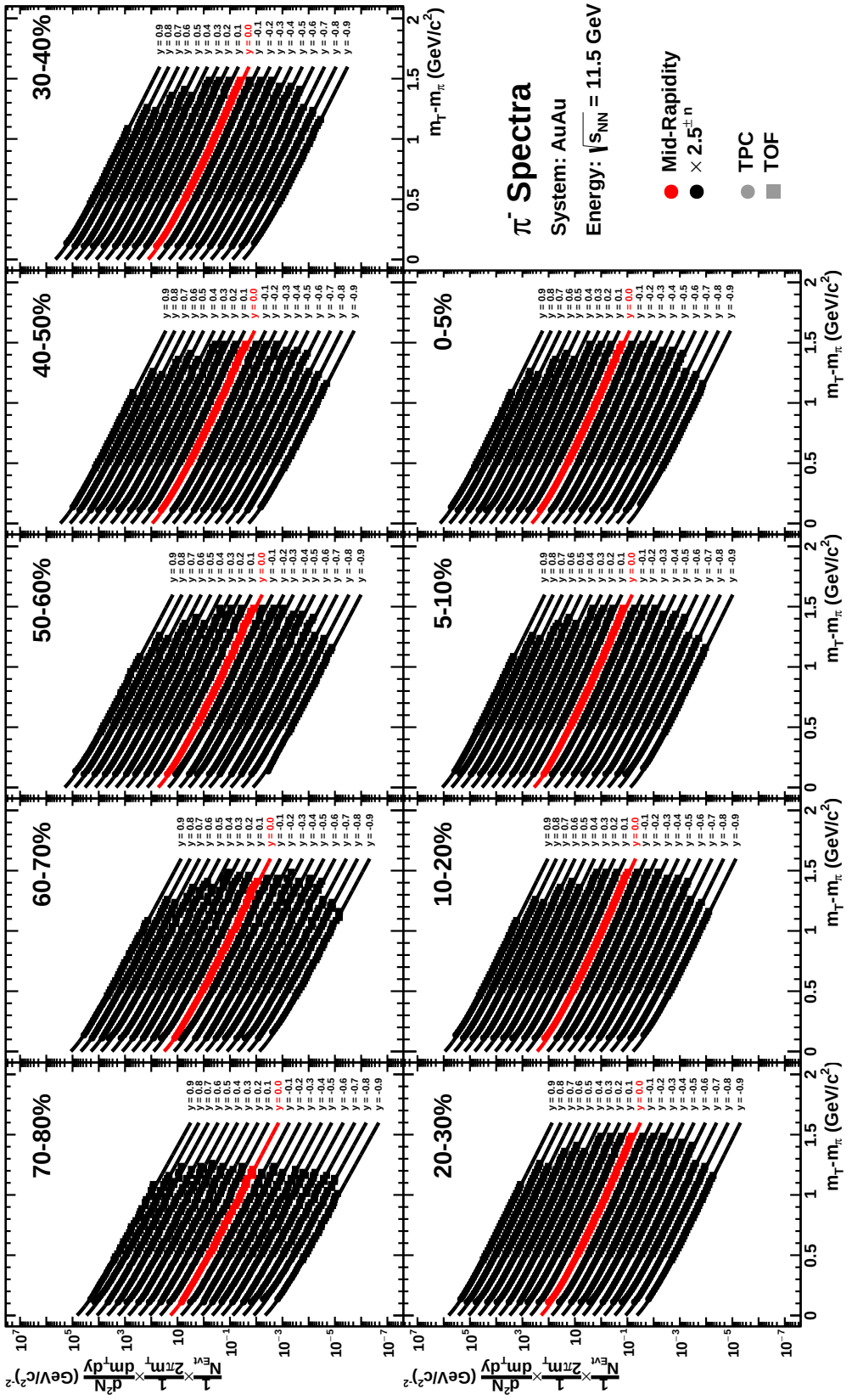

Figure 8.8: Transverse Mass Spectra: π^- ColliderCenter $\sqrt{s_{NN}} = 11.5$ GeV

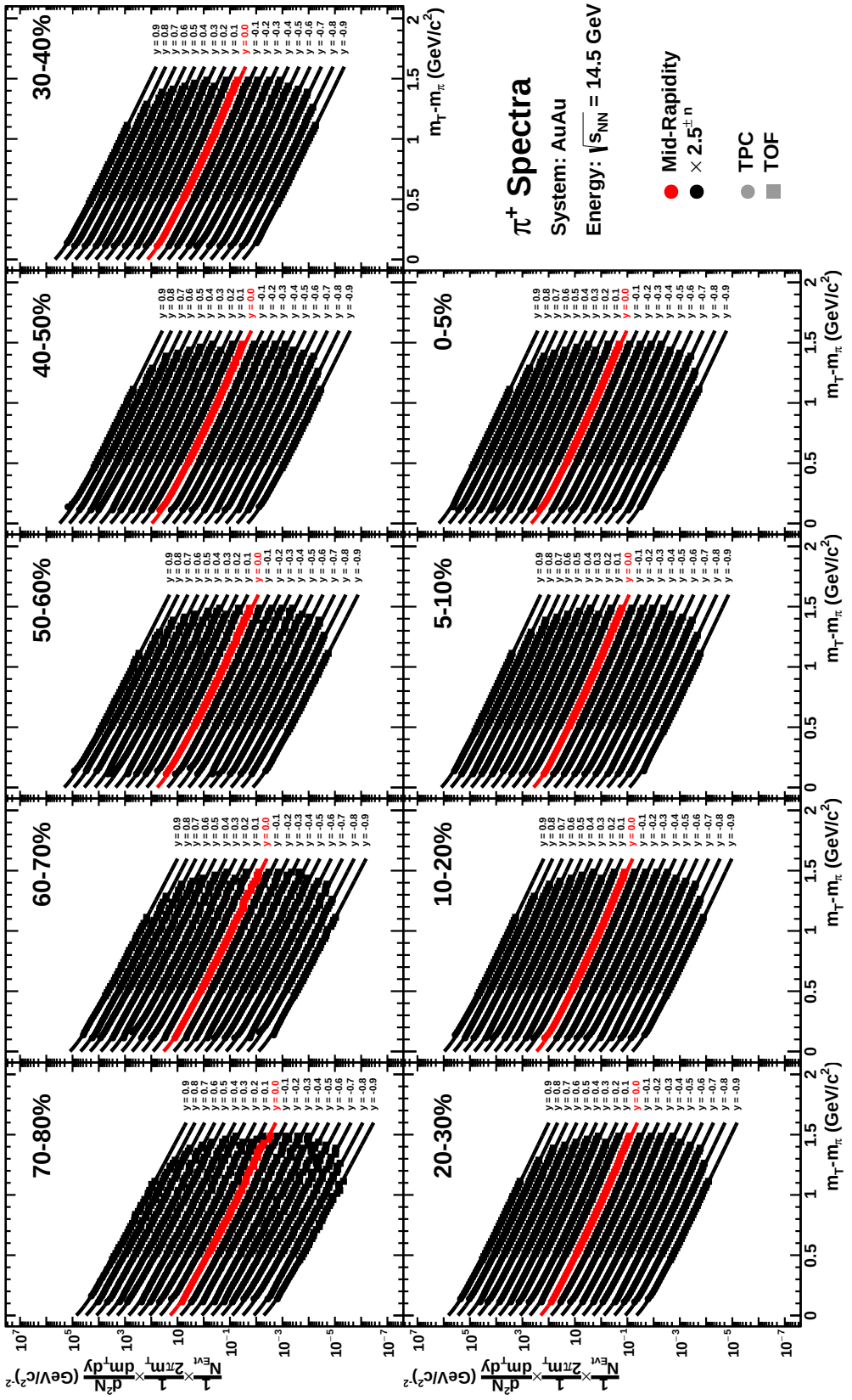

Figure 8.9: Transverse Mass Spectra: π^+ ColliderCenter $\sqrt{s_{NN}} = 14.5$ GeV

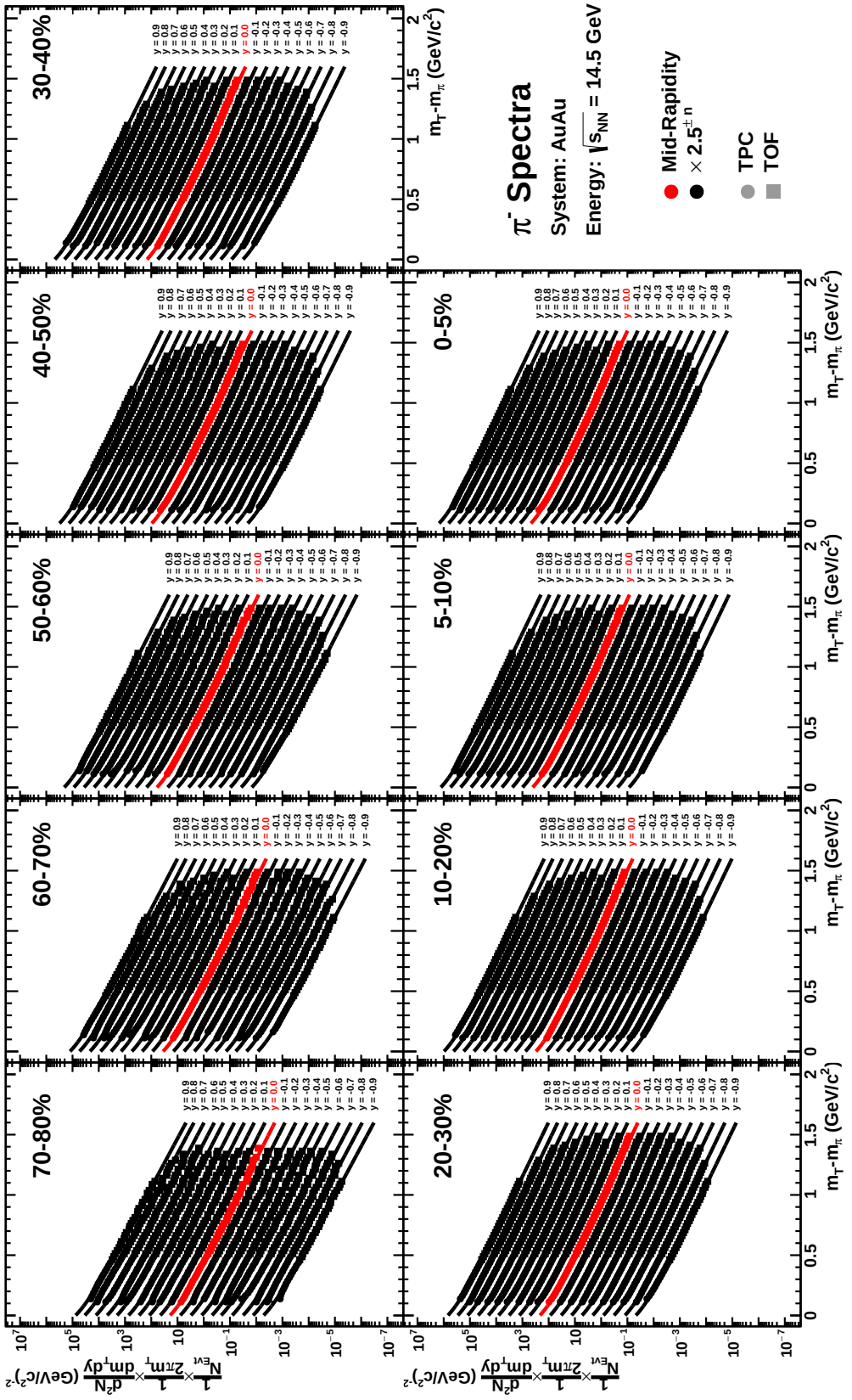

Figure 8.10: Transverse Mass Spectra: π^- ColliderCenter $\sqrt{s_{NN}} = 14.5$ GeV

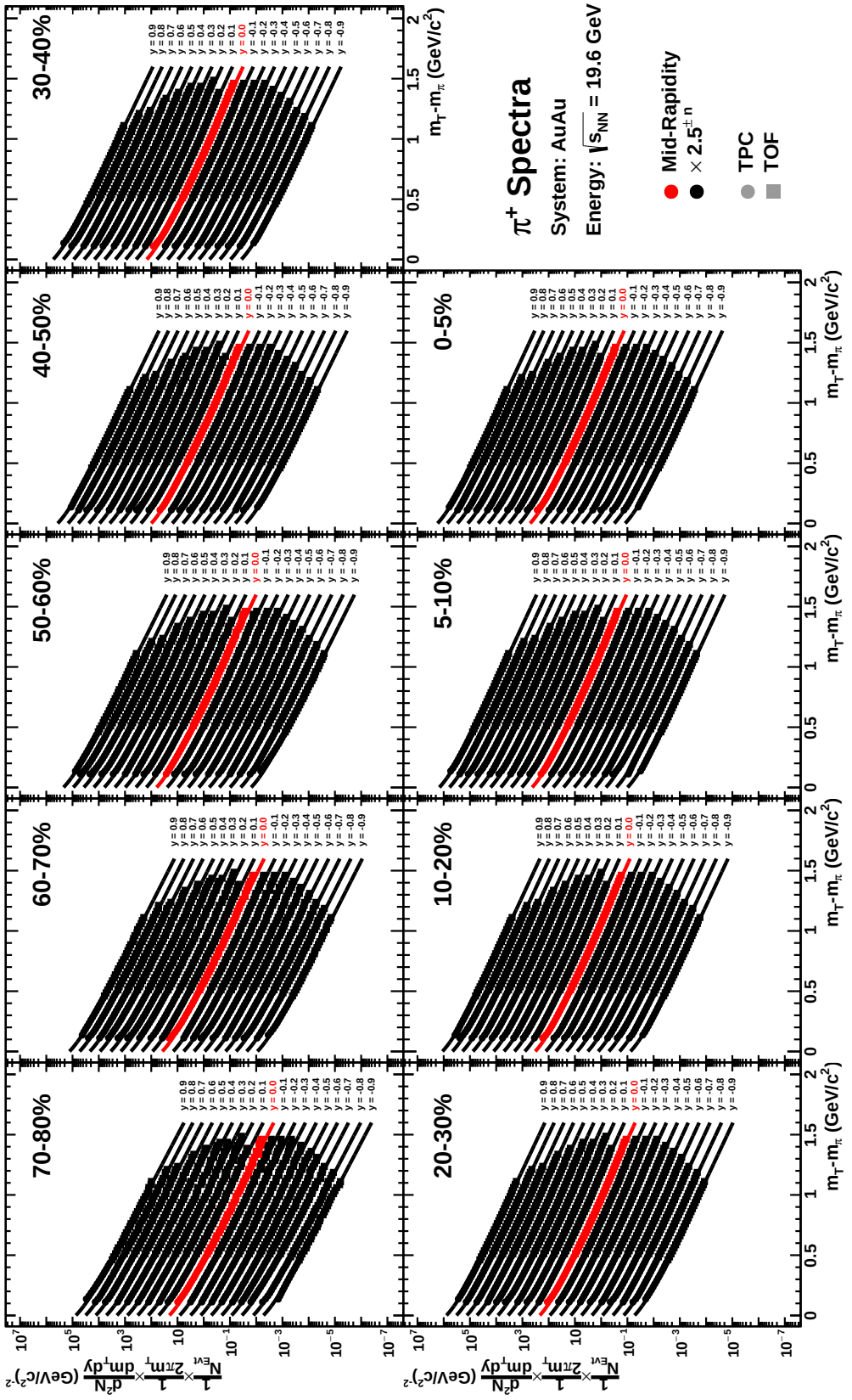

Figure 8.11: Transverse Mass Spectra: π^+ ColliderCenter $\sqrt{s_{NN}} = 19.6$ GeV

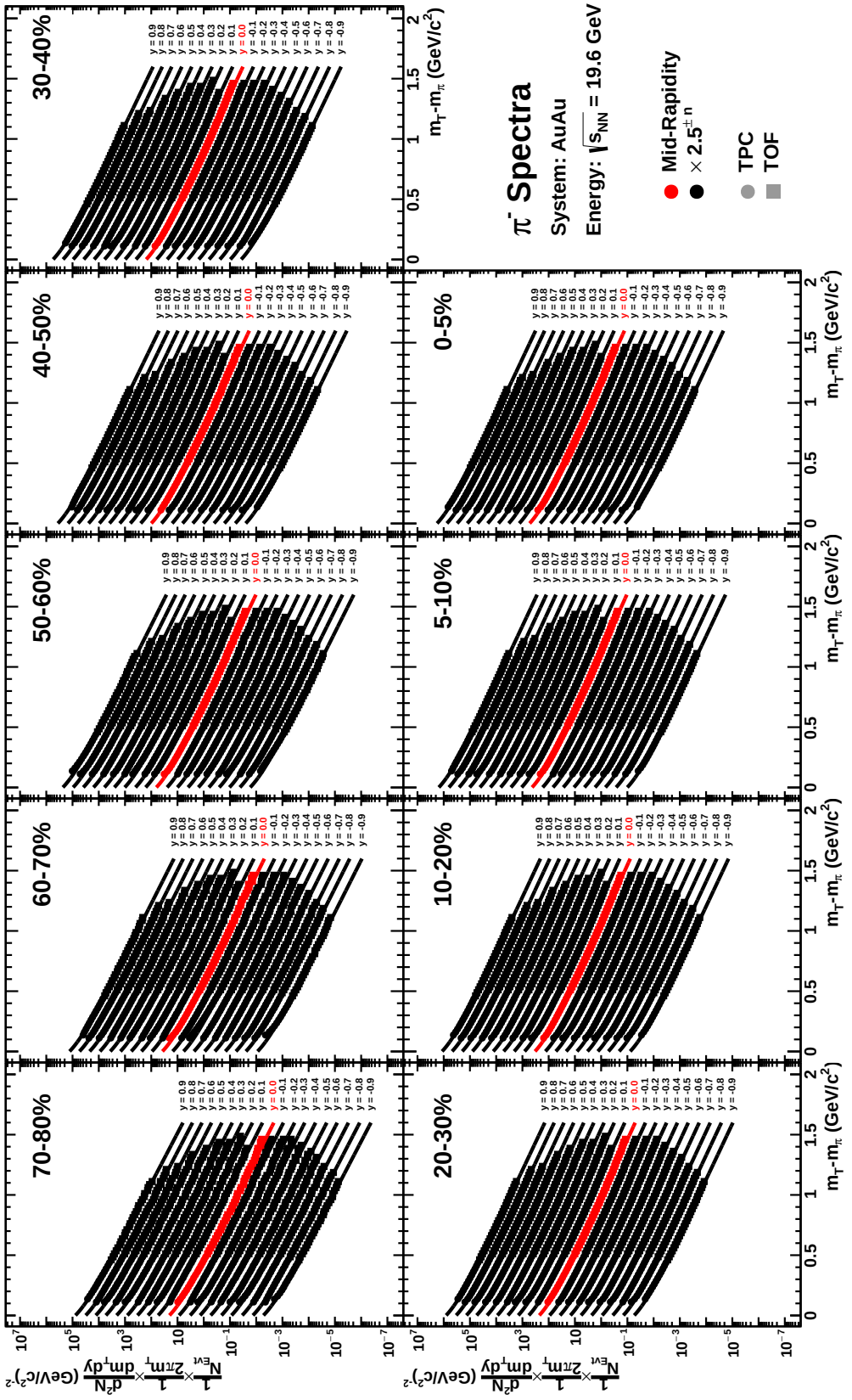

Figure 8.12: Transverse Mass Spectra: π^- ColliderCenter $\sqrt{s_{NN}} = 19.6$ GeV

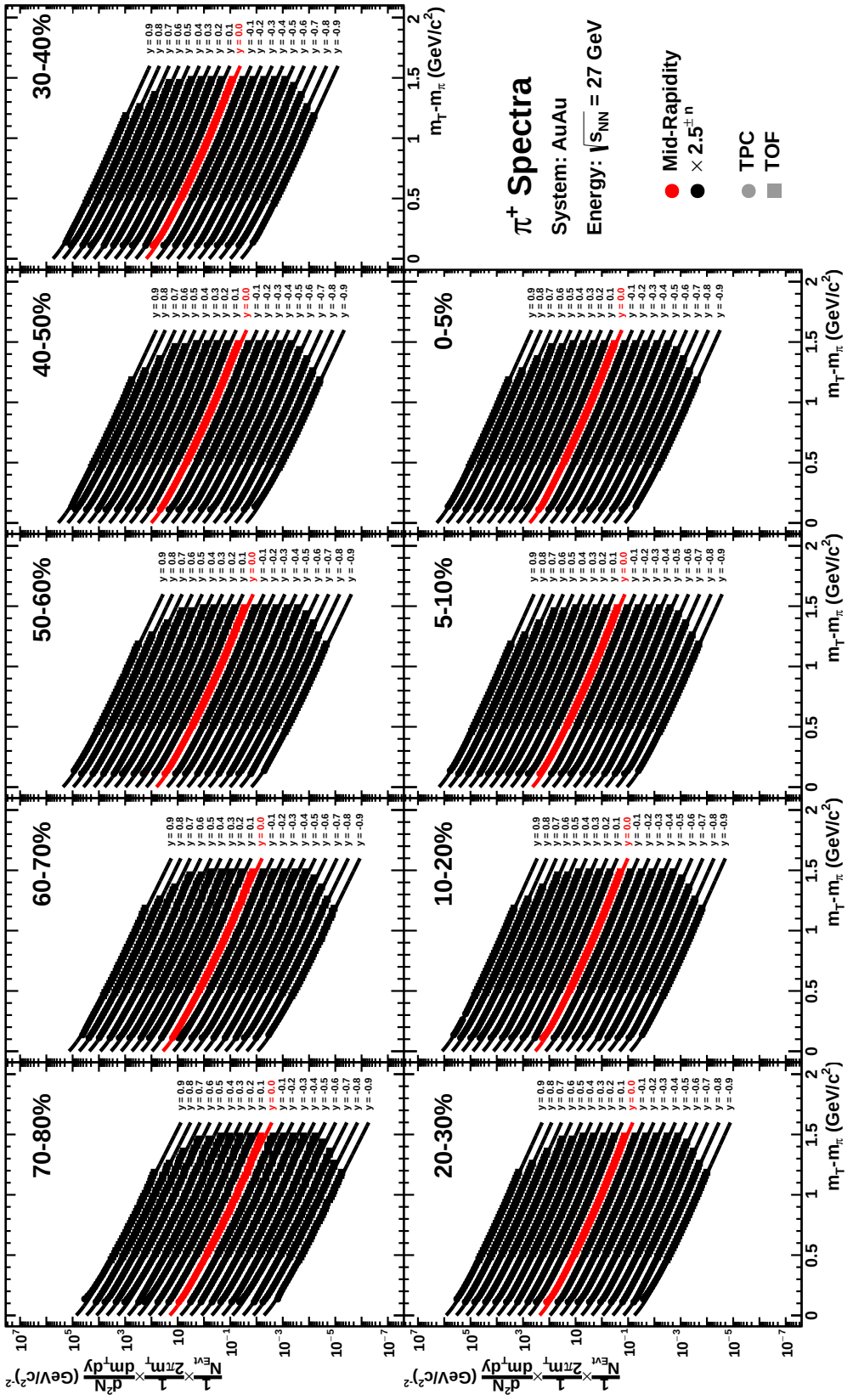

Figure 8.13: Transverse Mass Spectra: π^+ ColliderCenter $\sqrt{s_{NN}} = 27.0$ GeV

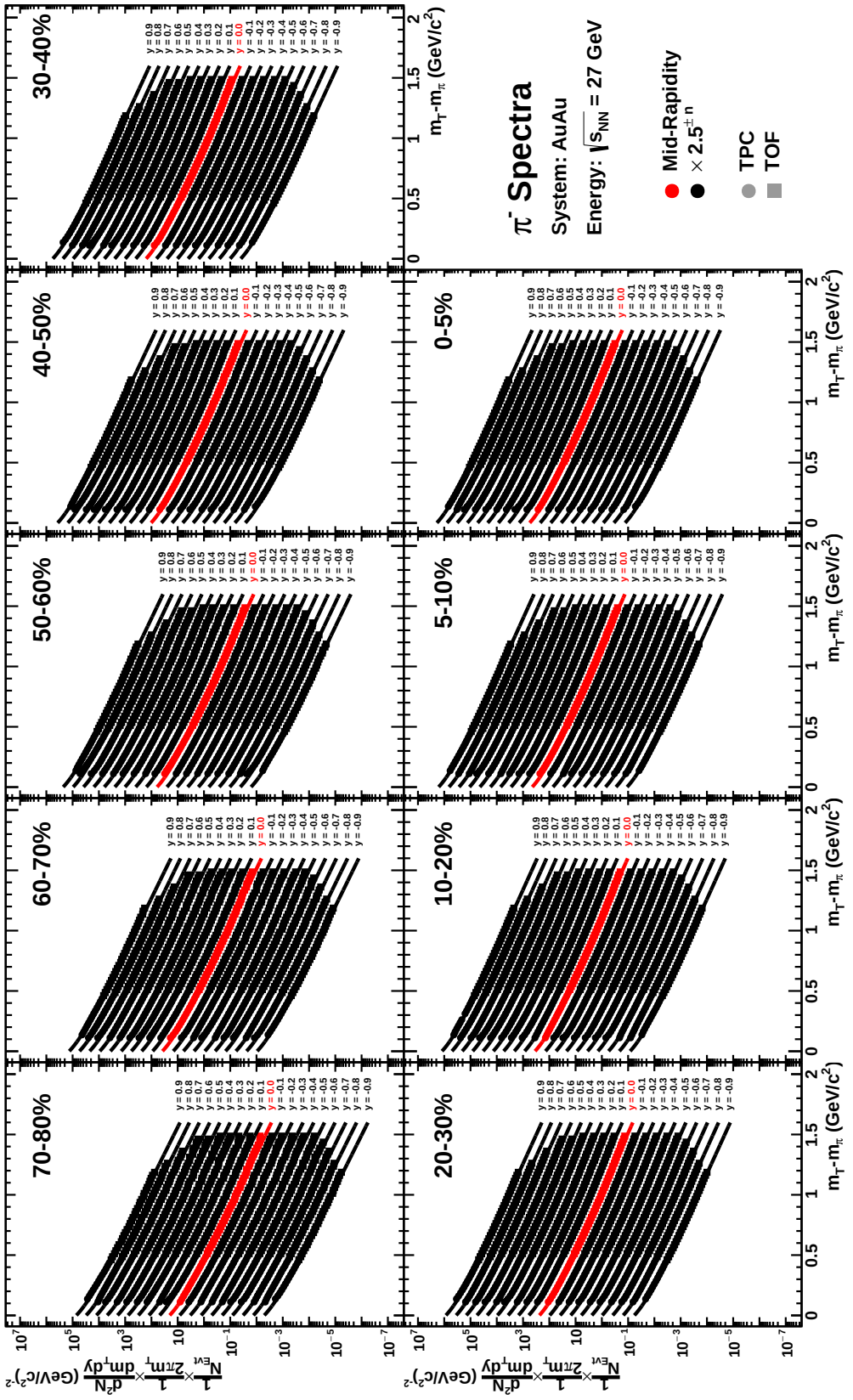

Figure 8.14: Transverse Mass Spectra: π^- ColliderCenter $\sqrt{s_{NN}} = 27.0$ GeV

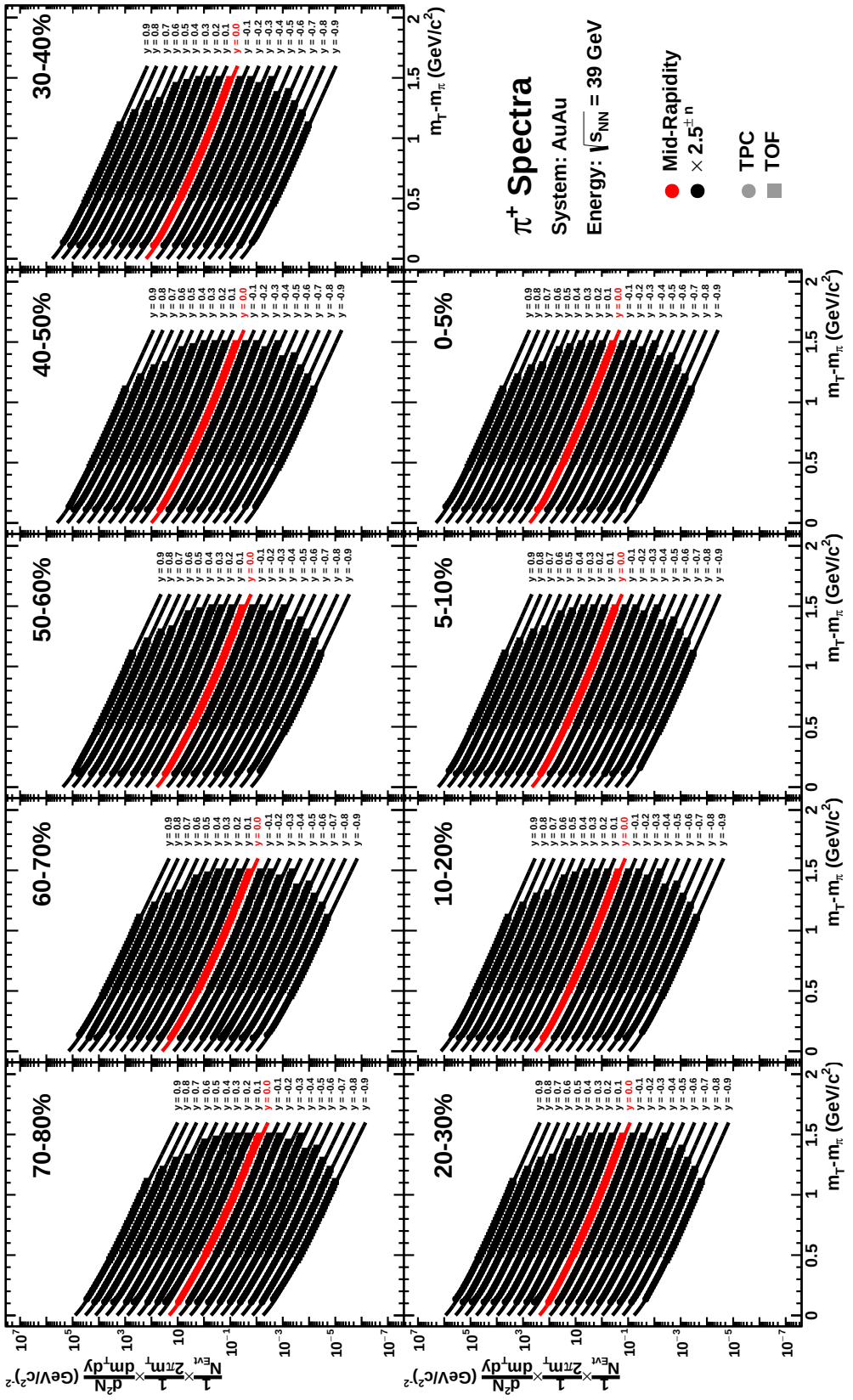

Figure 8.15: Transverse Mass Spectra: π^+ ColliderCenter $\sqrt{s_{NN}} = 39.0$ GeV

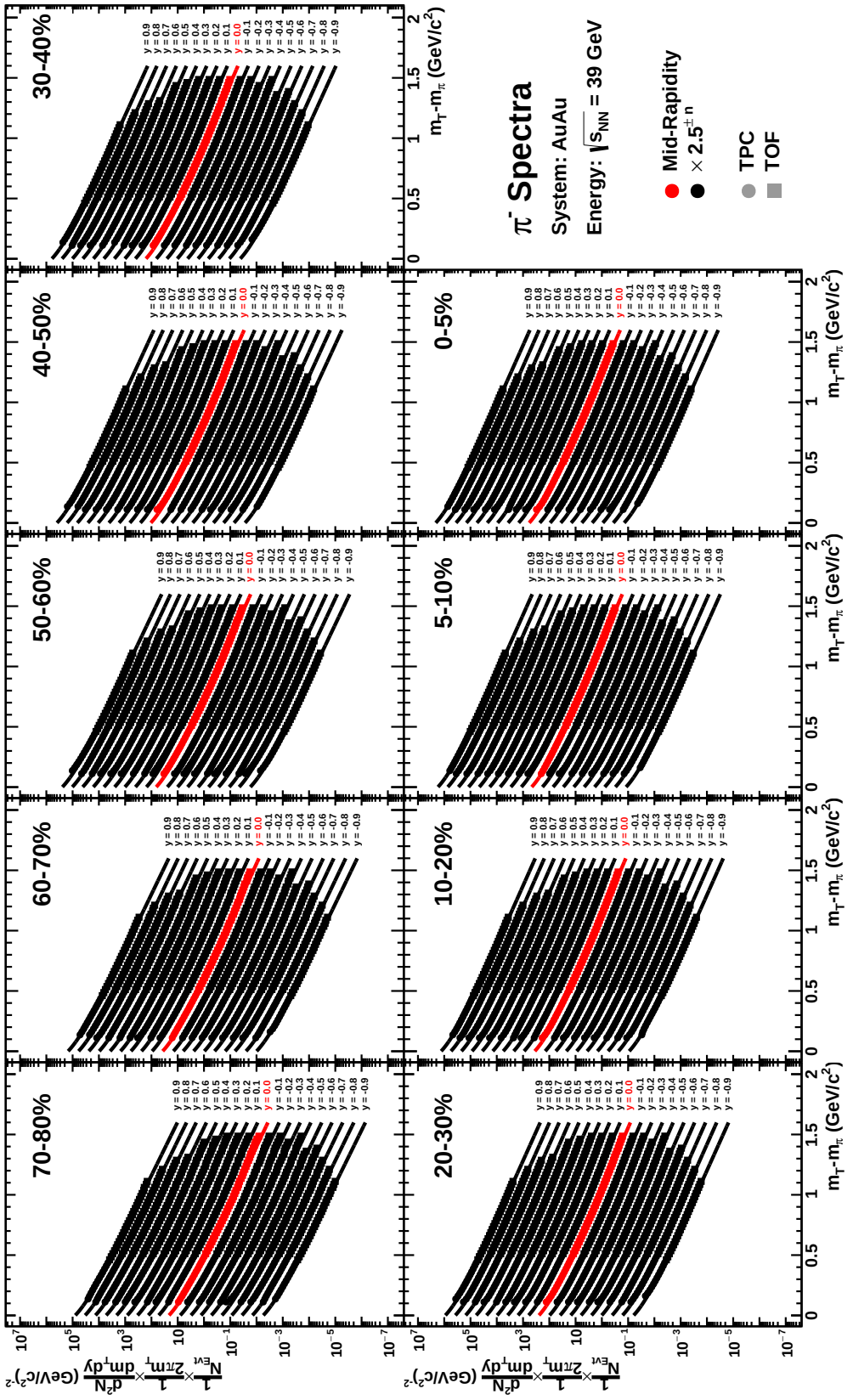

Figure 8.16: Transverse Mass Spectra: π^- ColliderCenter $\sqrt{s_{NN}} = 39.0$ GeV

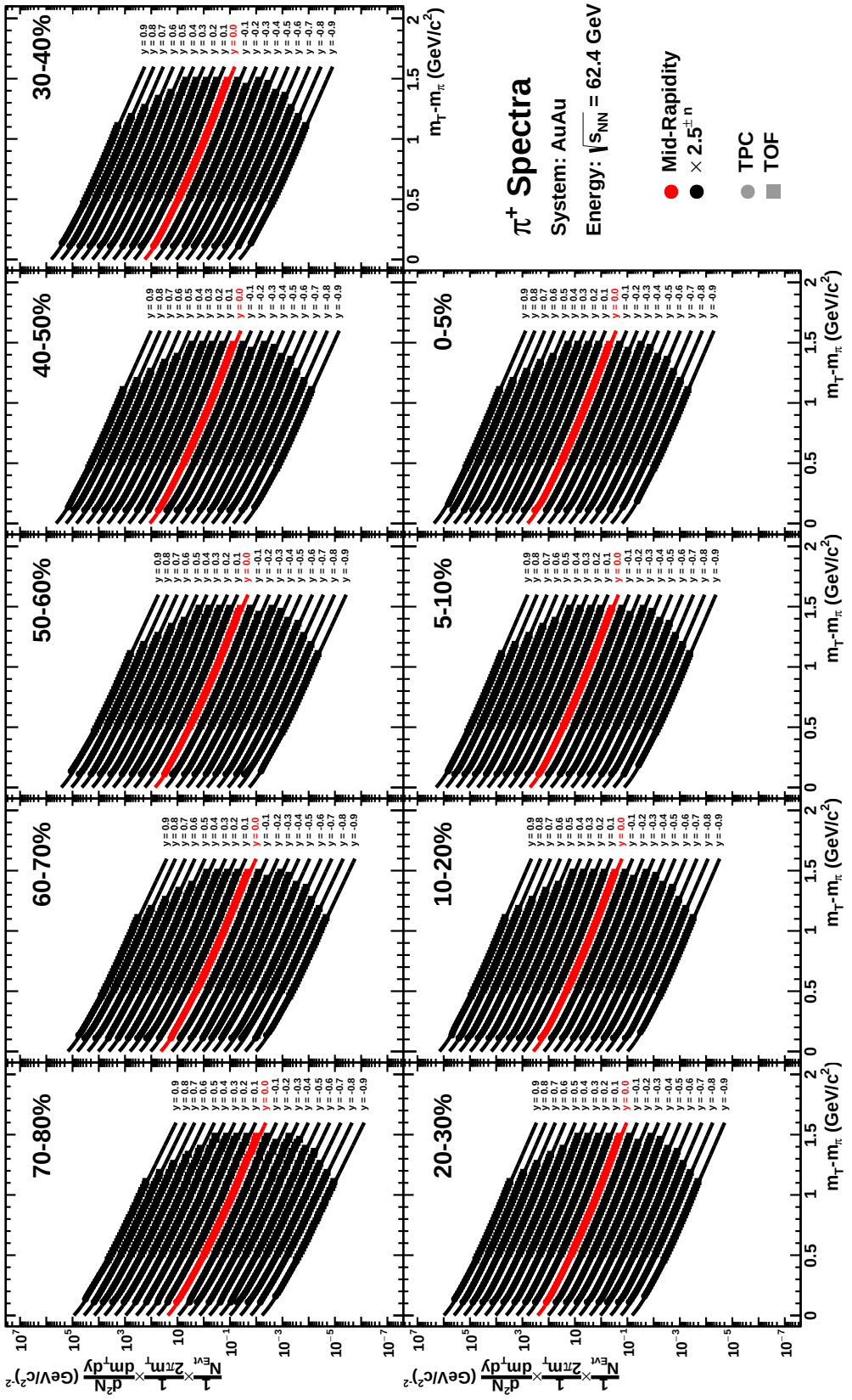

Figure 8.17: Transverse Mass Spectra: π^+ ColliderCenter $\sqrt{s_{NN}} = 62.4$ GeV

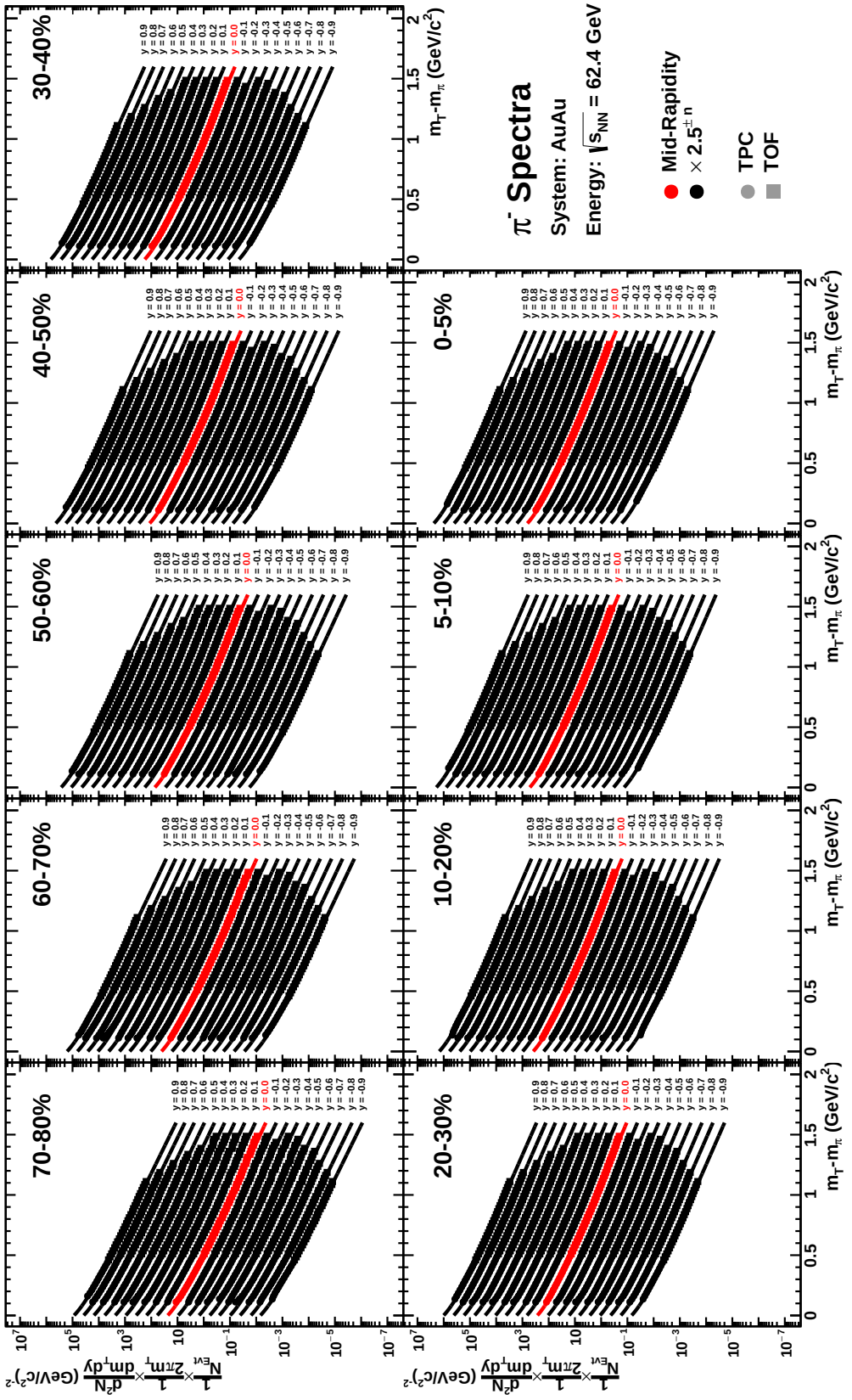

Figure 8.18: Transverse Mass Spectra: π^- ColliderCenter $\sqrt{s_{NN}} = 62.4$ GeV

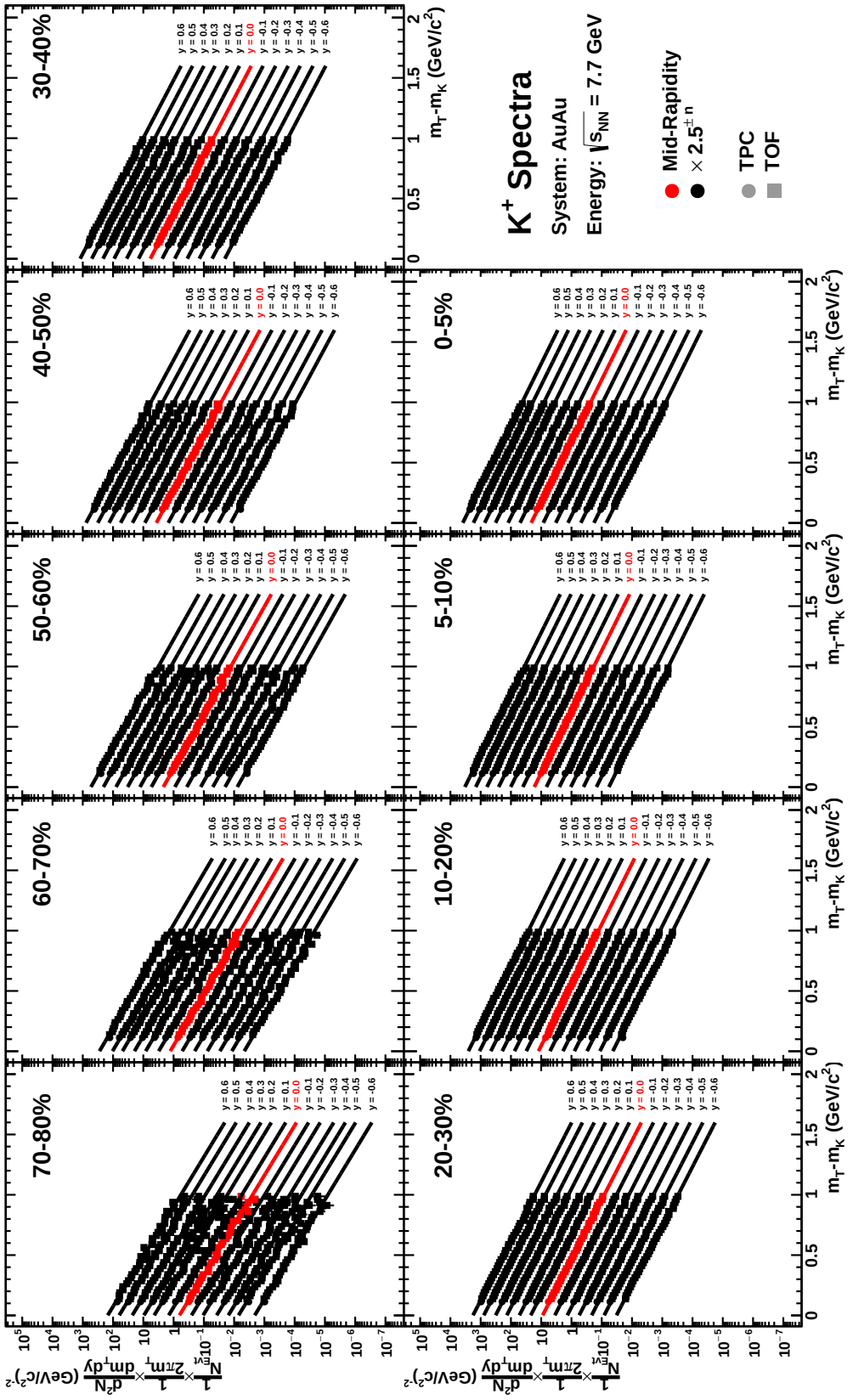

Figure 8.19: Transverse Mass Spectra: K^+ ColliderCenter $\sqrt{s_{NN}} = 7.7$ GeV

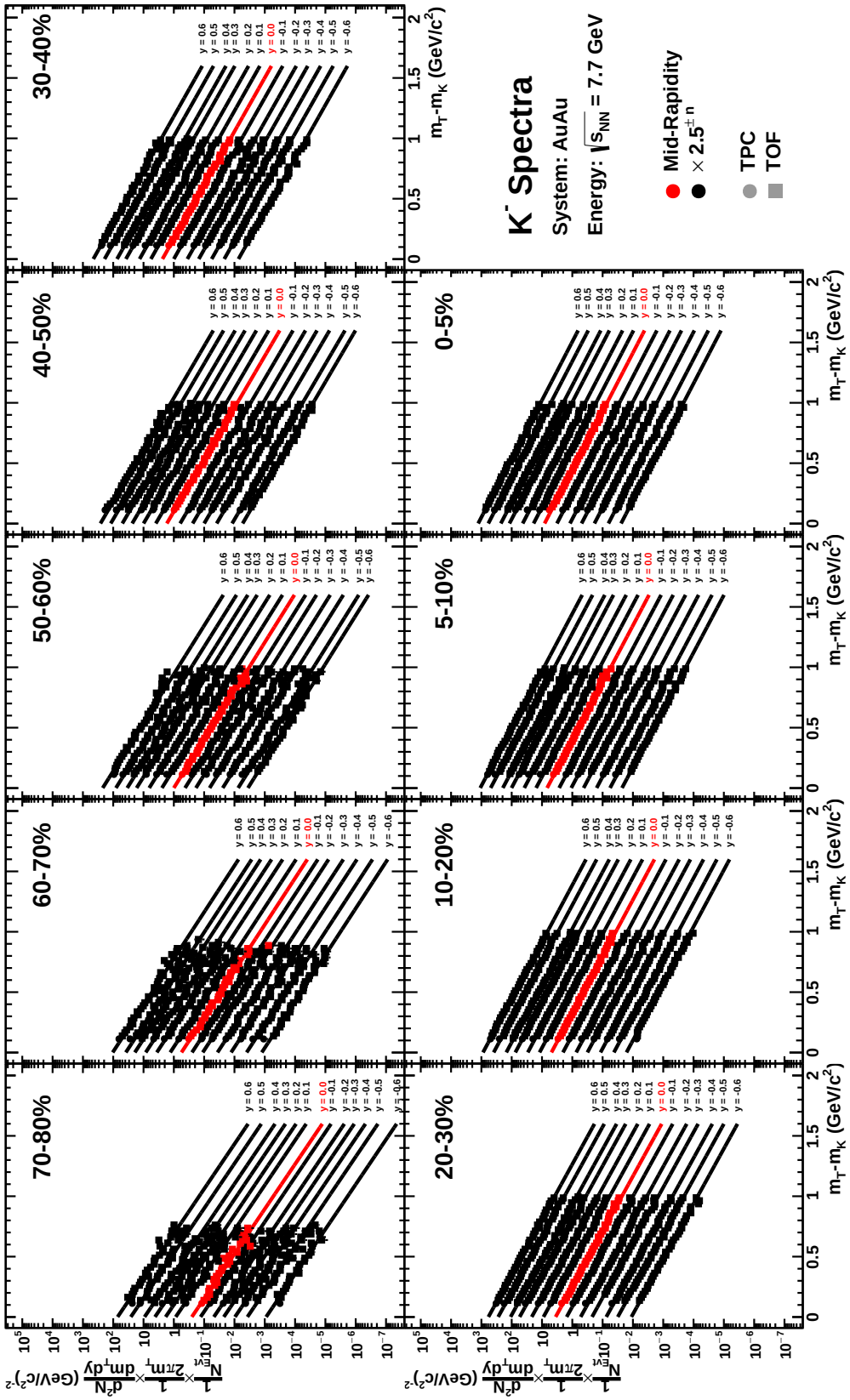

Figure 8.20: Transverse Mass Spectra: K^- ColliderCenter $\sqrt{s_{NN}} = 7.7$ GeV

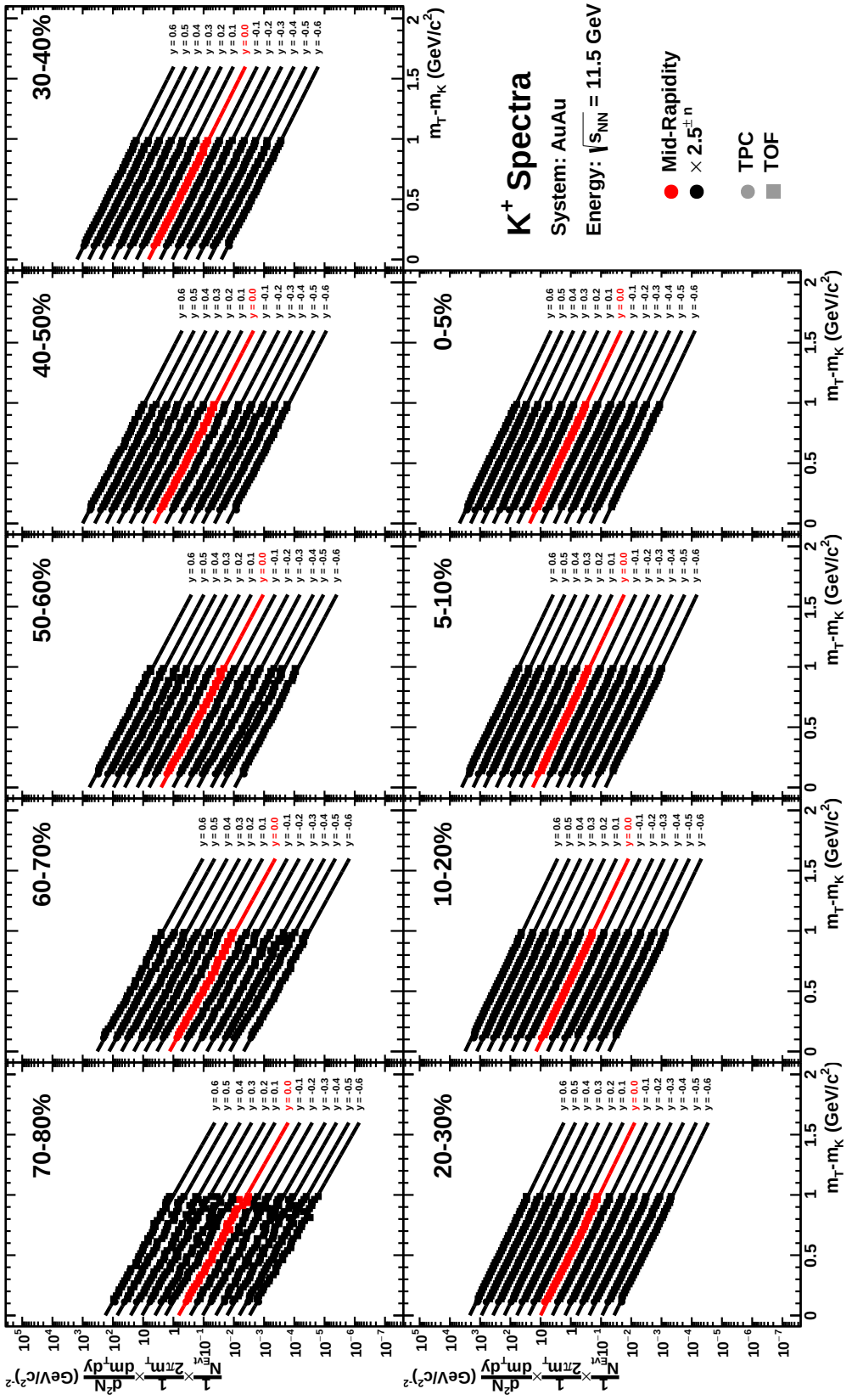

Figure 8.21: Transverse Mass Spectra: K^+ ColliderCenter $\sqrt{s_{NN}} = 11.5$ GeV

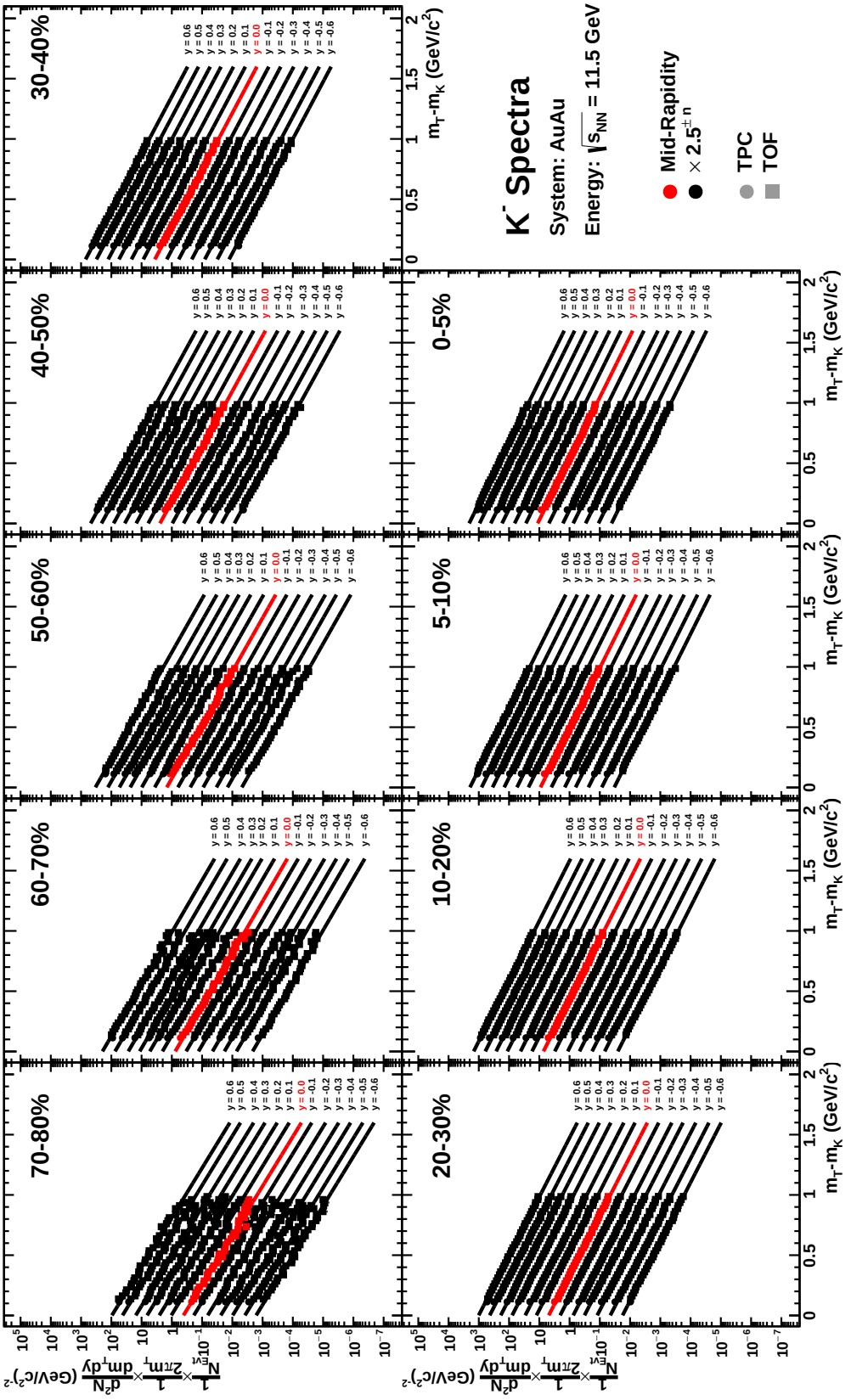

Figure 8.22: Transverse Mass Spectra: K^- ColliderCenter $\sqrt{s_{NN}} = 11.5$ GeV

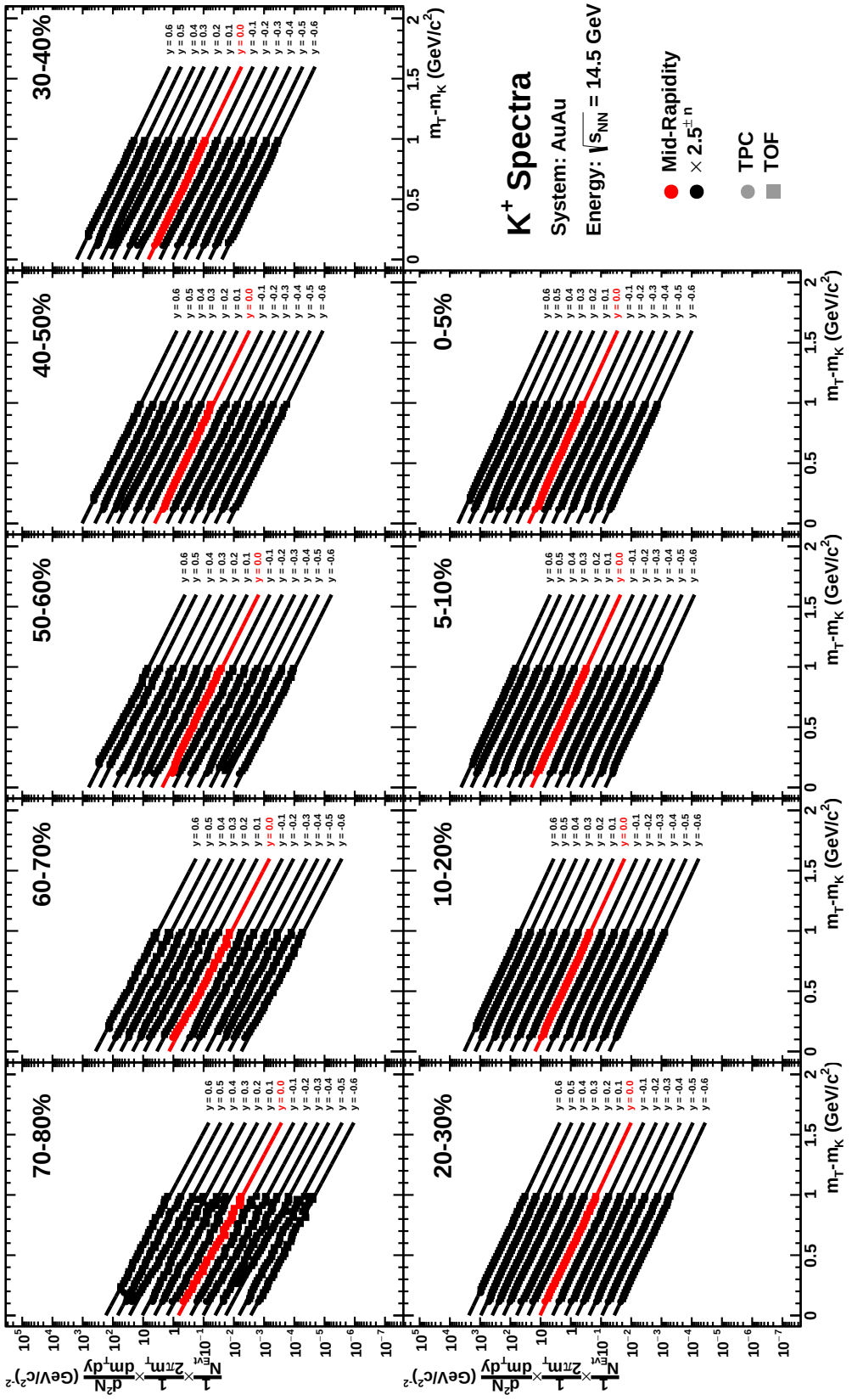

Figure 8.23: Transverse Mass Spectra: K^+ ColliderCenter $\sqrt{s_{NN}} = 14.5$ GeV

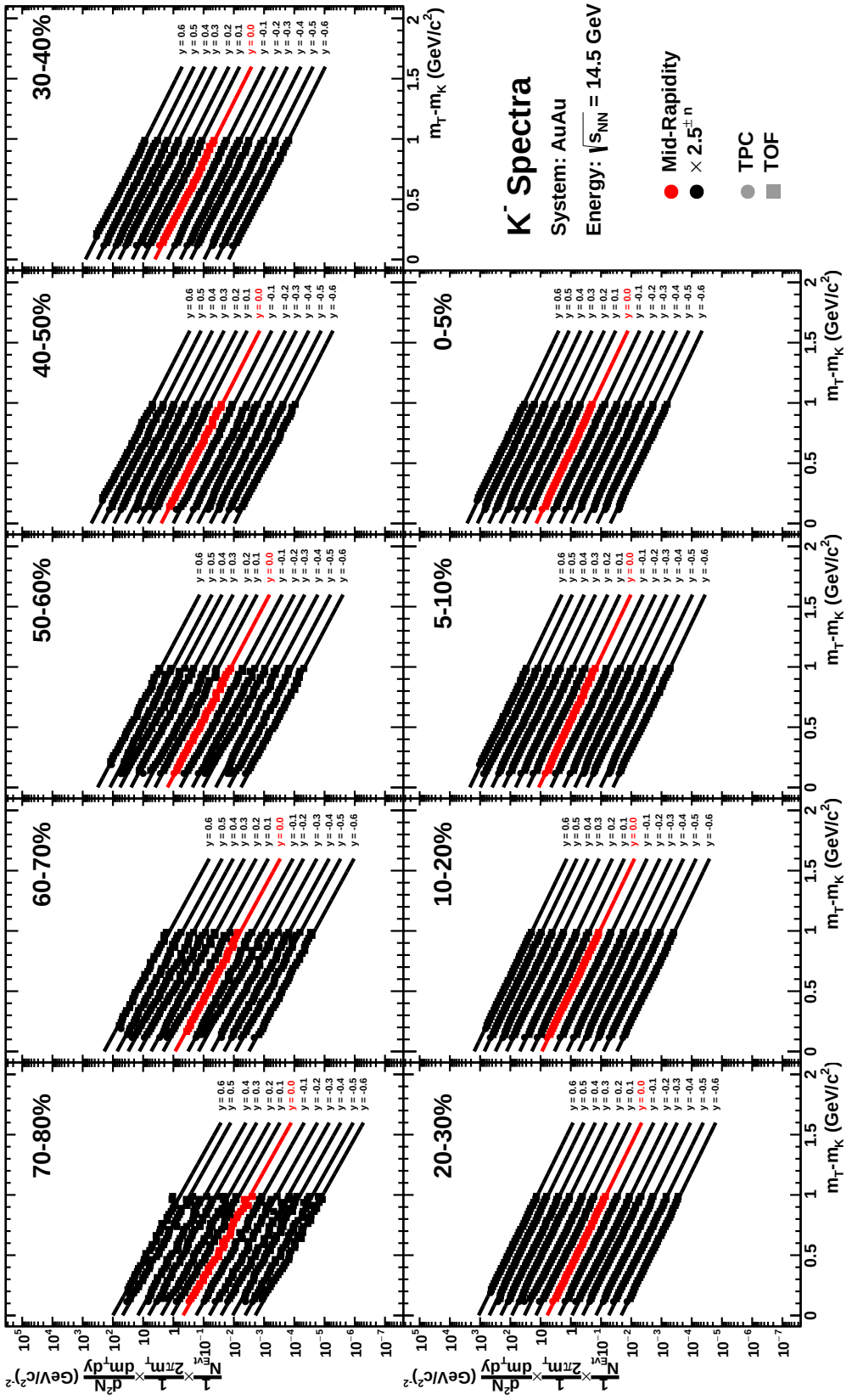

Figure 8.24: Transverse Mass Spectra: K^- ColliderCenter $\sqrt{s_{NN}} = 14.5$ GeV

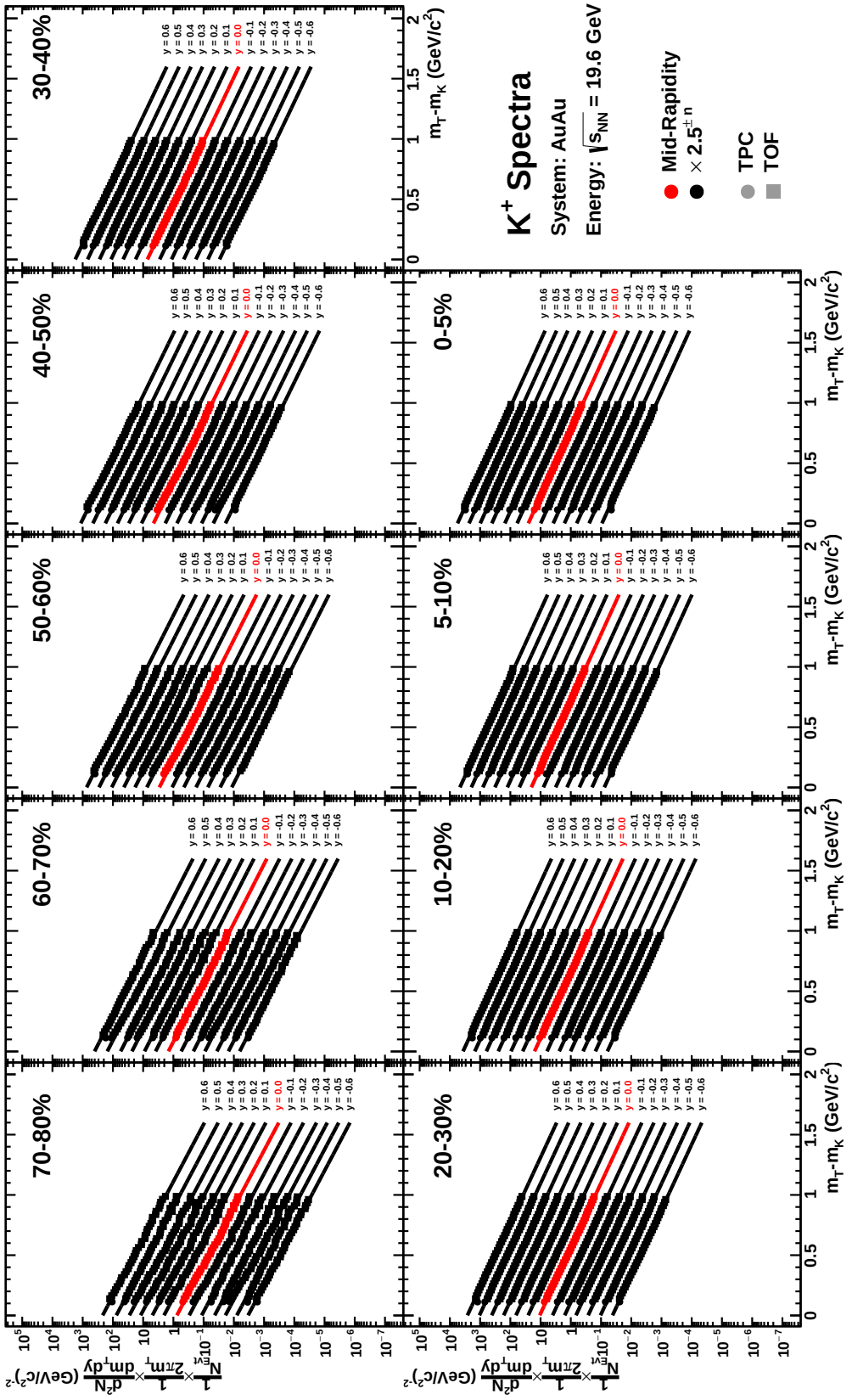

Figure 8.25: Transverse Mass Spectra: K^+ ColliderCenter $\sqrt{s_{NN}} = 19.6$ GeV

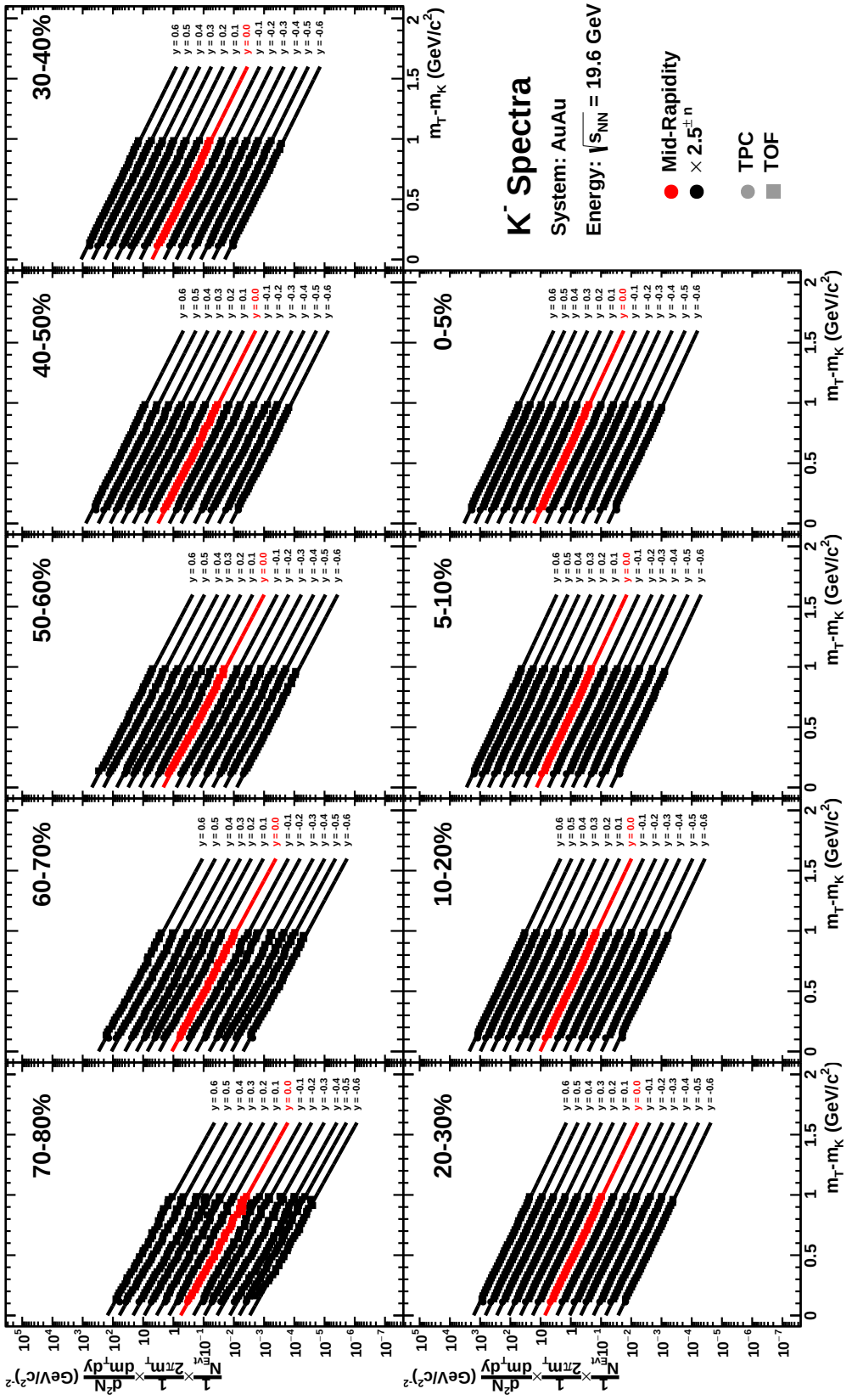

Figure 8.26: Transverse Mass Spectra: K^- ColliderCenter $\sqrt{s_{NN}} = 19.6$ GeV

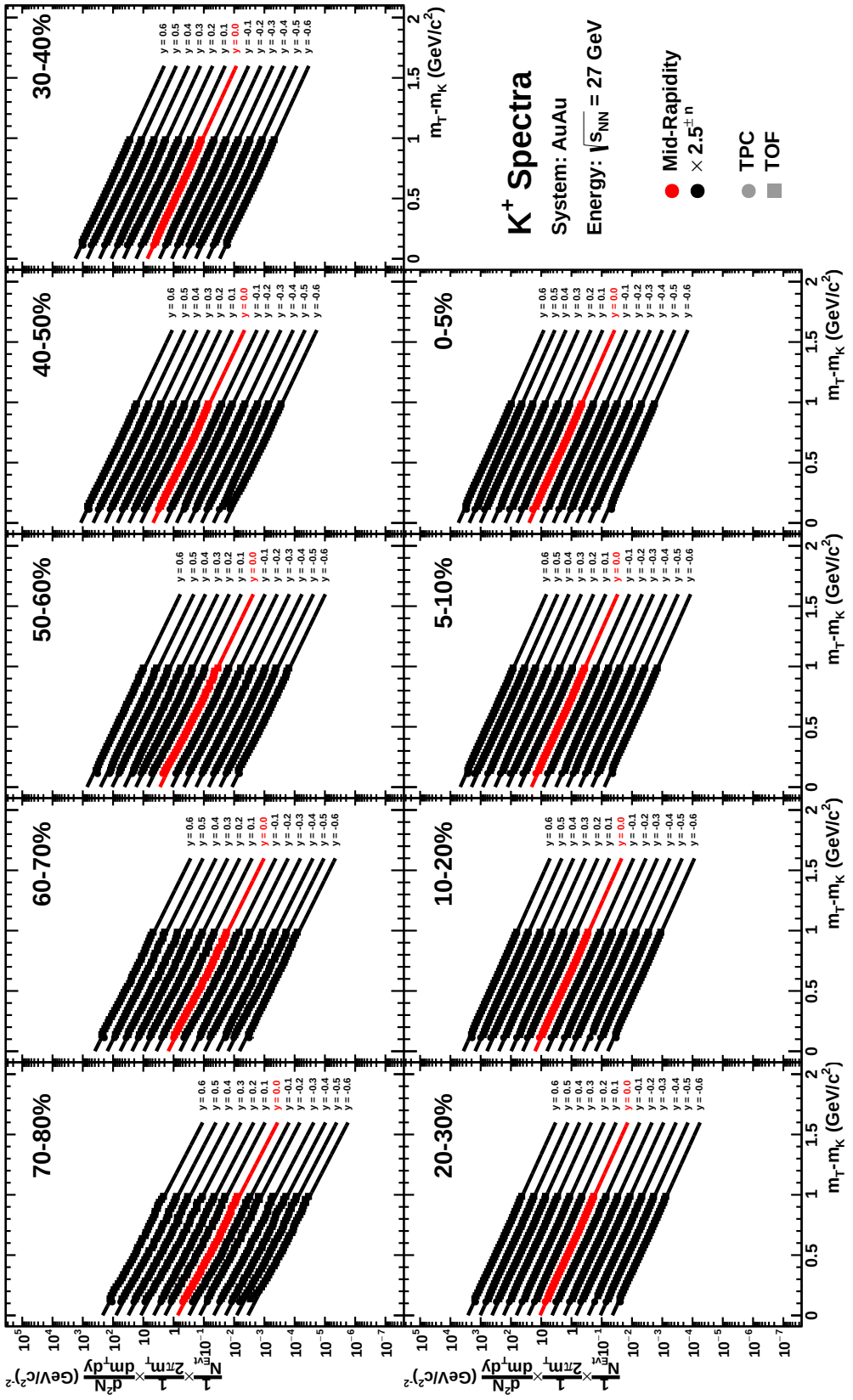

Figure 8.27: Transverse Mass Spectra: K^+ ColliderCenter $\sqrt{s_{NN}} = 27.0$ GeV

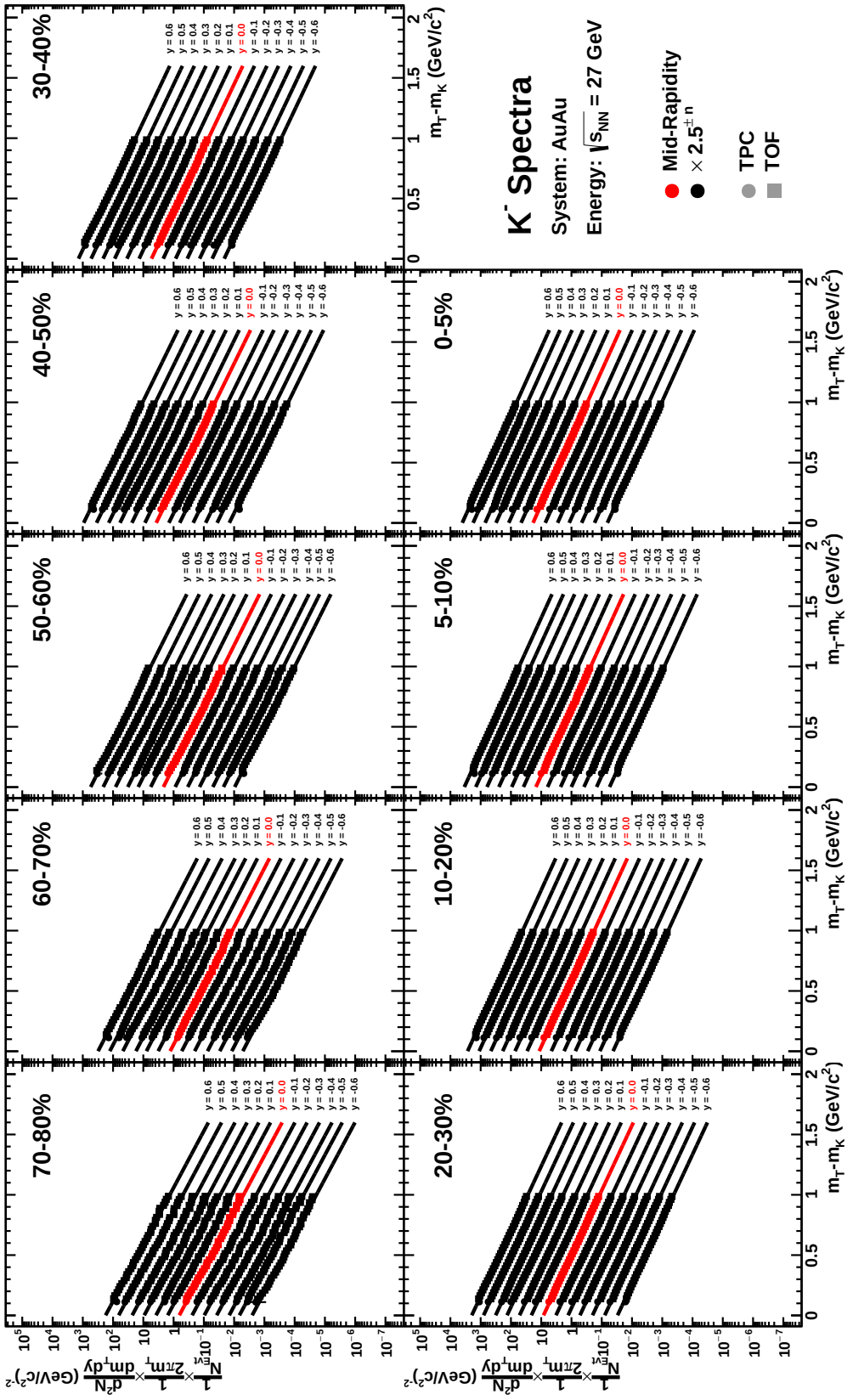

Figure 8.28: Transverse Mass Spectra: K^- ColliderCenter $\sqrt{s_{NN}} = 27.0$ GeV

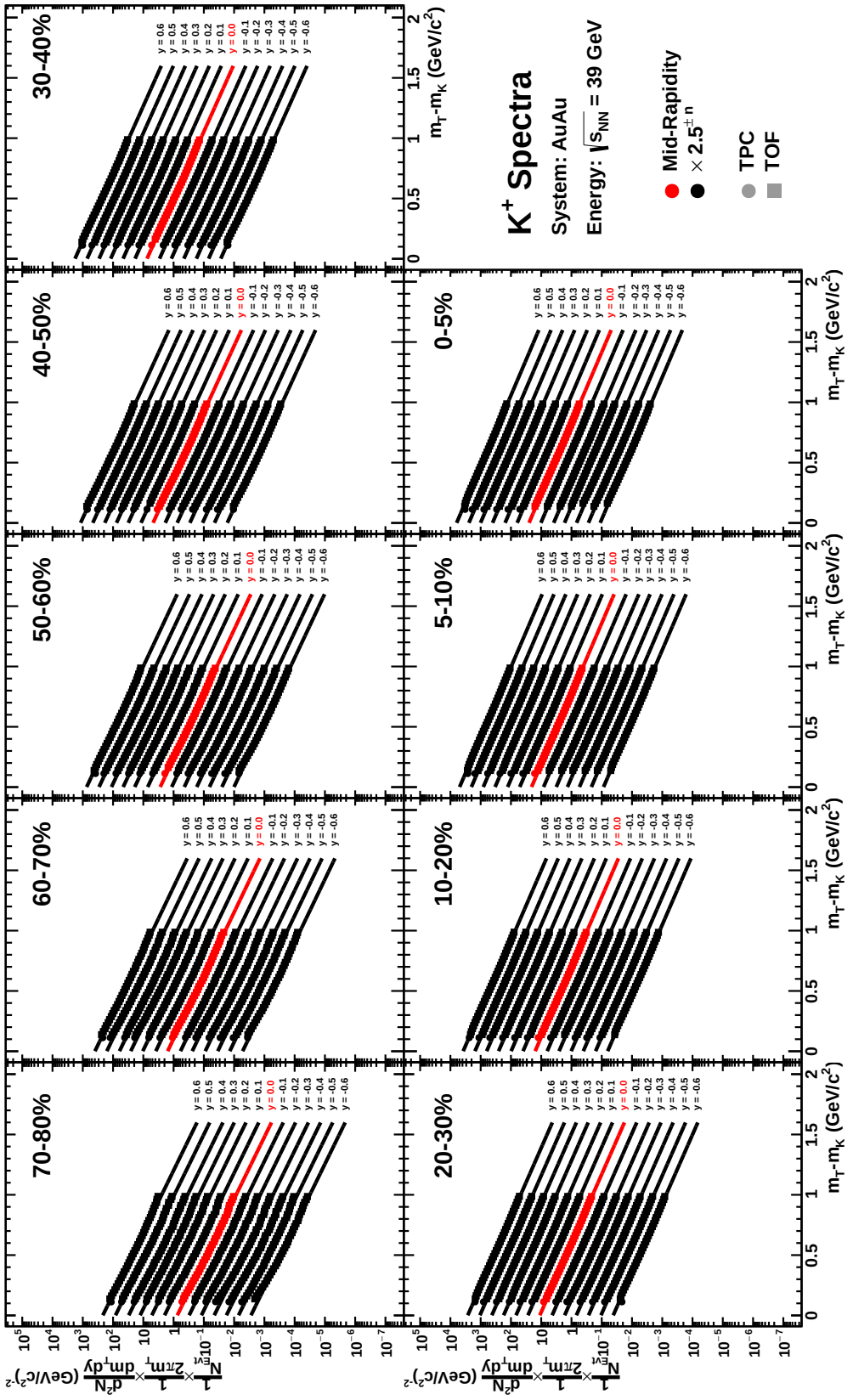

Figure 8.29: Transverse Mass Spectra: K^+ ColliderCenter $\sqrt{s_{NN}} = 39.0$ GeV

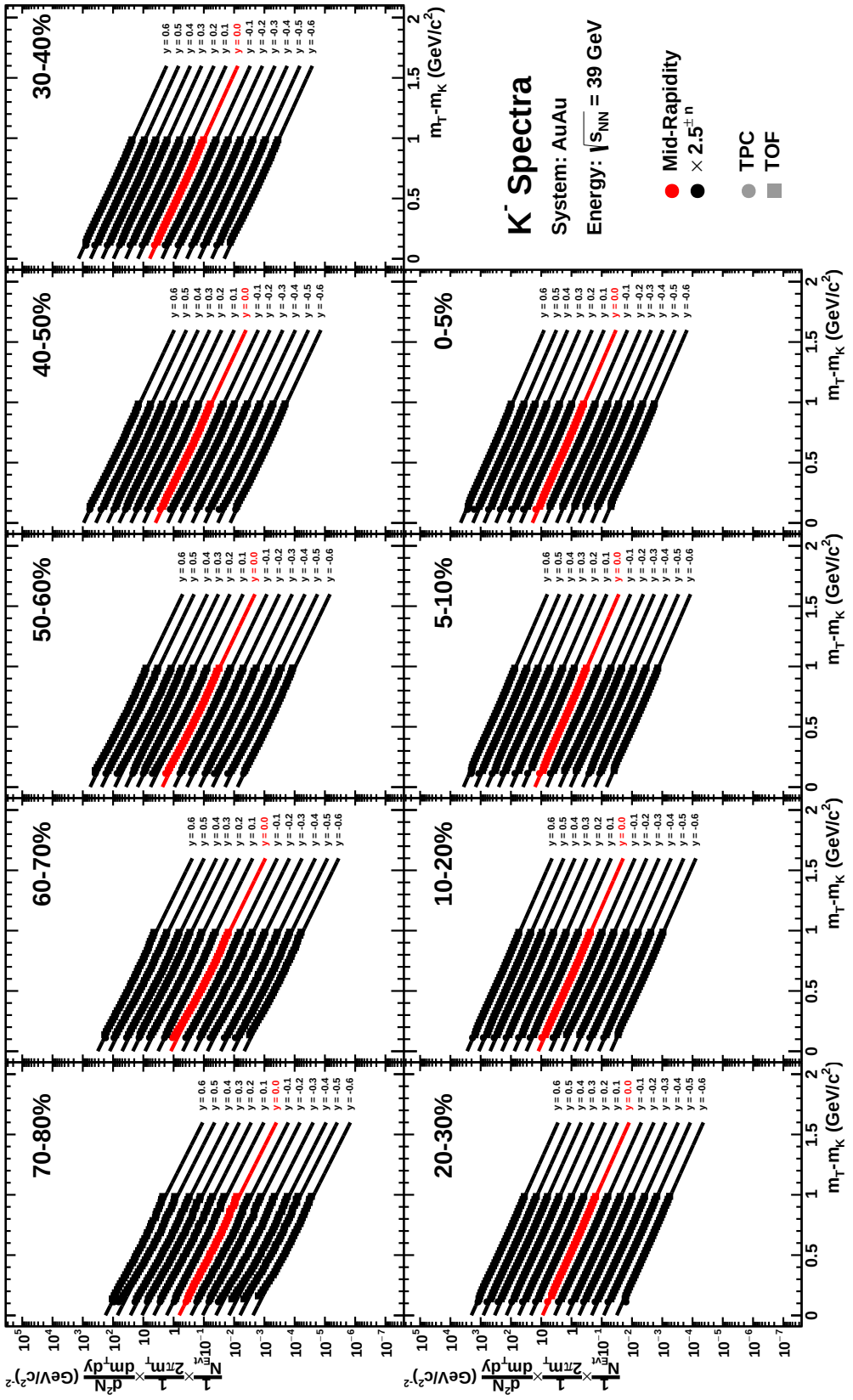

Figure 8.30: Transverse Mass Spectra: K^- ColliderCenter $\sqrt{s_{NN}} = 39.0$ GeV

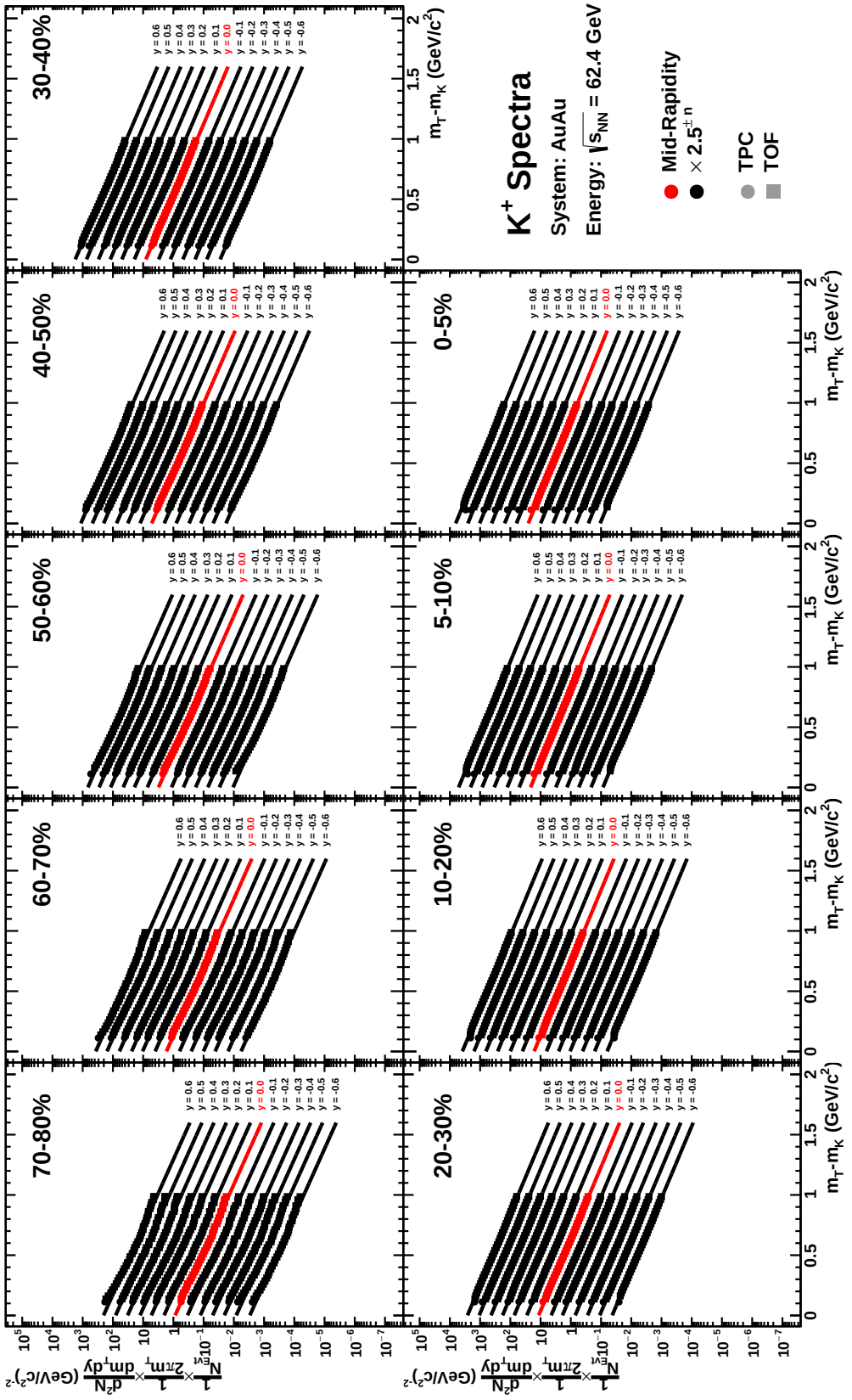

Figure 8.31: Transverse Mass Spectra: K^+ ColliderCenter $\sqrt{s_{NN}} = 62.4$ GeV

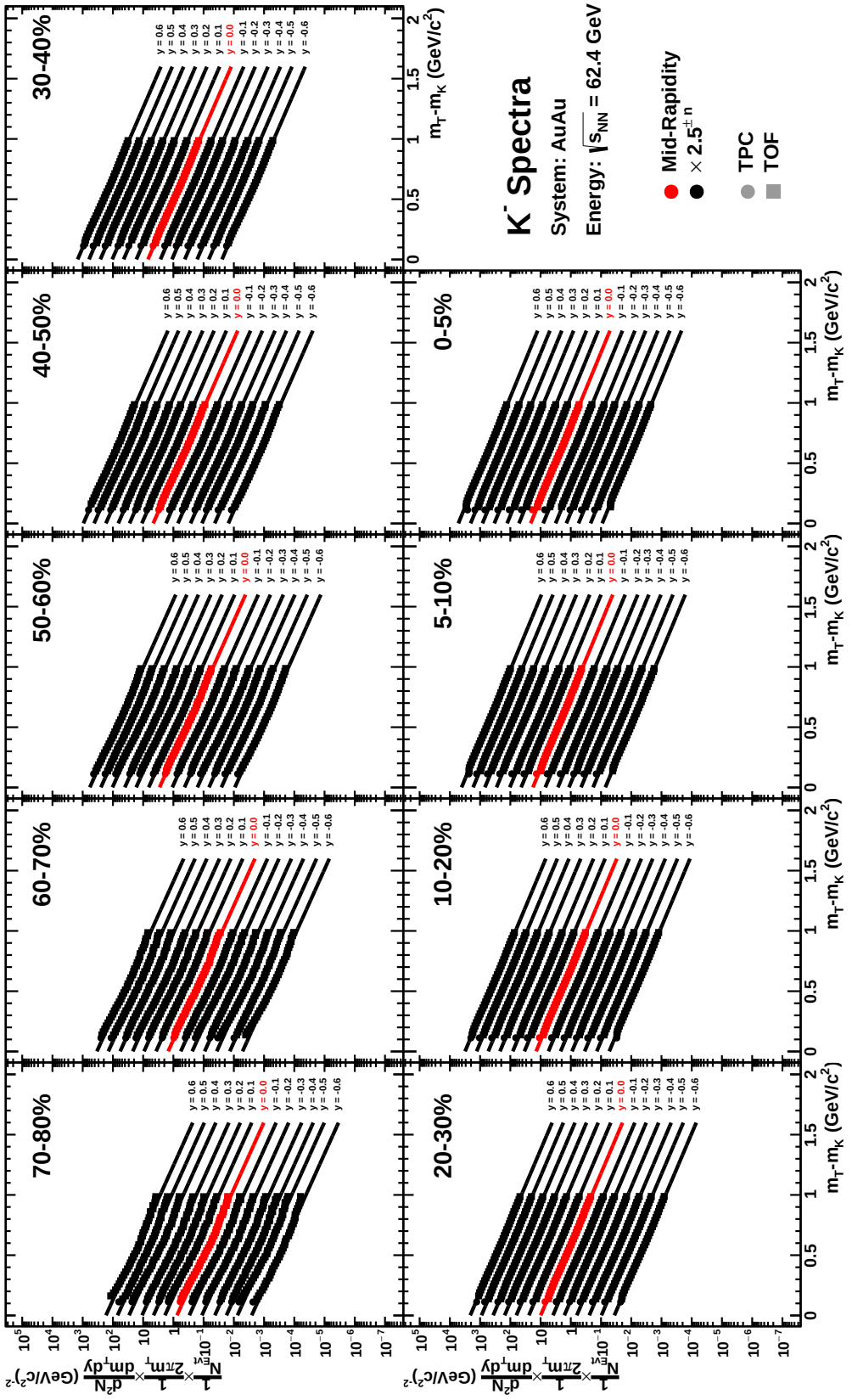

Figure 8.32: Transverse Mass Spectra: K^- ColliderCenter $\sqrt{s_{NN}} = 62.4$ GeV

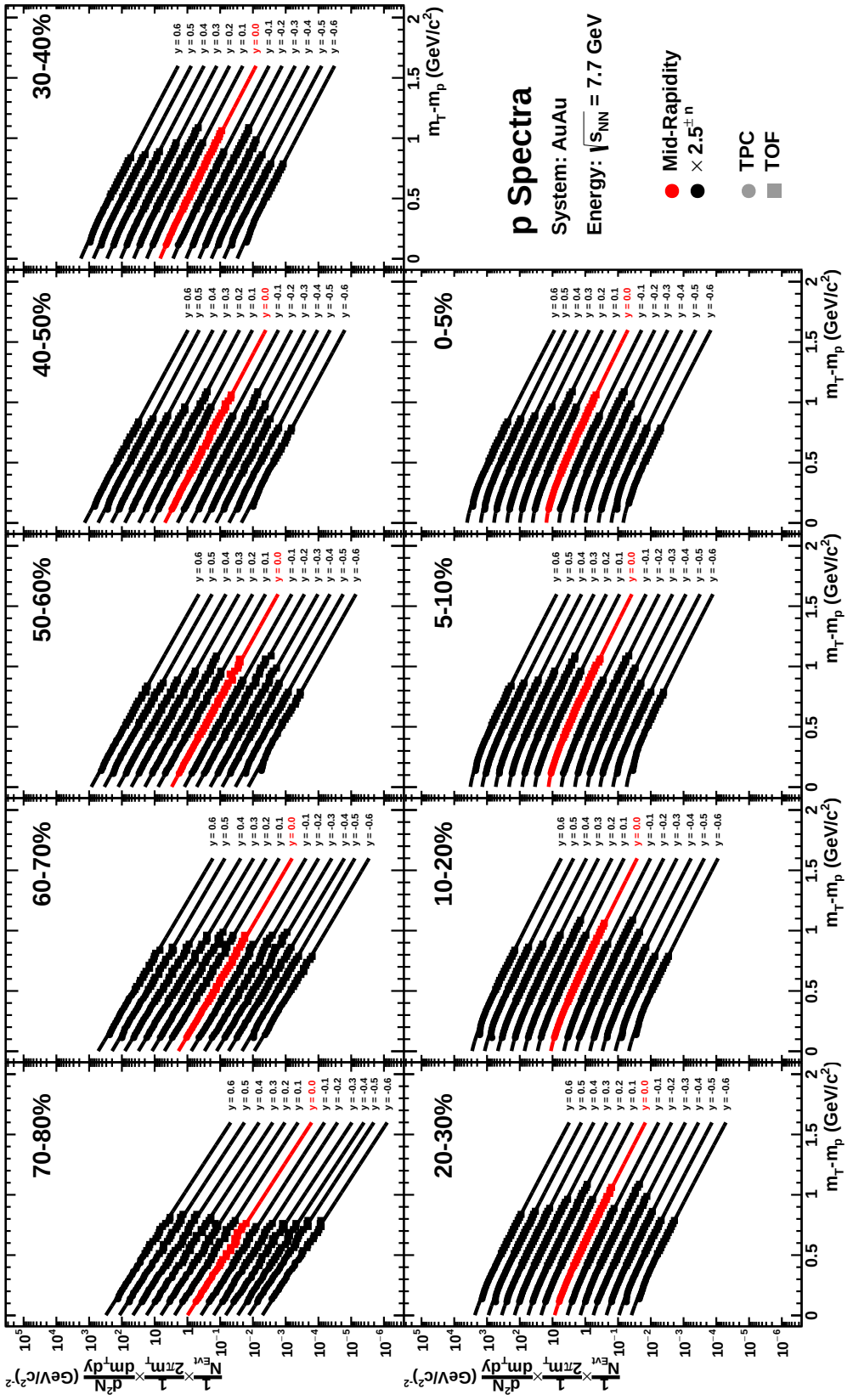

Figure 8.33: Transverse Mass Spectra: p ColliderCenter $\sqrt{s_{NN}} = 7.7$ GeV

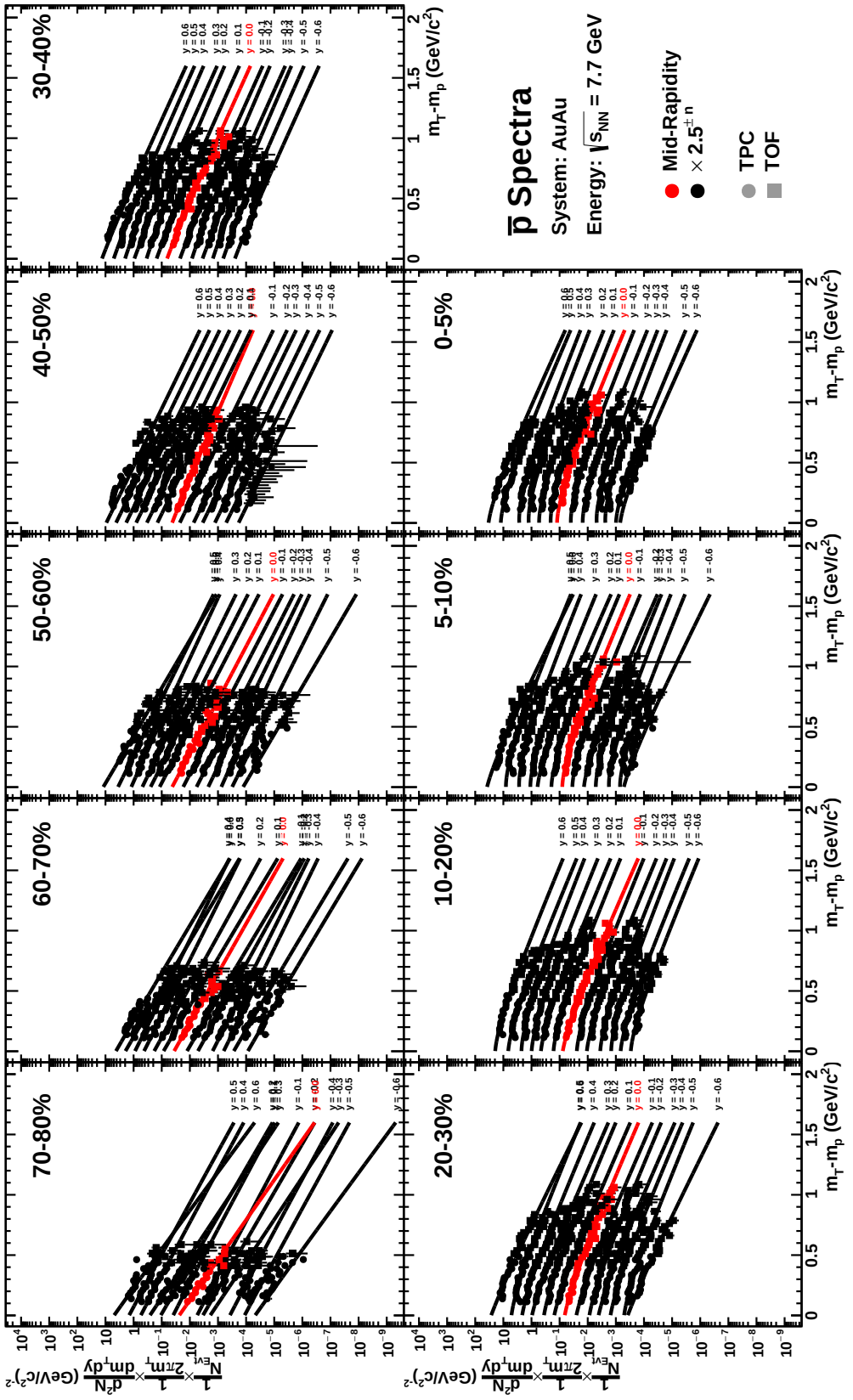

Figure 8.34: Transverse Mass Spectra: $\bar{p}$ ColliderCenter $\sqrt{s_{NN}} = 7.7$ GeV

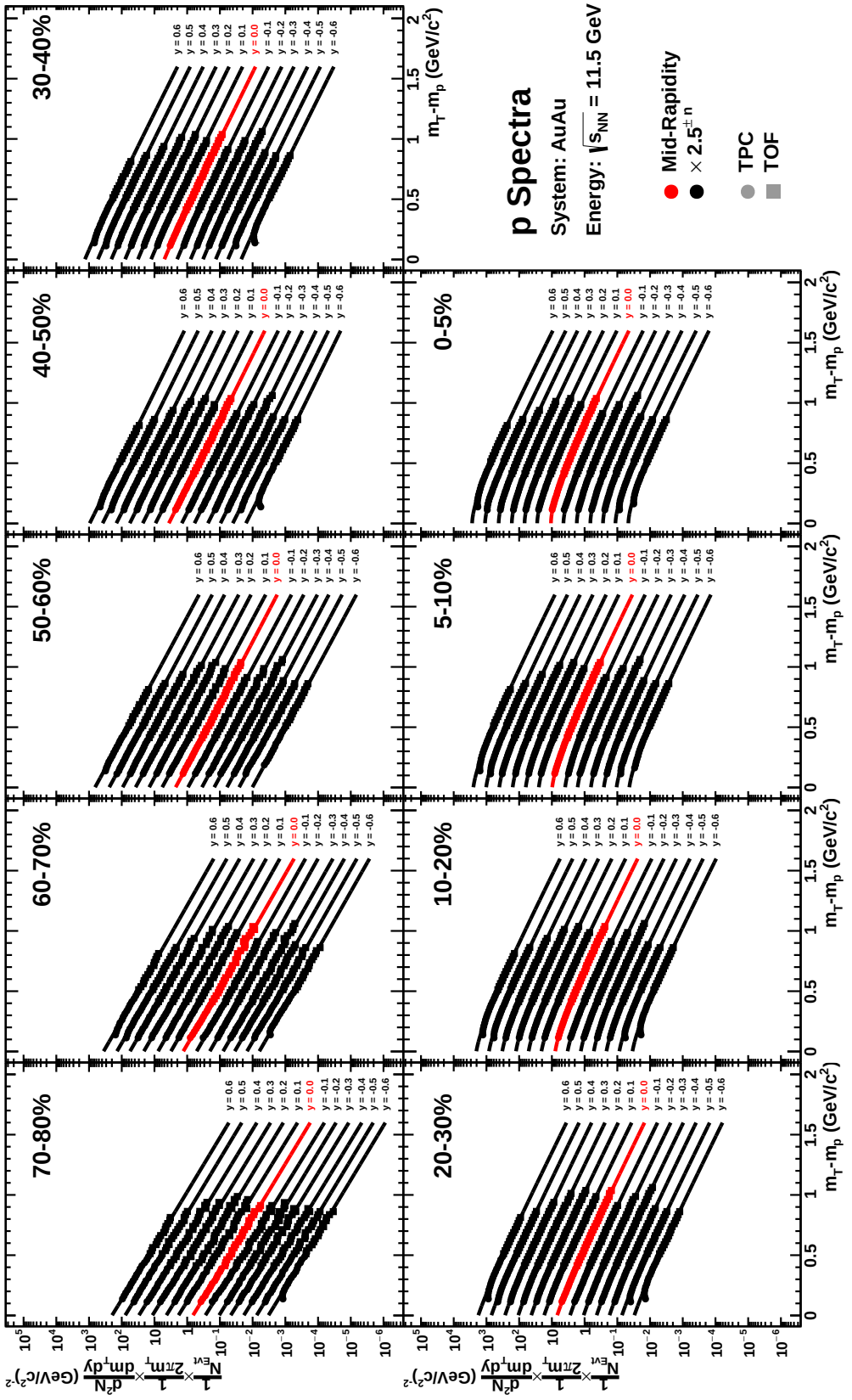

Figure 8.35: Transverse Mass Spectra: p ColliderCenter $\sqrt{s_{NN}} = 11.5$ GeV

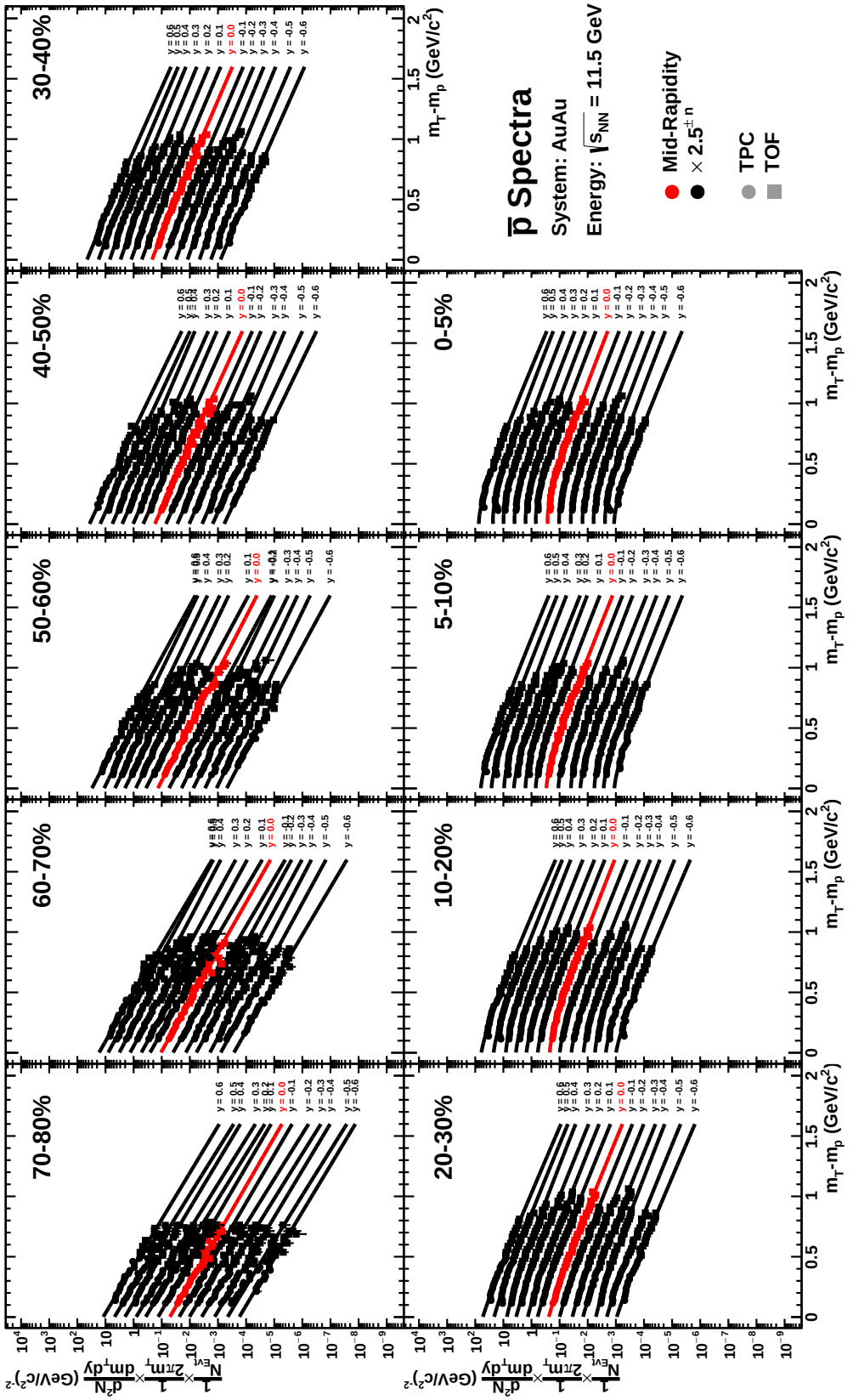

Figure 8.36: Transverse Mass Spectra: $\bar{p}$ ColliderCenter $\sqrt{s_{NN}} = 11.5$ GeV

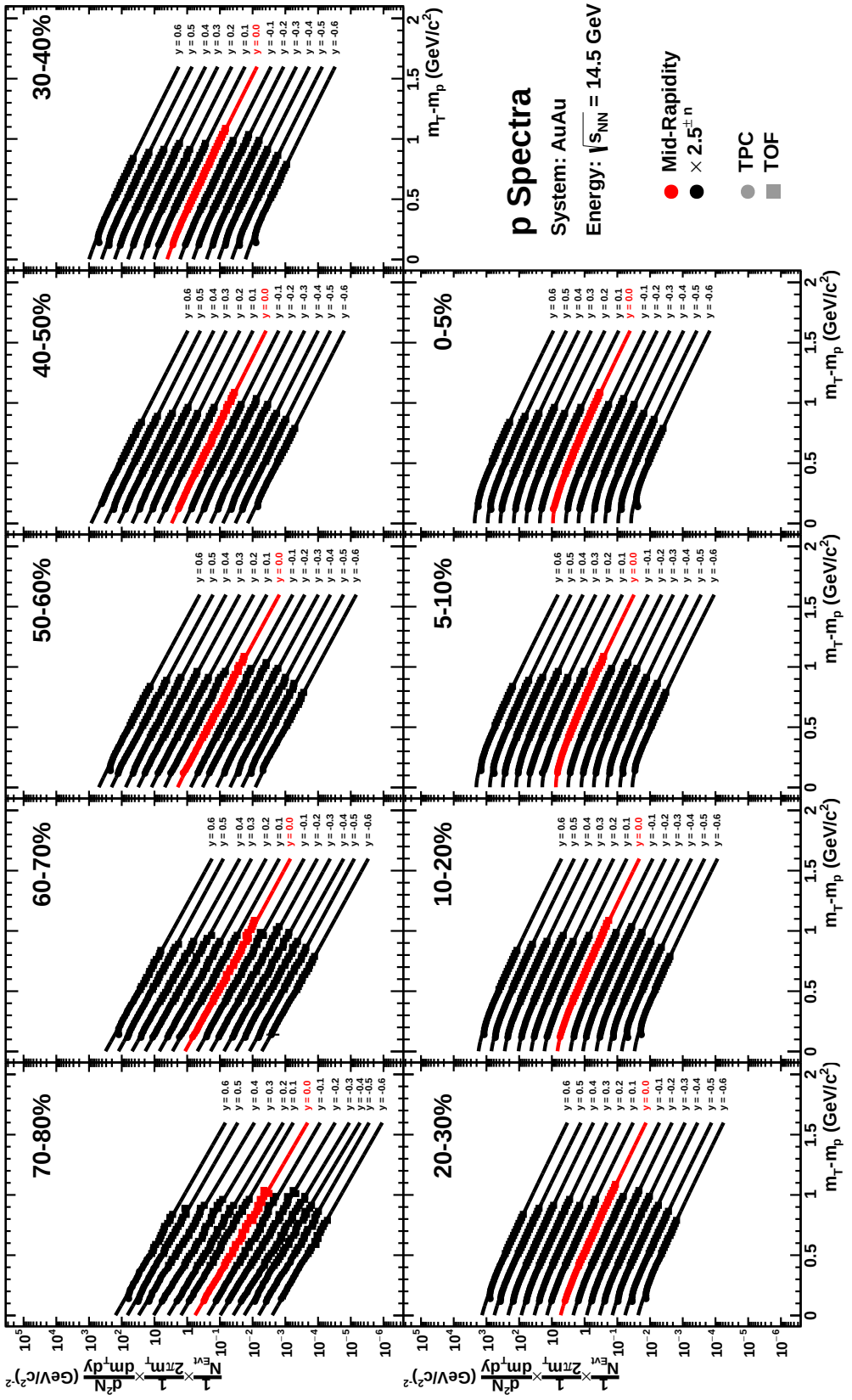

Figure 8.37: Transverse Mass Spectra: p ColliderCenter $\sqrt{s_{NN}} = 14.5$ GeV

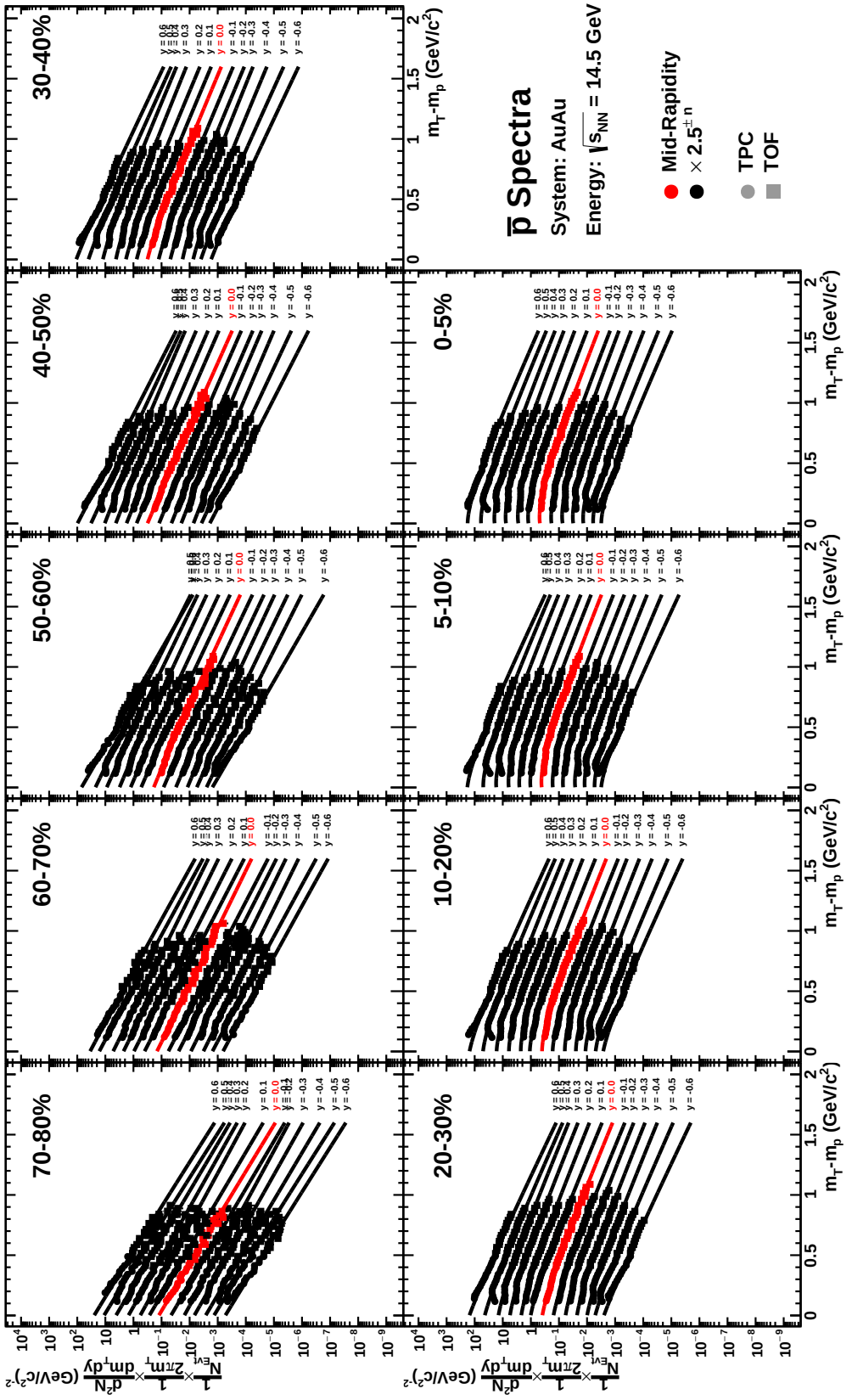

Figure 8.38: Transverse Mass Spectra: $\bar{p}$ ColliderCenter $\sqrt{s_{NN}} = 14.5$ GeV

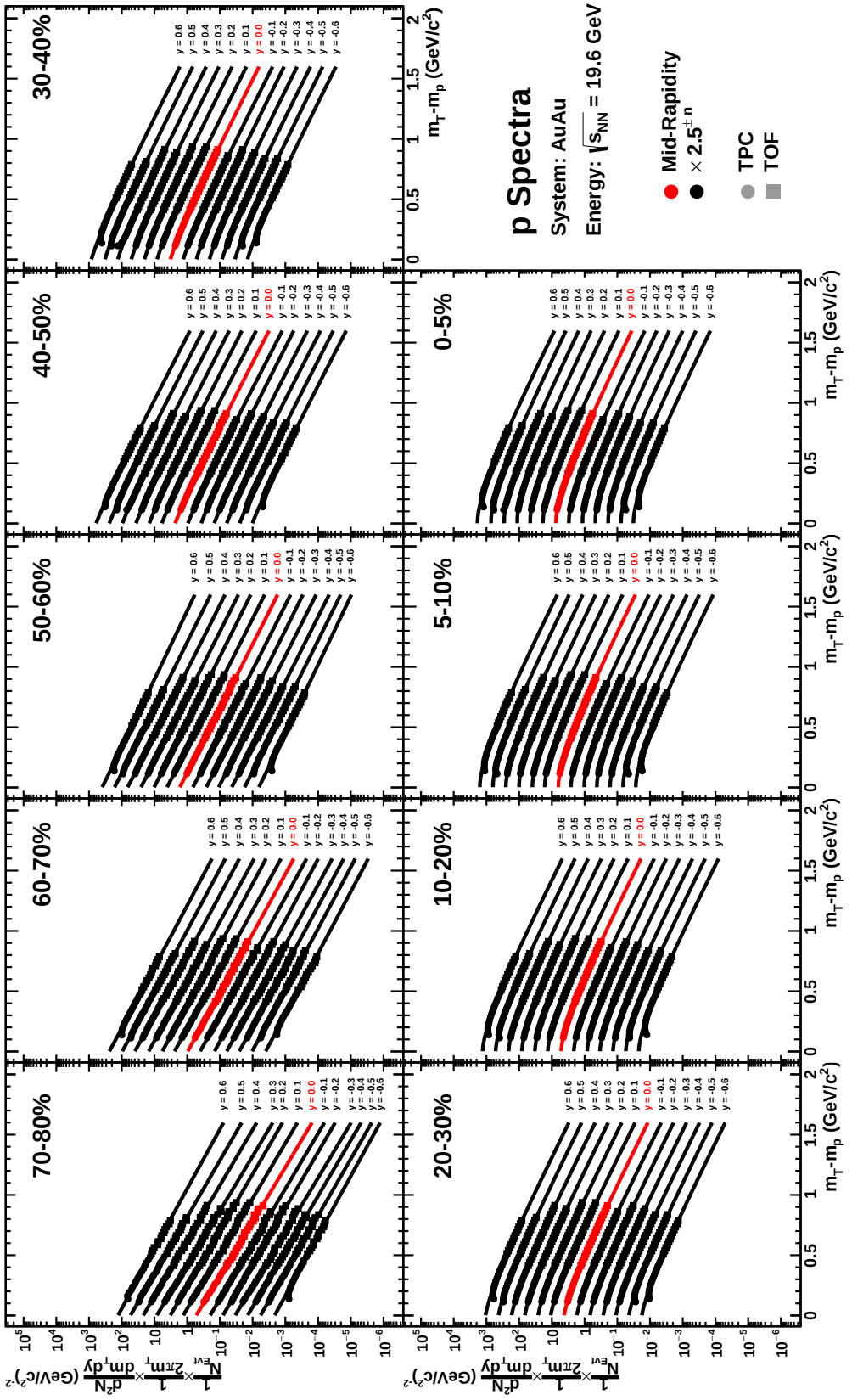

Figure 8.39: Transverse Mass Spectra: p ColliderCenter $\sqrt{s_{NN}} = 19.6$ GeV

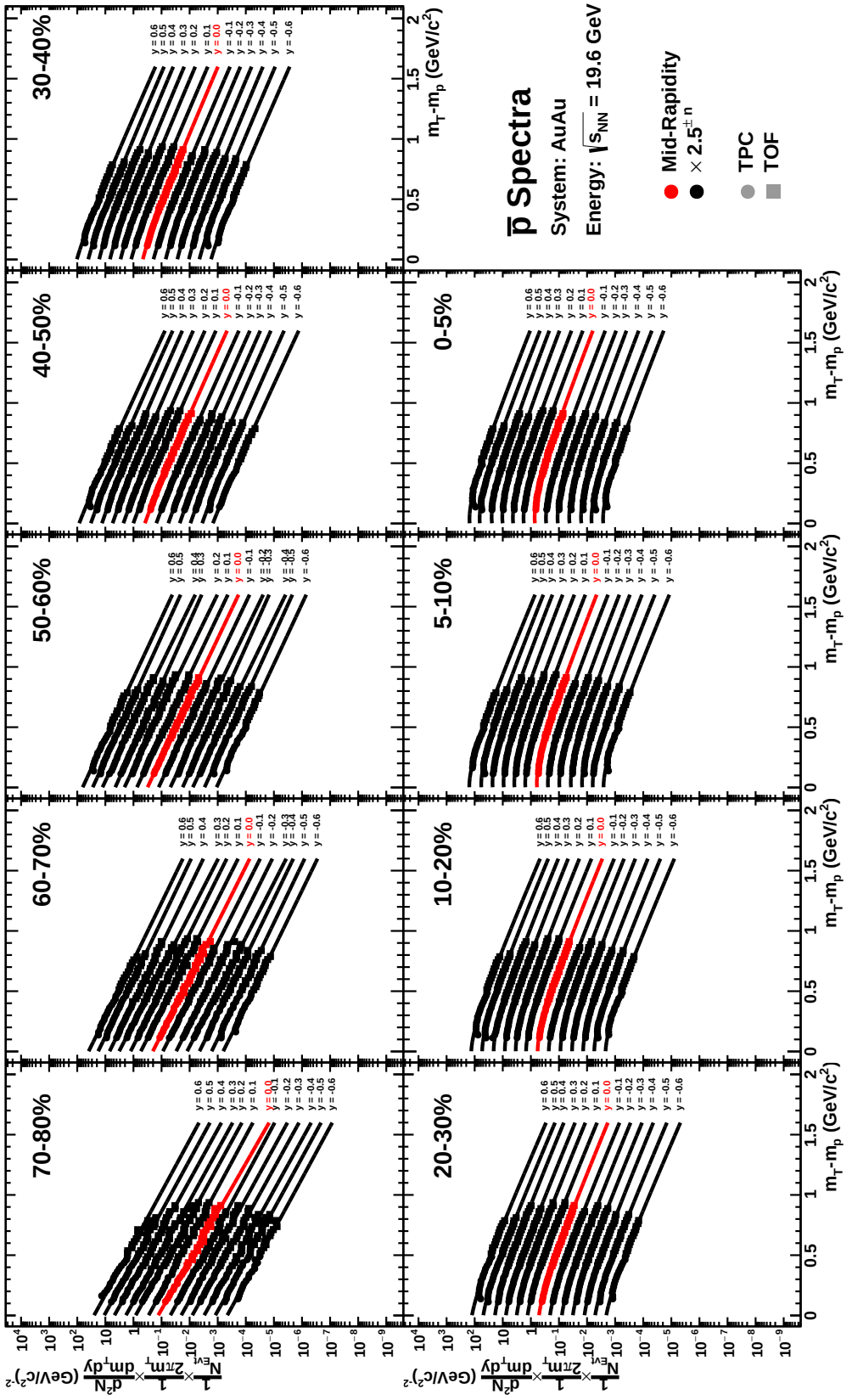

Figure 8.40: Transverse Mass Spectra: $\bar{p}$ ColliderCenter $\sqrt{s_{NN}} = 19.6$ GeV

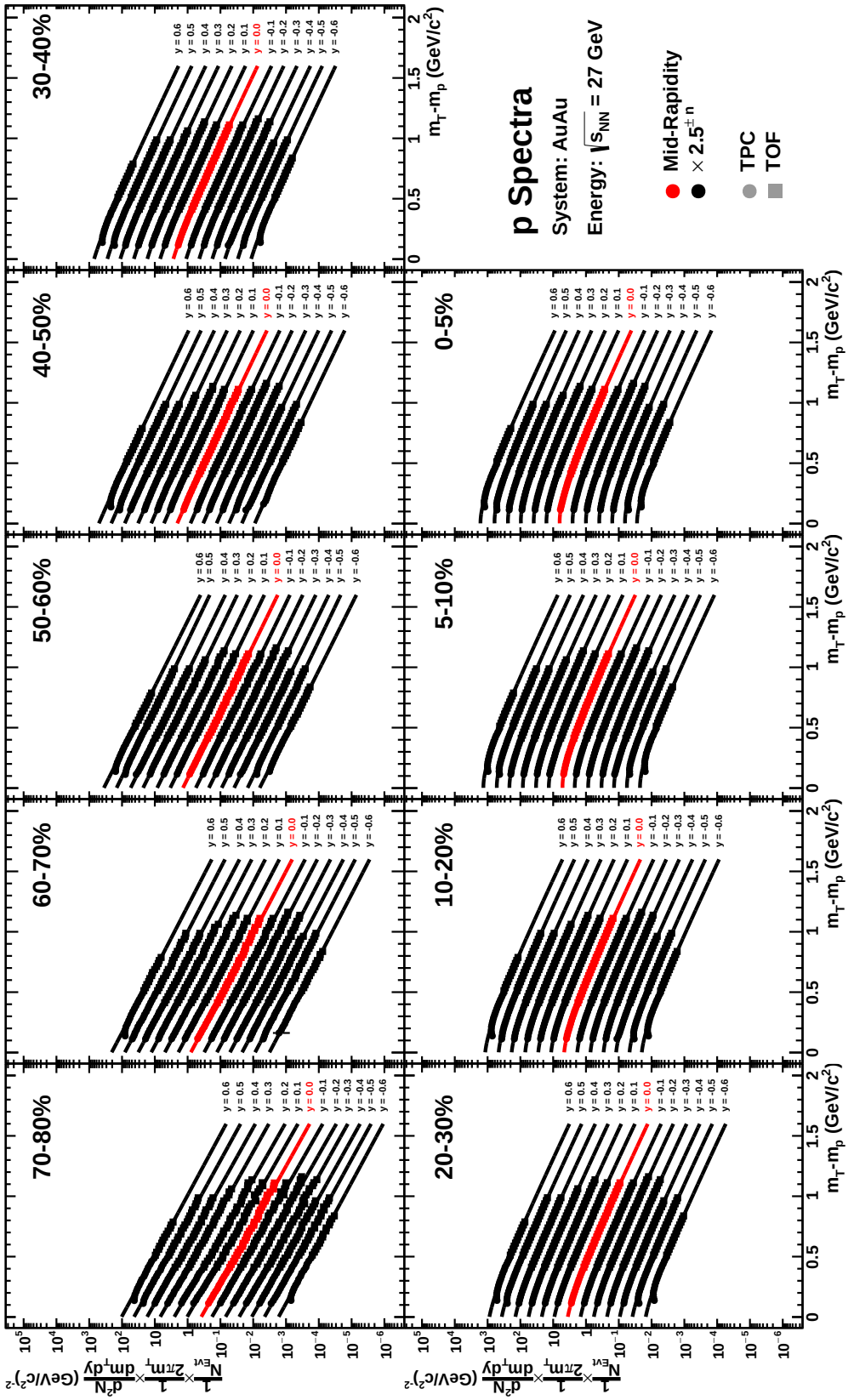

Figure 8.41: Transverse Mass Spectra: p ColliderCenter $\sqrt{s_{NN}} = 27.0$ GeV

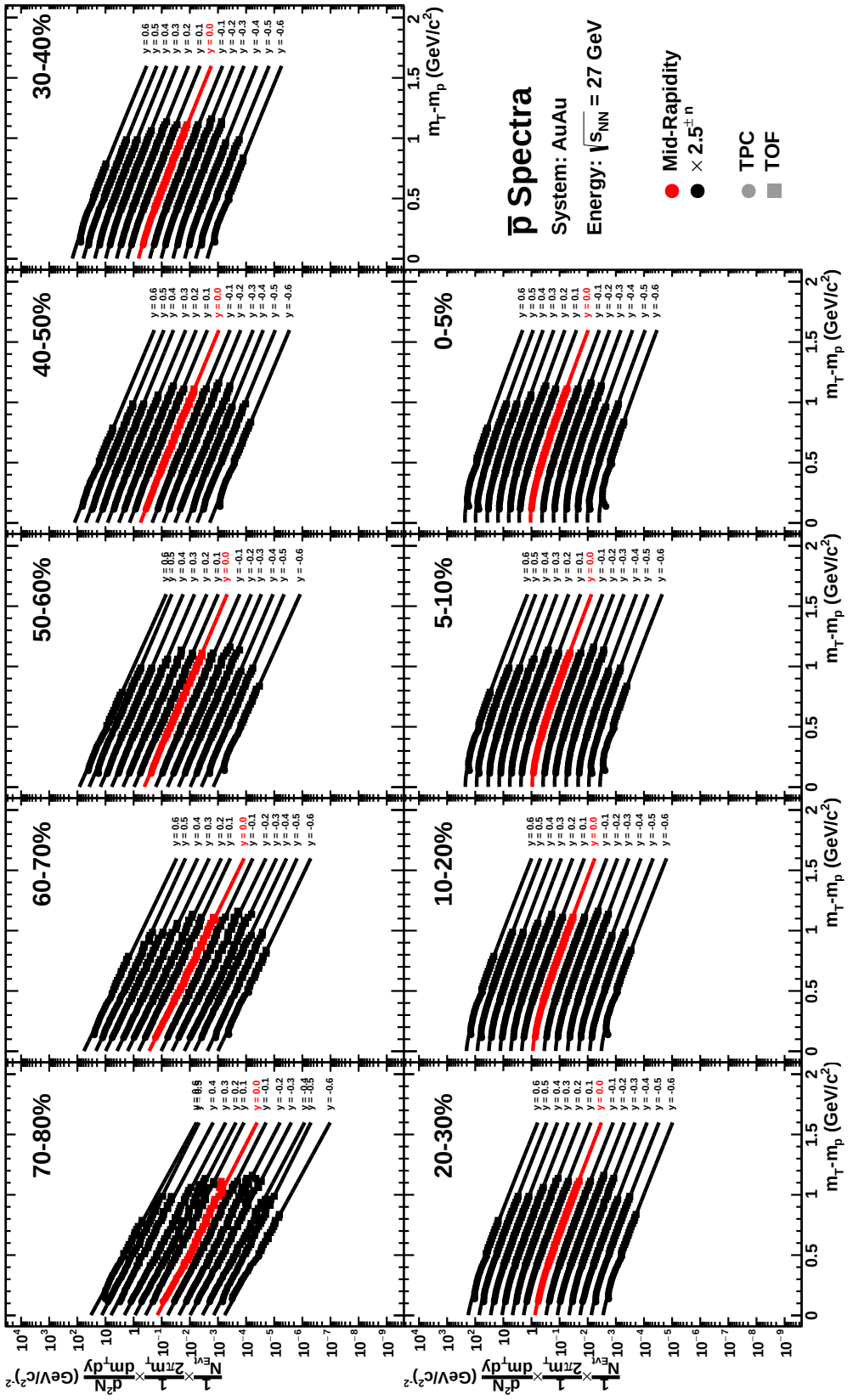

Figure 8.42: Transverse Mass Spectra: $\bar{p}$ ColliderCenter $\sqrt{s_{NN}} = 27.0$ GeV

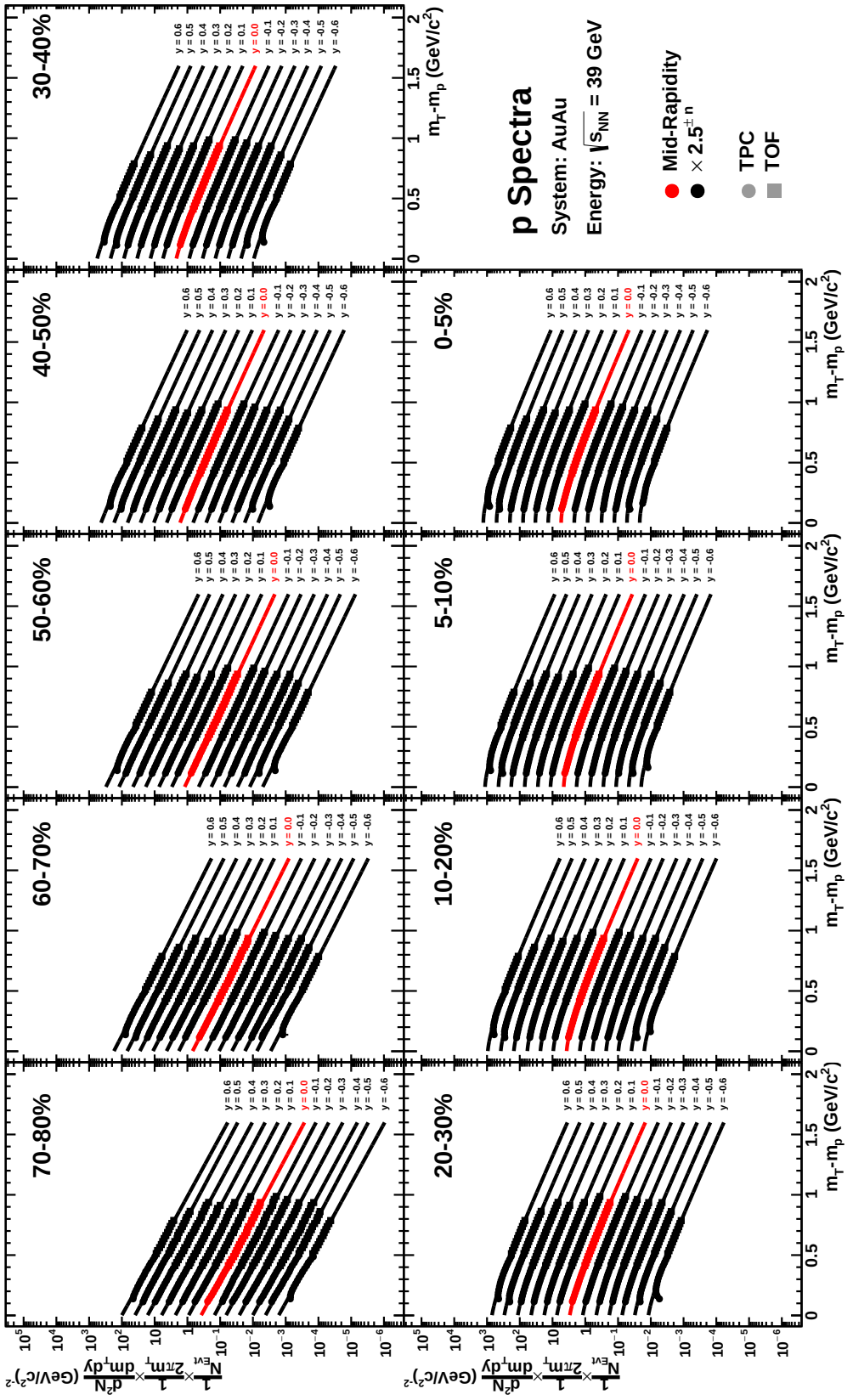

Figure 8.43: Transverse Mass Spectra: p ColliderCenter $\sqrt{s_{NN}} = 39.0$ GeV

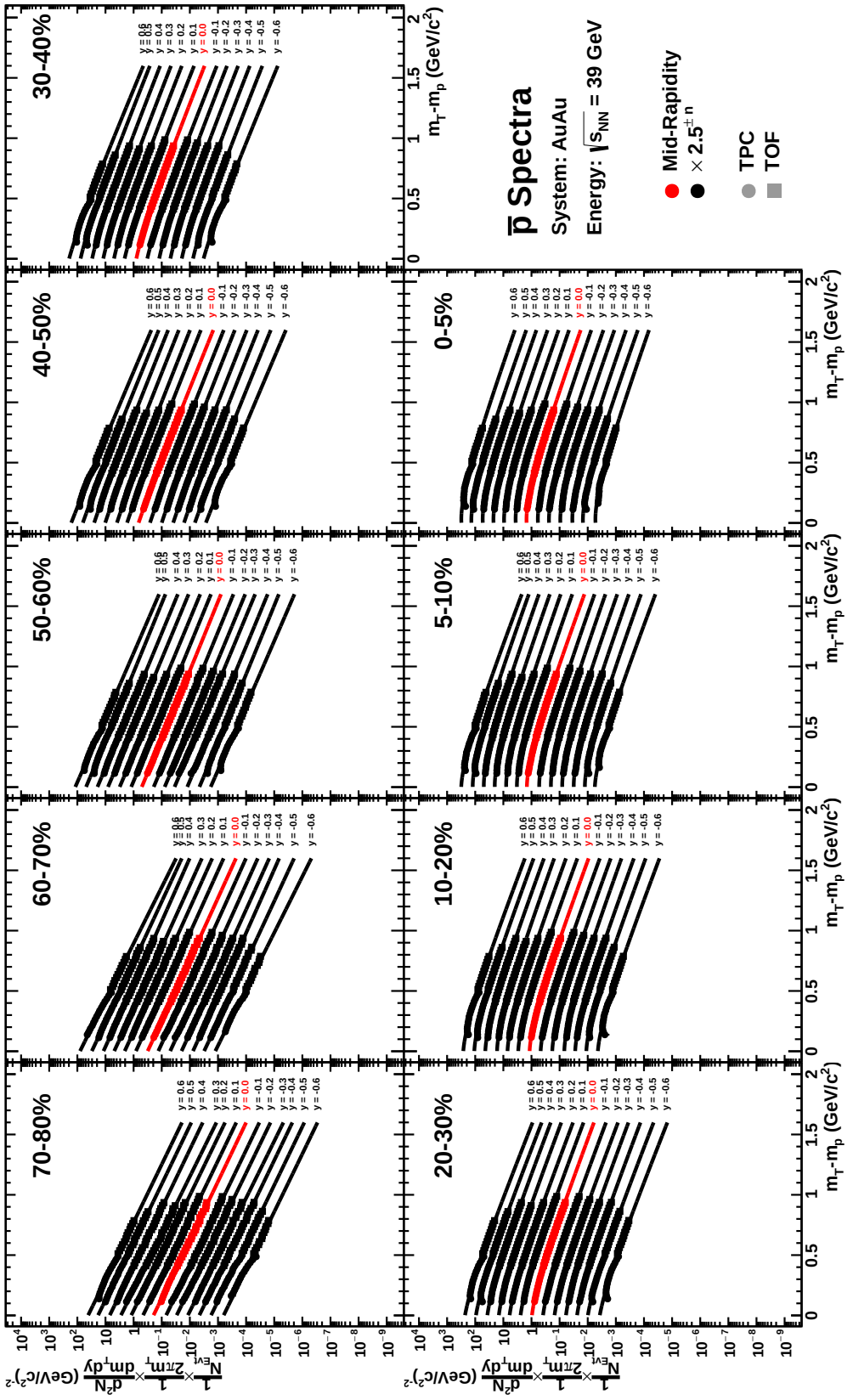

Figure 8.44: Transverse Mass Spectra: $\bar{p}$ ColliderCenter $\sqrt{s_{NN}} = 39.0$ GeV

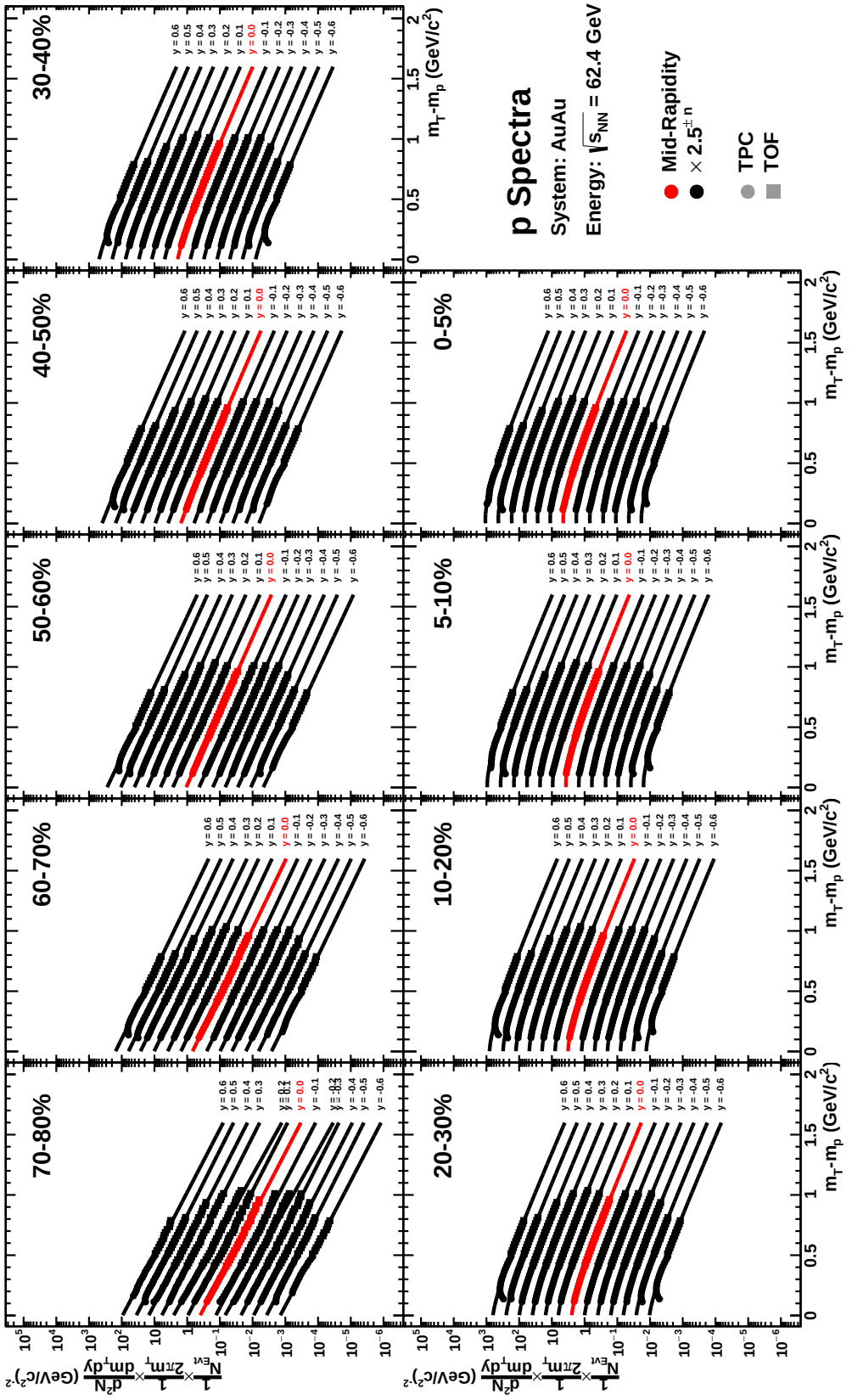

Figure 8.45: Transverse Mass Spectra: p ColliderCenter $\sqrt{s_{NN}} = 62.4$ GeV

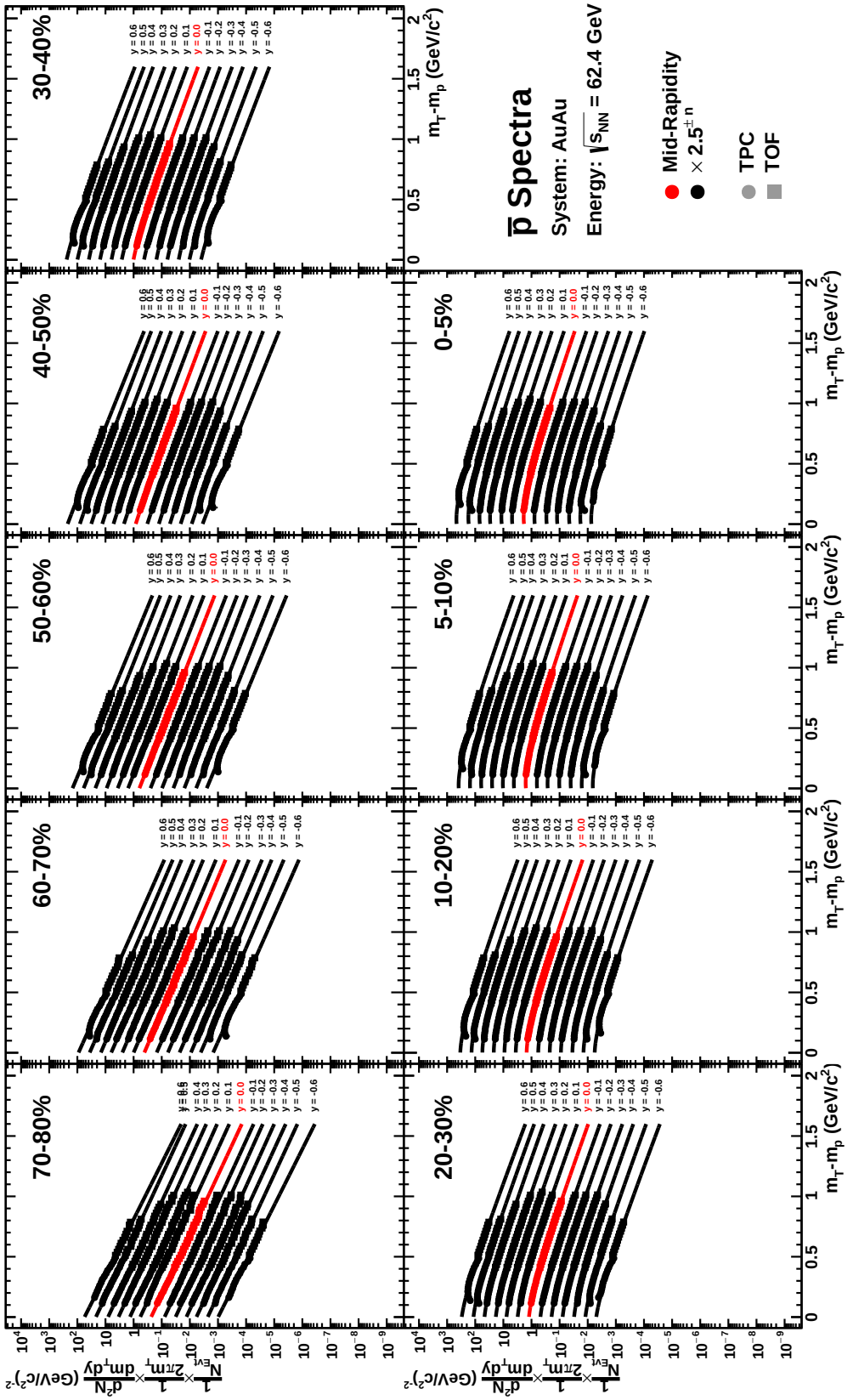

Figure 8.46: Transverse Mass Spectra: $\bar{p}$ ColliderCenter $\sqrt{s_{NN}} = 62.4$ GeV

8.3 Rapidity Density Distributions

In this section the rapidity density distributions for each collision energy, particle, and centrality bin are presented. As previously mentioned, the yield of each particle species at each collision energy and for each combination of centrality and rapidity bin is obtained by integrating the nominal fit function which was extrapolated into the unmeasured regions of transverse mass. Since the shape parameters of the spectra in equal forward/backward rapidity ranges were required to be the same, the only difference between the dN/dy quantities in the forward/backward bin is a difference in overall normalization. To find the dN/dy for a bin at absolute value of rapidity the weighted average of the dN/dy obtained in the forward/backward bin is computed. The weights are the inverse square of the statistical errors. Note that since the midrapidity point is only measured once, it is left unchanged.

Since the asymmetry in the dN/dy values should have no dependence on rapidity, that is, the difference should not become larger or smaller as a function of rapidity, the relative errors on the weighted averages are used to obtain an average relative error. This average relative error is then applied to each point in the rapidity density distribution. The results of this procedure are shown in the figures of this section. The closed symbols represent the weighted averages while the open symbols are their reflections about midrapidity. The centrality of the events contributing to each distribution is denoted at the top right of each panel.

The largest source of systematic errors on the dN/dy values is the extrapolation of the fit function to the unmeasured, low transverse mass region. As discussed above, this error has been estimated by obtaining the dN/dy using two different functional forms to fit each spectrum. We report this systematic error as a "global" error for each energy and particle species combination. The quantity is computed by calculating the average percent difference between the nominal and alternative fits across all centrality and rapidity bins for a particle species and energy combination. Rather than adding complexity to the figures of this section, the systematic errors are shown in table 8.1.

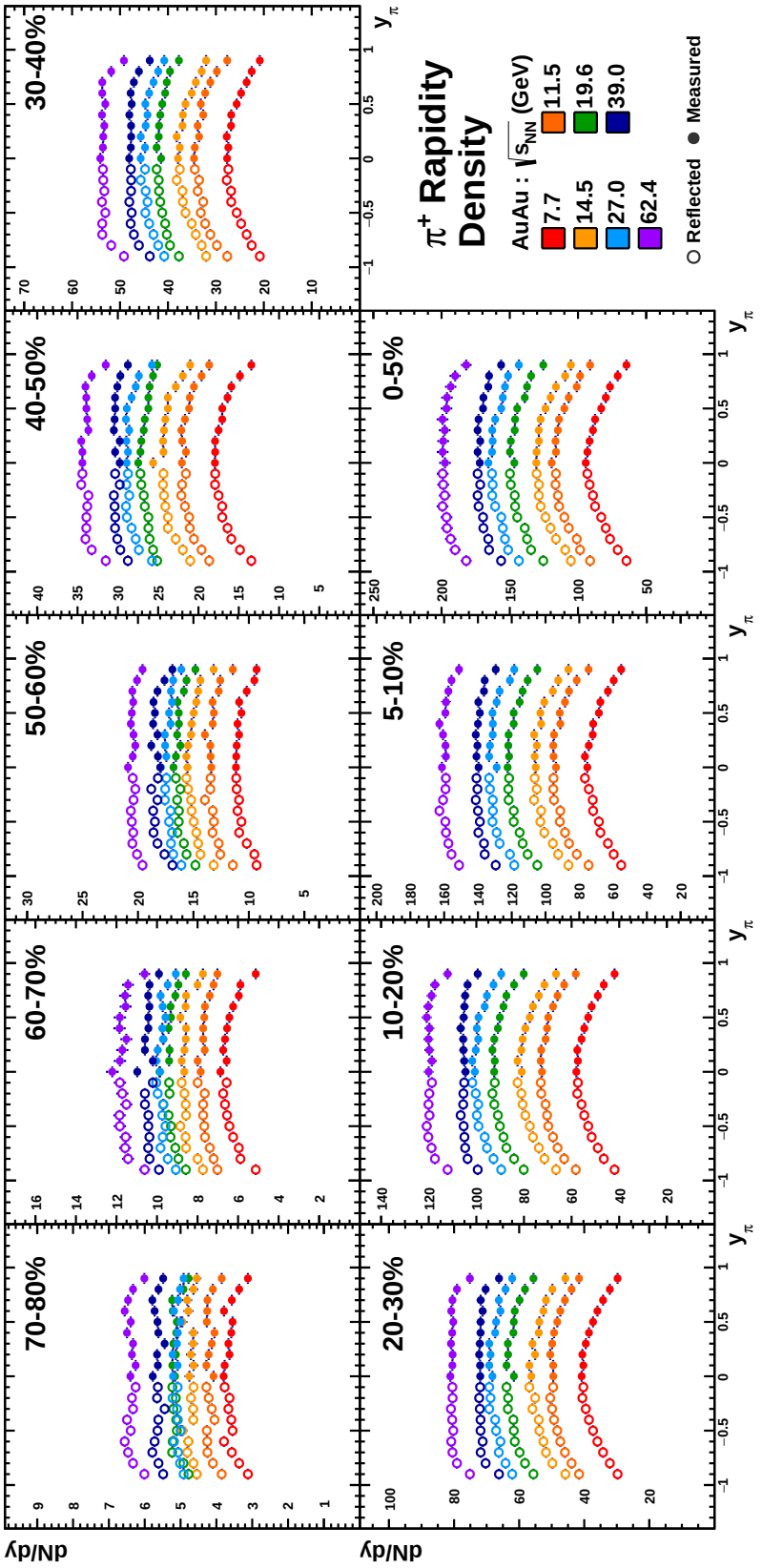

Figure 8.47: Rapidity Density: π^+ ColliderCenter All Energies

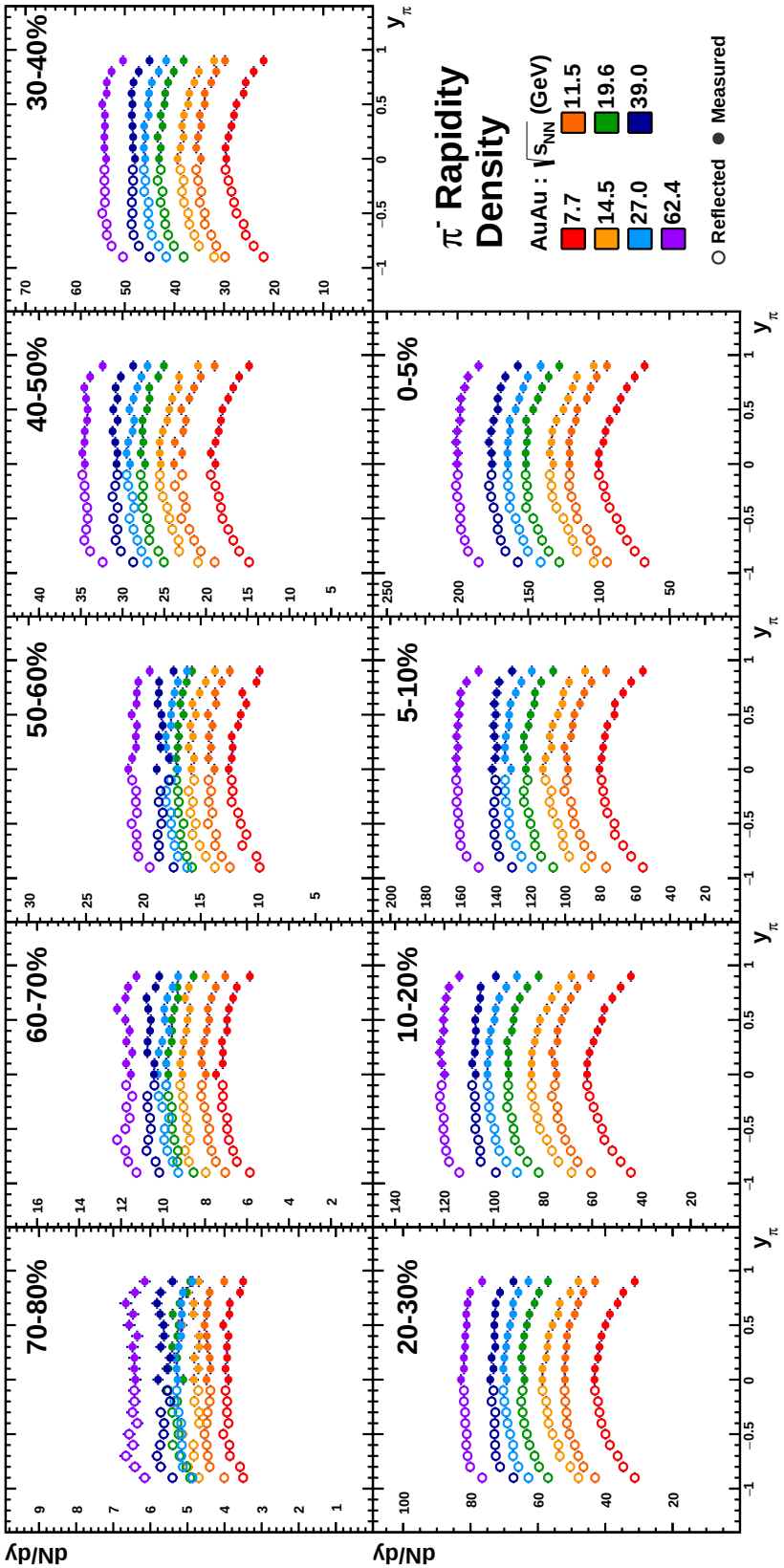

Figure 8.48: Rapidity Density: π^- ColliderCenter All Energies

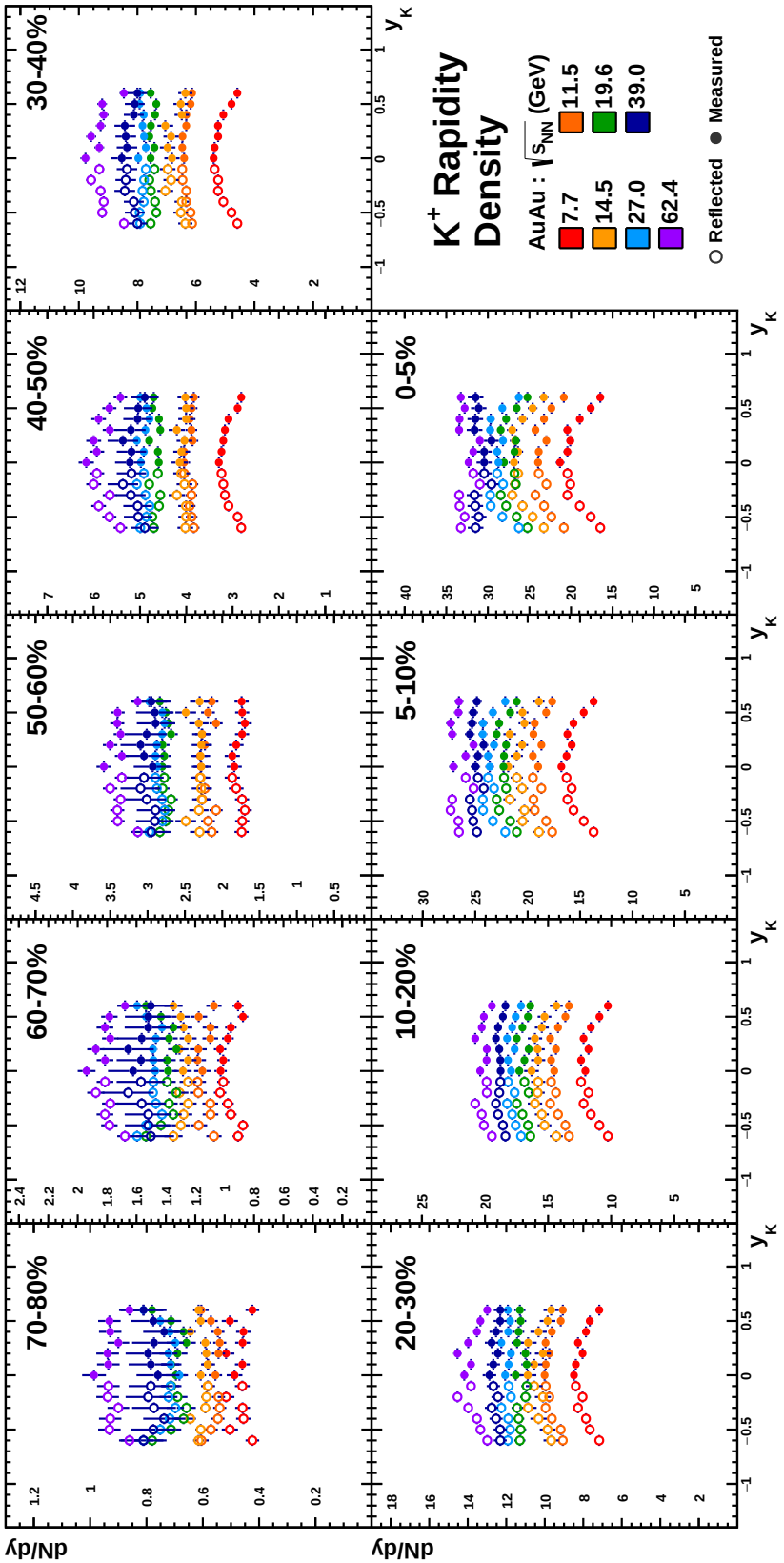

Figure 8.49: Rapidity Density: K^+ ColliderCenter All Energies

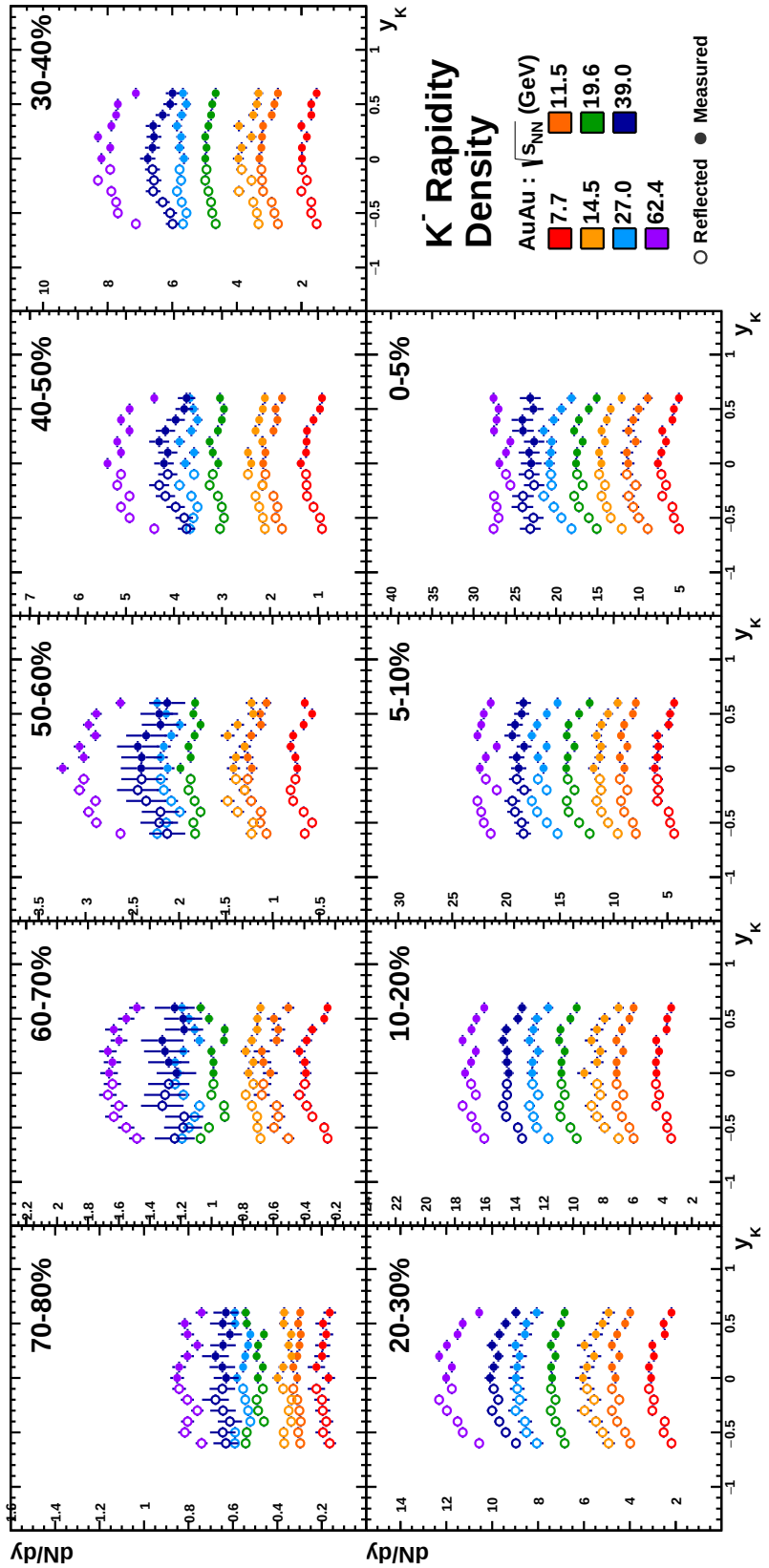

Figure 8.50: Rapidity Density: K^- ColliderCenter All Energies

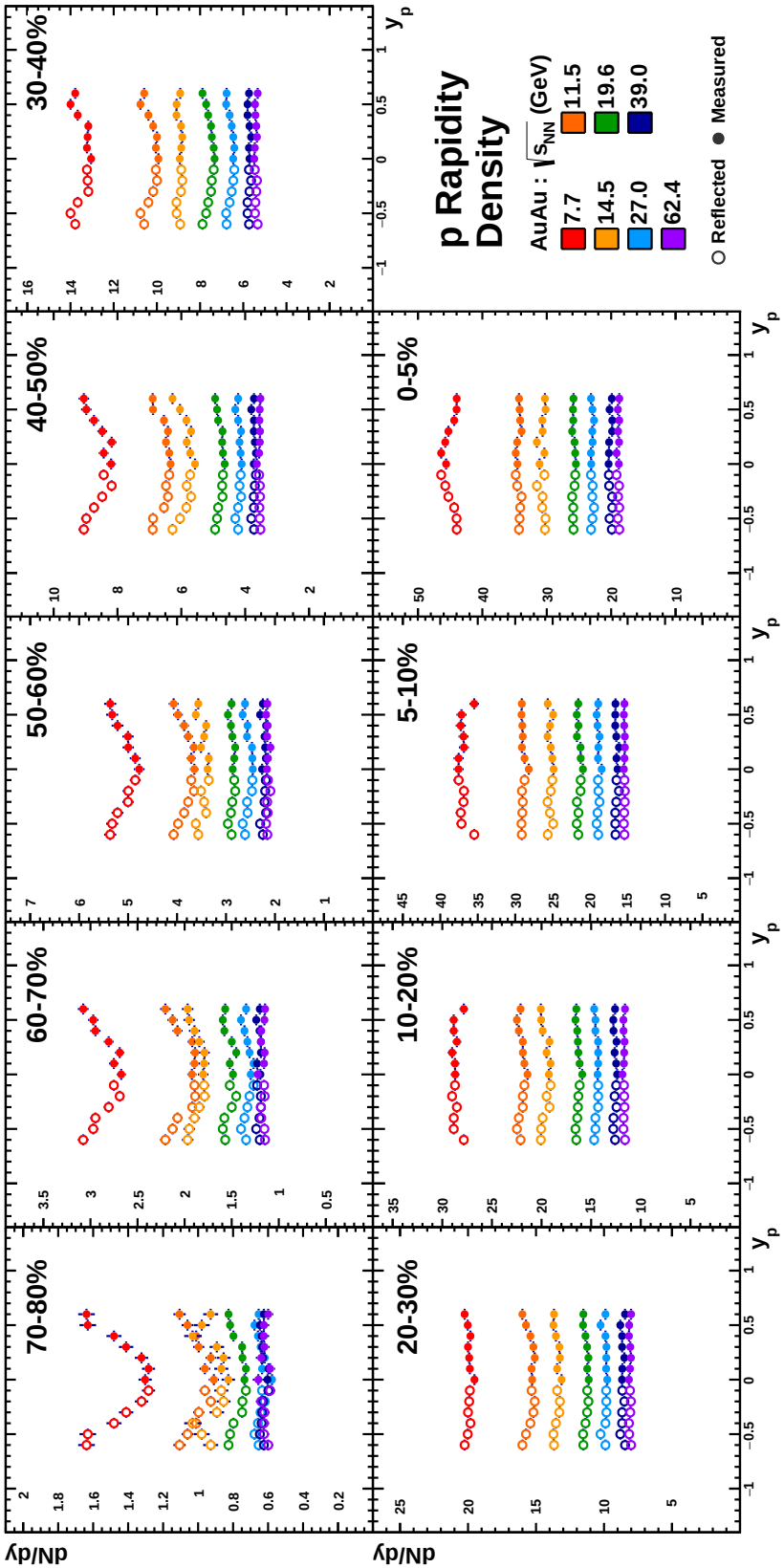

Figure 8.51: Rapidity Density: p ColliderCenter All Energies

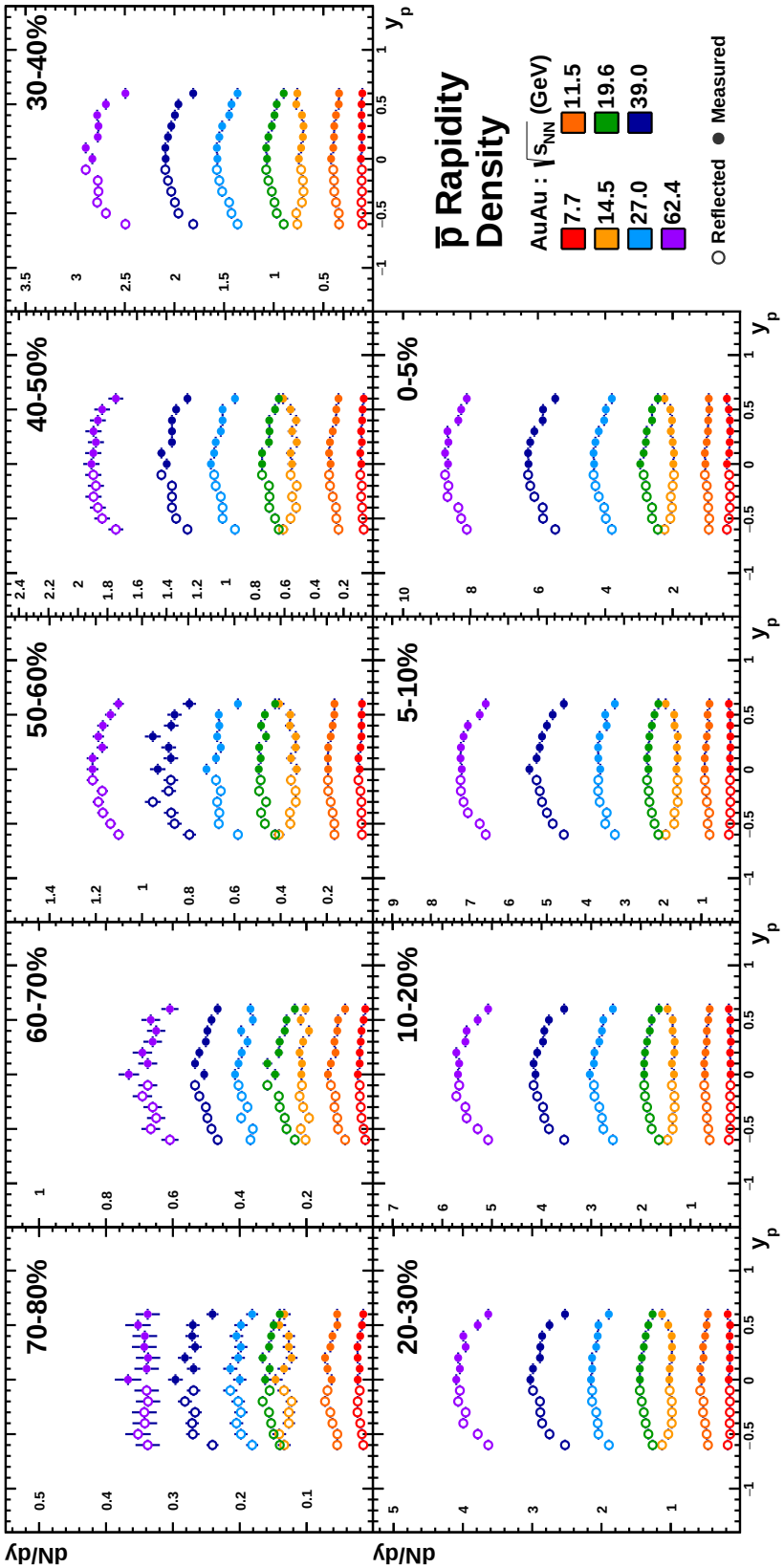

Figure 8.52: Rapidity Density: $\bar{p}$ ColliderCenter All Energies

$\sqrt{s_{NN}}$ **(GeV)**	π^+	π^-	K^+	K^-	p	$\bar{p}$
7.7	4.0 %	3.6	4.5	4.3	3.0	4.7
11.5	5.2	5.0	5.4	5.1	4.3	4.7
14.5	6.1	5.9	6.2	6.0	4.1	5.2
19.6	6.3	6.2	6.4	5.9	2.2	3.6
27.0	7.2	7.1	6.8	6.4	1.9	1.9
39.0	7.8	7.7	7.3	7.3	2.9	1.9
62.4	8.0	7.8	7.0	7.0	2.5	1.8

Table 8.1: The percent systematic error on the dN/dy values associated with the extrapolations to the unmeasured transverse mass regions. The errors are computed using the average percent difference between the dN/dy values obtained from the nominal and alternative fit functions. The average is computed using the results from all centrality and rapidity bins for each combination of collision energy and particle species.

8.4 Full Phase Space Yields of $\pi^{\pm}$

The full phase space yields of the particles can now, in principle, be obtained from the rapidity density distributions. However, only the pion rapidity density distributions extend far enough in rapidity to be fit with a model. We use the Landau hydrodynamics model, discussed in the introductory chapter, to fit the $\pi^{\pm}$ rapidity density distributions with Gaussian functions. For direct comparison to previous results, we only perform this analysis for the most central collisions at each energy. Figure 8.53 shows the results of these fits. As in previous figures, the solid symbols are the result of the forward/backward weighted averaging and the open symbols are their reflections. The Gaussian functions (solid curves) are constrained to have a mean at midrapidity and are fit from midrapidity forward. The function is then reflected about midrapidity (dashed curve). The Gaussian fits are then integrated to obtain the full phase space (4π) yields for π^+ and π^-. Figure 8.54 shows the full phase yields obtained in this analysis (red stars) compared to previous results obtained by the E895 [15], NA49 [16, 17], and BRAHMS [18] experiments.

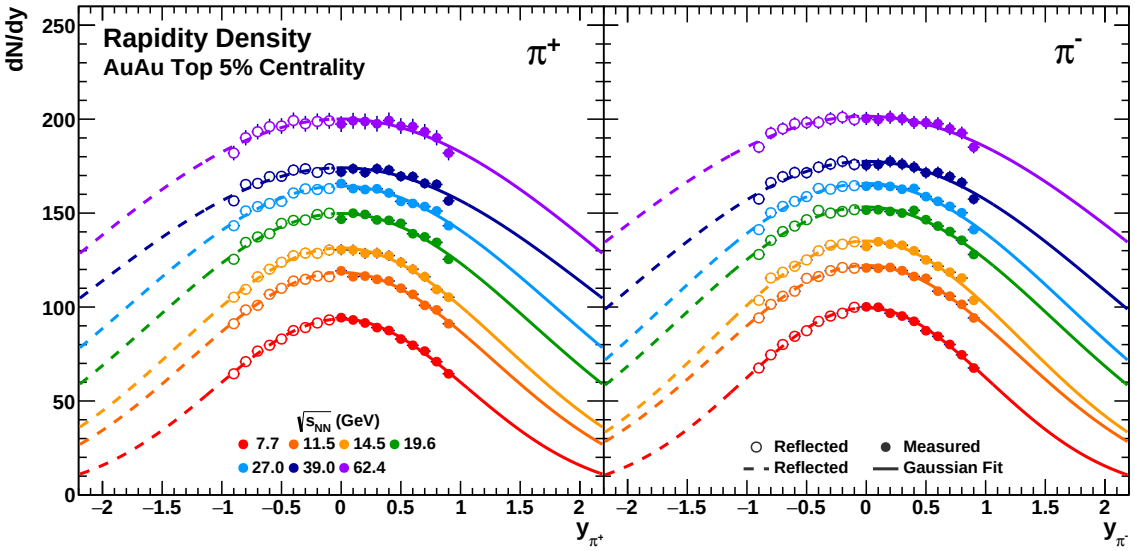

Figure 8.53: The rapidity density distributions of π^+ (left) and π^- (right) of the most central 5% Au+Au collisions at each energy in the present analysis. The closed symbols are the forward/backward weighted averages and the open symbols are their reflections. The closed symbols are fit with a single Gaussian function with the mean fixed to zero. The function extrapolation to the reflected region is shown as a dashed line.

In an effort to create as close a comparison as possible, two additional effects have been taken into account in the figure. First, the rapidity density distributions reported from the previous analyses were obtained and refit using the same single Gaussian methodology as described above. This ensures that all yields are obtained the same way. The single Gaussian model is found to describe the data from previous experiments quite well. Second, the NA49 experiment measured collisions between lead nuclei rather than the gold nuclei measured by the other experiments. In addition, the centrality percentile of the collisions measured from the NA49 collision vary slightly compared to the other experiments. To account for these two differences, which both affect the system size, the yields have been scaled by the average number of participating nucleons, $N_{\rm part}$. The results from the previous experiments have been scaled by the $N_{\rm part}$ values reported by their respective collaborations, as shown in table 8.2. The results from this analysis are scaled by the values of $N_{\rm part}$ obtained in chapter three. The uncertainties on the results from this analysis include both the statistical errors associated with the yield extraction methodology and the total error associated with the determination of $N_{\rm part}$.

The full phase space yields obtained from this analysis are observed to follow the trend established by the E895 experiment, the low energy NA49 points, and extrapolate smoothly to the BRAHMS result. It is curious that mid to high energy results of NA49 are systematically higher than those obtained in this analysis. We postulate that this is due to the extraction method used by the NA49 collaboration. As discussed in ref [17] , the NA49 collaboration extracted their π^- spectra by measuring the yield of all negative tracks. Then the contribution to these spectra from K^-, $\bar{p}$, e^-, and other backgrounds were subtracted using an event generator and detector simulation. Because strangeness production is turning on rapidly in this energy range, it is possible that the event generator produced insufficient strangeness and thus a correction factor that was too low to account for the true yield of kaons. This would account for why the full phase space yields agree at the lower energies where strangeness production is insignificant, but then increasingly diverge at higher energies where strangeness production becomes increasingly important.

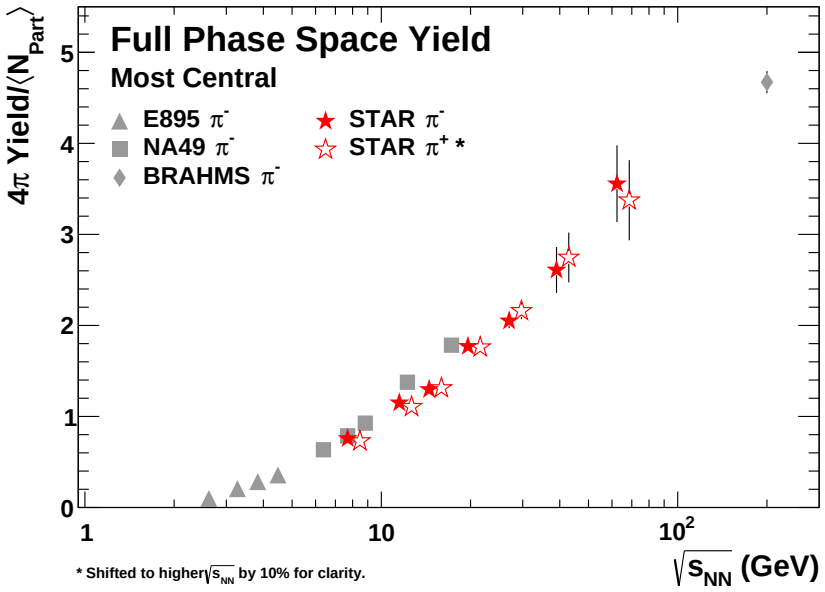

Figure 8.54: Full phase space yield of $\pi^{\pm}$ from central Au+Au collisions at each energy investigated in this analysis (red) scaled by the number of average participating nucleons from table 3.5. The results for π^{+} are shifted to higher $\sqrt{s_{NN}}$ by 10% for clarity. Where available, results from previous collaborations (E895 [15], NA49 [16, 17], and BRAHMS [18]) for π^{-} are also shown (gray). See the main text for details.

$\sqrt{s_{NN}}$ (GeV)	Experiment	% Centrality	$\langle N_{\mathbf{Part}} \rangle$
2.6	E895 [15]	0-5	364 ± 5
3.3	E895 [15]	0-5	366 ± 5
3.8	E895 [15]	0-5	365 ± 5
4.5	E895 [15]	0-5	363 ± 5
6.4	NA49 [16]	0-7.2	349 ± 5
7.7	NA49 [16]	0-7.2	349 ± 5
8.8	NA49 [17]	0-7.2	349 ± 5
12.4	NA49 [17]	0-7.2	349 ± 5
17.3	NA49 [17]	0-5.0	362 ± 5
200	BRAHMS [79]	0-5	363 ± 9.3

Table 8.2: Centrality percentage and average number of participating nucleons for data reported by previous collaborations.

8.5 The Dale Observable

We now return to one of the observables used to argue for the onset of deconfinement – the Dale Observable. The widths of the pion rapidity density distribution for each collision energy were obtained from the fits in the previous section and are shown in figure 8.55 as a function of collision energy. As before, results obtained by refitting the rapidity density distributions of previous experiments are also shown. For comparison the expected width of the pion rapidity density distribution from Landau hydrodynamics is shown as a curve. For clarity the π^+ results have been shifted to higher $\sqrt{s_{NN}}$ by 10%.

The results obtained from this analysis are consistent with the increasing trend in the measured energy range established by previous experiments. The large errors in the highest energy results from this analysis are due to broadening of the rapidity density distributions beyond acceptance of the detector. That is, the measured region of rapidity space is insufficient to constrain the width of the Gaussian fit. Reducing these errors was one of the objectives of the displaced vertices in the $PosY$ and $NegY$ configurations in this analysis. However, those event configurations are only available for the lowest four energies where the small error indicates that the value is well constrained. This demonstrates one of the reasons why the $PosY$ and $NegY$ events were redundant.

As noted in the introductory chapter, the measured width of the $\pi^{\pm}$ rapidity density distributions can be compared to the expected width from Landau hydrodynamics. The minimum ("Dale") that was observed in the ratio of the quantities as a function of collision energy was argued to indicate a softening of the equation of state (EoS) of the system and thus interpreted as an indicator of a first-order phase transition.

The results of this ratio obtained from this analysis are shown in figure 8.56 along with results from previous experiments obtained via the aforementioned refitting procedure. The increasing trend in the measured range is consistent with the previous observation of a minimum. Again, the large errors on the ratio at the high energies of this analysis result from being unable to sufficiently constrain the width of the Gaussian fits due to the acceptance limitations of the detector. Measurements at lower energies, aimed at confirming the rise of the ratio, are an objective of the fixed-target program at STAR. As

discussed in the introduction, such an observation would be consistent with the medium existing in a mixed phase in the energy range of the minimum.

8.6 Energy Dependence of the Most Central, Midrapidity Results

We conclude the results chapter by investigating the energy dependence of the most central, midrapidity results. Where possible we include similar results from previous experiments to provide context for the interpretation of the results from this analysis. Many of the quantities shown in this section have been previously measured and reported by the STAR Collaboration. The quantities obtained from this analysis are included here for completeness and for comparison to previously published results.

We begin by showing the most central, midrapidity spectra of all particles in the first section. We then proceed to show the fit parameters of the nominal spectra functions, use the nominal spectral functions to obtain the mean transverse mass, and finally show the particle yields and ratios.

8.6.1 Most Central, Midrapidity Spectra

The most central, midrapidity spectra of all particles studied in this analysis are shown grouped by collision energy in figure 8.57 and grouped by species in 8.58. The spectra are shown unscaled in all cases. As before, particles with negative charge are shown in solid symbols, particles with positive charge are shown in open symbols, and the difference in the symbol type denotes the detector used for the yield extraction. The functions in figure 8.57 are the nominal spectral shapes for each species.

The energy scaling of particle production is evident in figure 8.58. The pions, kaons, and anti-protons are produced more numerously with collision energy, as expected. Also as expected, but showing the opposite energy dependence, are the protons. Because baryon stopping is reduced with collision energy, more protons result from collisions at lower energies where baryon stopping is most significant.

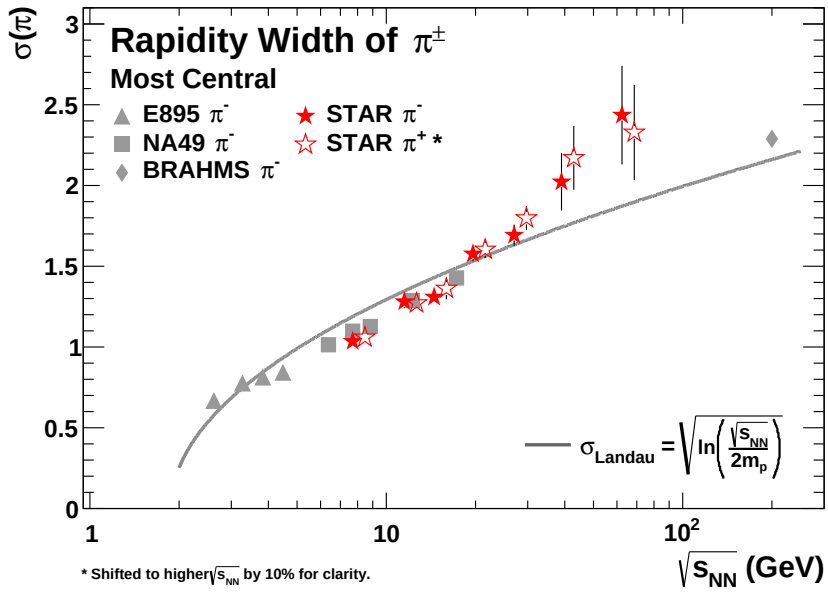

Figure 8.55: The width of the $\pi^{\pm}$ rapidity density distributions at each energy in the present analysis (red). Where available results from previous collaborations for π^- are also included. (E895 [15], NA49 [16, 17], and BRAHMS [18])

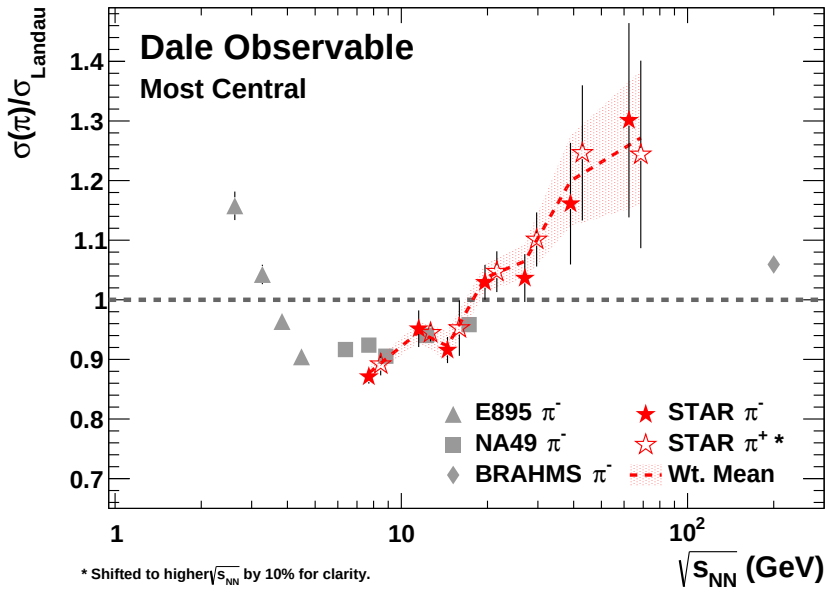

Figure 8.56: The width of the $\pi^{\pm}$ rapidity density distributions divided by the expected Landau width at each energy. (E895 [15], NA49 [16, 17], and BRAHMS [18])

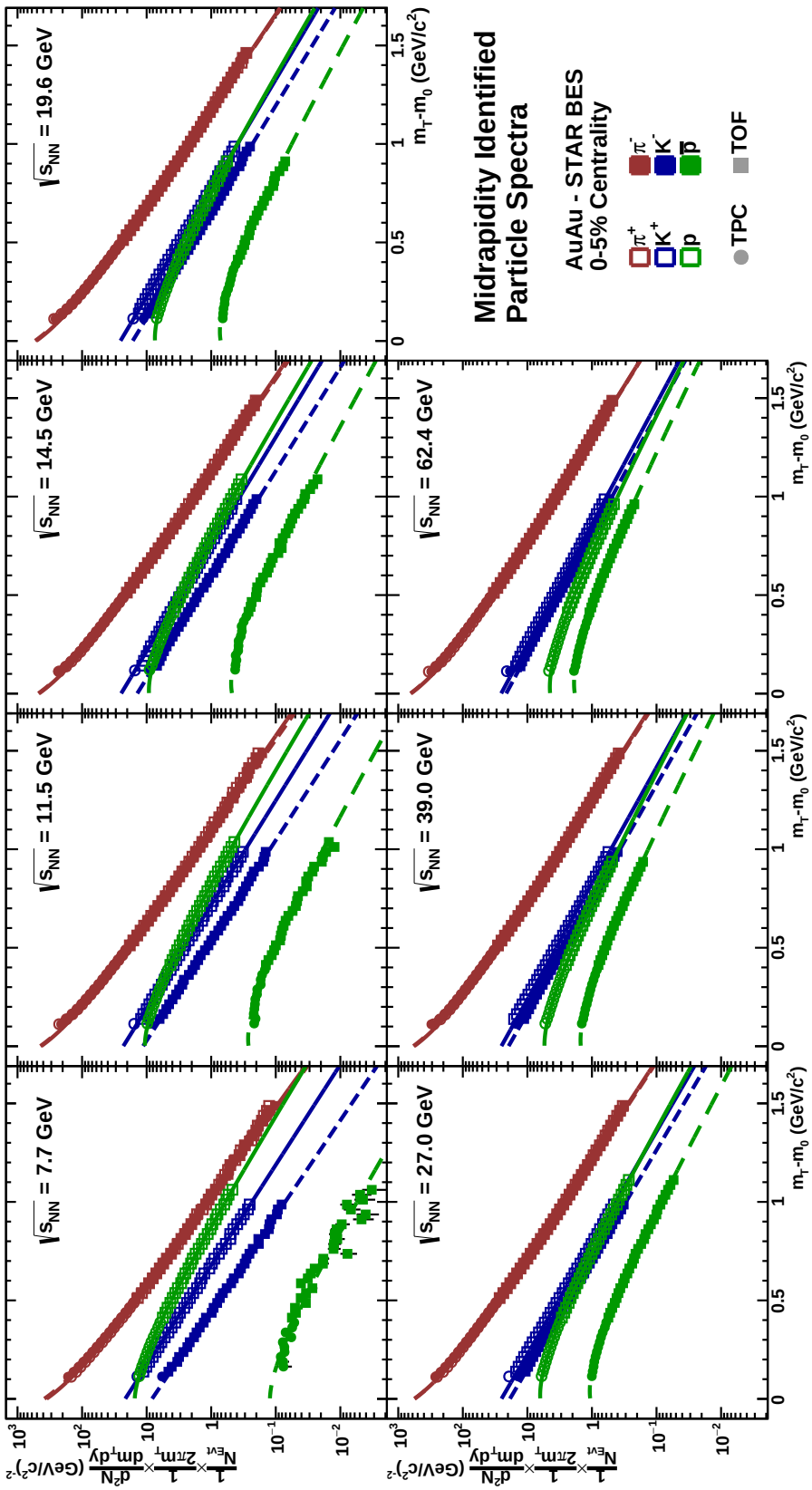

Figure 8.57: The most central, midrapidity spectra of all particle species grouped by collision energy. The curves are the nominal fits previously described.

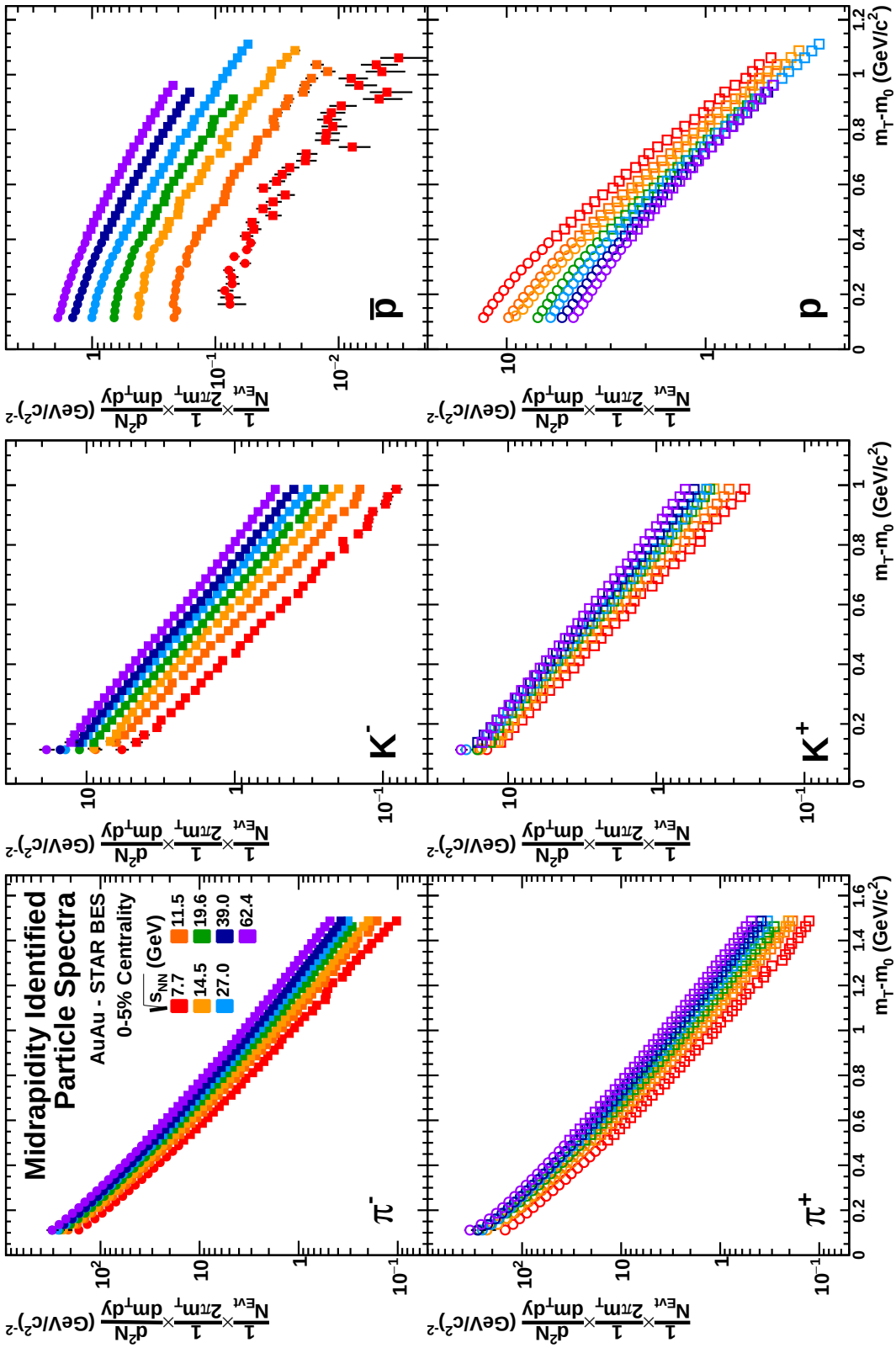

Figure 8.58: The most central, midrapidity spectra of all particle species studied in this analysis grouped by species.

8.6.2 Spectral Model Parameters

The parameters in the spectral fit functions can be used to infer how the thermal and expansion properties of the medium resulting from a heavy-ion collision develop as a function of energy. Figure 8.59 shows the shape parameters of the nominal functions that are left free in the fits to the most central, midrapidity spectra as a function of collision energy. The effective temperatures, $T_{\rm slope}$, of the pions and kaons are observed to increase gradually over the BES energy range. The kinetic freeze-out temperature, $T_{\rm kin}$, the surface velocity, $\beta_{\rm surf}$, and the average transverse velocity, $\langle\beta\rangle$, obtained from the simultaneous blast wave fits to the proton and anti-proton spectra are observed to vary little over the range of the BES energies. Both the energy independence and magnitude of the quantities are consistent with results previously reported by STAR in [39], as can be seen via a comparison to figure 8.60.

Its worth noting that the agreement of the blast wave parameters exists despite several different analysis choices. Recall that in this analysis the blast wave fits, and therefore these parameters, are determined exclusively from the proton and anti-proton spectra, that the proton and anti-proton fits do not share the same $\beta_{\rm surf}$ parameter, and are for a single choice of the velocity profile parameter, n. Further, recall that the proton spectra in this analysis have been corrected for feed down contributions. On the other hand, in [39] the blast wave parameters are obtained from simultaneous fits of $\pi^{\pm}$, $K^{\pm}$, p, and $\bar{p}$ spectra with the n parameter left free and where the proton spectra are inclusive.

Figure 8.61 shows the mean transverse mass obtained from the nominal spectra fits to the most central, midrapidity spectra as a function of collision energy from this analysis. The energy dependence of the measurement is the same as the slope parameters by definition. As with the slope parameters, both the energy dependence and magnitude of the quantities are consistent with previously reported results from STAR which are shown in figure 8.62. The exception is the larger difference between the average transverse mass of the proton and anti-proton in this analysis. This is due to allowing the proton and anti-proton spectra to have different $\beta_{\rm surf}$ parameters. This choice was made to obtain the best possible fits to the spectra for the purposes of extracting dN/dy.

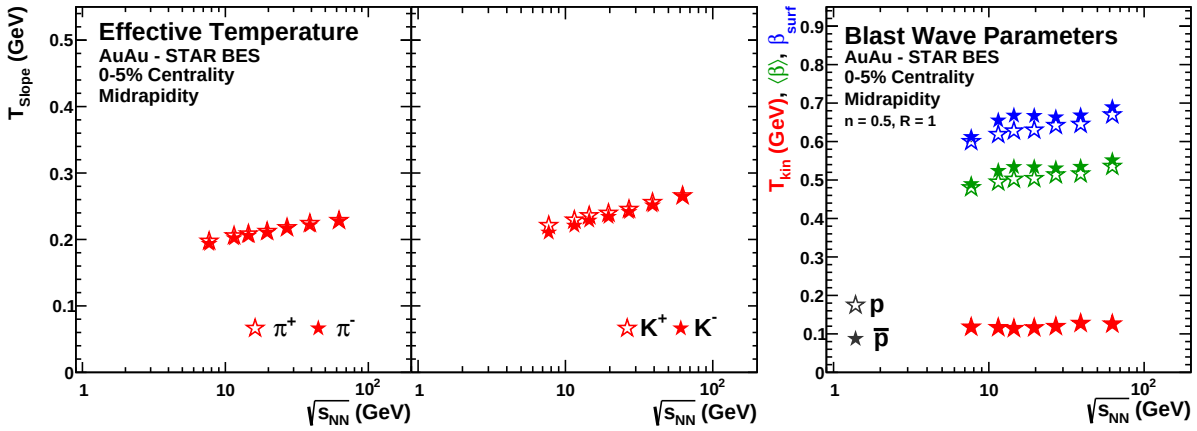

Figure 8.59: Shape parameters obtained from the nominal spectral fit shapes of the most central, midrapidity spectra as a function of collision energy. In the case of the blast wave parameters, average transverse velocity, $\langle\beta\rangle$, is obtained via $\langle\beta\rangle = (2/(2+n))\beta_{\rm surf}$.

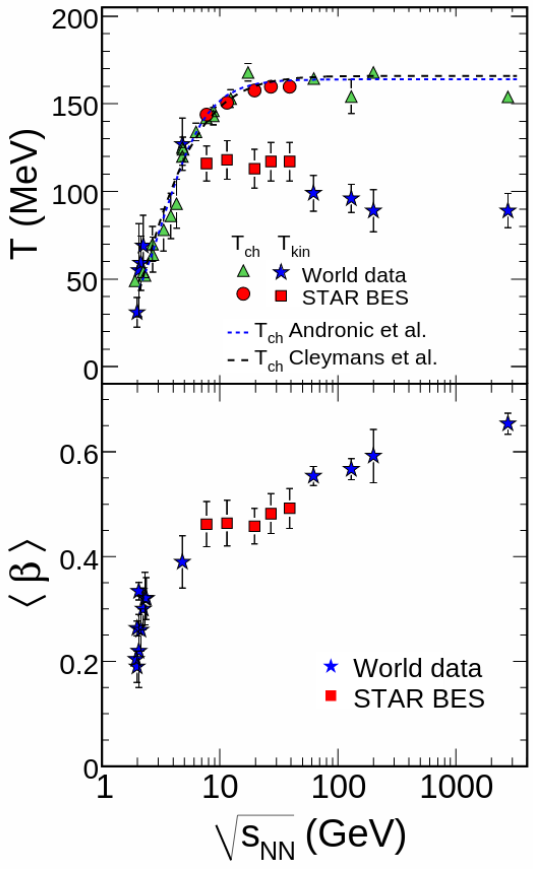

Figure 8.60: Freeze-out temperatures and average transverse velocities obtained from previous experiments and analyses. Of particular relevance are the red squares. These show the kinetic freeze-out temperature (top) and average transverse velocities (bottom) obtained from previous STAR measurements and are directly comparable to the blast wave results in figure 8.59. This figure was obtained from [39].

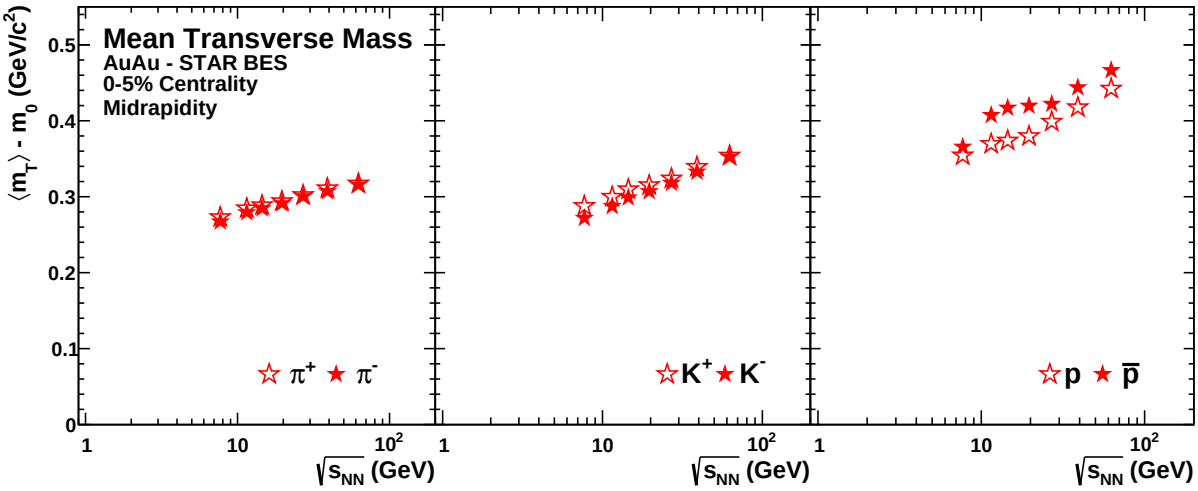

Figure 8.61: The energy dependence of the average transverse mass of all particle species studied in this analysis obtained from the nominal fits of the most central, midrapidity spectra.

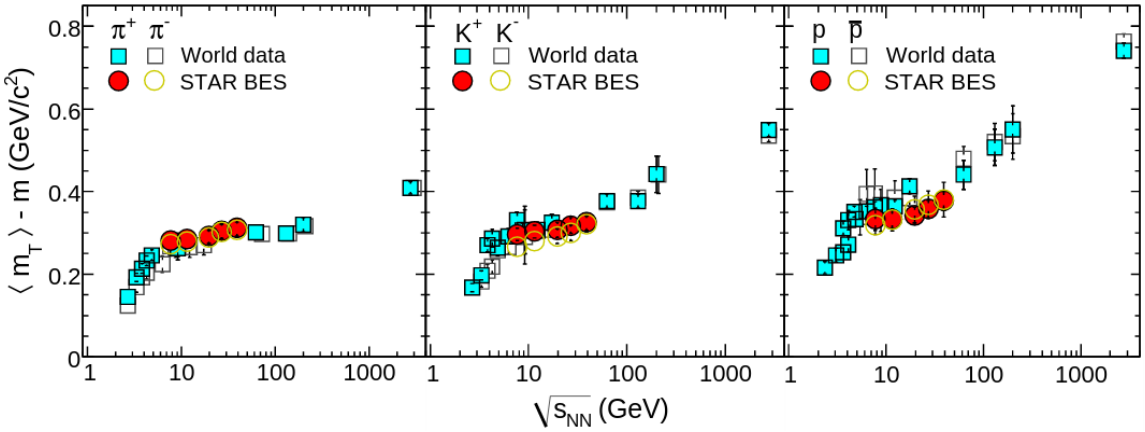

Figure 8.62: The mean transverse mass of pions, kaons, and protons obtained from previous analyses and experiments. Of particular interest are the closed red and open yellow symbols as they are results previously reported by STAR and are directly comparable to the results from this analysis in figure 8.61. This figure was obtained from [39].

8.6.3 Particle Yields and Ratios

The yields and ratios of the various particle species produced in heavy-ion collisions can be used to assess the chemistry of the medium. Figures 8.63 and 8.65 show the energy dependence of the yields of all particle species and their particle to antiparticle ratios respectively. The results are from the most central collisions and at midrapidity. In the case of figure 8.63, the results have been scaled by the number of participant pairs to remove the effect of the collision system volume and for direct comparison to previous results shown in figures 8.64 and 8.66 [39]. In all cases, comparison of trends and magnitudes of the results from this analysis to those previously reported by STAR [39] show excellent agreement.

Except for the proton, the yields of all species increase monotonically with collision energy. The proton yield is reduced with collision energy due to the reduction in baryon stopping and hence the $\bar{p}/p$ ratio tends to unity. The pion ratio is observed to be very near unity over the entire energy range. The largest deviation from unity occurs at $\sqrt{s_{NN}}$ = 7.7 GeV and is due to the increasing production of strongly decaying resonances such as the Δ baryon at low energies. The Δ states rich in d quarks, which decay to π^-, are produced in larger quantities due to the surplus of d quarks over u quarks. The d to u imbalance, itself, also results from the degree of baryon stopping since incoming nuclei are rich in neutrons and thus contain more d quarks.

Given their equivalent mass and quark content flavors, one might expect the yields of K^+ and K^- to be nearly identical in the same way the yields π^+ and π^- are nearly identical. However, u quarks outnumber $\bar{u}$ quarks because u quarks are deposited into the system by the incoming baryons. Thus the yield of K^+ ($u\bar{s}$) is larger than the yield of K^- ($\bar{u}s$). The difference between the K^+ and K^- yields decreases with increasing collision energy as observed by the K^-/K^+ ratio. This is also due to the reduction in baryon stopping. Since fewer incoming baryons are stopped as the collision energy increases, the ratio of $\bar{u}/u$ tends to unity and, so too, does the K^-/K^+ ratio.

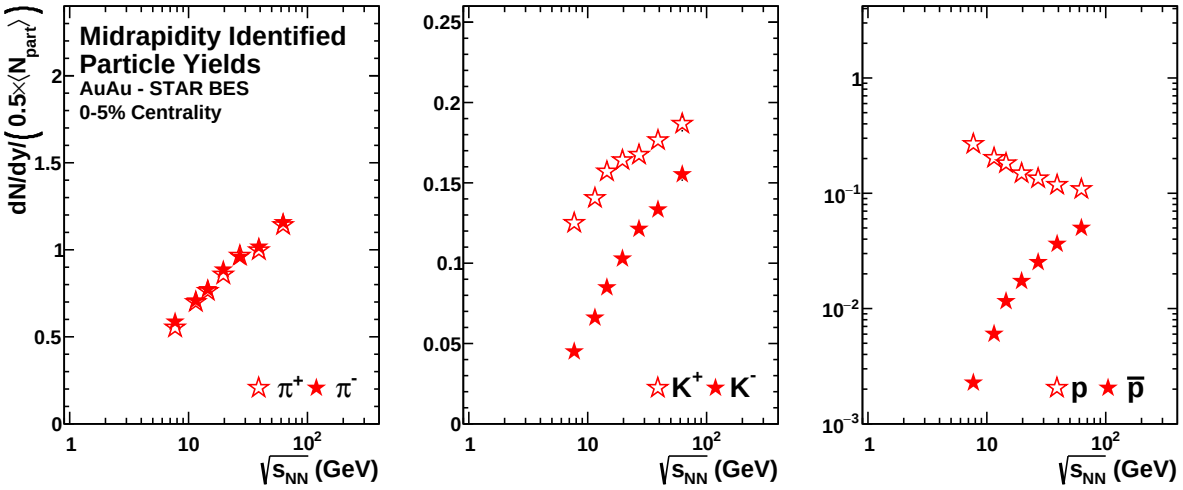

Figure 8.63: The energy dependence of the yield of all particle species studied in this analysis produced at midrapidity in the most central collisions.

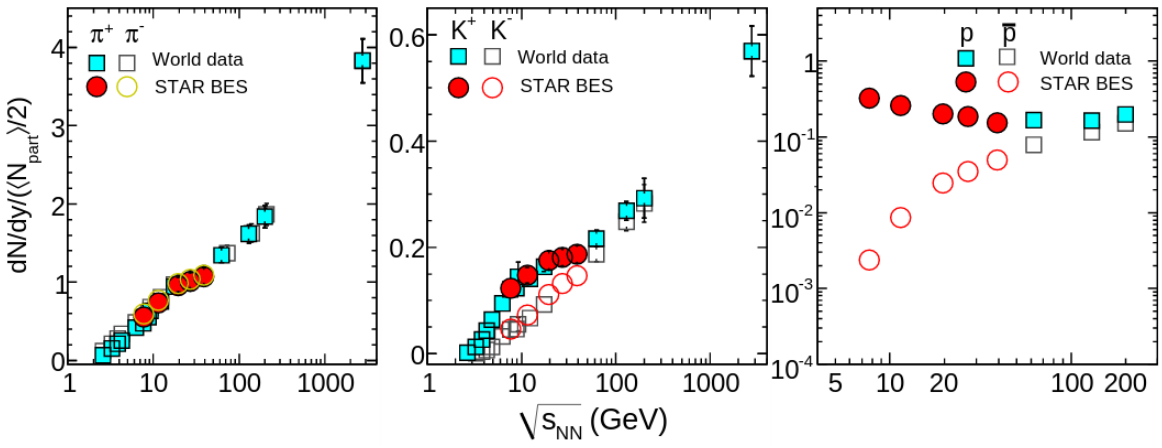

Figure 8.64: Previously reported yields of particles from central heavy-ion collisions at midrapidity as a function of collision energy. Of particular relevance are the closed red and open yellow circles as they are previously reported results from STAR and are directly comparable to the results in figure 8.63. This figure was obtained from [39].

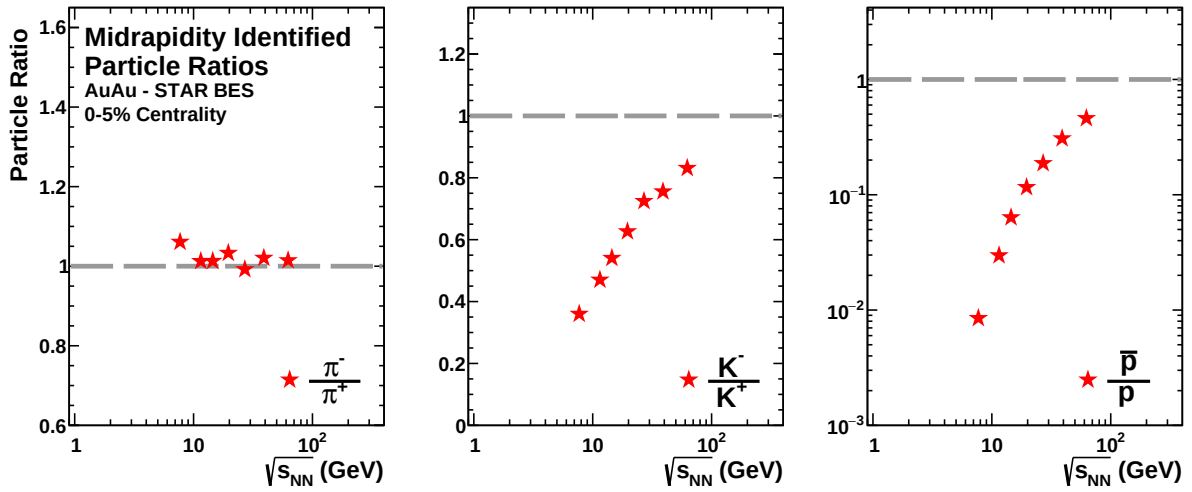

Figure 8.65: The energy dependence of the ratio of midrapidity particle yields from the most central collisions studied in this analysis.

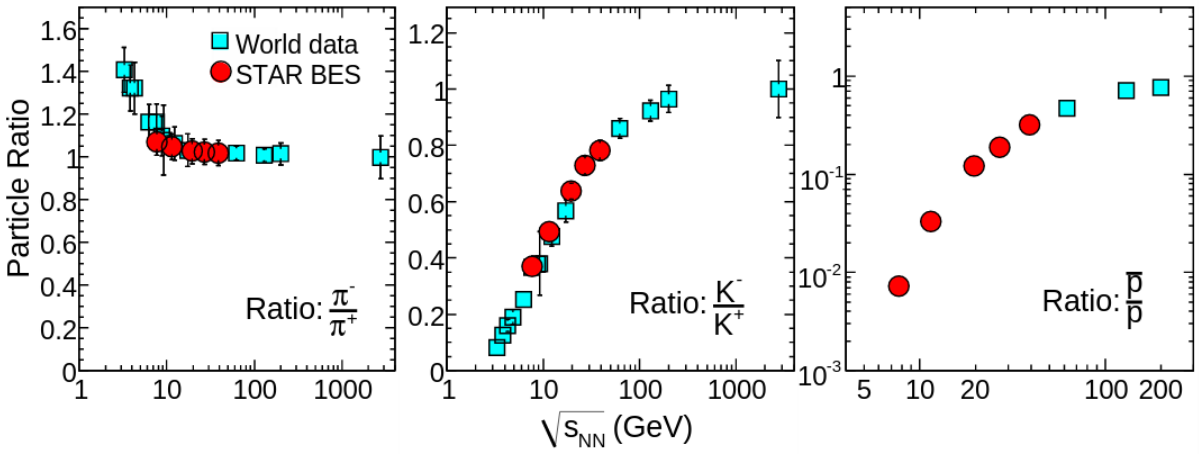

Figure 8.66: Previously reported particle ratios from central heavy-ion collisions as a function of collision energy. The particular relevance are the closed red and open yellow circles as they are results previously reported by STAR and are directly comparable to the results reported from this analysis in figure 8.65. This figure was obtained from [39].

8.6.4 Coulomb Analysis

Previously, we discussed the concave shape of the pion spectra and attributed its observed concavity to contributions from resonances and its Bose-Einstein nature. We have not discussed, however, the subtle difference observed between the low transverse mass shapes of the π^+ and π^- spectra. This difference is due to the electromagnetic charge of the medium produced in the collision. Since the incoming nuclei are positively charged the medium itself has a net positive charge. This results in a Coulomb potential that affects the kinematics of the produced particles. Namely, the velocity of the negatively charged pions is retarded and the velocity of the positively charged pions is accelerated. This effect can be clearly seen in figure 8.67, which shows the ratio of the *uncorrected* pion spectra at midrapidity for each energy studied in this analysis. The uncorrected spectra are used because all of the corrections effectively cancel in the ratio.

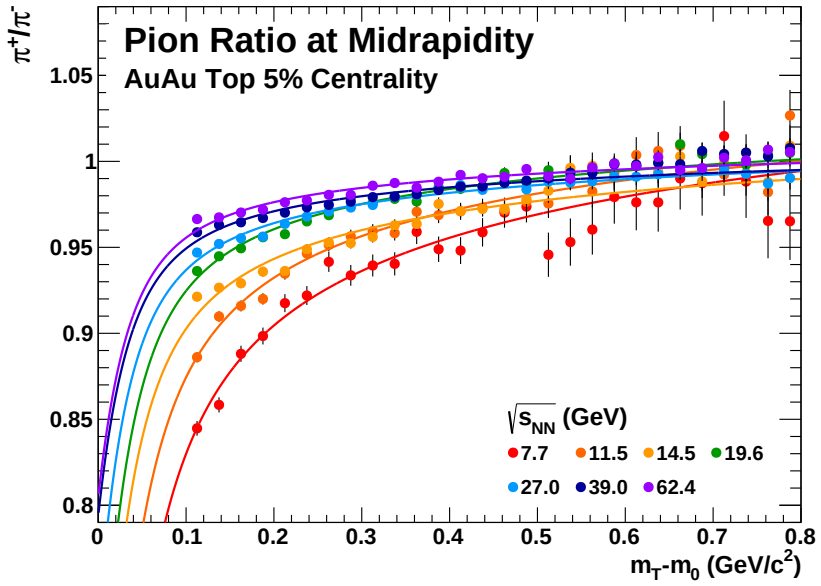

Figure 8.67: The ratio of the uncorrected, midrapidity pion spectra for each collision energy studied in this analysis. The curves are fits of the form of equation 8.7.

Notice that the degree of curvature in the ratio is reduced with higher collision energy. This is due to the reduction in baryon stopping as a function of collision energy discussed in chapter one. Because the net charge of the medium is determined entirely by the charge of the stopped baryons, a reduction in baryon stopping results in a lower net positive

charge. Consequently, the Coulomb potential is reduced and, so too, is the difference between the shapes of the spectra.

The sensitivity of the pion ratio to the Coulomb potential suggests that the ratio can be used to measure it. Indeed, functional forms have been developed to extract the Coulomb potential, V_C, and initial pion ratio, R_i, from the ratio of the pion spectra. The function used to fit the ratios in figure 8.67 is shown in equation 8.7. It was developed in [80] to account for the expanding nature of the medium produced during the collisions of heavy-ions. The pion ratio to be fit is the final state ratio. Quantities in the function which are final state quantities are denoted with the subscript "f." The model assumes that the protons carry the bulk of the net charge. Further, the expansion of the medium is accounted for by introducing an effective Coulomb potential, V_{eff}, that describes the potential due to the protons enclosed by the sphere of pions at a given energy, $E_{\max}$. The function can be adjusted to treat the medium as being static using the condition $E_{\max} \to \infty$ so that $V_{\text{eff}} = V_C$.

$$
\begin{aligned}
R_f\left(E_f\right) &= \frac{E_f - V_{\text{eff}}}{E_f + V_{\text{eff}}} \frac{\sqrt{\left(E_f - V_{\text{eff}}\right)^2 - m_\pi^2}}{\sqrt{\left(E_f + V_{\text{eff}}\right)^2 - m_\pi^2}} \frac{n^+\left(E_f - V_{\text{eff}}\right)}{n^-\left(E_f + V_{\text{eff}}\right)} \\
E_f &= m_T \cosh(y) \\
V_{\text{eff}} &= V_C\left(1 - e^{-E_{\max}/T_p}\right) \\
E_{\max} &= \sqrt{\left(m_p p_\pi / m_\pi\right)^2 + m_p^2} - m_p \\
\frac{n^+\left(E_f - V_{\text{eff}}\right)}{n^-\left(E_f + V_{\text{eff}}\right)} &= R_i \frac{e^{\left(E_f + V_{\text{eff}}\right)/T_\pi} - 1}{e^{\left(E_f - V_{\text{eff}}\right)/T_\pi} - 1} \\
R_i &= \frac{A^+}{A^-}
\end{aligned}
\tag{8.7}
$$

The temperature parameters, T_π and T_p, are fixed in the fits and are obtained from the nominal fits of the pion (average of π^+ and π^- temperatures) and proton spectra respectively. The rapidity, y, is fixed to the center of the rapidity bin being analyzed. In this case, $y = 0$ so that E_f is solely determined by the transverse mass. The quantity p_π

is the momentum of the pion and is computed from E_f.

The only free parameters of the fit are the quantities V_C and R_i. Their energy dependence can be observed in figure 8.68. In addition, results obtained by reanalyzing the pion spectra of previous experiments during the development of equation 8.7 [80, 81] are shown. The results from this analysis are observed to extend the collision energy trends developed by the previous results, as expected.

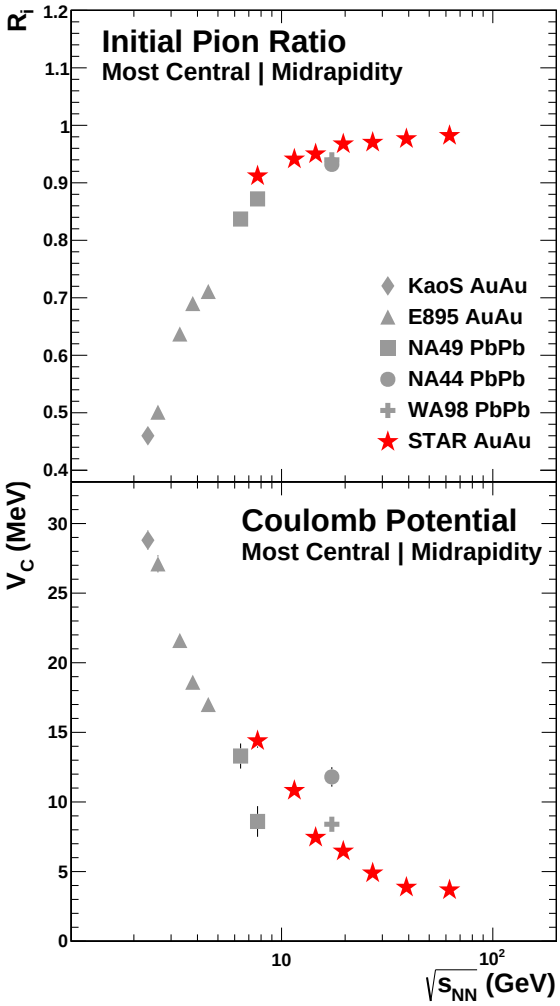

Figure 8.68: The extracted initial pion ratio, R_i (top), and Coulomb potential, V_C (bottom), from this analysis (red stars) as a function of collision energy. The results from previous experiments (gray symbols) were compiled in [80] and provided by [81].

Chapter 9

Conclusion

The goals of this analysis, as set out in the introductory chapter, have been accomplished. Data collected during the BES program at RHIC in 2010, 2011, and 2014 have been analyzed and used to obtain the yields of pions ($\pi^{\pm}$), kaons ($K^{\pm}$), and protons (p,$\bar{p}$) for each of the seven collision energies available, $\sqrt{s_{NN}}$ = 7.7, 11.5, 14.5, 19.6, 27.0, 39.0, and 62.4 GeV. For each energy the yields have been reported differentially as transverse mass spectra in nine centrality bins and over as wide a rapidity range as the STAR detector's acceptance and particle identification capabilities allowed. Each transverse mass spectrum was fit with at least two spectral shapes and the fits were used to obtain the integrated particle yield in each rapidity bin.

The rapidity density distributions of each particle species were then reported for each combination of energy and centrality bin. A Landau hydrodynamic model was used to extract the width of the rapidity density distributions of pions for the most central collisions at each collision energy. The width of the distributions were scaled by the expected value from the Landau hydrodynamic model and presented in the context of the Dale Observable. We observed that the results from this analysis were consistent with the expected, increasing trend of the Dale quantity in the measured energy range. Further, we noted that ongoing studies at lower energies will allow for the confirmation of the previously observed minimum near the lowest energy studied in this analysis. These results, many of which are the first at their respective energies, will allow for a more precise understanding of the longitudinal expansion dynamics of the medium produced in

heavy-ion collisions.

The Landau hydrodynamic fits to the rapidity density distributions also allowed for the extraction of the full phase space yields of pions from the most central collisions at each energy. The full phase space yields of π^+ reported in this analysis mark the first time such measurements have been made in this energy range. Likewise, the full phase space yield of π^- at $\sqrt{s_{NN}}$ = 19.6, 27.0, 39.0, and 62.4 GeV are the first of their kind.

The energy dependence of the midrapidity spectra from the most central collisions and their spectral forms were compared to those previously reported by STAR. The kinetic freeze-out temperatures and average transverse velocities obtained from blast wave fits to the proton and antiproton spectra in this analysis compare favorably to those previously reported. Likewise, the average transverse mass, particle yields, and particle ratios obtained in this analysis were found to be in excellent agreement with those previously reported at midrapidity. This provides confidence that the results from this analysis, which offer a vastly extended kinematic range, will provide a consistent picture of particle production away from midrapidity.

The ratio of the midrapidity pion spectra from the most central events were used to extract the Coulomb potential and initial pion ratio for each energy. In many cases, these are the first measurements of their kind in this energy range. Comparison of these results to those previously reported by other experiments at lower energies show that they smoothly extend the trends into the measured energy range as expected.

Cumulatively, these results advance our knowledge about the complex medium produced in collisions of ultra-relativistic heavy-ions. They offer insights into the medium's chemistry, thermal condition, and expansion properties. These qualities, when studied across multiple collision energies and combined with previous results, can offer insights into the phase structures of QCD matter. Further, the consistent methodology used in this analysis allows for an equally consistent interpretation of the results across a broad range of collision energies. These extend from previous experiments such as NA49 to near the top energy RHIC results.

To accomplish the measurements above several computational challenges were over-

come. For example, a full-featured Glauber Monte Carlo and particle production model were implemented to provide collision centrality determination for the full z-vertex length of the STAR detector - a feat which, although ultimately unneeded, was a first. Further, a data analysis pipeline capable of allowing computation on such a large and varied dataset was conceived, designed, and implemented. The analysis pipeline contains utilities for sourcing and skimming the large data files accessible to the entire STAR Collaboration, characterizing the particle identification capabilities of the STAR TPC and TOF detectors, assessing the acceptance and tracking efficiency characteristics of the detector, and accounting for various background contributions to identified particle spectra. Finally, the analysis pipeline includes a comprehensive methodology for the application of all the necessary corrections to the spectra and data structures designed to efficiently allow for the characterization of the spectra and the resulting rapidity density distributions.

Presently, the analysis pipeline developed in support of the study in this document is being used in the analysis of fixed-target collisions at lower energies. Other parts of the analysis utilities are being utilized for studies involving new detector systems for STAR. It is hoped that the tools built for this analysis will continue to be useful to members of the UC Davis Nuclear Group well beyond the author's tenure.

The author hopes that the care with which this analysis was performed and the comprehensive way in which it was presented offers a small glimpse of the deep intellectual interest he has come to have for the subject, the pleasure he has had working in this field, and the sense of satisfaction that comes with reporting these results.

Bibliography

[1] Enrico Fermi. "High Energy Nuclear Events". In: *Progress of Theoretical Physics* 5.4 (1950), p. 570. DOI: 10.1143/ptp/5.4.570. eprint: /oup/backfile/content_public/journal/ptp/5/4/10.1143/ptp/5.4.570/2/5-4-570.pdf. URL: +%20http://dx.doi.org/10.1143/ptp/5.4.570.

[2] L. D. Landau. "On the multiparticle production in high-energy collisions". In: *Izv. Akad. Nauk Ser. Fiz.* 17 (1953), pp. 51–64.

[3] Ramona Vogt. *Ultrarelativistic Heavy-Ion Collisions*. Amsterdam, The Netherlands: Elsevier B.V., 2007. ISBN: 9780444521965.

[4] R. Hagedorn and J. Rafelski. "Hot hadronic matter and nuclear collisions". In: *Physics Letters B* 97.1 (1980), pp. 136–142. ISSN: 0370-2693. DOI: http://dx.doi.org/10.1016/0370-2693(80)90566-3. URL: http://www.sciencedirect.com/science/article/pii/0370269380905663.

[5] F. Karsch. "Lattice QCD at finite temperature: A status report". In: *Zeitschrift für Physik C Particles and Fields* 38.1 (1988), pp. 147–155. ISSN: 1431-5858. DOI: 10.1007/BF01574529. URL: http://dx.doi.org/10.1007/BF01574529.

[6] A. Bazavov et al. "QCD equation of state to $\mathcal{O}(\mu_B^6)$ from lattice QCD". In: *Phys. Rev. D* 95 (5 Mar. 2017), p. 054504. DOI: 10.1103/PhysRevD.95.054504. URL: https://link.aps.org/doi/10.1103/PhysRevD.95.054504.

[7] T. Matsui and H. Satz. "J/Ψ suppression by quark-gluon plasma formation". In: *Physics Letters B* 178.4 (1986), pp. 416–422. ISSN: 0370-2693. DOI: http://dx.doi.org/10.1016/0370-2693(86)91404-8. URL: http://www.sciencedirect.com/science/article/pii/0370269386914048.

[8] S. Digal, P. Petreczky, and H. Satz. "Quarkonium feed-down and sequential suppression". In: *Phys. Rev. D* 64 (9 Oct. 2001), p. 094015. DOI: 10.1103/PhysRevD.64.094015. URL: https://link.aps.org/doi/10.1103/PhysRevD.64.094015.

[9] Marek Gazdzicki and Mark I. Gorenstein. "On the early stage of nucleus-nucleus collisions". In: *Acta Phys. Polon.* B30 (1999), p. 2705. arXiv: hep-ph/9803462 [hep-ph].

[10] Marek Gazdzicki. "Entropy in nuclear collisions". In: *Zeitschrift fur Physik C Particles and Fields* 66.4 (1995), pp. 659–662. ISSN: 1431-5858. DOI: 10.1007/BF01579641. URL: http://dx.doi.org/10.1007/BF01579641.

[11] C. Alt et al. "Pion and kaon production in central Pb + Pb collisions at 20A and 30A GeV: Evidence for the onset of deconfinement". In: *Phys. Rev. C* 77 (2 Feb. 2008), p. 024903. DOI: 10.1103/PhysRevC.77.024903. URL: https://link.aps.org/doi/10.1103/PhysRevC.77.024903.

[12] Marek Gazdzicki. "Strangeness and pion production as signals of QCD phase transition". In: *Journal of Physics G: Nuclear and Particle Physics* 23.12 (1997), p. 1881. URL: http://stacks.iop.org/0954-3899/23/i=12/a=012.

[13] Katarzyna Grebieszkow. "NA49 and NA61/SHINE experiments: Results and perspectives". In: *Acta Phys. Polon.* B41 (2010), pp. 427–440. arXiv: 0911.1902 [nucl-ex].

[14] Marcus Bleicher. "Evidence for the Onset of Deconfinement from Longitudinal Momentum Distributions? Observation of the Softest Point of the Equation of State". In: (2005). URL: https://arxiv.org/abs/hep-ph/0509314.

[15] J. L. Klay and et al. "Charged pion production in 2A to 8A GeV central Au + Au Collisions". In: *Phys. Rev. C* 68 (5 Nov. 2003), p. 054905. DOI: 10.1103/PhysRevC.68.054905. URL: https://link.aps.org/doi/10.1103/PhysRevC.68.054905.

[16] C. Alt et al. "Pion and kaon production in central Pb + Pb collisions at 20A and 30A GeV: Evidence for the onset of deconfinement". In: *Phys. Rev. C* 77 (2 Feb. 2008), p. 024903. DOI: 10.1103/PhysRevC.77.024903. URL: https://link.aps.org/doi/10.1103/PhysRevC.77.024903.

[17] S. V. Afanasiev et al. "Energy dependence of pion and kaon production in central Pb+Pb collisions". In: *Phys. Rev. C* 66 (5 Nov. 2002), p. 054902. DOI: 10.1103/PhysRevC.66.054902. URL: https://link.aps.org/doi/10.1103/PhysRevC.66.054902.

[18] I.G. Bearden et al. "Charged Meson Rapidity Distributions in Central Au + Au Collisions at $\sqrt{s_{NN}} = 200$ GeV". In: *Phys. Rev. Lett.* 94 (16 Apr. 2005), p. 162301. DOI: 10.1103/PhysRevLett.94.162301. URL: https://link.aps.org/doi/10.1103/PhysRevLett.94.162301.

[19] Anar Rustamov. "The Horn, Kink and Step, Dale: from few GeV to few TeV". In: *Central Eur. J. Phys.* 10 (2012), pp. 1267–1270. DOI: 10.2478/s11534-012-0148-2. arXiv: 1201.4520 [nucl-ex].

[20] Frank S. Crawford. "The hot chocolate effect". In: *American Journal of Physics* 50.5 (1982), pp. 398–404. DOI: 10.1119/1.13080. eprint: http://dx.doi.org/10.1119/1.13080. URL: http://dx.doi.org/10.1119/1.13080.

[21] Steve Mould. "The Surprising Sound Coming From Your Coffee". In: (). URL: https://youtu.be/7Hr_zFdNW5Q?t=103.

[22] Raimond Snellings. "Elliptic flow: a brief review". In: *New Journal of Physics* 13.5 (2011), p. 055008. URL: http://stacks.iop.org/1367-2630/13/i=5/a=055008.

[23] K. Aamodt et al. "Elliptic Flow of Charged Particles in Pb-Pb Collisions at $\sqrt{s_{NN}} = 2.76$ TeV". In: *Phys. Rev. Lett.* 105 (25 Dec. 2010), pp. 252–302. DOI: 10.1103/PhysRevLett.105.252302. URL: https://link.aps.org/doi/10.1103/PhysRevLett.105.252302.

[24] K. H. Ackermann and et al. "Elliptic Flow in $Au + Au$ Collisions at $\sqrt{s_{\mathrm{NN}}} = 130$GeV". In: *Phys. Rev. Lett.* 86 (3 Jan. 2001), pp. 402–407. DOI: 10.1103/PhysRevLett.86.402. URL: https://link.aps.org/doi/10.1103/PhysRevLett.86.402.

[25] Paul Sorensen. "Evidence from identified particles for active quark and gluon degrees of freedom". In: *Journal of Physics G: Nuclear and Particle Physics* 32.12 (2006), S135. URL: http://stacks.iop.org/0954-3899/32/i=12/a=S17.

[26] P. K. Kovtun, D. T. Son, and A. O. Starinets. "Viscosity in Strongly Interacting Quantum Field Theories from Black Hole Physics". In: *Phys. Rev. Lett.* 94 (11 Mar. 2005), p. 111601. DOI: 10.1103/PhysRevLett.94.111601. URL: https://link.aps.org/doi/10.1103/PhysRevLett.94.111601.

[27] J. Adams et al. "Evidence from d + Au Measurements for Final-State Suppression of High-p_T Hadrons in Au + Au Collisions at RHIC". In: *Phys. Rev. Lett.* 91 (7 Aug. 2003), p. 072304. DOI: 10.1103/PhysRevLett.91.072304. URL: https://link.aps.org/doi/10.1103/PhysRevLett.91.072304.

[28] L. Adamczyk et al. "Suppression of Υ production in d+Au and Au+Au collisions at $\sqrt{s_{NN}} = 200$ GeV". In: *Physics Letters B* 735 (2014), pp. 127–137. ISSN: 0370-2693. DOI: https://doi.org/10.1016/j.physletb.2014.06.028. URL: http://www.sciencedirect.com/science/article/pii/S0370269314004316.

[29] S. Chatrchyan et al. "Observation of Sequential Υ Suppression in PbPb Collisions". In: *Phys. Rev. Lett.* 109 (22 Nov. 2012), p. 222301. DOI: 10.1103/PhysRevLett.109.222301. URL: https://link.aps.org/doi/10.1103/PhysRevLett.109.222301.

[30] Y. Aoki et al. "The Order of the Quantum Chromodynamics Transition Predicted by the Standard Model of Particle Physics". In: *Nature* 443 (2006), pp. 675–678. DOI: 10.1038/nature05120. URL: http://dx.doi.org/10.1038/nature05120.

[31] Stephen. Horvat. "Measurement of hadron suppression and study of its connection with vanishing v3 at low $\sqrt{s_{NN}}$ in Au+Au collisions with STAR". In: *Nuclear Physics A* 956 (2016), pp. 838–841. ISSN: 0375-9474. DOI: http://dx.doi.org/10.1016/j.nuclphysa.2016.03.051. URL: http://www.sciencedirect.com/science/article/pii/S0375947416300379.

[32] L. Adamczyk et al. "Elliptic flow of identified hadrons in Au+Au collisions at $\sqrt{s_{NN}} = 7.7 - 62.4$ GeV". In: *Phys. Rev. C* 88 (1 July 2013), p. 014902. DOI: 10.1103/PhysRevC.88.014902. URL: https://link.aps.org/doi/10.1103/PhysRevC.88.014902.

[33] L. Adamczyk et al. "Beam-Energy Dependence of the Directed Flow of Protons, Antiprotons, and Pions in Au+Au Collisions". In: *Phys. Rev. Lett.* 112 (16 Apr. 2014), p. 162301. DOI: 10.1103/PhysRevLett.112.162301. URL: https://link.aps.org/doi/10.1103/PhysRevLett.112.162301.

[34] Masayuki Asakawa and Masakiyo Kitazawa. "Fluctuations of conserved charges in relativistic heavy ion collisions: An introduction". In: *Progress in Particle and Nuclear Physics* 90 (2016), pp. 299–342. ISSN: 0146-6410. DOI: https://doi.org/10.1016/j.ppnp.2016.04.002. URL: http://www.sciencedirect.com/science/article/pii/S0146641016300023.

[35] M. A. Stephanov. "Non-Gaussian Fluctuations near the QCD Critical Point". In: *Phys. Rev. Lett.* 102 (3 Jan. 2009), p. 032301. DOI: 10.1103/PhysRevLett.102.032301. URL: https://link.aps.org/doi/10.1103/PhysRevLett.102.032301.

[36] M. A. Stephanov. "Sign of Kurtosis near the QCD Critical Point". In: *Phys. Rev. Lett.* 107 (5 July 2011), p. 052301. DOI: 10.1103/PhysRevLett.107.052301. URL: https://link.aps.org/doi/10.1103/PhysRevLett.107.052301.

[37] M A Stephanov. "QCD critical point and event-by-event fluctuations". In: *Journal of Physics G: Nuclear and Particle Physics* 38.12 (2011), p. 124147. URL: http://stacks.iop.org/0954-3899/38/i=12/a=124147.

[38] Xiaofeng Luo. "Energy Dependence of Moments of Net-Proton and Net-Charge Multiplicity Distributions at STAR". In: *PoS* CPOD2014 (2015), p. 019. arXiv: 1503.02558 [nucl-ex].

[39] L. Adamczyk et al. "Bulk Properties of the Medium Produced in Relativistic Heavy-Ion Collisions from the Beam Energy Scan Program". In: (2017). arXiv: 1701.07065 [nucl-ex].

[40] H. Hahn, E. Forsyth, and et. al. "The RHIC Design Overview". In: *Nuclear Instruments and Methods in Physics Research A* 499 (2003), pp. 245–263. DOI: 10.1016/S0168-9002(02)01938-1.

[41] Howard Matis. "STAR Coordinate System". In: *STAR Note csn0121* (1993). URL: http://www.star.bnl.gov/public/archives/integration/STAR/STAR_Notes/csn0121.pdf.

[42] K.H. Ackermann et. al (STAR Collaboration). "STAR Detector Overview". In: *Nuclear Instruments and Methods in Physics Research A* 499 (2003), pp. 624–632. DOI: 10.1016/S0168-9002(02)01960-5.

[43] Alex Schmah. Collaboration Communications.

[44] M. Anderson et. al (STAR Collaboration). "The STAR Time Projection Chamber: A Unique Tool for Studying High Multiplicity Events at RHIC". In: *Nuclear Instruments and Methods in Physics Research A* 499 (2003), pp. 659–678. DOI: 10.1016/S0168-9002(02)01964-2.

[45] Gene Van Buren. Collaboration Communications.

[46] K.A. Olive et. al. "Particle Data Group". In: *Chinese Physics C* 38(9) (2014), p. 090001. DOI: 10.1088/1647-1137/38/9/090001.

[47] Hans Bichsel. "A Method to Improve Tracking and Particle Identification in TPCs and Silicon Detectors". In: *Nuclear Instruments and Methods in Physics Research A* 562 (2006), pp. 154–197. DOI: 10.1016/j.nima.2006.03.009.

[48] The STAR TOF Collaboration. "Proposal for a Large Area Time of Flight System for STAR". In: (2004). URL: https://www.star.bnl.gov/public/tof/publications/TOF_20040524.pdf.

[49] F.Geurts, M. Shao, and B. Bonner et. al. "Performance of the Prototype MRPC detector for STAR". In: *Nuclear Instruments and Methods in Physics Research A* 533 (2004), pp. 60–64. DOI: 10.1016/j.nima.2004.07.001.

[50] W.J. Llope and F.Geurts et. al. "The TOFp/pVPD Time-Of-Flight System for STAR". In: *Nuclear Instruments and Methods in Physics Research A* 522 (2004), pp. 252–273. DOI: 10.1016/j.nima.2003.11.414.

[51] Micahael L. Miller et. al. "Glauber Modeling in High Energy Nuclear Collisions". In: *Annual Review of Nuclear and Particle Science* 57 (2007), pp. 205–243. DOI: 10.1146/annurev.nucl.57.090506.123020.

[52] R. J. Glauber. "High-Energy Collision Theory, Lectures in Theoretical Physics". In: *W.E. Brittin, Interscience: New York* 1 (1959), p. 315. URL: http://www.worldscientific.com/doi/pdf/10.1142/9789814415293_others01.

[53] W. T. Milner, C. E. Bemis, and F. K. McGowan. "Quadrupole and hexadecapole deformations in the actinide nuclei". In: *Phys. Rev. C* 16 (4 Oct. 1977), pp. 1686–1687. DOI: 10.1103/PhysRevC.16.1686. URL: http://link.aps.org/doi/10.1103/PhysRevC.16.1686.

[54] C. E. Bemis et al. "$E2$ and $E4$ Transition Moments and Equilibrium Deformations in the Actinide Nuclei". In: *Phys. Rev. C* 8 (4 Oct. 1973), pp. 1466–1480. DOI: 10.1103/PhysRevC.8.1466. URL: http://link.aps.org/doi/10.1103/PhysRevC.8.1466.

[55] H. DE Vries, C.W. DE Jager, and C. DE Vries. "Nuclear Charge-Density-Distribution Parameters From Elastic Electron Scattering". In: *Atomic Data and Nuclear Data Tables* 36 (3 May 1987), pp. 495–536. DOI: 10.1016/0092-640X(87)90013-1. URL: http://www.sciencedirect.com/science/article/pii/0092640X87900131.

[56] Beat Hahn, D. G. Ravenhall, and Robert Hofstadter. "High-Energy Electron Scattering and the Charge Distributions of Selected Nuclei". In: *Phys. Rev.* 101 (3 Feb. 1956), pp. 1131–1142. DOI: 10.1103/PhysRev.101.1131. URL: http://link.aps.org/doi/10.1103/PhysRev.101.1131.

[57] R.C. Barrett. "Nuclear Charge Distributions". In: *Reports on Progress in Physics* 37 (1 1974), pp. 1–54. DOI: 10.1088/0034-4885/37/1/001. URL: http://iopscience.iop.org/article/10.1088/0034-4885/37/1/001.

[58] P. Moller et al. “Nuclear Grount-State Masses and Deformations”. In: *Atomic Data and Nuclear Data Tables* 59 (2 1995), pp. 185–381. DOI: 10.1006/adnd.1995.1002. URL: http://www.sciencedirect.com/science/article/pii/S0092640X85710029.

[59] H. Goldstein, P. Poole, and J. Safko. *Classical Mechanics Third Edition*. Pearson, 2001. ISBN: 9780201657029.

[60] P.G. Jones and et al. “Hadron yields and hadron spectra from the {NA49} experiment”. In: *Nuclear Physics A* 610 (1996). Quark Matter ’96, pp. 188–199. ISSN: 0375-9474. DOI: http://dx.doi.org/10.1016/S0375-9474(96)00354-5. URL: http://www.sciencedirect.com/science/article/pii/S0375947496003545.

[61] A. Bialas, M. Bleszynki, and W. Czyz. “Multiplicity distributions in nucleus-nucleus collisions at high energies”. In: *Nuclear Physics B* 111 (1976), p. 461.

[62] Dmitri Kharzeev and Marzia Nardi. “Hadron production in nuclear collisions at {RHIC} and high-density {QCD}”. In: *Physics Letters B* 507.1 - 4 (2001), pp. 121–128. ISSN: 0370-2693. DOI: http://dx.doi.org/10.1016/S0370-2693(01)00457-9. URL: http://www.sciencedirect.com/science/article/pii/S0370269301004579.

[63] B. B. Back, M. D. Baker, and M. Ballintijn. “Collision geometry scaling of Au + Au pseudorapidity density from $\sqrt{s_{NN}} = 19.6$ to 200 GeV”. In: *Phys. Rev. C* 70 (2 Aug. 2004), p. 021902. DOI: 10.1103/PhysRevC.70.021902. URL: http://link.aps.org/doi/10.1103/PhysRevC.70.021902.

[64] Christer Fuglesang. “UA5 MULTIPLICITY DISTRIBUTIONS AND FITS OF VARIOUS FUNCTIONS”. In: *Multiparticle dynamics: A meeting ground between particle and statistical physics. A dialog between experiment and theory. Festschrift for Leon van Hove. Proceedings, Conference, La Thuile, Italy, March 20-22, 1989*. 1989. URL: http://ccdb5fs.kek.jp/cgi-bin/img/allpdf?198912013.

[65] T. Ulilrich and Z. Xu. “Treatment of Errors in Efficiency Calculations”. In: (2008). URL: arXiv:physics/0701199%20[physics.data-an].

[66] Evan W. Sangaline. "Ups and Downs with a Bit of Strange: A STAR Analysis of π/K/p Spectra at High p_T in Au+Au collisions at $\sqrt{s_{NN}}$ = 7.7, 11.5, 19.6, 27.0, 39.0, and 62.4 GeV and Its Physics Implications". In: (2014). URL: http://nuclear.ucdavis.edu/thesis/EWS_thesis_v5.pdf.

[67] Daniel Brandenburg and Evan Sangaline et. al. "Analysis Note: Charged Hadron R_{CP} in the RHIC Beam Energy Scan". In: (2016). URL: http://www.star.bnl.gov/protected/lfspectra/jdb/AN/bes_rcp/an.pdf.

[68] S. Agostinelli et. al. "GEANT4 - a simulation toolkit". In: *Nuclear Instruments and Methods in Physics Research A* 506 (2003), pp. 250–303. DOI: 10.1016/S0168-9002(03)01368-8. URL: http://geant4.web.cern.ch/geant4/.

[69] S.A. Bass et. al. "Microscopic Models for Ulatrarelativistic Heavy Ion Collisions". In: *Prog. Part. Nucl. Phys.* 41 (1998), p. 255. DOI: 10.1016/S0146-6410(98)00058-1. URL: http://www.sciencedirect.com/science/article/pii/S0146641098000581.

[70] M. Bleicher et. al. "Relativistic hadron-hadron collisions in the ultra-relativistic quantum molecular dynamics model". In: *J. Phys. G: Nucl. Part. Phys.* 29 (1999), p. 1859. URL: http://iopscience.iop.org/0954-3899/25/9/308.

[71] B. Abelev et. al (STAR Collaboration). "Systematic measurements of identified particle spectra in pp, d + Au, and Au + Au collisions at the STAR detector". In: *Phys. Rev. C* 79 (3 Mar. 2009), p. 034909. DOI: 10.1103/PhysRevC.79.034909. URL: http://link.aps.org/doi/10.1103/PhysRevC.79.034909.

[72] The STAR Collaboration. "Bulk Properties of the Medium Produced in Relativistic Heavy-Ion Collisions from the Beam Energy Scan Program". In: (2017). arXiv: 1701.07065 [nucl-ex]. URL: http://arxiv.org/abs/1701.07065v1.

[73] Roppon Picha. "Charged Hadron Distributions in 19.6 GeV Au+Au Collisions". In: (2005). URL: http://nuclear.ucdavis.edu/thesis/RP_thesis.pdf.

[74] M. Hofmann et al. "Stopped Δ-matter source in heavy-ion collisions at 10 GeV/nucleon?" In: *Phys. Rev. C* 51 (4 Apr. 1995), pp. 2095–2098. DOI: 10.1103/PhysRevC.51.2095. URL: https://link.aps.org/doi/10.1103/PhysRevC.51.2095.

[75] Josef Sollfrank, Peter Koch, and Ulrich Heinz. "The influence of resonance decays on the pT spectra from heavy-ion collisions". In: *Physics Letters B* 252.2 (1990), pp. 256–264. ISSN: 0370-2693. DOI: http://dx.doi.org/10.1016/0370-2693(90)90870-C. URL: http://www.sciencedirect.com/science/article/pii/037026939090870C.

[76] Jennifer Lynn Klay. "Transverse Mass and Rapidity Spectra of Pions and Protons from Au+Au Collisions at the Alternating Gradient Synchrotron". In: (2001). URL: http://nuclear.ucdavis.edu/thesis/JLK_thesis.pdf.

[77] Ekkard Schnedermann, Josef Sollfrank, and Ulrich Heinz. "Thermal phenomenology of hadrons from 200A GeV S+S collisions". In: *Phys. Rev. C* 48 (5 Nov. 1993), pp. 2462–2475. DOI: 10.1103/PhysRevC.48.2462. URL: https://link.aps.org/doi/10.1103/PhysRevC.48.2462.

[78] Philip J. Siemens and John O. Rasmussen. "Evidence for a Blast Wave from Compressed Nuclear Matter". In: *Phys. Rev. Lett.* 42 (14 Apr. 1979), pp. 880–883. DOI: 10.1103/PhysRevLett.42.880. URL: https://link.aps.org/doi/10.1103/PhysRevLett.42.880.

[79] Djamel Ouerdane. "Charged Pion and Kaon Production in Central Au+Au Collisions at $\sqrt{s_{NN}} = 200$ GeV". In: (2003). URL: http://www4.rcf.bnl.gov/brahms/WWW/thesis/djam_thesis.ps.

[80] D. Cebra et al. "Coulomb effect in Au+Au and Pb+Pb Collisions as a Function of Collision Energy". In: (2014). arXiv: 1408.1369 [nucl-ex]. URL: http://arxiv.org/abs/1408.1369v1.

[81] Daniel Cebra. Private Communications.